

# **Increasing the Resource Efficiency of the Aluminum Extrusion Industry**

by

Gregory J. Oberhausen

A dissertation submitted in partial fulfillment  
of the requirements for the degree of  
Doctor of Philosophy  
(Mechanical Engineering)  
in the University of Michigan  
2023

Doctoral Committee:

Assistant Professor Daniel R. Cooper, Chair  
Professor Albert Shih  
Professor Alan Taub  
Professor Ming Xu

Gregory J. Oberhausen

oberhg@umich.edu

ORCID iD:

0000-0002-9737-4839

@Gregory J. Oberhausen 2023

## **Dedication**

This dissertation is dedicated to my family and friends who encouraged and supported me through the many years of my educational journey. Special thanks to my parents for giving me the courage to pursue this path, and for instilling in me a desire to learn.

## **Acknowledgements**

First and foremost, I would like to thank my advisor, Dr. Daniel R. Cooper. Without his advice and guidance this journey would not have been possible.

Special thanks to the researchers and staff at both Michigan Technological University (MTU) and Lightweight Innovations for Tomorrow (LIFT) for their support and patience in helping to plan and carry out the respective physical extrusion trials.

To the countless extrusion industry leaders who gave me their time and allowed me to learn firsthand the intricacies of this historied field, thank you. I would like to especially thank Gemini Group Thumb Tool & Engineering for their advice over the entire length of my work, and to Norsk Hydro for providing regular advice through our National Science Foundation - Partnerships for Innovation project.

Finally, thanks to all the funders that made this work possible: Michigan Translational Research & Commercialization (MTRAC), Ford Motor Company, and the National Science Foundation (NSF).

# Table of Contents

Dedication .....	ii
Acknowledgements .....	iii
List of Figures .....	x
List of Tables .....	xvii
List of Appendices .....	xix
Abstract .....	xx
<b>Chapter 1. Introduction.....</b>	<b>1</b>
1.1 The contribution of the aluminum industry to climate changes.....	1
1.2 Current opportunities and efforts to reduce aluminum environmental impacts .....	3
1.3 The contribution of the aluminum extrusion industry to climate change .....	3
1.4 The aluminum extrusion process .....	4
1.5 Thesis Structure .....	7
<b>Chapter 2. Reducing the Environmental Impacts of Aluminum Extrusion .....</b>	<b>9</b>
2.1 Section introduction .....	9
2.1.1 Previous work on the environmental impacts and costs of extrusion .....	11
2.1.2 Scope of Work .....	12
2.2 Environmental impact and cost models for aluminum extrusion.....	12
2.2.1 Case study methodology .....	13
2.2.2 Intrinsic environmental impacts and costs .....	15
2.2.3 Case study results.....	18
2.2.4 Global parametric models of extrusion process impacts and costs .....	21
2.3. Material flow analysis of the North American extrusion industry.....	26

2.3.1 Constructing a map of aluminum extrusion flows .....	26
2.3.2 MFA data reconciliation (S4) .....	26
2.3.3 MFA results .....	28
2.4 Section discussion .....	30
2.4.1 Reducing billet preheating and extrusion press energy requirements .....	30
2.4.2 Opportunities for material efficiency .....	31
2.4.3 Scale of the opportunity and industry trends.....	33
2.5 Section conclusion .....	34
<b>Chapter 3. Modeling the Strength of Aluminum Extrusion Transverse Welds using the Film Theory of Solid-State Welding.....</b>	<b>35</b>
3.1 Section introduction .....	36
3.1.1 Previous work on reducing transverse weld scrap .....	37
3.1.2 Candidate welding models for predicting the transverse weld strength.....	38
3.1.3 Scope of this work .....	39
3.2 Derivation of the transverse weld strength model.....	39
3.2.1 Testing the new model assumptions: Fragmentation of billet-billet interface oxides.....	42
3.2.2 Updating the C-A model.....	48
3.2.3 Calculating the local transverse weld strength.....	51
3.3 Methodology for evaluating transverse weld strengths .....	52
3.3.1 Extrusion trials and alloys.....	52
3.3.2 Evaluating the experimental weld strengths .....	54
3.3.3 Determining model inputs.....	55
3.3.4 Model implementation .....	58
3.4 Results: Experimental and modeled weld strengths.....	60
3.4.1 Weld strength in the round rod and rectangular bar.....	60
3.4.2 Weld strengths in the complex hollow extrusion.....	63

3.4.3 Weld fracture morphology .....	64
3.4.4 Sources of error.....	68
3.5 Section discussion .....	68
3.5.1 Accuracy of the new model .....	68
3.5.2 Industry implications.....	69
3.6. Section conclusions.....	71
<b>Chapter 4. Reducing the Aluminum Extrusion Transverse Weld Length.....</b>	<b>72</b>
4.1 Reducing aluminum extrusion transverse weld process scrap .....	72
4.1.1 Section background.....	73
4.1.2 Section methodology.....	76
4.1.3 Section results .....	83
4.1.4 Section discussion .....	85
4.1.5 Section conclusions.....	88
4.2 Exploring a novel process for reducing aluminum extrusion process scrap using profiled dummy blocks and billets.....	88
4.2.1 Section introduction .....	89
4.2.2 Design process for profiled dummy blocks that deliver front-end scrap savings .....	92
4.2.3 Testing the design method .....	96
4.2.4 Section experimental results and discussion .....	109
4.2.5 Section conclusions and future work .....	113
<b>Chapter 5. Conclusions and Future Work.....</b>	<b>114</b>
5.1 Contributions of this thesis .....	114
5.2 Future work.....	115
5.2.1 Reducing the effects of quench distortion in extruded profiles .....	115
5.2.2 The potential benefits of improved transverse weld strength modeling .....	121
5.2.3 Overcoming the hurdles for implementation of novel profiled dummy blocks into industry..	123

<b>Appendices.....</b>	<b>126</b>
<b>Appendix A: Reducing the Environmental Impacts of Aluminum Extrusion – Supporting Information</b>	<b>127</b>
A.1 Extrusion case study equipment and measuring the transverse weld length.....	127
A.1.1 Extrusion equipment .....	127
A.1.2 Measuring the transverse weld length of the case study profiles.....	129
A.2 European extruder dataset.....	129
A.2.1 Data representation .....	130
A.2.2 Derivation of inventory values for Table 3 of main article.....	132
A.3 Global parametric model and uncertainty analysis .....	132
A.3.1 Mechanical energy required for extrusion .....	133
A.3.2 Example profile inputs .....	134
A.3.3 Uncertainty analysis.....	135
A.4 Data Reconciliation.....	136
A.4.1 Wire frame map .....	137
A.4.2 Initial values.....	137
A.4.3: Methods for calculating residuals in the least squares optimization.....	141
A.4.4 Optimization results .....	142
A.5 Flow estimate sources and derivations.....	143
A.5.1 Summary of aluminum processing and extrusion billet making process yields .....	143
A.5.2 Extrusion to fabrication.....	144
A.5.3 Shape and alloy of extruded goods .....	145
A.5.4 Fabrication to end-use goods .....	146
A.5.4 End-use products indirect trade.....	148
A.5.4.2 Transport quantity extrusion estimates .....	150
A.6 MFA structure.....	152



A.6.1 Full matrix .....	152
A.6.2 Data confidence weighting.....	155
A.6.3 Matrix node and flow data with weighting .....	155
A.6.4 MFA Data Uncertainty.....	162
A.7 Effect of billet geometry on the extrusion energy and force requirement.....	162
A.8 References .....	165
<b>Appendix B. Weld Shear Strengths in Accumulative Roll Bonding .....</b>	<b>168</b>
<b>Appendix C. An Exploratory Study on Reducing Transverse Weld Scrap from Complex Extrusions Using Profiled Billets and Dummy Blocks.....</b>	<b>169</b>
C.1 Section introduction .....	169
C.2 Conventional tooling design.....	172
C.3 Section methodology.....	173
C.3.1 Profile studied .....	173
C.3.2 FEA .....	174
C.4 Section results .....	178
C.4.1 Technical Trade-offs .....	178
C.4.2 Financial Trade-offs .....	180
C.4.3 Environmental Impacts.....	186
C.3.3 Experimental Validation of FEA.....	187
C.3.4 Dummy block design .....	189
C.5 Section discussion .....	197
C.5.1 Opportunities .....	197
C.5.2 Barriers to Implementation.....	199
C.6 Conclusion and Next steps .....	201
C.7 References .....	202
<b>Appendix D. Previous LIFT Rectangular Bar Trial Using DEFORM Point Tracking Algorithm. 205</b>	

D.1 DEFORM Model.....	205
D.2 The Billet Assembly.....	206
D.3 Point Tracking and Billet Design .....	207
D.4 LIFT Trial 1 Results.....	208
D.5 Learnings and the Design of the Second Trial .....	210
<b>Bibliography .....</b>	<b>212</b>

## List of Figures

Figure 1.1: The (a) global anthropogenic emissions by category, and (b) the breakdown of industrial emissions (IEA, 2008). Image adapted from Zhu (2021). .....	1
Figure 1.2: The embodied emissions of the primary production of the five key materials (aluminum, steel, plastic, paper, concrete) for global anthropogenic emissions (Cooper and Gutowski, 2017).....	2
Figure 1.3: Typical process flow at aluminum extruder (Tomczyk, 2019).....	5
Figure 1.4: (a) Example solid die stack. (b) Example hollow die stack. (MMG Extrusions, 2023).....	6
Figure 2.1: Schematic of consecutive direct extrusion (a) before and (b) after extrusion of a new billet ..	11
Figure 2.2: System boundaries for environmental impact and cost models.....	13
Figure 2.3: Active power, cumulative energy and ram force during extrusion of case study profiles. ....	19
Figure 2.4: The (a) Global Warming Potential (GWP), (b) Cumulative Energy Demand (CED) and, (c) Costs of the two case study profiles.....	20
Figure 2.5: Sensitivity analysis on the costs, GWP, and CED of an automotive AA6082 battery tray profile (Table A4). The star in each plot represents the current industry standard. ....	25
Figure 2.6: Top: Sankey diagram representation of the material flow of aluminum extrusions in North America (N.A.: U.S. and Canada) in 2018 (Note: Aluminum alloying is done during billet production and it is only placed after extrusion here to clearly show the flow of fabricated profiles). Bottom: The flow of aluminum for a typical extrusion from DC cast log to unfabricated aluminum profile showing the range of scrap generated at each stage of the extrusion process as a red hashed area. ....	28
Figure 3.1: The formation and strength of aluminum extrusion transverse welds.....	35
Figure 3.2: The formation of a transverse weld in a solid aluminum profile extruded from single-piece billets. Note: The micrographs are on welds created using anodized billets. ....	36
Figure 3.3: The driving mechanisms of Cooper and Allwood’s (2014a) original model. The equations for the model inputs highlighted in red must be updated to account for the non-plane strain deformation at the billet-billet interface during transverse weld formation. Figure inspired by Kolpak et al. (2019). ....	41
Figure 3.4: Shear lag modeling of oxide fragmentation at the billet-billet interface. Final oxide fragment lengths are expected to vary from $\lambda_1$ to $2\lambda_1$ . ....	44
Figure 3.5: Experimentally observed oxide fragmentation of 0.9 $\mu\text{m}$ anodized billets in (a) single-piece and (b) two-piece billet extrusion. Weld line % oxide is total length of observed oxide along weld line (irrespective of fragmentation mode) divided by the straight line or circular weld length. It is not indicative of weld area % oxide in cases of interface buckling.....	46

Figure 3.6: Microscopy of circumferential oxide fragmentation for single-piece billet extrusion. (a) Optical microscopy showing (near complete) coherent oxide fragmentation. (b) Optical microscopy showing incoherent oxide fragmentation. (c) Optical and SEM (inset) of the weld nose (12% new billet). (d) SEM of oxides at 41% new billet.....	47
Figure 3.7: Calculating the minimum micro-extrusion pressure ( $p_{ex}$ ) .....	50
Figure 3.8: Implementation of the new transverse weld strength model. ....	52
Figure 3.9: Flow curves for the aluminum alloys used in the extrusion trials. ....	54
Figure 3.10: Shear test sample machining process using wire EDM.....	54
Figure 3.11: Comparison of experimental and simulated weld geometries.....	56
Figure 3.12: DEFORM <sup>®</sup> simulation output is used to calculate the local traction vector ( $Tt$ ) and unit normal vector ( $nt$ ).....	58
Figure 3.13: Tracking the deformation conditions across the major axis plane on the billet-billet interface during extrusion of the rectangular bar. Modeled for $\gamma=0$ . ....	60
Figure 3.14: Experimental and modeled aluminum extrusion transverse weld strengths for the AA6061 round bar and rectangular bar profiles. ....	62
Figure 3.15: Surface exposures and stresses along material streamlines from the die entrance to exit. Welding can occur when the normal contact stress exceeds the threshold (minimum). Modeled for $\gamma=0$ . 63	63
Figure 3.16: Predicted (left, $\gamma=0$ ) transverse weld strengths versus experimental weld visibility (right) for the complex multi-hollow profile. ....	64
Figure 3.17: Shear test fracture morphology. The samples were extracted from the AA6061 round bar, single-piece billet extrusion, with butt shear (except where specified otherwise). ....	65
Figure 3.18: Electron Backscatter Diffraction (EBSD) images of the grain structure at the transverse weld and in the bulk of the profile. All quoted weld strengths are experimental (not modeled).....	68
Figure 3.19: Plot of principal in-plane strain histories for points along the bonding interface.....	70
Figure 4.1: Major sources of scrap in consecutively extruded billets. ....	74
Figure 4.2: Experimental, plasticine clay direct extrusion press used in this study. ....	76
Figure 4.3: From left to right: Axisymmetric die set; rectangular die set; complex dies with dual-circle die on top, cross die on bottom. ....	76
Figure 4.4: Flow curves of four different colors of plasticine. ....	77
Figure 4.5: Axisymmetric solid rod ring compression test results: experimental data points for different lubricants, and simulated curves for different modeled friction levels. ....	78
Figure 4.6: (a) Transverse weld geometry formed in conventional extrusion (top) and profiled dummy block and billet extrusion (bottom). (b) Section view of elliptical concave ram used in profiled dummy block and billet experiments. (c) The convex forming element used as part of the profiled billet mold. ....	79

Figure 4.7: Estimated velocity field for solid axisymmetric extrusion. Velocity discontinuities are seen as circular arcs on this 2D image.....	80
Figure 4.8: Incremental cross-sectional “salami-slicing” cuts of the cross profile.....	82
Figure 4.9: Transverse weld lengths in axisymmetric solid profiles at varying extrusion ratios, die angles, and friction coefficients. ....	83
Figure 4.10: Transverse weld lengths against (a) the ratio of profile cross sectional perimeter to area and (b) the profile minimum section thickness. All profiles represent an extrusion ratio of 4.....	84
Figure 4.11: Transverse weld lengths in axisymmetric solid profiles and rectangular solid profiles at varying extrusion ratios and die angles.....	84
Figure 4.12: Transverse weld profiles produced from (a) flat and (b) concave profiled dummy blocks....	85
Figure 4.13: Longitudinal cross sectional cut after partial extrusion of second billet to show DMZ of (a) Extrusion ratio = 4, and (b) Extrusion ratio = 25. DMZ is in green. Aspect ratio of billets (diameter : initial length) = 1.....	86
Figure 4.14: A (a) floating and (b) fixed dummy block (Robbins et al., 2016).....	90
Figure 4.15: The (a) conventional and (b) proposed extrusion process chains.....	91
Figure 4.16: (a) Profiled dummy block and billet design process. (b) The velocity field method for generating the idealized profiled dummy block and billet geometry.....	93
Figure 4.17 Onset of cracking observed on room temperatures (a) cylinder, (b) flange, (c) taper, and (d) shear samples in Christiansen et al. (2017).....	95
Figure 4.18: Comparison of experimental and simulated weld geometries on the (a) base-case round bar, (b) square hollow, (c and d) rectangular bar, and (e) multi-hollow profiles.....	98
Figure 4.19: Contour maps with plotted profile-specific billet designs for the (a) base-case round bar, (b, c, and d) multi-hollow, (e and f) rectangular bar, and (g, h and i) square hollow profiles.....	100
Figure 4.20: The two-piece billet assemblies for the (a and b) round bar and (c and d) rectangular bar profiles.....	102
Figure 4.21: The base-case round bar profile-specific billet design 2 plotted against the contour maps of the (a) small and (b) large round bar profiles.....	103
Figure 4.22: The simulated plastic strain expected on the (a) base-case round bar profile-specific dummy block design 2 and (b) base-case round bar profile-specific dummy block design 3, as well as the (c) the multi-hollow profile-specific dummy block design.....	104
Figure 4.23: Simulated damage values across four explored damage models during billet forging for the base-case round bar profile-specific billet design 3, for 50% weld length reduction. The billet is AA6061 with an initial diameter of $\varnothing 88.9$ mm, a length of 200 mm, and was heated to a temperature of 425°C prior to forging.....	106

Figure 4.24: Experimental samples tested in the ductile damage derivation procedure. ....	107
Figure 4.26: Expected and achieved weld length reductions using profiled billets. The base-case profile-specific billet designs 1 and 2 were different designs intended to achieve a 75% weld length reduction in the base case (mid-sized) round bar. 1: This same design was then also used during extrusion of the smaller and larger diameter round bars. 2: The multi-hollow profile was not evaluated experimentally due to unavailability of the press and die.....	109
Figure 4.25: Experimental conventional and profiled billet transverse weld geometries. *The small and large round bar profile billet designs were not profile-specific, and instead were designed for the base-case round bar (extrusion ratio = 15). ....	109
Figure 4.27: Longitudinal cross section of the conventional billet and profile-specific billet design 2 welds for the base-case round bar profile produced experimentally. ....	110
Figure 4.28: (a) The location of the back-end defect in the conventional and (b) base-case round bar profile-specific design 3, aimed at a 50% weld length reduction, given varying billet skin thicknesses. ....	112
Figure 5.1: Aluminum phase diagram showing the typical route from (1) post-extrusion temperatures through the (2) quench and (3) aging processes (Techno, 2018). ....	116
Figure 5.2: Example of significant plastic strain on quench cooled Ford F150 battery tray side rail profile (Ford, 2021). Left: Normal, Right: Quench distorted. ....	117
Figure 5.3: Ford F150 side rail profile, and the six locations that tensile test samples were taken. ....	118
Figure 5.4: Cooling rate of the six sample locations on the Ford F150 battery tray side rail profile across a range of quench film coefficients.....	119
Figure 5.5: Stress-strain curves from tensile tests at the six sample locations on the Ford F150 side wall. ....	120
Figure 5.6: Example of conformal channel die, with channels carrying quench solution from the outside of the die through the die bridges and down through the mandrel into the profile's hollows.....	121
Figure 5.7: Outline of (a) machined billet dummy block trial, and (b) closed-die forging of profiled billet trial. ....	125
Figure A1: Example cross sections of case study profiles (a) rectangular solid (70% billet 2 area) and (b) 80-20 T-slot bar (23% billet 2 area) used to measure the transverse weld length. ....	129
Figure A2: Comparison of energy consumption for case study and European extruder profiles. ....	131
Figure A3: Ideal force vs displacement graph for extrusion of one billet.....	133
Figure A4: Uncertainty in Cost, GWP and CED for the modeled profile. ....	136
Figure A5: Wireframe map of aluminum extrusion industry.....	137

Figure A6: Optimization result for different $x_l$ values (in kt) for equation 5 (original residual calculation from Kopec et al. and Zhu et al.) and equation A6 (new, average, residual calculation used in this work). .....	142
Figure A7: The feasibility and objective function value of the optimization as it converged to the final solution.....	143
Figure A8: The flow of extrusions to end-use categories, by alloy. ....	146
Figure A9: Network of nodes and flows represented in matrix form. Data entries represent the existence of flow between two nodes.....	154
Figure A10: The average residuals of the flows representing the 2018 North American aluminum extrusion industry. The magnitude of the residuals is indicated by the darkness of the flow.....	162
Figure A11: The effect of billet diameter (at a constant billet volume) on the mechanical energy and maximum ram force requirement. The various plots show how the relationships change for large versus small profile cross-sectional area (top versus bottom) and large versus small billet volumes (left versus right). The above plots were constructed for an aluminum material with $Y_f = 15$ MPa (at the extrusion temperature) and a profile geometry equivalent to $K_x = 1.0751$ . In all cases, the press energy was calculated assuming that the mechanical energy accounted for 5% of the total press energy. ....	164
Figure A12: Ram force versus displacement graph for equal volume billets. Billets are $\varnothing 8''$ and $\varnothing 10''$ and extruded at 850F and 800F (Chien et al., 2018). ....	165
Figure C1: Flat, reduced length welds can be produced through concave, novel dummy block geometries. .....	171
Figure C2: Dummy block cross section with parts labels. Adapted from Robbins et al. (2016). ....	172
Figure C3: The (a) extrusion die used to create the (b,c) Ford battery tray profile studied. ....	174
Figure C4: Billet material properties selected from DEFORM <sup>®</sup> . Data from Heinemann (1961). ....	176
Figure C5: 3D velocity field point cloud exported from Altair Inspire Extrude model.....	177
Figure C6: Profile cross section with the seven weld regions labeled A-G.....	187
Figure C7: Comparison of (a) Experimental and (b) Velocity Field cross sections at 890 mm from the stop mark (SM) or 492 mm from the nose. ....	188
Figure C8: Plane of points (blue) generated at the die entrance to be traced through the velocity field (Orange). This represents tracking the billet-billet interface in conventional flat billet / flat dummy block extrusion.....	190
Figure C9: The conventional billet-billet interface can be tracked forwards through the velocity field method to determine the weld geometry. Planes of points can then be back-tracked from a reduced weld length through the velocity field method to determine novel dummy block geometries. ....	191
Figure C10: 3D representation of Ford / Can Art transverse weld. ....	192

Figure C11: The (a) x-axis and (b) a-axis view of the Ford / Can Art ideal dummy block geometry, determined through backtracking of the plane of points at the location of satisfactory weld strength on the conventional weld geometry for a 100% weld length reduction. Note that the concavities are expanding from the dummy block face (0 mm plane). The points in green represent the outer diameter of the billet/dummy block. .... 193

Figure C12: Two example tooling geometries for concavity A (Ideal and Reduced X & Y) plotted against the weld length reduction contours for the x and y axes of concavity A. .... 194

Figure C13: (a) Ideal dummy block geometry and (b) semi-ellipsoids of best fit for weld length reduction of 155 mm. The green circles represent the outer diameter of the dummy block. Note the seven semi-ellipsoids present, one for each of the seven die portholes and weld noses. .... 194

Figure C14: Weld geometry of (a) conventional transverse weld and (b) 15.5% reduced length transverse weld. .... 195

Figure C15: Derived plastic stress strain curve for H13 steel based on elastic properties and assumed offset and hardening terms. .... 197

Figure C16: The maximum effective stress in dummy block profiles ranging from 3 to 15.5% weld length reduction. .... 179

Figure C17: The maximum radial displacements of the outer edge in dummy block profiles ranging from 3 to 15.5% weld length reduction. .... 179

Figure C18: The stress and radial displacement on the conventional (a, c) and profiled dummy block (b, d). .... 180

Figure C19: The savings of the 15.5% weld length reduction dummy block with additional tooling costs ranging from \$0 to 2000. Legend is labeled as the additional dummy block costs (\$), the lifespan as a % of the conventional block, and the % weld length reduction. .... 183

Figure C20: The savings of the 15.5% weld length reduction dummy block with dummy block lifespan ranging from 50 to 100% the conventional value. .... 184

Figure C21: The savings associated with dummy block's of weld length reduction 5, 12 and 15.5% for a \$1,000 additional tooling cost with 75% tooling lifespan. Legend is labeled as the additional dummy block costs (\$), the lifespan as a % of the conventional block, and the % weld length reduction. .... 184

Figure C22: The reduction in (a) GWP and (b) CED for dummy blocks of weld length reduction 5, 12 and 15.5%. .... 186

Figure C23: The 2018 North American Extrusion Industry material flow analysis (Oberhausen et al., 2022). .... 198

Figure C24: Results of preliminary FEA comparing the extruded back-end defect length in an axisymmetric extrusion using (a) conventional, flat dummy block and (b) a novel, concave profiled dummy block. ... 201



Figure D1: The material properties of AA6061 at 530°C at several strain rates. ....	205
Figure D2: The modeled and experimental transverse weld curves on the rectangular billet major and minor axes. ....	206
Figure D3: The profiled-billet pairs extruded during the 2021 rectangular bar study. ....	206
Figure D4: Conventional and profiled weld geometry from the billet-billet interface starting plane of Z = 140 mm. ....	208
Figure D5: Detailed comparison of weld geometry from conventional (blue), profiled (red) and ideal (black) weld geometry. Locations from stop mark are denoted in brackets [], and the distances between key locations are marked with double sided arrows. ....	209
Figure D6: The comparison between profiled design 2, and the ideal dummy block interface geometry based on observations in experimental results. ....	210
Figure D7: New, velocity field design plotted against DEFORM-based design tested in this section. ....	211

## List of Tables

Table 2.1: Descriptions of the solid and hollow case study profiles. ....	14
Table 2.2: Intrinsic environmental impacts and costs. ....	17
Table 2.3: Extrusion characteristics for predictive models (A2). Uncertainties correspond to 1 standard deviation and are modeled as normal distributions calculated from the respective data sources. ....	22
Table 3.1: Details of the experimental extrusion trials performed in this work. Note: One set of axisymmetric single-piece billet experiments tested continuous extrusion without use of the butt shear. ....	52
Table 4.1: The values of the parameters studied in each of the sets of experiments. ....	82
Table 4.2: Profiles and billet sizes examined in this study. ....	96
Table 4.3: Critical damage values from ductile damage criterion derivation. ....	107
Table A1: Description of the machines used in the case studies. ....	127
Table A2: Annual energy consumption of European extruder for 2011 segregated by process and energy type.....	130
Table A3: Derived inventory values for Table 2.3 of main text. ....	132
Table A4: Example profile inputs used to perform sensitivity analysis in main text (Figure 2.5) .....	134
Table A5: Yield strengths of common extrusion alloys at extrusion temperatures. ....	135
Table A6: Node coordinate system used in this analysis. ....	136
Table A7: Initial values and reconciled results of all data points in MFA.....	137
Table A8: North American Extrusion Billet Ecosystem.....	144
Table A9: North American Extrusion.....	144
Table A10: North American Fabrication. ....	146
Table A11: North American fabrication by end use product.....	147
Table A12: North American End-use Indirect Trade.....	148
Table A13: Comtrade North American Extrusion Data.....	148
Table A14: Confidence weighting criteria for flow data sources. ....	155
Table A15. The most important sources of material flow data used to create the aluminum extrusion MFA. ....	155
Table A16: Sources used to form matrix node and flow data used as inputs for the data reconciliation process, and their confidence score (weight). ....	156

Table A17: Matrix node and flow data used as inputs $(x_i, j)$ to the data reconciliation with source and weighting factor. Note that an MFA data record that refers to either the scrap generated or the associated yield is designated by a third index, “x.x.2” for scrap flows, and “x.x.3” for yields.....	157
Table B1: Plane strain and non-plane strain ARB results. The mean is from at least 3 tests. ....	168
Table C1: Order of appearance in various weld models compared to experimental results. SM = Stop Mark, Nose = Nose of furthestmost weld. ....	188
Table C2: Distance of appearance in various weld models compared to experimental results. ....	189
Table C3: Estimated scrap rates for Ford extrusion profile. Adapted from Oberhausen et al., (2022) ....	182
Table C4: The knowledge gaps, technical barriers and corresponding tasks in the ongoing PFI project to overcome novel dummy block implementation into the extrusion industry.....	202

## List of Appendices

A	Reducing the Environmental Impacts of Aluminum Extrusion – Supporting Information. ....	127
B	Weld Shear Strengths in Accumulative Roll Bonding. ....	168
C	An Exploratory Study on Reducing Transverse Weld Scrap from Complex Extrusions Using Profiled Billets and Dummy Blocks. ....	169
D	Previous LIFT Rectangular Bar Trial Using DEFORM Point Tracking Algorithm. ....	205

# Abstract

Industrial greenhouse gas (GHG) emissions must be dramatically reduced by 2050 to avoid the worst consequences of climate change. Aluminum is one of five key materials (steel, cement, paper, plastic, aluminum) that together contribute over half of all industrial GHG emissions annually, and previous material flow analyses (MFA)s have shown that extrusion billet accounts for 20% of all semifinished aluminum. The goal of this research is to reduce the environmental impacts of the extrusion industry.

There has been little work on quantifying or reducing extrusion's environmental impacts. Therefore, this work first derives cradle-to-gate cumulative energy demand, greenhouse gas emissions, and cost models for direct aluminum extrusion using data collected from industry extruders, life cycle inventory measurements (e.g., electricity demand) from case studies, and physics-based extrapolations. Cost modeling is included to understand the economic (dis)incentives for pursuing the carbon abatement strategies. These models show significant scope for decreasing the process energy requirements and increasing material efficiency; however, only the latter will lead to both significant environmental benefits and cost savings. Subsequently, an alloy-shape-application MFA of the North American extrusion industry is derived to highlight opportunities for improved material utilization throughout the supply chain. The greatest source of material inefficiency is found to be the scrapping of profile sections containing the elongated solid-state transverse weld that forms between consecutively extruded billets, which is weaker than the surrounding material. This scrap stream may be reduced by either strengthening the weld (avoiding the need for its removal) or shortening the weld length (reducing the profile length that is scrapped).

Understanding of the transverse weld bonding mechanism is incomplete and no predictive model of the weld strength exists. A new transverse weld strength model is derived by adapting the film theory of solid-state bonding to non-plane strain conditions informed by experiments on oxide fragmentation of anodized billets. Experimental shear strength tests are used to evaluate the model on rod, bar, and multi-hollow profiles. The proposed model correctly predicts the experimental trends and suggests that the pressures within the die are sufficient to ensure micro-extrusion of the substrate aluminum through any cracks in the surface layers, therefore the local surface exposure to reveal substrate aluminum is the driving mechanism for bonding.

Shortening of the transverse weld has been achieved in previous work through extrusion process parameter optimization (e.g., billet temperature, ram speed, friction conditions, etc.), but is limited to approximately a 15% reduction. We explore a novel process for significant scrap savings using profiled dummy blocks to generate shorter welds by compensating for the differential metal flow velocities across

the billet cross-section as the billet flows through the die ports. For a given part and press, we first define an ideal dummy block shape by extracting the velocity field from finite element simulations of the conventional process. Next, we rationalize the tool shape using stress and deflection limits for the dummy block (preventing plastic deformation and interference with the container wall) and ductile damage limits for the billet to prevent cracking. The methodology is demonstrated for four profiles of increasing complexity: solid round and rectangular bars, a square-tube hollow, and a complex multi-hollow profile. The process' potential is evaluated experimentally using billets machined to match the ideal dummy block shape. The results show that dummy blocks with a profile-specific design can achieve weld length reductions >50%.

## Chapter 1. Introduction

It is understood that anthropogenic greenhouse gas emissions are the cause of global warming (IPCC, 2018). Since 1950, many extreme climate events (e.g. more frequent extreme weather, shrinking glacier, and rising sea levels) have occurred as a result of climate change driven temperature rises (IPCC, 2018). To avoid the worst consequences of climate change, the Intergovernmental Panel on Climate Change (IPCC) recommends a 40-70% reduction of global annual anthropogenic greenhouse gas (GHG) emissions by 2050 compared to the 2010 levels (IPCC, 2018).

### 1.1 The contribution of the aluminum industry to climate changes

Industrial emissions (those that derive from material production and processing) account for 35% of anthropogenic emissions (Figure 1.1a; excludes agriculture and land use changes) (Allwood et al., 2012; Zhu, 2021). The emissions from production of materials more than doubled between 1995 and 2015 (IRP, 2020). Today, half of all industrial emissions originate from the production of five key materials (steel, cement, paper, plastic and aluminum; Figure 1.1b). Aluminum is the smallest contributor of these five materials, responsible for 2% of global emissions in 2020 (World Economic Forum, 2020). However, the embodied emissions of primary aluminum (the emissions from production of aluminum from naturally

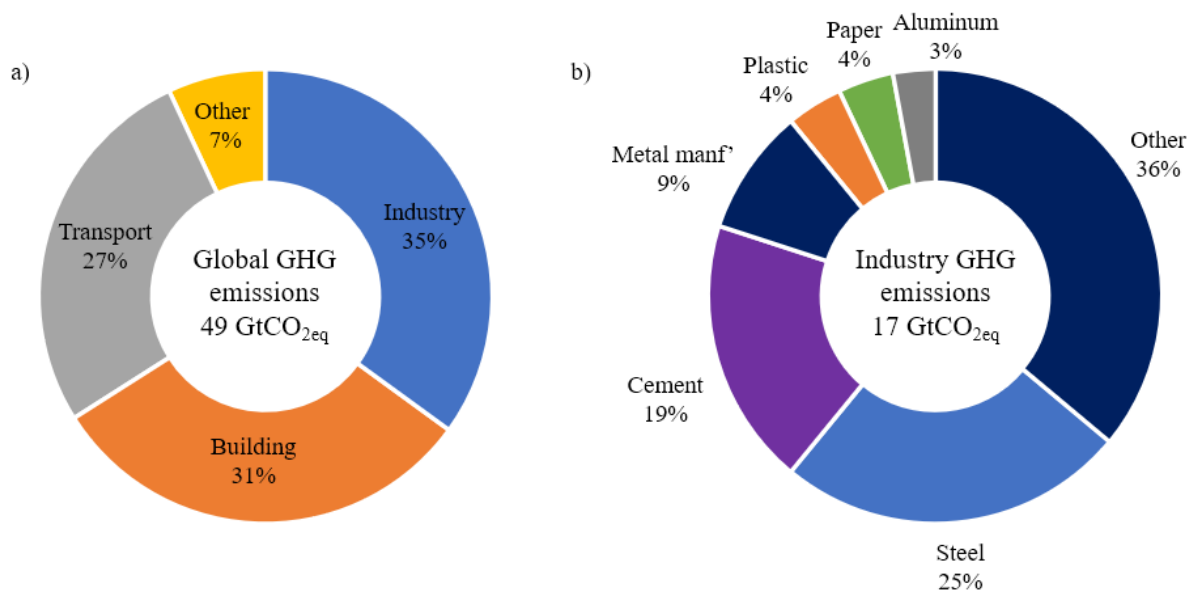


Figure 1.1: The (a) global anthropogenic emissions by category, and (b) the breakdown of industrial emissions (IEA, 2008). Image adapted from Zhu (2021).

occurring bauxite ores) is the highest of these five materials by a large margin (Figure 1.2); the embodied emissions of aluminum is approximately 12 kg CO<sub>2-eq</sub> / kg<sub>primary</sub>, whereas its metallic counterpart, steel, requires just 2.0 CO<sub>2-eq</sub> / kg<sub>primary</sub> to produce (Cooper and Gutowski, 2017).

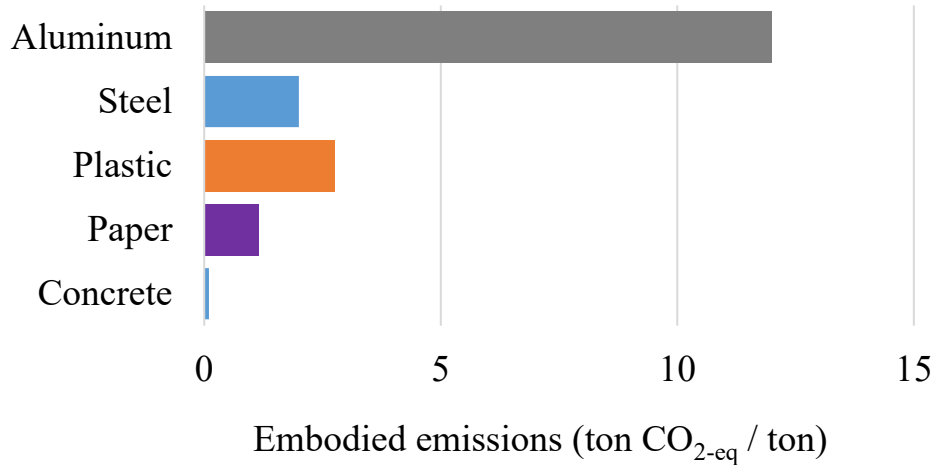


Figure 1.2: The embodied emissions of the primary production of the five key materials (aluminum, steel, plastic, paper, concrete) for global anthropogenic emissions (Cooper and Gutowski, 2017).

This difference in production requirement, combined with a growing demand for aluminum and a stagnating demand for steel will inevitably lead to an increased importance of aluminum to global emissions; aluminum demand is projected to grow 125% by 2060 from 2014 levels, compared to just 30% projected growth for steel demand in the same timeframe (International Energy Agency, 2017). Even given its relative scale today, primary production of aluminum is responsible for energy consumption equal to 5% of total global electricity production (Envist and Klevnäs, 2018). This formidable energy requirement (13-15 MWh per metric ton of aluminum) drives the high emissions intensity.

Primary aluminum production is performed in two major steps (Envist and Klevnäs, 2018). The first is the Bayer process during which bauxite, the raw ore containing aluminum compounds, is heated in a solution of sodium hydroxide under pressure to selectively dissolve out sodium aluminate solution. This solution is seeded with alumina hydrate to precipitate out alumina hydroxides which are filtered, washed, and then calcined to produce crystalline alumina. In the next major step, the Hall-Héroult process (commonly referred to as electrolysis) is used to extract aluminum from the purified alumina. Carbon electrodes are used to apply a current through the aluminum oxide dissolved in a molten salt (cryolite), producing pure aluminum. This process is commonly referred to as electrolysis. Altogether, the energy requirements to refine bauxite into aluminum through these two processes account for 80% of the aluminum industry’s GHG emissions (Tabereaux & Peterson, 2014), driven in large part by the requirements of electrolysis. Secondary aluminum production is production from scrap metal (recycling) and is typically



performed in rotary and reverberatory furnaces (Zhu, 2021). The energy and emissions intensity of secondary production is much lower at 8.7 and 0.75 (Oberhausen et al., 2022).

## **1.2 Current opportunities and efforts to reduce aluminum environmental impacts**

The efficiency of the electrolysis process has improved from 85% to 96% over the last century and is now nearing the maximum thermodynamic efficiency (Tabereaux & Peterson, 2014). Innovative production technologies such as the use of inert anodes (Allwood et al., 2012) can reduce projected emissions values by approximately 23% (Allwood et al., 2010), well short of the 50% emissions reduction target by 2050 suggested by the IPCC (2018). It is therefore necessary to study alternative means of emissions reductions such as decarbonization of the energy grid, or more efficient usage of material.

The use of near-zero emissions energy could reduce aluminum industry GHG emissions by up to 83% (Liu et al., 2011), however, this transition will occur upstream from the aluminum industry and will require partnership with the power industry (World Economic Forum, 2020). Historically, aluminum production has been performed alongside hydroelectric stations to meet the steep energy demand. In 2010, hydropower represented 40% of electricity consumption in the industry (IEA, 2022). However, the past decade has seen a shift in the reverse direction; the share of hydroelectricity has fallen to just 30% as aluminum production has moved to China, where 80% of the electricity is produced from coal (International Aluminum Institute, 2021; Cooper et al., 2017). Furthermore, availability of decarbonized energy sources is applicable to and desired by all industries. A shift to decarbonized energy will therefore be restricted in scale by a limited volume and supply of resources (Chen and Önal, 2016; Ryberg et al, 2019) as well as require a restructuring of the grid (Pedneault et al., 2021). Additionally, the energy industry is struggling to amass the capital and raw materials necessary to build the vast number of renewable energy sources and infrastructure required to power the entire US grid (The Economist, 2021).

More efficient use of material in manufacturing can be achieved through two main methods: production of goods with less material in the final product (e.g. lightweighting), or generation of less manufacturing scrap during the production of goods (e.g. yield improvements). Material production currently accounts for 23% of global anthropogenic GHGs (Ritchie et al., 2020); a main driver for industrial emissions (Cullen and Cooper, 2022). Strategies which target improvements to material efficiency have been identified as a key path forward in reducing industrial GHG emissions (Milford et al., 2011).

## **1.3 The contribution of the aluminum extrusion industry to climate change**

Previous material flow analysis (MFA) of the aluminum industry reveals that around 20% of all aluminum produced in 2007 was extruded (Cullen and Allwood, 2013). The same MFA shows significant

scope within the aluminum extrusion industry for more efficient material usage, highlighting a 25% manufacturing scrap rate (from billet to unfinished extruded profile).

The scale and scope of this opportunity continues to grow in size with the aluminum extrusion industry; at 8% market growth per year (Precedence Research, 2022), demand for extrusions is doubling every 9 years. This growth surpasses even the overall aluminum market (Precedence Research, 2022). The quickest growing market for North American (NA) extrusions is the automotive sector (Schoenberger, 2016), in which the drive towards lightweight and electric vehicles (EVs) has caused an increase in the use of extrusions. More extrusions are used in EVs than any other type of vehicle (Dinsmore, 2018), including applications such as the battery housings (e.g., in the Ford Mustang Mach-E EV (Page, 2020)) as well as trim and crash management systems (Ducker Worldwide, 2017a).

To understand the best path forward in improving material efficiency and decarbonizing the aluminum extrusion industry it is important to both quantitatively and qualitatively explore available opportunities. Quantitatively it must be understood in which parts of the extrusion process the significant environmental impacts are generated, and the scale in reduction of impacts achievable from potential improvements. Qualitatively the feasibility of these improvements to occur in the present or future must be evaluated.

#### **1.4 The aluminum extrusion process**

The extrusion process is used to produce long parts of constant cross-section. The extruded profiles can be as simple as cylindrical rods used as machining stock (Norsk Hydro, 2020a), to as complex as custom automotive parts such as roof bows (e.g., Tesla Model S (Design News Staff, 2014)), front end and roof structures (e.g., Ford F-150 (AEC, 2014)), or multi-hollow rocker and engine cradle components (e.g., Cadillac CT6 (Aluminum Extruders Council, 2015)). The raw material for the extrusion process is aluminum billet, produced and delivered to extruders in log form (6-12 inches in diameter, and ~7 m in length (Aluminum Extruders Council, 2021)). The first step of the extruder is to section these logs into lengths suitable for extrusion (0.66 - 1.83 m (Aluminum Extruders Council, 2021)). Some length of the log will be remaining, known as billet cutting scrap (Sheppard, 1999), as the billet length will not likely be evenly divisible into the log length. Next, the billet, container and die stack are preheated to between 300-595°C (Misiolek and Kelly, 2005). The temperature to which they are preheated depends on the alloy being used and the profile being produced: complex extrusions will heat up to a greater extent during the extrusion process due to increased surface area and therefore frictional forces in the die and will therefore be preheated to a lower temperature as to not exceed a temperature of unacceptable surface quality (Misiolek and Kelly, 2005).

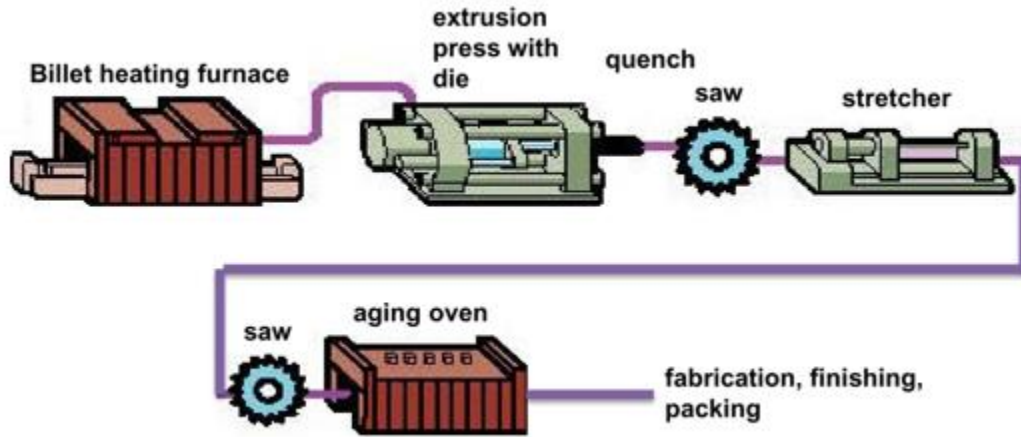


Figure 1.3: Typical process flow at aluminum extruder (Tomczyk, 2019)

The heated die stack is then placed into the die slide, a steel ring with an open top which houses the die stack at the exit of the extrusion press. In solid extrusion the die stack contains the die plate, and backer (Figure 1.4a) ( Aluminum Extruders Council, 2018). The die plate is a solid steel plate cut with an opening in the shape of the extruded cross section; the billet is pushed into and shaped by the die plate. The backer sits behind the die plate and provides extra support against the extrusion pressures. The opening on the backer is larger than the profile as to not contact the formed metal which would cause surface quality defects on the extruded profile. In some cases, there is an additional component in the die stack, known as the feeder plate which instead is at the front of the die stack and performs an initial deformation of the billet. This is most common in dies which simultaneously produce several copies of the same profile, as shown in Figure 1.4a.

Behind the die stack sits the bolster, a thick, heavy steel ring with a diameter equal to or greater than the die ring acting to provide even more support to the die stack against the pressure of the stem and billet. The support of the backer and bolsters help to minimize deflection within the tool stack, resulting in greater quality, faster extrusion speeds and tighter tolerances on the extruded profile (Aluminum Extruders Council, 2018).

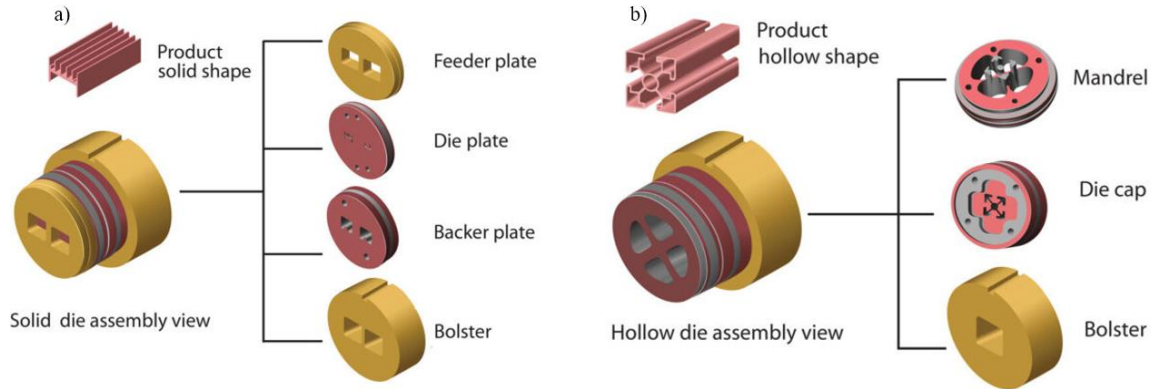


Figure 1.4: (a) Example solid die stack. (b) Example hollow die stack. (MMG Extrusions, 2023)

For hollow profiles the die stack composition differs slightly. The die and backer plates are replaced by the mandrel and die cap. The front of the mandrel has several portholes which act to divide the billet into different sections. The billet material is split around the die bridges (which support the central mandrel, forming the interior hollow section(s) of the profile) and then rejoin before die exit (Xie et al., 1995) to form longitudinal (seam) welds.

With the die now in place at the exit of the container (a hollow steel chamber designed to hold the pressurized billet), the heated billet is loaded into the container (Sheppard, 1999). The hydraulic stem of the extrusion press is then brought forward to force the billet within the container through the die. On the front of the stem is the dummy block, a sacrificial addition to the stem subject to the wear of contacting the billet (Aluminum Extruders Council, 2018). Modern dummy blocks are designed to rest at a diameter smaller than that of the container, with an internal spring mechanism which acts to expand the outer diameter of the block to minimize the gap with the container wall as the billet is pushed (Robbins et al., 2016). This variable expansion has the benefit of maintaining a sufficiently small gap between the container and block to avoid backward extrusion during billet push, while also contracting to reduce friction and therefore also forces during ram retraction (Robbins et al., 2016; Thumb Tool and Engineering, 2021).

As the profile exits the die, a puller attaches to the front end and pulls on the profile with just a small force; this helps to keep the profile relatively straight as it travels along the run-out table (Aluminum Extruders Council, 2018). If the material is heat-treatable then the puller will bring the extruding profile through a quench curtain, which rapidly cools the profile from extrusion temperatures to room temperatures. This rapid cooling locks the microstructure of the aluminum in a supersaturated solid solution (Saha, 2000), offering improved mechanical properties following a subsequent heat treatment process. Construction restrictions limit the quench curtain from being located directly at the exit of the die. After each billet stroke, the length of material which rests between the die exit and the quench curtain entrance is not appropriately

cooled and must be removed as quench curtain scrap due to its sub-standard mechanical properties (Magnode Corporation, 2019).

Each billet is extruded to approximately 86%-90% of its length and the stem and dummy block are then retracted (Johannes et al., 1996; Lou et al., 2017). The billet is stopped short for two reasons. Firstly, the flow of material from the container into the die follows an angular path around dead metal zones. Extruding through these dead metal zones would cause a massive spike in pressure, and likely damage to the die (Thumb Tool and Engineering, 2019). Secondly, this section of the billet contains the billet skin, a 0.05 mm to 0.5 mm (Hydro, 2022; Bauser et al., 2006) thick layer of oxides and casting defects on the outside of the billet. The effect of friction between the outer diameter of the billet and the inner diameter of the container causes the skin to flow to the rear of the billet. To prevent this material from entering the extrudate and causing both mechanical and aesthetic issues (Saha, 2000) in the final product, a hydraulic shear is brought down to cut off the remaining length of the billet in a scrap source known as the back-end defect (Jowett et al., 2008). The profile is simultaneously cut at the die exit and brought to the stretcher, a device used to eliminate any bends in the extruded product that may occur due to friction or velocity differentials across the profile. The stretcher imposes a 1-3% elongation of the profile (Saha, 2000). The length of profile which was within the grips of the stretcher are then cut off as stretcher scrap before the extrudate is put through a heat-treatment in the aging oven (Aluminum Extruders Council, 2018), if it is a heat-treatable alloy. Following heat treatment, the profile is finished as requested by the customer with post-extrusion fabrication and any surface finish (e.g., painting or anodizing).

The extrusion process proceeds with continuous extrusion of additional billets. The interface between consecutively extruded billets is joined together in a solid-state welding process, forming what is known as the transverse weld. The interface is elongated due to the friction between the billet and the container walls to inhabit up to 20% of the extrudate length (Sheppard, 1999). The section of material containing the transverse weld is weaker than the surrounding material and therefore must be removed in safety-critical applications (den Bakker et al., 2016; Lou et al., 2019; Tang et al., 2022; Yu et al., 2019; Oberhausen et al., 2023).

Other sources of scrap include: the die-fill scrap, which is the material leftover in the die after an extrusion run is finished; and the overlength scrap from leftover material after sectioning the full-billet length of extrudate into the length of the finished product.

## **1.5 Thesis Structure**

Considering the review laid out in Chapter 1, this dissertation will present research on decreasing the environmental impacts and costs of aluminum extrusion.

Chapter 2 will act as a guidepost for extrusion research, and will seek to answer the following research questions:

- What are the greatest opportunities to reduce the extrusion process' environmental impacts for minimum cost?
- Where are the supply chain opportunities to increase material efficiency?

One of the main conclusions of Chapter 2 is the importance of a manufacturing scrap source known as the transverse weld to the overall costs and environmental impacts of aluminum extrusion. The transverse weld is the interface between consecutively extruded billets. The interface becomes elongated due to the friction on the container and die walls (Sheppard, 1999) and must be removed from the extruded profile due to weaker mechanical properties than the surrounding material (den Bakker et al., 2016; Tang et al., 2022).

The aim of Chapter 3 will be to investigate the formation of the transverse weld and the cause of its sub-standard strength. The objectives will be to:

- Understand surface film fragmentation and welding of the consecutive-billet interface during extrusion.
- Derive a new transverse weld strength model through adaptation of the film theory of solid-state bonding to non-plane strain conditions.

The derived model predicts the trends of transverse weld strength along the weld's length and across individual weld profiles; however, the results also highlight unreliability in the strength. In Chapter 4, the focus is instead on reduction of transverse weld scrap through control of the weld's length. The chapter will include:

- Development a profiled dummy block design methodology for reduction of the transverse weld length.
- Overcoming barriers to implementation for the novel dummy block into industry processes and supply chains.

A summary of the research will be presented in Chapter 5, along with potential future research to support and build on the presented work.

## **Chapter 2. Reducing the Environmental Impacts of Aluminum Extrusion**

The aluminum extrusion industry is growing rapidly; however, there has been little work on quantifying or reducing extrusion's environmental impacts. This article first derives cradle-to-gate cumulative energy demand, greenhouse gas emission, and cost models for direct aluminum extrusion using data collected from extrusion companies, life cycle inventory measurements (e.g., electricity demand) from our own case studies, and physics-based extrapolations. These models show there is significant scope for increasing both the process energy and material efficiency; however, only increasing the material efficiency will lead to significant environmental benefits and cost savings. Subsequently, an alloy-shape-application material flow analysis of the 2018 North American extrusion industry is conducted to highlight opportunities for improved material utilization throughout the supply chain. Material flow data were collated from existing academic and gray literature in addition to semi-structured interviews with North American extrusion experts. The material flow analysis reveals that around 40% of all aluminum cast into extrusion billets is scrapped before completion in a fabricated product, which increases the cost of the fabricated profile by approximately 16% and the greenhouse gas emissions and cumulative energy demand by approximately 40%. Most of this scrap is created by removing structural and surface finish extrusion defects that are inherent to the current process. Process adaptations that might reduce the material scrapped due to these defects are identified and discussed. Even a 10% reduction in extrusion process forming scrap could save the North American (U.S. and Canada) extrusion industry 270–311 million USD per year and prevent the release of 0.5–2.3 Mt.CO<sub>2</sub>eq annually.

### **2.1 Section introduction**

Production of just five key materials (aluminum, steel, cement, paper, and plastic) accounts for over half of all the greenhouse gas (GHG) emissions released by industry worldwide each year (Sutherland et al., 2020). Primary aluminum making is by far the most emissions intensive of these materials per unit of production (Argonne National Laboratory, 2020). Further GHG emissions are released downstream of aluminum production in manufacturing processes that shape, heat treat, join, and finish aluminum components (Seow et al., 2013). Additional environmental concerns include the loss of land to bauxite mining operations and accidental toxic releases such as of red mud produced in the Bayer process for refining aluminum ore (Metson, 2011; BBC, 2010).

Emissions released from aluminum supply chains must be reduced to help prevent the worst consequences of climate change (Allwood et al., 2012; Cann et al., 2020). There are, however, limited opportunities to improve the aluminum production process where the energy efficiency is approaching the thermodynamic limit (Allwood, et al., 2010; Gutowski et al., 2013) and where the GHG emissions intensity has increased in recent years due to the rapid global shift to Chinese production, where 90% of the aluminum-making electricity is generated using emissions-intensive coal (International Aluminum Institute, 2021; Cooper et al., 2017). Reducing aluminum material and energy requirements in downstream manufacturing is therefore a priority.

This article focuses on the aluminum extrusion supply chain because of its significance to the overall industry. Cullen and Allwood's (2013) material flow analysis (MFA) shows that around a fifth of all the aluminum produced worldwide in 2007 was extruded. More recently, Bertram et al.'s (2017) dynamic MFA shows that global demand for extrusion ingot has grown rapidly since 2000 and, by 2014, far exceeded demand for casting ingots and was comparable to rolled ingot demand. In 2017, 28 Mt of extruded aluminum profiles were produced globally (Rodriguez León and Stark, 2018). These profiles were used across construction (e.g., commercial façade and window frames), transport (e.g., bumper components), equipment (e.g., ladders and scaffolding), consumer durables (e.g., air conditioner tubing), and electronics (e.g., extruded plates milled to make laptop enclosures) (Misiolek and Kelly, 2005; Sherman, 2009). Aluminum extrusion is increasingly popular because it permits the use of part-consolidated lightweight profiles with optimized cross-sections, integrated connections, and a high quality surface finish that can be further enhanced with anodizing or powder coating (Misiolek and Kelly, 2005). Aluminum's high thermal conductivity combined with the ability to extrude high surface area profiles makes it an attractive choice for heat sinks and as structural material enclosing electronics.

In a typical direct extrusion plant, long ( $\approx 7$  m), homogenized, direct chill (DC) cast aluminum alloy logs ( $\text{Ø}6\text{-}12''$ ) are cut to shorter billet lengths (0.66-1.83 m) (AEC, 2021) which are then preheated (400-550°C) before being placed in a heated extrusion chamber and pushed through a die using a dummy block and stem attached to a hydraulic ram (Figure 2.1). Profiles made from heat treatable alloys may be cooled using a water spray quench curtain as they leave the die. The extruded profiles may subsequently be artificially aged (heat treated) and/or anodized and painted.



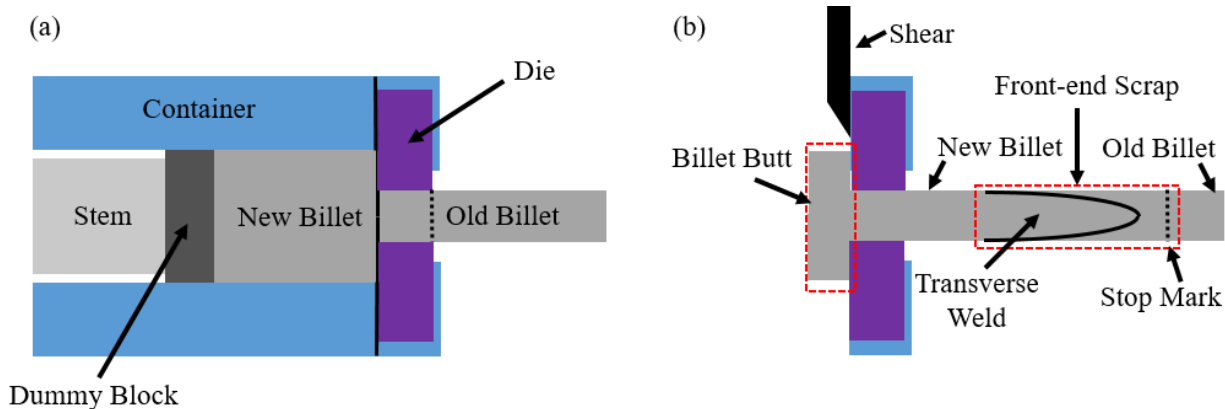


Figure 2.1: Schematic of consecutive direct extrusion (a) before and (b) after extrusion of a new billet

### 2.1.1 Previous work on the environmental impacts and costs of extrusion

Several efforts have been made in recent years to improve the efficiency and reduce the costs of aluminum extrusion. Recent developments include more efficient burners in billet preheating furnaces (U.S. DOE, 2003; Wüning, 2007) and start-stop hydraulic pump systems for reducing press electricity requirements (SMS Group, 2020). However, the overall relevance of these developments is not clear without a holistic analysis of the environmental impacts and costs in aluminum extrusion, which can also be used to prioritize future research and development.

Despite the significance of the extrusion industry, there has been little work on quantifying extruded profile environmental impacts or mapping material flows. For example, Haraldsson and Johansson (2018), in a review of measures for improved energy efficiency in aluminum processing, found no academic articles on improving extrusion's energy efficiency across the ten years' worth of publications they examined (2007-2016). Elsewhere, Ingarao et al. (2014) compare the primary energy required to extrude versus machine a given part, and Furu et al. (2017) perform an optimization to find the minimum cost and environmental impacts of aluminum alloys used in the extrusion process by changing only material properties (e.g., yield stress). The most extensive analyses are in the non-peer reviewed literature. The European Aluminum Association (EAA) (EAA, 2018) published an environmental profile report based on a survey of 29% of European extruders, and the Aluminum Extruders Council (AEC) (Mulholland, 2016) performed an Environmental Product Declaration (EPD) (ISO, 2016a, 2016b) based on data provided by approximately 33% of North American extruders. The EAA's report presents a limited gate-to-gate Life Cycle Assessment (LCA) from cast billet to extruded profile, excluding the impacts associated with the tooling, lubricant, and capital equipment as well as energy-intensive aluminum production, casting, and potential post-extrusion processes (e.g., heat-treatment). The AEC's EPD is a cradle-to-gate LCA; it includes the environmental impacts of some tooling (extrusion dies) and finishing processes (e.g.,

anodizing), and reports the average billet recycled content of survey respondents (54%). The EPD excludes the environmental impact of the lubricant, the capital equipment, or post-extrusion heat-treatment. Both the EAA and AEC studies aggregate energy and material flows (e.g., different scrap flows) and report point values rather than providing predictive models.

Alongside LCA, supply chain MFA is a foundational tool in industrial ecology used to identify scalable opportunities for material efficiency (e.g., increased recycled contents and reduced process yield losses). Other than high-level aluminum industry MFAs (Bertram et al., 2017; Cullen and Allwood, 2013) and a study on the use of aluminum extrusions in French commercial buildings (Billy, 2012), there are to the authors' knowledge no detailed MFAs of the extrusion industry. This forms a significant literature gap given that the AEC EPD found material inputs to be the most significant driver of environmental impacts.

Manufacturing economic analyses are necessary to understand the viability of any proposed process changes that decrease environmental impacts. There have been few attempts at modeling extrusion costs. Low (2009) conducted a case study on the equipment, overhead, material, labor, tooling and maintenance costs for extruding a heatsink profile, finding that production costs were dominated by material costs (66.6%) with equipment depreciation (13.7%), tooling costs (9.9%) and energy costs (5.6%) also significant. Elsewhere, Nieto (2010) developed a feature based cost model for aluminum extrusion to help extrusion die designers predict extrusion profile production costs; however, not all scrap sources are included and energy costs are subsumed in overhead, preventing an energy efficiency cost analysis.

### **2.1.2 Scope of Work**

This work focuses on answering two questions:

- What are the greatest opportunities to reduce the extrusion process' environmental impacts for minimum cost?
- Where are the supply chain opportunities to increase material efficiency?

The first question is answered in section 2 by creating parametric cradle-to-gate environmental impact and extrusion cost models informed by both industry data and case studies conducted for the purpose of this work. The presented models can be used to make predictions based on as little information as the billet properties and profile geometry. The second question is answered in section 3 by conducting an alloy-shape-application MFA of the North American extrusion industry. Section 4 then includes a discussion of the opportunities identified in this work and the scale of these opportunities in relation to current industry trends.

## **2.2 Environmental impact and cost models for aluminum extrusion**

This section focuses on measuring the electrical power draw of the extrusion process and then evaluating the overall environmental impacts and costs by considering the other inputs and outputs. Subsequently, parametric models are constructed (with uncertainty) that allow the impacts and costs of making any (applicable) part to be predicted.

The environmental impacts are modeled in Umberto (ifu hamburg, 2020) with case study data supplemented by lifecycle inventories based on ecoinvent 3.1 database values (Wernet et al., 2016). The impacts considered are cumulative energy demand (CED), also known as primary or embodied energy, and the cumulative carbon dioxide equivalents emitted, which is a measure of global warming potential (GWP) with a 100-year time horizon. These two environmental indicators have been chosen due to the urgency required to address climate change and because CED is a good proxy for a range of other environmental impacts (Ashby, 2021; Penny et al., 2012). Figure 2.2 shows the boundaries of the ‘cradle-to-gate’ LCAs and cost models. The functional unit is 1 kg of finished extruded profile ready for original equipment manufacturer (OEM) fabrication and assembly. The impacts and costs of tooling and equipment are amortized over the total mass of profiles produced before replacement. In order to reduce confusion, ‘MJ’ refers to the CED, while ‘kWh’ and ‘therms’ refer to delivered (metered) electricity and the energy released from burning natural gas respectively. The indirect costs and impacts from facilities, facility-wide energy requirements (e.g., lighting), administration, and design etc. are not included.

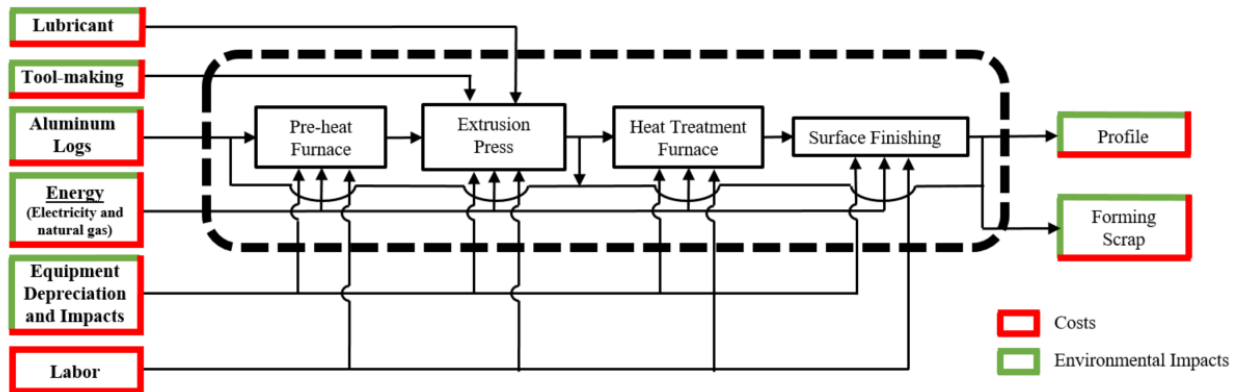


Figure 2.2: System boundaries for environmental impact and cost models

### 2.2.1 Case study methodology

Case studies were conducted on a 12 MN Danieli Breda hot direct extrusion press situated at the *Lightweight Innovations for Tomorrow* (LIFT) Manufacturing USA Institute in Detroit, Michigan. Table 2.1 presents descriptions of the case study profiles and extrusion parameters, and Table A1 describes the equipment.

Table 2.1: Descriptions of the solid and hollow case study profiles.

		<b>Case Study Profile 1</b>	<b>Case Study Profile 2</b>
	<b>Profile Description<sup>1</sup></b>	<b>Solid rectangular bar</b>	<b>Hollow T-slot 80/20 profile</b>
Profile	Alloy	AA6061	AA6063
	Alloy yield strength ( $Y_f$ ) @ 530 °C (MPa)	15	11
	Linear density (kg/m)	1.00	1.38
	Billet Recycled Content (%)	54	54
	Billet Cost (\$/kg)	2.52	2.49
Lubricant	Type	Boron Nitride	Boron Nitride
	Mass (grams/billet)	10	10
Tooling	Material	H-13 tool steel	H-13 tool steel
	Die Type	Solid	Hollow
	Die Plate Mass (kg)	Blank: 37.8	Blank: 37.8
		Removed: 3.1	Removed: 6.6
		Final: 34.7	Final: 31.2
	Die Bolster Mass (kg)	Blank: 160.9	Blank: 160.9
		Removed: 11.5	Removed: 11.5
		Final: 149.4	Final: 149.4
	Die Lifespan <sup>2</sup> (kg)	106,000	20,000
	Die Cost <sup>3</sup> (\$)	660	1,600
	Dummy Block Mass (kg)	26	26
	Dummy Block Cost (\$)	1,000	1,000
	Dummy Block Lifespan <sup>4</sup> (kg)	680,000	680,000
	Container Mass (kg)	129	129
Container Cost <sup>5</sup> (\$)	30,000	30,000	
Container Lifespan <sup>6</sup> (kg)	15 million	15 million	
Equipment	Equipment Mass (kg)	675,000	675,000
	Equipment Cost <sup>7</sup> (\$M)	10	10
	Equipment Lifespan <sup>8</sup> (Mt)	9	9
Extrusion	Billet Preheat Temperature (°C)	530	530
	Container Temperature (°C)	450	450
	Die Temperature (°C)	530	530
	Ram Speed <sup>9</sup> (mm/s)	5.6	3.1
	Billet Geometry (mm)	Length: 800	Length: 800
		Diameter: 152	Diameter: 152
	Extrusion Ratio (ER)	50	30
	Front-end defect length removed (mm)	3500	2800
Billet butt length removed (mm)	50.8 (6% of billet mass)	50.8 (6% of billet mass)	
Process	Labor Requirement (persons)	4	4

Notes: 1: No heat treatment or surface finishing processes were conducted in these case studies. 2: Die life spans range from 20-106 t of extruded billet. Dies for extruding simple profiles have longer lifespans. (Thumb Tool & Engineering, 2018). 3: Die costs based on average for solid and short hollow profiles (MI Metals, 2019). Short refers to the depth of the die, a light profile will have a shallow depth as less support is necessary in the die stack. 4: Dummy block lifespan represents 6,500 billet pushes (Superior Aluminum, 2019). 5: Container costs for medium sized press, Ø6-7" (Superior Aluminum, 2020). 6: Container lifespan represents 6 months of production (MI Metals, 2019). 7: Equipment costs encompass a new extrusion press with ancillary equipment (MI Metals, 2019). 8: Equipment lifespan represents 10 years of production (MI Metals, 2019). 9: The ram speed when extruding complex hollow profiles is lower to reduce the required press force and die wear.

Electrical power measurements were taken using Fluke 434 (series II) 3-phase power analyzers with a sampling period of 0.25 s. Two material flows were tracked during the case studies: the aluminum billets and the boron nitride lubricant applied to the dummy block face to prevent sticking. In the case studies, aluminum billets (rather than logs) were provided by the metal supplier. A billet cutting process yield loss of 4% was used to account for the process scrap created as a result of the log length typically not being an

exact multiple of the billet length (Sheppard, 1999). The other case study scrap sources were the billet butt and front-end defect (transverse weld and stop mark, Figure 2.1). The billet butt corresponds to the last 5-15% of an extruded billet, which is typically not extruded through the extrusion die and is instead removed from the container between press strokes by a descending hydraulic shear and scrapped (Figure 2.1). Billet impurities (e.g., oxides, spinels, and intermetallics) are initially dispersed in the billet surface skin but are concentrated in the billet butt during the ram stroke due to the metal flow towards the rear of the billet (Oberhausen et al., 2021). Inclusion of these impurities in the final profile would reduce its aesthetic, mechanical and electrical properties (Saha, 2000). Around 7-20% of an extruded profile contains the transverse weld (Mahmoodkhani et al., 2014; MI Metals, 2019), which is an elongated solid-state weld that forms between consecutively extruded billets and has a lower strength than surrounding material (Den Bakker et al., 2016). In the case studies, the transverse weld lengths were determined by sectioning, polishing and macro-etching the extruded profiles to reveal the weld line (Section S1.2). Some applications do not require removal of the transverse weld (e.g., concrete screeds (Mag Specialties, 2019)); however, removal is typically mandated by automotive OEMs (Ford Motor Company, 2013). The stop mark is an easy-to-identify blemish on the surface of the profile from where the profile has been pressed against the die exit between ram strokes.

### **2.2.2 Intrinsic environmental impacts and costs**

Intrinsic environmental impacts and costs (per unit input) were determined from the literature and are presented in Table 2.2. U.S. electricity impacts were derived using the U.S. Environmental Protection Agency's (EPA) (2020) inventory of GHG emissions and sinks, as well as Argonne National Lab's (2020) Greenhouse gases, Regulated Emissions, and Energy use in Transportation (GREET) model. The GWP of natural gas (combustion) was determined using the GREET model, and the CED was modeled as *Heat Production, Natural Gas, at Industrial Furnace* from the ecoinvent 3.1 database. Electricity and natural gas costs were modeled as the average of industrial rates for the Midwest region sampled monthly between 2011-2020 (U.S. Bureau of Labor Statistics, 2021a; 2021b). Boron nitride was modeled as a *Generic Lubricating Oil*, also from the ecoinvent 3.1 database, and costs were determined from commercially available sprays (Zyp Coatings, 2021).

The intrinsic impacts of the aluminum alloy billets were determined using the 'recycled content' method, reflecting a "strong" sustainability perspective where scrap recycling is not assumed to displace primary production like in the 'avoided burden'/'end-of-life' approach (Frischknecht, 2010). For each alloy, the impacts of producing primary aluminum and the alloying elements were determined using the ecoinvent database, which includes the impacts from casting. The billet cost is determined by the cost of primary metal, secondary metal, the Midwest premium (covering the cost of importing and transporting the

aluminum into the US (S&P Global Platts, 2019)), and the billet premium (covering the cost of casting aluminum into billets from the ingot form (MI Metals, 2019)). The CES EduPack 2020 database (Granta Design Limited, 2020) was used to estimate the cost of each of the primary alloys. The price of secondary (post-industry) aluminum extrusion scrap was modeled as 87% of primary material (Schlesinger, 2014). The Midwest premium was determined as the average of monthly values in 2020 (S&P, 2019). The billet premium was determined from a range provided by MI Metals (2019).

The embodied environmental impacts of the machinery and the tooling were calculated using the mass of the extrusion equipment (press and billet heating furnace) and tooling (container, dummy block, and die-set) as well as the intrinsic impact values for *Steel Primary Production* and *Chromium Steel Milling, average* obtained from the ecoinvent 3.1 database.

The labor cost is the median wage reported for *U.S. Extruding and Drawing Machine Setters, Operators, and Tenders, Metal and Plastic* (U.S. Bureau of Labor Statistics, 2020a) increased by 45% to account for benefits (U.S. Bureau of Labor Statistics, 2020b).

Table 2.2: Intrinsic environmental impacts and costs.

Input	Density		CED		GWP		Cost	
	mean	uncertainty	mean	uncertainty <sup>1</sup>	mean	uncertainty <sup>1</sup>	mean	uncertainty <sup>1</sup>
<b>Energy (I<sub>energy</sub>, C<sub>energy</sub>)</b>								
Electricity (i <sub>elec</sub> , c <sub>elec</sub> )	-		MJ/kWh		kgCO <sub>2</sub> e/kWh		\$/kWh	
Medium voltage electricity			10.30	0.26	0.41	0.01	0.13	0.077
Gas (i <sub>gas</sub> , c <sub>gas</sub> )	-		MJ/Therm		kgCO <sub>2</sub> e/Therm		\$/Therm	
Natural gas			117.90	2.95	5.96	0.15	0.84	0.066
<b>Billet Material (I<sub>billet</sub>, C<sub>billet</sub>)</b>	kg/m <sup>3</sup>		MJ/kg		kgCO <sub>2</sub> e/kg		\$/kg	
Primary aluminum (i <sub>primary</sub> , c <sub>primary</sub> )								
High purity aluminum	2696	-	173.07	4.33	14.80	0.37	2.27	0.13
6061	2713	-	174.88	4.37	14.89	0.37	2.52	0.14
6063	2696	-	174.31	4.36	14.88	0.37	2.49	0.13
6082	2700	-	174.03	4.35	14.82	0.37	2.49	0.13
7075	2796	-	170.50	4.26	14.47	0.36	5.05	0.28
Secondary aluminum (i <sub>secondary</sub> , c <sub>secondary</sub> , c <sub>scrap</sub> )								
6XXX extrusion <sup>2</sup>	-	-	8.74	0.22	0.74	0.02	2.19	0.12
7XXX extrusion <sup>2</sup>	-	-	8.53	0.21	0.72	0.02	4.39	0.24
Billet premium (C <sub>billet-premium</sub> )	-	-	-	-	-	-	0.29	0.01
Midwest premium (C <sub>midwest-premium</sub> )	-	-	-	-	-	-	0.33	0.06
<b>Tooling (I<sub>tooling</sub>)</b>	kg/m <sup>3</sup>		MJ/kg		kgCO <sub>2</sub> e/kg		-	
Die Material (i <sub>die</sub> )								
Tool Steel	7800	-	30.44	0.76	3.25	0.08		
Die machining (i <sub>removed</sub> )	kg/m <sup>3</sup>		MJ/kg <sub>removed</sub>		kgCO <sub>2</sub> e/kg <sub>removed</sub>		-	
Tool Steel	7800	-	111.44	2.79	7.15	0.18		
Lubricant (i <sub>lubricant</sub> , c <sub>lubricant</sub> )	-		MJ/kg		kgCO <sub>2</sub> e/kg		\$/kg	
Boron Nitride			83.05	2.08	1.13	0.03	50	1.25
Labor (C <sub>labor</sub> )	-		-		-		\$/hr	
Operator							26.13	6.90

Notes: 1: All uncertainties are modeled as normal distributions and the numerical value refers to one standard deviation calculated from the sample data reported in the data sources. For example, the primary alloy cost uncertainties were calculated from the range of values reported by the CES Edupack 2020 database. The CED and GWP intrinsic impact uncertainties were derived fromecoinvent's reported 2SD uncertainty values. 2: In these rows, the CED and GWP refer to the environmental impacts of recycled extrusion scrap. The cost, however, refers to the price of the extrusion scrap before recycling. The GWP and CED are assumed to be 5% of their primary values (Blomberg and Söderholm, 2009).

### 2.2.3 Case study results

Electricity was used to preheat the billets and dies in an electric preheat furnace and to power the extrusion press hydraulics, container cartridge heaters, billet butt shear, and auxiliary equipment. The electricity to heat two 40-kg billets to 530°C over 5.5 hours was 48 kWh. Prior to extruding the billets, the press container was heated over 12 hours from room temperature to 450°C, which required 216 kWh of electrical energy. This press preheating energy requirement dwarfs the energy needed to extrude a single billet but in industry this press preheating is only needed after replacement of the press container, a process which requires the press to be cooled but typically only occurs after every  $\approx 15$  kt of extruded profile (about six months of production (Superior Aluminum, 2019)). Therefore, the environmental impacts and costs of press preheating are negligible when normalized to the functional unit of 1 kg of un-fabricated profile. In industry, billet preheating typically uses continuous natural gas fired furnaces rather than electric ovens; however, the direct energy requirements in the case studies are within the expected range from industry (Figure A2). The billet preheating energy efficiency ( $\eta_{preheat}$ ) is defined as the minimum energy needed to heat the billet ( $mc\Delta T$ ) divided by the actual, measured, energy delivered to heat the billet, be it electrical energy or thermal energy from combustion of natural gas. In the case studies,  $\eta_{preheat}$  was found to be 21%.

Electrical energy is required after press preheating to maintain the container temperature during idling, to operate the hydraulic ram to extrude the billet, and to operate the hydraulic shear to remove the billet butt. Figure 2.3 shows the electrical power consumed by the press during the case studies. The active power correlates with the measured ram force; both are at their maximum at the start of the ram stroke and decrease as the ram extrudes the billet and the area between billet and container decreases, reducing frictional resistance. The mean power factor during the case study extrusion process is 0.82. The power factor peaks at 0.96 at the beginning of each ram stroke but drops to 0.39 during idling. Press idling consumes 9-27 kW as the cartridge heaters turn on intermittently. For the case of the solid rectangular bar, over a complete press cycle (600 seconds, from the start of one ram stroke to the next), 10.15 kWh of electricity was consumed of which 3 kWh was attributable to baseload energy requirements including during idle, 6.79 kWh was the increased energy required to extrude the billet, and 0.36 kWh was attributable to operating the shear.



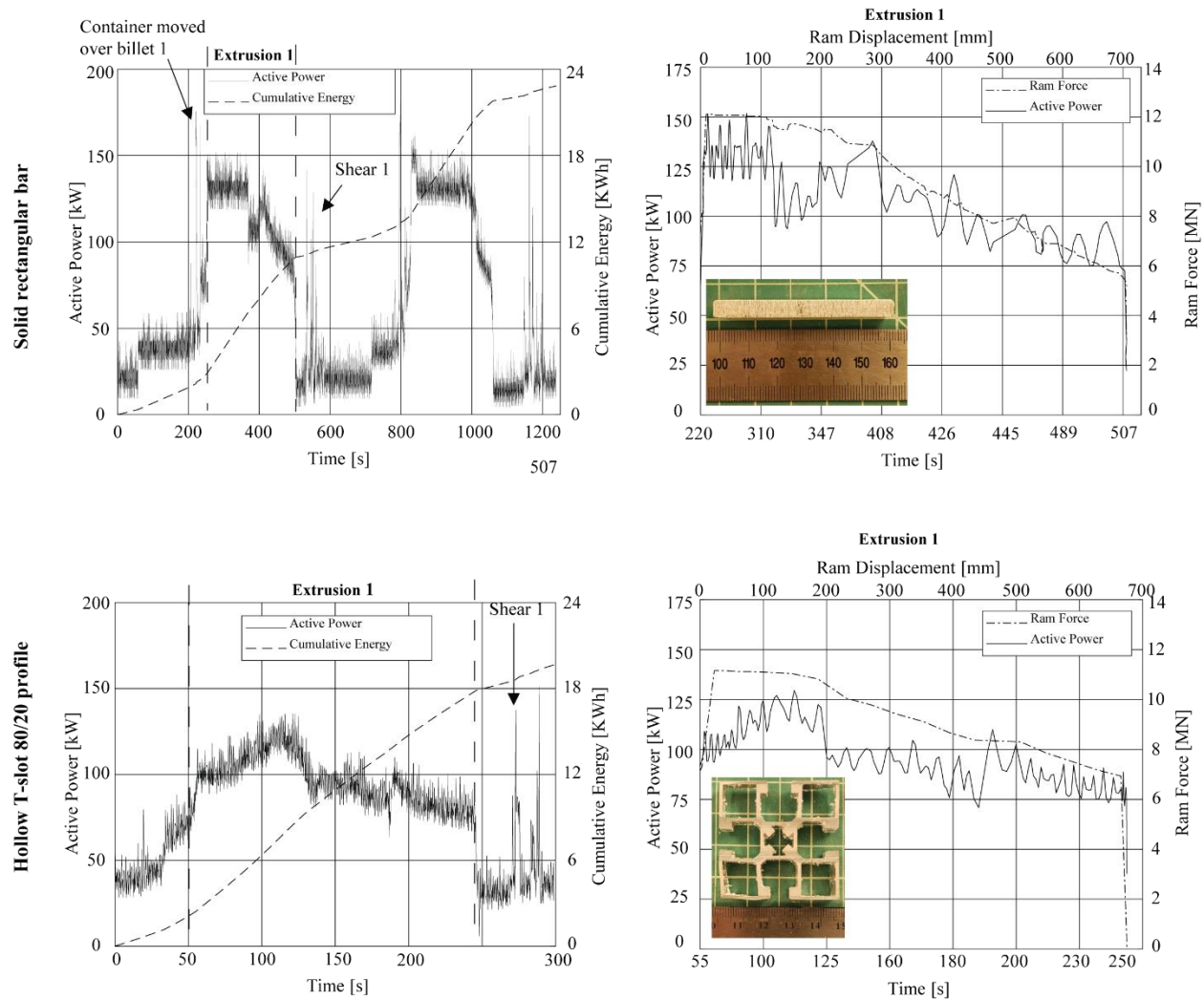


Figure 2.3: Active power, cumulative energy and ram force during extrusion of case study profiles.

The extrusion press energy efficiency ( $\eta_{press}$ ) is defined as the minimum mechanical energy needed to extrude the billet (the area under the ram force-displacement curve on the right hand side of Figure 2.3) divided by the actual electrical energy delivered to extrude a billet (the area under the power-time curve on the right hand side of Figure 2.3). In the case studies,  $\eta_{press}$  was 6.3% and 8.2% for the solid and hollow profiles respectively.

The total impacts and costs of the case studies are presented in Figure 2.4. It is shown that the aluminum material represents the vast majority of the environmental impacts and costs; e.g., 95.2% of the GWP, 90.7% of the CED and 91.8% of the costs in the solid rectangular profile case study. The material utilization from aluminum log to finished profile was 82% for the solid profile and 81% for the hollow profile. The front-end scrap was the largest source of scrap, closely followed by the billet butt. These process yield

losses increase the material impacts and costs, and also the direct energy requirements because extra material must be heated, extruded, and sheared. The relative increase in material costs that results from the yield loss is not as significant as the increase for material CED and GWP because of the significant monetary value of extrusion scrap.

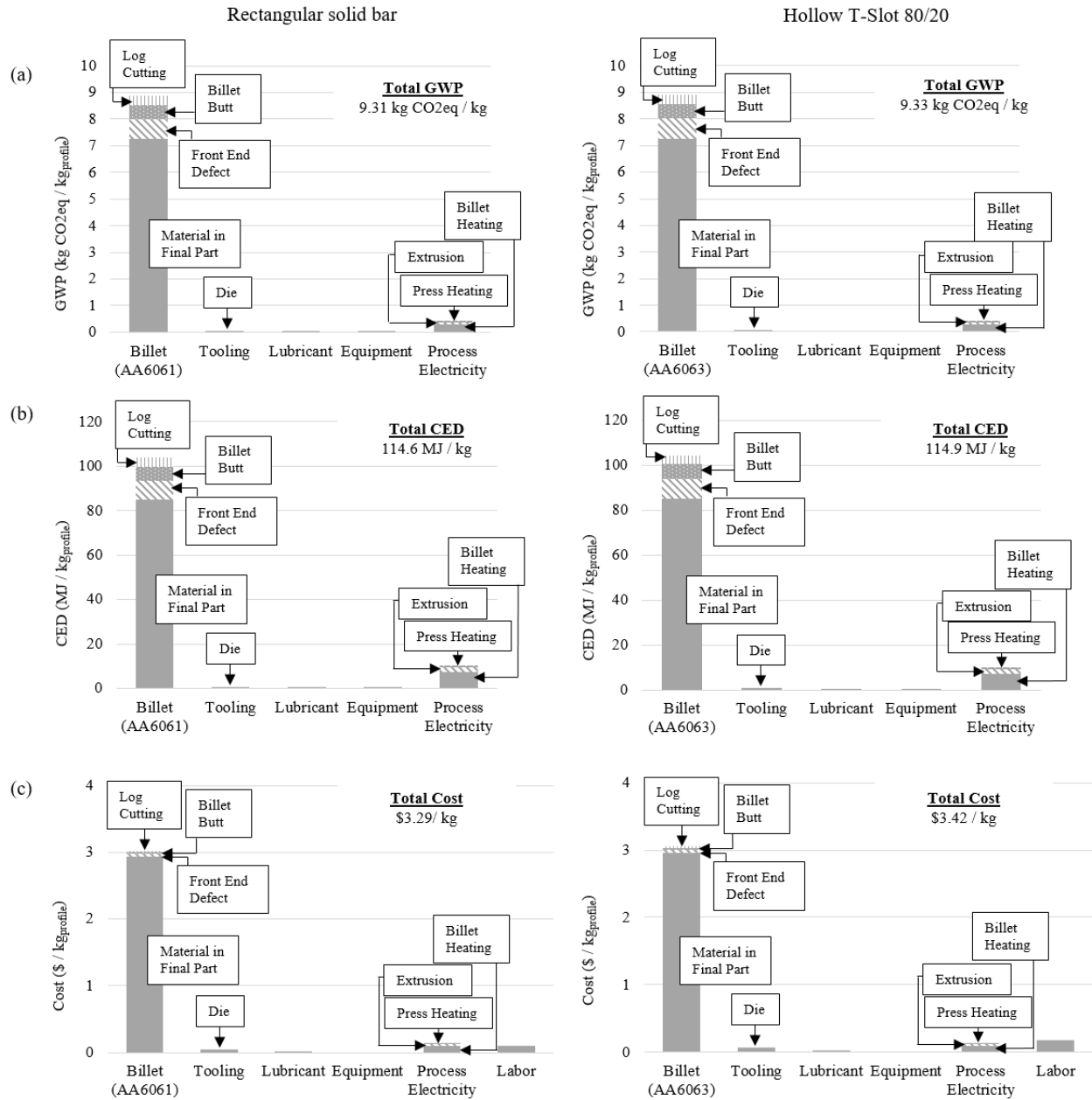


Figure 2.4: The (a) Global Warming Potential (GWP), (b) Cumulative Energy Demand (CED) and, (c) Costs of the two case study profiles.

Figure 2.4 shows that direct energy and labor requirements also have a noticeable financial burden, representing 4% and 3% of the costs respectively in the rectangular solid bar, and 4% and 5% of the costs respectively in the hollow profile. The labor costs are higher in the hollow profile case study because of the lower ram and extrudate speed (Table 2.1). The boron nitride lubricant, press equipment, container, and dummy block tool have a negligible impact ( $\ll 1\%$ ) on the environment impacts and costs. The relatively short lifespan of the extrusion die (Table 2.1), however, means that it only accounts for approximately 1% of the total cost.

## 2.2.4 Global parametric models of extrusion process impacts and costs

### 2.2.4.1 Deriving global models

Equations 2.1 and 2.2 present simple representations of the environmental impact ( $I$ ) and cost ( $C$ ) per kg of un-fabricated profile based on the main contributing factors determined using the case studies.

$$I_{per\ kg\ profile} = [I_{log} + I_{tooling} + I_{direct\ energy}]_{per\ kg\ profile} \quad (2.1)$$

$$C_{per\ kg\ profile} = [(C_{log} - C_{scrap}) + C_{tooling} + C_{direct\ energy} + C_{labor}]_{per\ kg\ profile} \quad (2.2)$$

The impacts and costs of the aluminum metal ( $I_{log}$  and  $C_{log}-C_{scrap}$ ), tooling dies ( $I_{tooling}$  and  $C_{tooling}$ ), direct energy requirements ( $I_{direct\ energy}$  and  $C_{direct\ energy}$ ), and labor ( $C_{labor}$ ) are expressed in equations 2.3-2.9, where  $\alpha$  is the overall material yield (0-1) from the DC-cast log to the final profile,  $R$  is the recycled content of the log (0-1),  $M_{produced}$  is the mass of total finished profile produced (in kg),  $L_{die}$  is the lifespan of the extrusion die (in kg of profile produced),  $M_{die}$  is the mass of the cast die (in kg),  $M_{removed}$  is the mass of the cast die that is machined away (in kg) to produce the final die shape,  $C_{die}$  is the upfront cost of the extrusion die (in USD), and  $G_X$  and  $E_X$  are the direct natural gas and electricity requirements needed to perform operation  $X$ .

$$I_{log, per\ kg\ profile} = \frac{R \cdot i_{secondary-at} + (1-R) \cdot i_{primary-at}}{\alpha} \quad (2.3)$$

$$(C_{log} - C_{scrap})_{per\ kg\ profile} = \left(\frac{1}{\alpha}\right) \cdot \left(R \cdot (C_{secondary-at} + C_{midwest-prem.} + C_{billet-prem.}) + (1-R) \cdot (C_{primary-at} + C_{midwest-prem.} + C_{billet-prem.})\right) - \left(\frac{1-\alpha}{\alpha}\right) \cdot C_{scrap} \quad (2.4)$$

$$I_{tooling, per\ kg\ profile} = \frac{\left[\frac{M_{produced}}{L_{die}}\right] \cdot (M_{die} \cdot i_{die} + M_{removed} \cdot i_{removed})}{M_{produced}} \quad (2.5)$$

$$C_{tooling, per\ kg\ profile} = \frac{\left[\frac{M_{produced}}{L_{die}}\right] \cdot C_{die}}{M_{produced}} \quad (2.6)$$

$$I_{direct\ energy, per\ kg\ profile} = i_{gas} \cdot (G_{preheat} + G_{heat\ treat} + G_{finishing}) + i_{electricity} \cdot (E_{press} + E_{heat\ treat} + E_{finishing}) \quad (2.7)$$

$$C_{direct\ energy,per\ kg\ profile} = c_{gas} \cdot (G_{preheat} + G_{heat\ treat} + G_{finishing}) + c_{electricity} \cdot (E_{press} + E_{heat\ treat} + E_{finishing}) \quad (2.8)$$

$$C_{labor,per\ kg\ profile} = \frac{0.96 \times P \cdot w}{60 \cdot \alpha \cdot \lambda \cdot V} \text{ where } w \text{ has units of } \$/\text{hour}, \lambda \text{ of } \text{kg}/\text{m}, \text{ and } V \text{ of } \text{m}/\text{min}. \quad (2.9)$$

Equations 2.7 and 2.8 model the direct energy requirements of a typical extrusion facility where natural gas is used to preheat the billets and in any post extrusion heat treatment. The labor costs (equation 2.9) are estimated using the number of line and supporting workers ( $P$ ), the hourly wage ( $w$ ), and the time to extrude 1 kg profile calculated using the linear density ( $\lambda$ ), forming yield, and the expected speed of the extrudate ( $V$ ) for a given profile.

Practitioners can substitute their own values into the equations where available. Otherwise, the intrinsic impacts and costs shown in Equations 2.1-2.9 (indicated by lowercase letters) are presented in Table 2.2, and representative values for the other life cycle inventory variables (indicated by uppercase letters) are presented in Table 2.3. Representative inventory values are compiled from industry publications (e.g., EAA, 2018), expert interviews (e.g., Superior Aluminum, 2019), and the case study data with physics-based extrapolations. A leading European extruder of automotive profiles provided aggregated direct energy (electricity and gas) data for one year of production (8.7 kt of profiles). The data (provided on the condition of anonymity) is analyzed in A2 and the mean values included in Table 2.3.

Table 2.3: Extrusion characteristics for predictive models (A2). Uncertainties correspond to 1 standard deviation and are modeled as normal distributions calculated from the respective data sources.

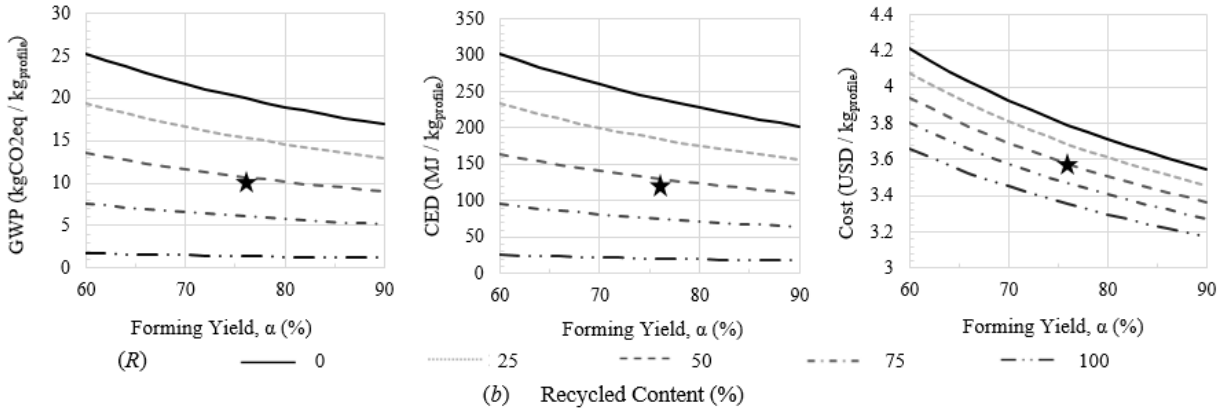
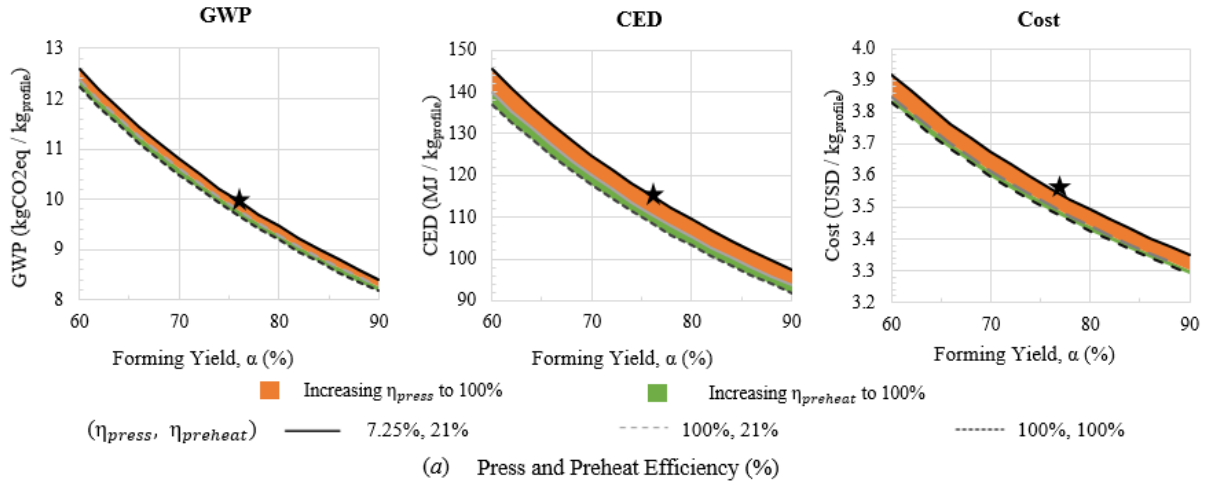
	Nominal value	Uncertainty
Recycled content, $R$ %	54	10% of nominal value
Process yield, $\alpha$ %	76.3	10% of nominal value
Extrusion press energy efficiency, $\eta_{press}$ %	7.25	10% of nominal value
Billet preheat energy efficiency, $\eta_{preheat}$ %	21	10% of nominal value
Die cost <sup>1</sup> , $C_{die}$ \$	$10,338.5 \times CCD + 234.2 \times P_{tot} \times S$	10% of nominal value
Die Lifespan <sup>2</sup> (average), $L_{die}$ kg <sub>profile</sub>	63,000	6,000
Hollow die	20,000	6,000
Solid Die	106,000	6,000
Mass die <sup>3</sup> , $M_{die}$ kg	$(3.81 \times 10^{(-8)}) \times \rho_{tool\ steel} \times \pi \times (2D_{container})^2$	10% of nominal value
Mass removed (solid) <sup>4</sup> , $M_{removed}$ kg	$0.15 * M_{die}$	10% of nominal value

Mass removed (hollow) <sup>4</sup> , $M_{removed}$ kg	$0.3 * M_{die}$	10% of nominal value
Number of workers <sup>5</sup> , $P$	4	0.5
Speed of the extrudate, $V$ m/min. (AA6061) <sup>6</sup> (AA6063) <sup>6</sup> (AA6082) <sup>7</sup> (AA7075) <sup>6</sup>	27 45 14.5 1.6	10% of nominal value
Preheat gas <sup>8</sup> , $G_{preheat}$ therms/kg <sub>billet</sub>	$\frac{0.96}{\alpha} \times \frac{900 \times (T_{billet} - T_{ambient})}{\eta_{preheat}} \times \frac{1}{29.3 \times 3600000}$ or European collaborator average: 0.014	10% of nominal value
Heat treat gas, $G_{heat treat}$ therms/kg <sub>profile</sub>	European collaborator average: 0.001	10% of nominal value
Finishing gas, $G_{finishing}$ therms/kg <sub>profile</sub>	European collaborator average: 0.022	10% of nominal value
Heat treat electricity, $E_{heat treat}$ kWh/kg <sub>profile</sub>	European collaborator average: 0.045	10% of nominal value
Finishing electricity, $E_{finishing}$ kWh/kg <sub>profile</sub>	European collaborator average: 0.960	10% of nominal value
Press electrical energy, $E_{press}$ kWh/kg <sub>profile</sub>	$\frac{0.96}{3600000} \times \frac{e_{mech}}{\eta_{press}}$ or European collaborator average: 0.56	10% of nominal value
Minimum mechanical energy to extrude the billet <sup>9</sup> , $E_{mech}$ MJ	$L_{billet} \frac{\pi D_{billet}^2}{4} K_x Y_f \left( \ln(ER) + \frac{L_{billet}}{D_{billet}} \right) \times 10^{-9}$	10% of nominal value
Minimum mechanical energy to extrude the billet per kg of billet, $e_{mech}$ MJ/kg	$\frac{1}{\rho} K_x Y_f \left( \ln(ER) + \frac{L_{billet}}{D_{billet}} \right)$	10% of nominal value
Shape Factor <sup>1,10</sup> , $K_x$	$0.98 + 0.02 \left( \frac{P_{tot}}{C_{eq}} \right)^{2.25}$	10% of nominal value

Notes: 1: Die cost model from Nieto (2010) based on an empirical multivariate regression analysis performed on quotes obtained from toolmakers and covering a wide range of die designs. The circumscribing circle diameter ( $CCD$ , measured in mm) describes the minimum circle diameter that fully encompasses the profile, the total perimeter ( $P_{tot}$ , measured in mm) is the total perimeter of the profile cross section (sum of internal and external perimeters) and the shape factor ( $S$ ) describes the type of die,  $S=1$  for solid profiles,  $S=2$  for semi-hollow profiles with at least one partially enclosed void,  $S=2$  for class 1 hollows (with a void of 25.4 mm or greater) and class 2 hollows (any hollow profile other than class 1 that does not exceed  $CCD = 127$  mm), and  $S = 1 + N_{voids}$ , where  $N_{voids}$  is the number of voids, for class 3 hollows (all hollow profiles that are not class 1 or class 2). 2: Based on discussions with TTE (2018). Extrusion dies are typically made from H13 tool steel. 3. Based on discussions with TTE (2018): Die diameter is twice container diameter and a 6" die thickness is typical.  $D_{container}$  is the diameter of the extrusion press container in mm. 4. Based on discussions with TTE (2018). 5. Based on discussions with Kaiser Aluminum (2020). 6. Data from Misiolek and Kelly (2005). 7: Data from Tomczyk (2019). 8. Specific heat capacity of aluminum = 900 J/Kg°C; Conversion from J to therms =  $\frac{1}{29.3 \times 3600000}$ ; default  $T_{billet}=450^\circ\text{C}$  and  $T_{ambient}=20^\circ\text{C}$ . 9. The mechanical energy ( $e_{mech}$ ) is calculated using a lower bound slab analysis to estimate the necessary extrusion force at the beginning and end of the press stroke and integrating over the ram stroke distance (see Section A3.1). Billet dimensions are measured in mm.  $Y_f$  is the aluminum yield stress at the extrusion temperature measured in MPa (see Table A5 for example data). 10.  $C_{eq}$  (in mm) is the equivalent circumference, or the circumference of a circle with an area equal to the profile cross-section. 11. In equations 2.1-2.9 and Table 2.3, the "0.96" coefficient accounts for the log-to-billet cutting yield loss of 4%.

#### 2.2.4.2 Sensitivity of impacts and costs to key extrusion parameters

The global models were used to determine the effect of key extrusion parameters on environmental impacts and costs: (1) Extrusion press and billet preheating energy efficiency ( $\eta_{press}$  and  $\eta_{preheat}$ ), (2) Forming yield ( $\alpha$ ), (3) Billet recycled content ( $R$ ), and (4) Process throughput measured as the extrudate speed ( $V$ ). Figure 2.5 presents the results for extruding a heat treated multi-hollow AA6082 battery tray rail (a typical automotive part) from Ø9" (Ø228.6 mm) billets (see Table A4 for complete details). For clarity, Figure 2.5 is constructed just using the nominal inventory and intrinsic impact values reported in Tables 2.2 and 2.3. Figure A4 presents the uncertainty in the results as determined from 100,000 Monte Carlo simulations. Across the parameter space, the uncertainty (one standard deviation) of the GWP and CED is 10.9% and 10.4%, respectively, and the uncertainty of the costs around 11.4%. These error bars mainly reflect the uncertainty in the intrinsic billet impacts (Table 2.2) and the billet and wage costs.



Changing throughput has a negligible effect on GWP via amortization of capital equipment emissions

Changing throughput has a negligible effect on GWP via amortization of capital equipment emissions

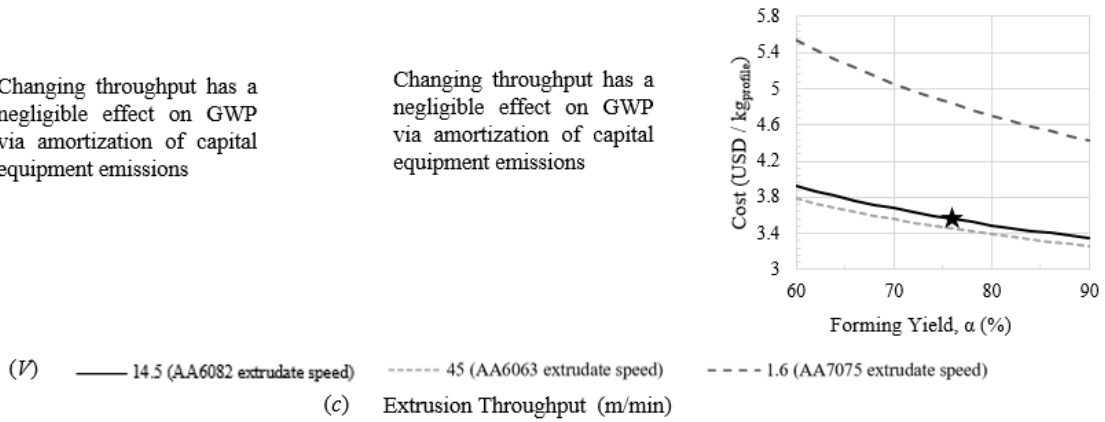


Figure 2.5: Sensitivity analysis on the costs, GWP, and CED of an automotive AA6082 battery tray profile (Table A4). The star in each plot represents the current industry standard.

At the current industry standard, for each 1 kg of battery tray profile, 0.021 therms of natural gas is used to preheat 1.31 kg of billet which is then extruded using 0.46 kWh of electricity. This conforms to

the range of aggregated direct energy values provided by the European automotive extruder (Figure SA2). Figure 2.5a shows that increasing the extrusion press and billet preheating energy efficiency can significantly lower the environmental impacts but cost savings are more modest:  $\approx 6\%$  reduction in CED and  $< 2\%$  reduction in costs for 100% energy efficiency. However, Figure 2.5b shows that the greatest reductions in environmental impacts are from increasing the process forming yield and the billet recycled content. A 10% increase in the forming yield from 76.3% to 83.9% results in GWP, CED and costs being reduced by 9.03%, 8.97% and 3.17% respectively. A 10% increase in recycled content reduces the environmental impacts by  $\approx 10\%$  but the costs by only  $\approx 0.7\%$ . Figure 2.5c shows the great increase in cost when using extrusion speeds similar to those used for AA7075 due to a low throughput.

### **2.3. Material flow analysis of the North American extrusion industry**

The analysis presented in Section 2.2.4 shows that increasing material efficiency (process yields and billet recycled contents) will have the greatest effect on reducing the environmental impacts and costs of the aluminum extrusion industry; however, no detailed MFAs exist showing the markets (e.g., alloys, section shapes, and applications) in which material efficiency efforts should focus. In this section, an MFA of the North American (U.S. and Canada) aluminum extrusion industry in 2018 is derived; North America in 2018 is the region and most recent year for which extensive data is available.

#### **2.3.1 Constructing a map of aluminum extrusion flows**

A wireframe map representation of the MFA (Figure A5) was produced based on existing industry analyses (e.g., Mulholland, 2016) and refined based on industry interviews. The wireframe map defines the key processes along the supply chain and the existence or absence of material flows between the different processes; e.g., the existence of a flow of imported ingots into North American secondary billet production. At each step along the supply chain, data ( $\hat{x}$ ) was collected on the material origin, mass of material processed, process yield, alloy, and destination/application. Over 100 MFA data records (Table A16) were collected from industry associations (e.g., *International Aluminum Institute* (2021)), national and international statistical agencies (e.g., UN Comtrade data (2018)), publicly available industry databases (e.g., Norsk Hydro (2020a, 2020b)), academic and grey literature, and 100 semi-structured interviews with industry experts from each part of the supply chain: billet production, extrusion, recycling, fabrication, and end-use. Table A14 summarizes the main data sources.

#### **2.3.2 MFA data reconciliation (S4)**

As is common in MFA, data records on many of the MFA parameters are either missing or inconsistent; i.e., different data sources record different (contradictory) values for the same MFA parameter or data



records on neighboring MFA parameters suggest a violation of the conservation of mass. For example, no reports were found quantifying the annual production volume of primary and secondary billet by alloy in North America in 2018. Elsewhere in the data collection process, the reported annual production of extrusions from Bertram et al. (2017) in conjunction with the reported fabrication process yield from Cullen and Allwood (2013) suggest that 2.65 Mt of fabricated extrusions were produced in 2018, which is inconsistent with the 2.28 Mt of fabricated extrusions reported by Sattlethight (2019). A set of internally consistent, mass-balanced MFA parameters ( $x_i$ ) is generated using an adaptation of Zhu et al.'s (2019) nonlinear least squares data reconciliation method, which itself is developed from earlier work by Kopec et al. (2016). Zhu et al.'s method is used because it is easily updatable, can handle a plethora of data types (e.g., process yield ratios), and presents a consistent method for assigning a confidence score ( $\phi_{i,j}$ : 0-1) to each collected data record. In the reconciliation, the objective function presented in equation 2.10 is minimized subject to conservation of mass constraints.  $r_{i,j}$  are the normalized residuals between the collected data ( $\hat{x}_{ij}$ ) and reconciled data ( $x_i$ ).  $J_i$  is the total number of empirical data records collected for each MFA parameter,  $i$ . For each data record, the confidence score ( $\phi_{i,j}$ ) was determined based on the alignment of the data record with the desired coverage (1-4; 1 = single case study; 4 = data from >50% of industry), frequency (1-4; 1 = single data point; 4 = at least monthly data collection), and spatial boundary of the source (1-4; 1 = data scaled from Global data and/or a different industry; 4 = data from only North American extrusion industry) (see Table A13); e.g., the AEC's annual end-use survey has a confidence score of 0.917 (coverage score of 4/4, frequency score of 3/4, spatial boundary score of 4/4, for a total score of 11/12=0.917). Table A16 presents a complete list of the collected data records ( $\hat{x}_i$ ) and the corresponding confidence scores ( $\phi_{i,j}$ ) used in this MFA data reconciliation.

$\text{Minimize: } \sum_{i=1}^I \frac{\sum_{j=1}^{J_i} \phi_{i,j} (r_{i,j})^2}{J_i} \text{ where } r_{i,j} = \frac{J_i(x_i - \hat{x}_{ij})}{\sum_{j=1}^{J_i} \hat{x}_{ij}}$	(2.10)
-----------------------------------------------------------------------------------------------------------------------------------------------------------------------------	--------

In order to increase the likelihood of convergence to a near global optimum solution, the initial set of values used in the nonlinear optimization is equal to the weighted mean (by confidence score) of all data records for each MFA parameter. If no recorded data is available, initial values are calculated using simple mass balance. The optimization was implemented with Matlab's fmincon algorithm using the "interior-point" method. It took 201 iterations for the objective function to converge (Figure A8): 20 minutes on an AMD Ryzen 5 2600 CPU, 3.40GHz with 16 GB of 3200 MHz RAM. The optimization achieved mass balance after an initial maximum constraint violation of 0.51 Mt (corresponding to a discrepancy between reported billet consumption, extrusion production and yield rate) and reduced the objective function by 42% from a maximum of 0.024 during mass balancing to 0.014 at convergence (Figure A8). The code and data used for this MFA reconciliation is available for download (see A6.3).

### 2.3.3 MFA results

The estimated 2018 North America aluminum extrusion material flow is shown in Figure 2.6 as a Sankey diagram, where the width of each line is proportional to the mass flow. The light gray lines represent scrap flows and the black lines represent system losses (e.g., cross generation).

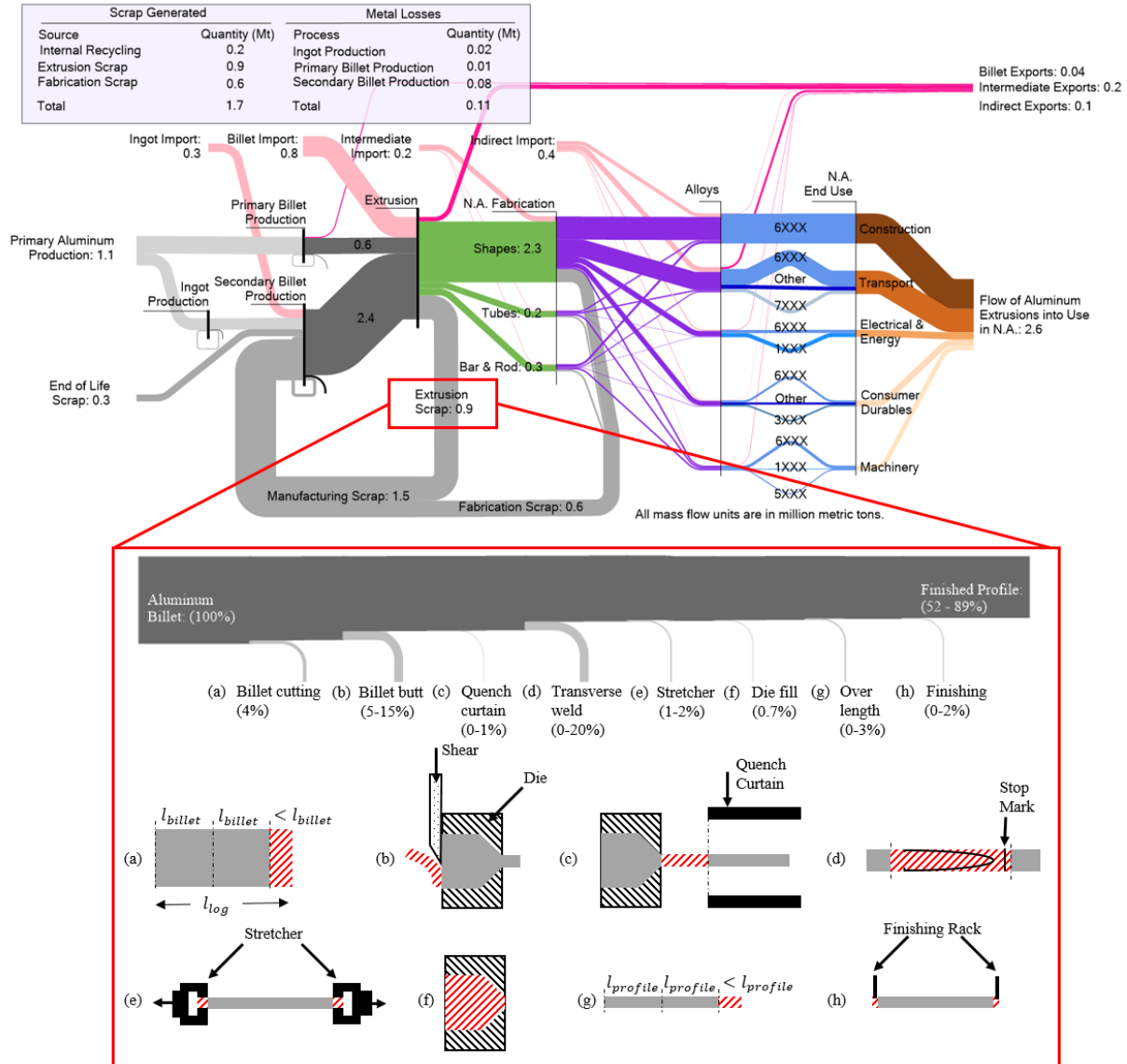


Figure 2.6: Top: Sankey diagram representation of the material flow of aluminum extrusions in North America (N.A.: U.S. and Canada) in 2018 (Note: Aluminum alloying is done during billet production and it is only placed after extrusion here to clearly show the flow of fabricated profiles). Bottom: The flow of aluminum for a typical extrusion from DC cast log to unfabricated aluminum profile showing the range of scrap generated at each stage of the extrusion process as a red hashed area.

In 2018, North America consumed approximately 2.6 Mt of fabricated aluminum profiles embedded within end-use products. The domestic North American industry consisted of around 500 extrusion presses

operated by approximately 130 extrusion companies (Consulting Collaborative, 2017) that produced a total of 2.9 Mt of un-fabricated profile (0.2 Mt for export) from 3.8 Mt of billet (76% mean process yield, excluding log-to-billet cutting) with over half (52%) of production from just five large companies: Hydro, Kaiser, Bonnell, UMEX and Extrudex (Consulting Collaborative, 2017). A further 20% of the aluminum was scrapped during fabrication into finished products. At all points along the supply chain, North America was a net importer of ingots, billets, intermediate (un-fabricated) profiles, and indirect (finished) goods.

Figure 2.6 shows that despite the dominance of secondary billet production in North America, relatively little end-of-life (post-consumer) scrap is used. Instead, secondary billet feedstock is largely manufacturing scrap and primary ingot. Extrusion process scrap is largely closed loop recycled into extrusion billet; however, secondary billet production creates more internal runaround scrap as well as  $\approx 3\%$  losses to dross generation. The North American extrusion industry produces many thousands of different profile shapes; however, these shapes can be categorized under three broad banners: (1) solid profile (and largely commodity) rod and bar, (2) simple tubes, and (3) complex shapes that account for 82% of the market. Figure 2.6 shows that 6xxx series alloys dominate production and that the transport sector end use demand is comparable to the construction industry. Figure A9 shows the flow of different alloys into different construction and transport subcategories. Commercial façade is the single greatest destination for extrusions across construction and transport, and the destination of transport extrusions is evenly split between cars and light trucks, semis and trailers, and ‘other’ (e.g., truck, bus, RV, rail). More extrusions are used in electric vehicles than any other type of vehicle (Dinsmore, 2018). Applications include simple cylindrical rods used as machining stock (Norsk Hydro, 2020b), to roof bows (e.g., Tesla Model S (Design News Staff, 2014)), battery housings (e.g., in the Ford Mustang Mach-E EV (Page, 2020)), and trim and crash management systems (Ducker Worldwide, 2017).

Figure 2.6 (bottom) shows the contribution of various process yield losses to the estimated 0.9 Mt of extrusion process scrap. These additional yield losses (beyond billet log cutting, billet butt, and front-end defect scrap) are often absent depending on the context (alloy, desired surface finish etc.). A quench box is used when the extruded profile is made from a heat treatable aluminum alloy (e.g., AA6082) that requires rapid water spray cooling in order to create a supersaturated solid solution (SSSS) in preparation for precipitation hardening. There is often a gap of approximately 1.2 m between the exit of the die and the start of the quench curtain due to imperfect integration of the press and quench box machine designs (Figure 2.6c). This gap results in the last section of extruded billet experiencing natural air cooling as it is left stationary between the die and quench curtain while the ram is retracted, the billet butt sheared, and a new billet loaded into the container. Natural cooling prevents the creation of a suitable SSSS that can be subsequently age hardened; therefore, this section of material between the die and the quench curtain is scrapped. After extrusion, lengths of profile equal to the run-out table length are typically straightened using

a stretcher machine that grips the ends of the profile and imposes a 1-3% tensile elongation. The material squeezed by the grippers is often deformed and scrapped. After a production run is finished, the extrusion die is allowed to cool and is cleaned before future use. Billet material entrapped within the die at the end of a production run is scrapped. When sectioning the stretched profile into desired lengths there are often leftover lengths of material that are discarded as scrap. Finally, scrap may also be created as a result of the finishing process (e.g., anodizing) when profiles are loaded on racks for finishing but where material in contact with the racks receives a poor finish and is subsequently trimmed.

A formal uncertainty analysis on the results presented in Figure 2.6 (top) is not possible because extrusion production statistics are not published with error bands. This is a common problem in MFA (Cullen et al., 2012). The uncertainty is mitigated in this study, as much as is possible, through the use of trustworthy data sources wherever possible, confidence scores to weigh the data records, and a mass-balancing data reconciliation of the collected MFA data records. The final reconciliation result is presented to the nearest 100,000 tons, or 1 significant figure in the case of values below 100,000 tons. Figure A10 shows the average residual for the MFA flow variables, and indicates the level of discrepancy between the final MFA result and the initial data records. The largest residual is close to 10% and originates from the difference between the reconciled value for the total production of extruded profiles fabricated in North America (2.7 Mt) compared to a value of 3 Mt from Sattlethight (2019). Despite the uncertainty in the final results, the global MFA presents an estimate of the North American extrusion industry that can be used to inform decision making in industry and academia.

## **2.4 Section discussion**

This work presents a comprehensive environmental analysis of aluminum extrusion including electrical energy measurements, aggregated industry data, predictive models, and material flow analyses, with the opportunities to reduce impacts compared to the likely effect on costs. Uncertainties in the numerical results are significant (Section 2.2.4, A.3.3) but these have not prevented the influential parameters from being identified. The global models show that there is significant scope for increasing the extrusion press and preheat energy efficiency; however, increasing the material efficiency (process yield and billet recycled content) of the extrusion process represents the greatest opportunity to reduce both the environmental impacts and the costs (Figure 2.5).

### **2.4.1 Reducing billet preheating and extrusion press energy requirements**

The extrusion process is energy-intensive: the primary energy of billet preheating and extrusion is greater than for aluminum remelting in recycling (Figures 2.4 and 2.5 versus Table 2.2). This article has found significant scope for improving the energy efficiency of the extrusion process. The case study data

are used to quantify an energy efficiency metric for billet preheating ( $\eta_{preheat}$ ) and for the press ( $\eta_{press}$ ) at 21% and  $\approx 7.25\%$  respectively. In targeting billet preheat efficiency improvements, a U.S. Department of Energy study (2003) found that replacing the burners in furnaces with new, more efficient burners could decrease natural gas consumption by 30-40% with a payback period of less than 1 year. These higher efficiency burners include self-regenerative burners that recycle the hot exhaust air as pre-heated combustion air; Wüning (2007) found that self-regenerative burners can generate energy savings of more than 20%.

One reason for the low extrusion press efficiency is that the full power capacity of the press is sized for generating the maximum forming force; however, these peak forces are only required for a small fraction of the cycle time at the beginning of the press stroke (see Figure 2.3) leading to low average and minimum power factors and high line currents, which increase line and transformer energy losses (Cooper et al., 2017). Furthermore, in conventional hydraulic presses all the main pumps are operating continuously even during idling (SMS Group, 2020). In a recent study (Schreiber et al., 2016), Danieli Breda (an extrusion press manufacturer) measured 5-20% extrusion press energy savings when switching from classic servo-piloted variable displacement pumps equipped with fixed-speed motors to variable displacement pumps and variable speed motors controlled by a variable frequency drive. As described by Cooper et al. (2017), these devices save energy by slowing (or stopping) a motor to match light loads and as energy use is proportional to the cube of the flow rate in the hydraulic system, small reductions in flow can yield disproportionately large energy savings (Nadel et al., 2002). Elsewhere, a recent aluminum extrusion plant retrofit in the Netherlands with a start-stop system led to a 10% reduction in the electrical energy consumption of the main press drives (SMS Group, 2020). Within North America, Superior Aluminum (2019) saw a 2-year payback period in energy savings following a pump and motor replacement in several of their presses. A greater number of new presses now have hybrid drives where hydraulics are used to generate the forming force but all other press movements are delivered through servo drives (Anacker, 2020; Macedonio, 2021). Another option for reducing the press' direct energy requirements is to reduce the mechanical energy needed to extrude the profile ( $e_{mech}$ , Table 2.3) by optimizing the billet geometry. Increasing the billet (and container) diameter while maintaining the billet volume will reduce the mechanical energy requirement but can increase the maximum ram force requirement and is constrained by the force limit of the press (see A7 for analysis and experimental evidence).

#### **2.4.2 Opportunities for material efficiency**

The reconciled MFA (Section 3) suggests that the average recycled content of profiles produced in North America is around 50% and that 40% of all aluminum cast into extrusion billets is scrapped before being used in a fabricated product. Increasing the billet recycled content would result in a significant

decrease in environmental impacts (see Figure 2.5). Manufacturing scrap produced in the extrusion industry is already (typically) closed-loop recycled back into extrusion billets but there are opportunities to increase recovery of end-of-life extrusion scrap, particularly from vehicles which contain increasing quantities of aluminum extrusions but which are currently shredded at end-of-life with contaminated mixed alloy aluminum scrap exported or downgraded as zorba/twitch (Zhu et al., 2021). Recovery of automotive extrusions will require greater disassembly or automated separation of scrapped vehicle materials. Currently, these activities are prohibitively expensive but might be aided in the future by a greater focus in vehicle design for recycling and emerging cheap and high throughput alloy separation recycling technologies (Zhu et al., 2021). Another barrier to increasing billet recycled contents is that extruders often exclusively use primary billet for safety-critical and aesthetic parts; e.g., wing spars in the aerospace industry (Boeing, 2020). Greater research into guaranteeing profile properties from secondary billet could prove fruitful here. Elsewhere, the embodied impacts for non-critical parts could be further reduced if conventional cast billets were substituted with chip billets of compacted machining swarf manufacturing scrap. Numerous researchers have studied this solid-state recycling technology for a decade and have shown that the scrap fragments weld together in the solid-state as they pass through the extrusion die, creating profiles with mechanical properties similar to those produced from conventional billets (Cooper, 2013; Tekkaya et al., 2009).

Figure 2.6 shows that the main sources of manufacturing scrap are extrusion process scrap (dominated by the billet log cutting scrap, the sheared billet butt scrap, and the transverse weld scrap), and fabrication scrap. There's the potential to employ billet selection and cutting optimization algorithms that help to minimize billet log cutting scrap (Masri and Warburton, 1998), particularly at smaller extruders where this technology is typically still not used today. Elsewhere, researchers have found modest reductions in the transverse weld length (up to ~15%) can be achieved by optimization of the ram velocity, ram-billet lubrication, and port-hole die geometry (Hatzenbichler and Buchmayr, 2010; Zhang et al., 2017). Recently, Oberhausen et al. (2021) showed preliminary evidence that novel dummy block and billet geometries could be used to control the flow of the billet-on-billet interface through the extrusion die and result in >50% reductions in transverse weld lengths, at least for simple profiles such as the rod and bar market revealed in Figure 6. For non-aesthetic profiles, there may also be the opportunity to utilize the profile between the stop mark and the "nose" of the transverse weld (0.15 m and 1 m in the solid and hollow profile case studies respectively) if this section is not already being used to grip the profile for stretching. Elsewhere, quench curtain scrap could be minimized by careful integration of equipment to minimize the die to quench curtain gap. New grippers and racks could also be designed to minimize stretcher and finishing scrap. Finally, profile fabrication yields might be increased through greater supply chain coordination between extruders

and manufacturers so that correct lengths are produced directly at the extrusion plant. The development of smart connected manufacturing systems as part of industry 4.0 might enable this efficiency.

### **2.4.3 Scale of the opportunity and industry trends**

The global parametric models (Section 2.2.4) are used to estimate the potential environmental and economic benefits of increasing the extrusion industry's material efficiency. For a typical North American extruder, producing 20 kt of final profile per year, a 10% increase in the material efficiency of the extrusion forming process (increasing from an average of 76.3% to 83.9%) would result in annual savings of 18 kt.CO<sub>2,eq</sub> and \$2.2 million. These emissions savings originate from avoiding the production and processing of billet material with a recycled content of 54%. Calculating the benefits of achieving higher process yields at a larger scale (e.g., nationally) is more complicated. On the one hand, an attributional approach can continue to be used to calculate the savings associated with avoiding production and processing of billet material with a recycled content of 54%. On the other hand, a consequential approach considers that a consequence of achieving higher process yields at a larger scale may be that the billet recycled content decreases as there will be less process scrap available for recycling (see Figure 2.6). At this larger scale, the consequential approach implies that the effect of higher process yields is to reduce the quantity of material that must be processed through the extrusion process and to shrink the return loop of scrap metal to billet production; therefore, the liquid metal production displaced due to higher process yields has a recycled content of around 96%, with 4% primary production accounting for metal losses during scrap remelting (Boin and Bertram, 2004). Subsequently, for North America (annual production: 2.6 Mt), it is estimated that a 10% increase in the material efficiency of the extrusion forming process would translate to annual savings of between \$270 million and 0.5 Mt.CO<sub>2,eq</sub> (consequential approach) and \$311 million and 2.3 Mt.CO<sub>2,eq</sub> (attributional approach). Finally, the global industry (annual production: 28 Mt) would save between \$2.9 billion and 5.4 Mt.CO<sub>2,eq</sub> (consequential approach) and \$3.35 billion and 25.2 Mt.CO<sub>2,eq</sub> (attributional approach). Despite the decrease in scrap availability due to higher process yields, the attributional savings could be achieved if the billet material recycled content were maintained through increased recycling of post-consumer scrap.

Current industry trends will only exacerbate the need to improve the extrusion industry's material efficiency. The MFA (Figure 2.6) shows that the extrusion of complex shape 6xxx profiles for the transport sector already accounts for 26% of extrusion demand. This market share is set to grow and is a sector where removal of the transverse weld scrap is typically mandated by the OEM. The industry interviews conducted for this study revealed a trend towards more complex cross-sections, thinner walls, and higher strength (7xxx series) profiles for lightweighting in the automotive market. However, deployment of these profiles, which would reduce transport use phase emissions, is hindered by the reduced throughput from extruding

thinner and harder material profiles and the increased reject rate from excessive distortion when quenching complex multi-cavity profiles. Figure 2.5c shows the large cost increase that accompanies the slower 7xxx alloy throughput. Increasing process yields could counter the effect of reduced extrusion speeds on the throughput and the inflated material costs of rejected parts by reducing the process time that is effectively dedicated to producing scrap.

## **2.5 Section conclusion**

In this work, extrusion cost and environmental impact models have been derived and a sensitivity analysis performed to identify the key inputs. The opportunities that have been identified include: (1) Reduction of the billet preheating energy requirements through the implementation of high efficiency burners, (2) Reduction of extrusion press energy requirements through variable frequency drive hydraulic pumps, (3) Increased billet (post-consumer scrap) recycled content in non-critical applications, and (4) Improved material efficiency through increased forming and fabrication yield rates. An MFA of the 2018 North American (U.S. and Canada) extrusion industry is used to evaluate the scope for material efficiency and subsequently the opportunities and barriers to increased process yields are discussed.



## Chapter 3. Modeling the Strength of Aluminum Extrusion Transverse Welds using the Film Theory of Solid-State Welding

Reducing production scrap, which increases process yield, is a key decarbonization strategy for the aluminum industry. For extrusion, the most scrap is generated by removing profile sections containing transverse (charge) welds because the welds are weaker than the surrounding material. No predictive

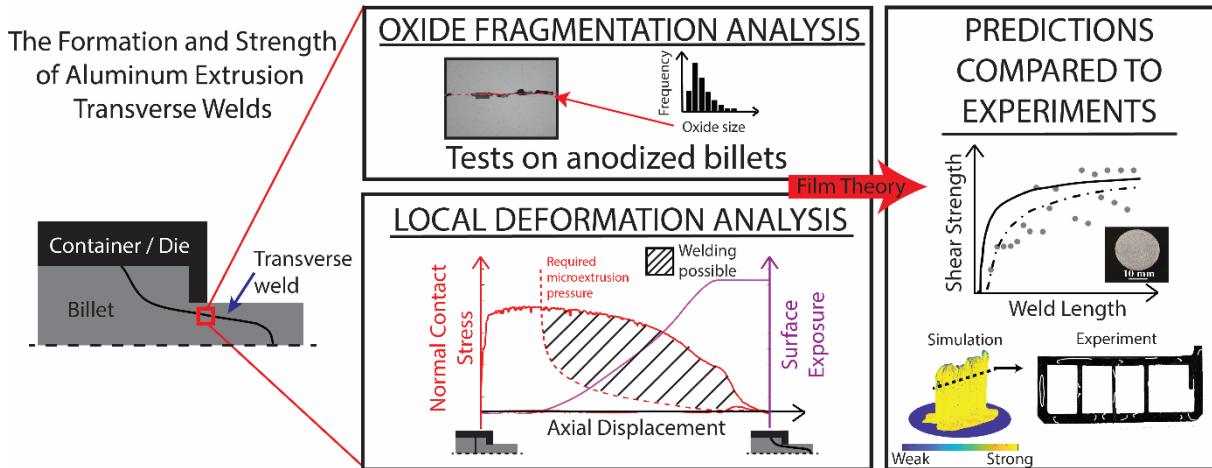


Figure 3.1: The formation and strength of aluminum extrusion transverse welds.

transverse weld strength model exists, preventing process optimization and development that might reduce the associated scrap. We derive a transverse weld strength model as a function of the billet material properties, extrusion temperature, and the evolving stress and strain states at the billet-billet interface during weld formation. The new model, based on the film theory of solid-state welding, updates Cooper and Allwood's plane strain welding model to account for the non-plane strain deformation at the billet-billet interface. These updates are informed by analyzing the oxide fragmentation patterns on transverse welds using shear lag modeling and microscopy of profiles extruded from anodized billets. Model strength predictions are evaluated against shear tests on welds created by extruding single and two-piece billets into rod, bar, and multi-hollow profiles. The experiments show negative (compressive) surface expansions at the weld nose cause interface buckling and low strengths. Surface expansions and weld strengths increase with distance from the nose. For non-axisymmetric profiles, deformation conditions and strengths vary across, as well as along, the weld. Two-piece billet welds are longer but experience a rapid increase in surface expansions and exhibit bulk strength long before the weld ends. The model predicts these trends and shows that die pressures are sufficient for micro-extrusion of any exposed substrate through cracks in the interface oxides. Hence, the importance of the local interface strains in exposing substrate and determining weld strength. The new model can help increase process yields by determining minimum lengths of weak profile to scrap and aiding die design optimization for increased weld strength.

### 3.1 Section introduction

Increasing manufacturing process yields is a key decarbonization strategy for the aluminum industry (IEA, 2019). Extrusion represents one of the most important aluminum supply chains to decarbonize, as around 20% of all aluminum is extruded (Cullen and Allwood, 2013) and there is an increase in extrusion demand driven by automotive and energy applications (Afseth, 2021; Aluminum Extruders Council, 2022; Lennon et al., 2022). There is significant scope for improving extrusion process yields. Oberhausen et al. (2022) estimate that around 40% of all aluminum cast into extrusion billets is scrapped before completion in a product. They find the greatest source of scrap is the removal of the transverse (charge) weld from extruded profiles. Reducing transverse weld scrap must therefore be targeted as part of the transition towards a low-carbon extrusion supply chain.

Transverse welds form between consecutively extruded billets in direct extrusion. The initially planar billet-billet interface is elongated as it passes through the die, forming tongue-shaped welds in the profile (Figure 3.2) with the number of welds equal to the number of die ports.

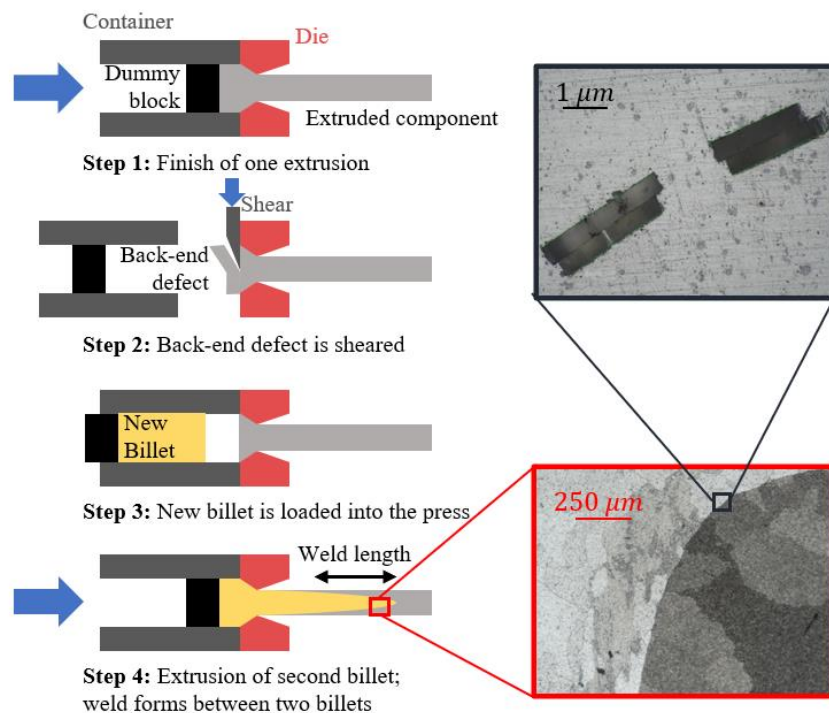


Figure 3.2: The formation of a transverse weld in a solid aluminum profile extruded from single-piece billets. Note: The micrographs are on welds created using anodized billets.

Concern about weld integrity generates process scrap in single-piece billet extrusion and limits scrap reuse via two-piece billet extrusion. In single-piece billet extrusion, the weld is often not removed from profiles destined for low-strength applications; e.g., concrete screed handles (Mag Specialties, 2019).

However, standard practice is to remove the section of profile containing the weld when the profile is destined for more high-performance applications. For instance, U.S. automotive OEMs insist on the removal of transverse welds (Ford Motor Company, 2013). This scrap can account for up to 20% of the initial billet mass (Oberhausen et al., 2022). Scrap from billet log cutting can be re-used via a two-piece billet extrusion process – when two short billets are loaded into the container. However, because this process creates an additional weld between the two short billets, it is constrained to low-performance applications, limiting the opportunity for its use (da Silva, 2016).

### **3.1.1 Previous work on reducing transverse weld scrap**

Transverse weld scrap could be reduced by either decreasing the length and/or increasing the strength of the welds. Several researchers have achieved weld length reductions of up to 15% with changes to the extrusion parameters: reductions in the die angle (Mahmoodkhani et al., 2014; Chen et al., 2015), friction coefficient (Hatzenbichler and Buchmayr, 2009), and ram speed (Zhang et al., 2017; Hatzenbichler and Buchmayr, 2009; Crosio et al., 2018). For hollow profiles using porthole dies, weld lengths might be reduced by optimizing the baffle plate height, welding chamber radius, the number and geometry of bridges (Yu et al., 2016a; Zhang et al., 2017; Reggiani and Donati, 2018), and the welding chamber and porthole height (Crosio et al., 2018). The extrusion ratio and profile shape also have an effect but are difficult to change for a given press size and profile design (Oberhausen et al., 2021). Recently, Oberhausen and Cooper (2023) proposed using profiled dummy blocks to generate shorter welds, requiring the billet butt to remain unsheared between ram strokes.

Multiple publications study the strength and microstructure of transverse welds. For example, den Bakker et al. (2016) and Tang et al. (2022) extract tensile test coupons from extruded profiles to evaluate the effect of the transverse weld on the lateral strength of hollow AA6082 aluminum and ZK60 magnesium profiles respectively. Elsewhere, Nanninga et al. (2011) evaluate the effect of the transverse weld on the fatigue life of a AA6082 hollow profile. A consistent finding is that the ductility and strength increases towards the rear of the weld. This finding has been explained qualitatively by reference to either the changing microstructure (e.g., Yu et al., 2019) and/or oxide distribution (e.g., den Bakker et al., 2016). Lou et al. (2019) find that the outer billet material surrounding the nose of a AA6061 weld is composed of fine, equiaxed grains while the new billet material inside the nose is composed of long, thin grains. Further back in the weld, the grain structure of the new billet material more closely resembles that of the old billet. Similarly, Tang et al. (2022) and Yu et al. (2019) find that the nose of the weld is characterized by a coarse structure distinctly separated from old billet material by the bonding interface, but that the grains become increasingly uniform and span across the interface as the weld progresses and recrystallization increases.

The above articles have examined the transverse weld quality; however, to the authors' knowledge no transverse weld strength model exists. Furthermore, the local weld strength has not been directly measured: previous work measures a proxy due to the difficulty of isolating the weld interface in the test coupon. Existing studies have focused on single-piece billet extrusion with use of a butt shear; however, transverse weld integrity concerns also limit two-piece billet extrusion applications. Additionally, some extruders still use presses without a butt shear (Mag Specialties, 2019) and for some new tooling concepts the billet butt is not sheared off (Cooper and Oberhausen, 2023).

### **3.1.2 Candidate welding models for predicting the transverse weld strength**

Over the last fifty years, several aluminum solid-state welding models have been proposed. For extrusion, researchers have focused on longitudinal welds in hollow profiles that form by the billet first splitting around the bridges in the porthole die and then rejoining before die exit (Xie et al., 1995). Longitudinal weld models predict if bonding has occurred based on whether a weld quality index exceeds some critical value. The index is calculated using deformation conditions at the interface. For example, Akeret (1972) proposed a maximum pressure criterion based on the peak normal contact stress at the interface. Plata and Piwnik (2000) introduced the pressure–time Q-criterion based on the integral of the ratio between the normal contact stress and effective stress over time. Later, Donati and Tomesani (2004, 2008) extended this further to the pressure-time-flow K-criterion to better account for the dead metal zones. They show the importance of high normal contact stresses to initiate bonding and to increase weld ductility. Yu et al. (2016b) introduced the J-criterion which also considers diffusion mechanisms for closing of microvoids at the welding interface. Most recently, Kniazkin and Vlasov (2020) modified the Plata and Piwnik (2000) model to include the effect of the different material stream velocities flowing from different die ports.

Multiple studies have shown that the above welding models provide a good indication of longitudinal weld quality for both aluminum (e.g., Yu et al. (2016a)) and magnesium alloys (e.g., Liu et al., (2017)). However, these models are weld quality indicators rather than quantitative predictors of weld strength. Furthermore, with the exception of the transient state when extruding into an empty die (Wang et al., 2022), the rejoining metal streams in longitudinal welding are free of oxides (Zhang et al., 2013; Reggiani et al., 2013). In contrast, the billet-billet interface in transverse weld joining is covered in oxides. These oxides likely increase the importance of interface stretching, as indicated by those studies that use novel setups to mimic longitudinal welding by squeezing together two samples but that, due to the setup, have been unable to avoid sample oxidation before bonding. For example, Edwards et al. (2006, 2009) examine whether bonding has occurred after pushing together the ends of (radially unconstrained) aluminum rods and Bai et al. (2017, 2019) examine bonding of aluminum and magnesium bars pushed together in a tool that

somewhat constrains spreading of the interface. These authors emphasize the importance of positive surface strains in achieving a bond in their experiments.

Examples of industrial solid-state welding processes where surface films are present include friction stir welding (FSW) and accumulative roll bonding (ARB). FSW is far from analogous to transverse weld formation as the stirring action in FSW causes a bulk material transfer across the interface (Cai et al., 2018; Singh et al., 2020). In ARB, sheets are stacked and then rolled, bonding them together as they pass through the roll bite (Saito et al., 1999). Bay (1983) proposed a weld strength model for cold roll bonding (plane strain deformation) based on the film theory of solid-state welding (Tylecote, 1968), which states that for welding to occur there must be intimate contact between clean metal surfaces. This necessitates that any surface films be broken to expose the reactive metal substrate (Ghalehbandi et al., 2019). With sufficient normal contact stress, the reactive substrate is then micro-extruded through cracks in the surface layer. If intimate contact between neighboring aluminum substrates of less than 10 atomic spacings is achieved then the attractive inter-atomic force will form a joint. Bay finds that a minimum expansion (threshold deformation) of the interface is required for any welding to occur in ARB. Cooper and Allwood (2014) build upon Bay's film theory model, revising it for a range of temperatures and including the effect of local shear stresses on the true contact area between bonding surfaces as well as oxidation of substrate metal exposed early in the bonding process due to air entrapped between the surfaces. Cooper and Allwood evaluate their extension to Bay's model over a range of temperatures and normal contact stresses using near plane strain conditions, finding dispersed experimental weld strengths that trend as indicated by the model.

### **3.1.3 Scope of this work**

While it is known that transverse weld strengths increase toward the rear of the weld, no predictive model of transverse weld strength exists. Longitudinal weld models are unsuitable because the oxides present during transverse weld formation are absent during longitudinal weld formation. In contrast, film theory models consider oxide fragmentation at the interface but have typically only been applied to (near) plane strain deformations, which are very different from the conditions at the billet-billet interface during extrusion. Therefore, the objectives of this paper are to extend the film theory of solid-state welding to predict the local transverse weld strength, to use the new model to identify the key determinants of the weld strength, and then to discuss the industry implications for reducing process scrap.

## **3.2 Derivation of the transverse weld strength model**

This work builds on the mechanistic Cooper and Allwood (2014) film theory model, defined in equation 1, and referred to from hereon as the C-A model. It assumes that the weld strength scales with the fraction

of the interface area ( $A_{nominal}$ ) that has bonded ( $A_{bonded}$ ). The C-A model can be divided into three key terms, as shown in Figure 3.3:

- The first term defines the fraction of the true versus nominal contact area, which is determined by the plastic flow at the asperity tip contacts induced by the normal contact stress ( $\sigma_n$ ) and interface shear stress ( $\tau_{app}$ ) (Figure 3.3a).
- The second term ( $v$ ) defines the fraction of the true contact area that consists of exposed substrate aluminum without a protective layer of oxide. This term accounts for surface stretching and oxidation of initially exposed substrate by entrapped air (Figure 3.3b).
- The third term defines the fraction of the exposed substrate on opposite sides of the interface that makes contact via micro-extrusion through the cracks in the oxide layer (Figure 3.3c). This depends on the normal contact stress ( $\sigma_n$ ), the flow stress of the substrate at the interface ( $\sigma_{flow}$ ), and the minimum normal contact stress ( $p_{ex}$ ) required to micro-extrude substrate aluminum through the oxide cracks.  $p_{ex}$  depends on the substrate flow stress and the oxide crack spacing ( $e$ ) through which the substrate must micro-extrude.

The resulting weld shear strength ( $\tau_b$ ) is the product of the three terms discussed above and  $\frac{1}{\sqrt{3}}\sigma_0$ , where  $\sigma_0$  is the bulk material room temperature tensile strength and the  $\frac{1}{\sqrt{3}}$  coefficient converts from tensile to shear strength via the von Mises criterion.

$$\tau_b = \frac{1}{\sqrt{3}}\sigma_0 \left( \left( \frac{0.8}{\sigma_{flow}} \sqrt{\sigma_n^2 + 3(\tau_{app})^2} \right)_{\leq 1} \cdot v_{\geq 0} \cdot \left( 0.8 \frac{\max(\sigma_n - p_{ex}, 0)}{\sigma_{flow}} \right)_{\leq 1} \right) \quad (3.1)$$

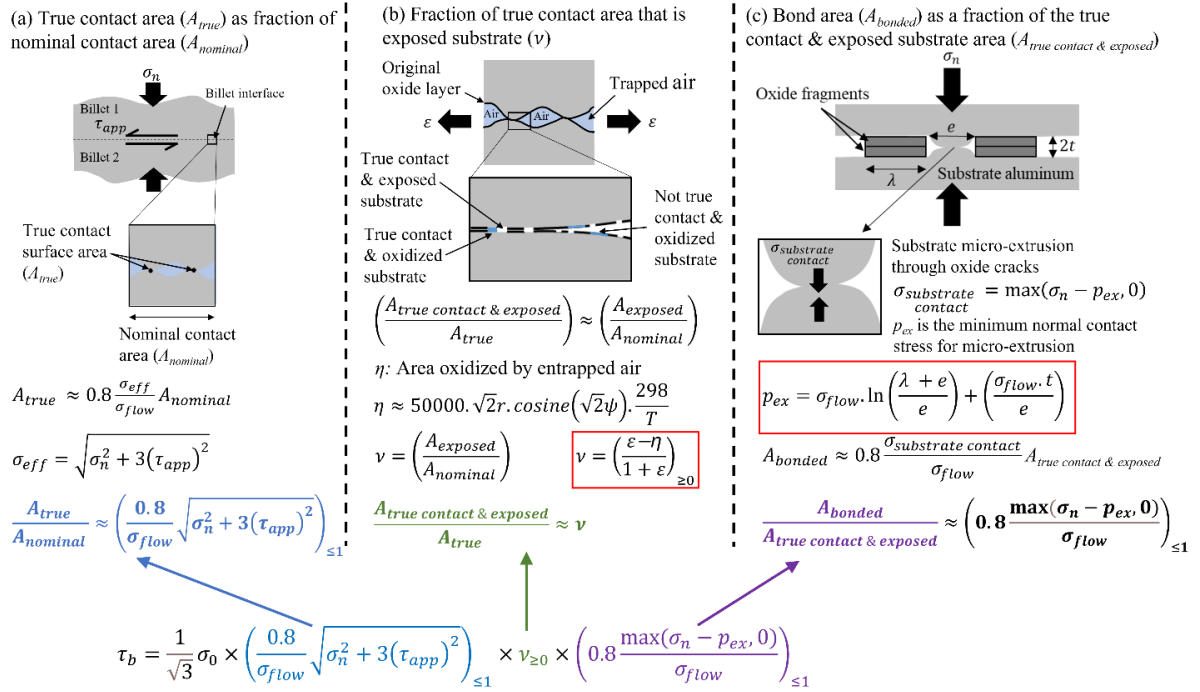


Figure 3.3: The driving mechanisms of Cooper and Allwood's (2014a) original model. The equations for the model inputs highlighted in red must be updated to account for the non-plane strain deformation at the billet-billet interface during transverse weld formation. Figure inspired by Kolpak et al. (2019).

Equation 3.1 is applicable to a range of deformation conditions. However, calculations of key C-A model inputs ( $v$  and  $p_{ex}$ ) were originally defined by Cooper and Allwood assuming (near) plane strain deformation. This limits the welding interface to experiencing in-plane stretching in one direction and does not reflect the biaxial strain state at the billet-billet interface during extrusion. Updating this aspect of the C-A model is important as the strain state affects how the surface oxides fragment and therefore the exposed substrate area ( $v$ ) and the minimum normal contact stress for substrate micro-extrusion ( $p_{ex}$ ).

In order to update the C-A model, we make four key assumptions about the biaxial oxide fragmentation at the billet-billet interface (A-D, below):

- When the local contact area expands, then:
  - A The length and width of the broken oxide fragments are equal and can be predicted using shear lag modeling.
  - B The broken oxide fragments are evenly spaced (locally) across the interface.
  - C The interface oxides break-up using a mix of coherent and incoherent fragmentation modes. Coherent fragmentation is when the oxides on opposite sides of the interface break-up at the same location, and incoherent fragmentation is when the oxides on opposite sides of the interface break-up at different locations.

- When the local contact area contracts, then:

A The local interface buckles, oxide cracking is limited, and no welding occurs.

We first show that assumptions A-D are justified by studying the fragmentation of billet-billet interface oxides (Section 3.2.1). The validated assumptions are used to revise the calculations of key C-A model inputs ( $v$  and  $p_{ex}$ , Section 3.2.2.), and we then define how the updated model is used to predict local transverse weld strengths (Section 3.2.3)

### 3.2.1 Testing the new model assumptions: Fragmentation of billet-billet interface oxides

As part of assumption A, we first use shear lag modeling to predict the length of the broken oxide fragments on the transverse weld (Section 3.2.1.1). We then test assumptions A-D by examining the oxide fragmentation patterns produced on welds extruded using anodized billets (Section 3.2.1.2).

#### 3.2.1.1 Shear lag model to predict oxide fragmentation

Building on the work of Agrawal and Raj (1989) and Le et al. (2004) on fracture of brittle films on ductile substrates, we use a simple shear lag model to estimate the oxide fragment size distribution for the case of local area expansion at the billet-billet interface. Figure 3a shows the contact between consecutively extruded billets with a normal contact stress squeezing the surfaces together and tensile stretching in the axial direction creating an initial oxide fragment of length  $L$ . Surface stretching induces plastic deformation of the ductile aluminum substrate beneath the brittle oxide, which creates a shear stress at the substrate-oxide interface up to the ideal (substrate) shear strength of the interface ( $k_{aluminum}$ ) and which reverses direction at the center of the oxide fragment. Force equilibrium dictates that a tensile stress ( $\sigma_t$ ) is developed within the oxide layer that is inversely proportional to the oxide thickness ( $t_{oxide}$ ) and increases with the distance from any existing cracks (Figure 3.4b). The oxide can fragment wherever the tensile stress reaches the fracture strength of the oxide ( $\sigma_{f,oxide} \approx 240 \text{ MPa}$ ), corresponding to region C-C' in Figure 3.4b. As the interface is stretched, new cracks will continue to form, and the oxides get shorter, until the oxide fragments are sufficiently small that the tensile stress in the oxide is always smaller than the oxide fracture strength, at which point the oxides have reached a stable size. The minimum oxide length occurs when a new crack forms at position C in Figure 3.4b (a distance  $\lambda_1$  from the adjacent crack) and the maximum oxide length occurs when a new crack forms at a distance  $2\lambda_1$  from the adjacent crack. Subsequently, the minimum oxide fragment size is  $\lambda_1$  and the maximum is  $2\lambda_1$ .

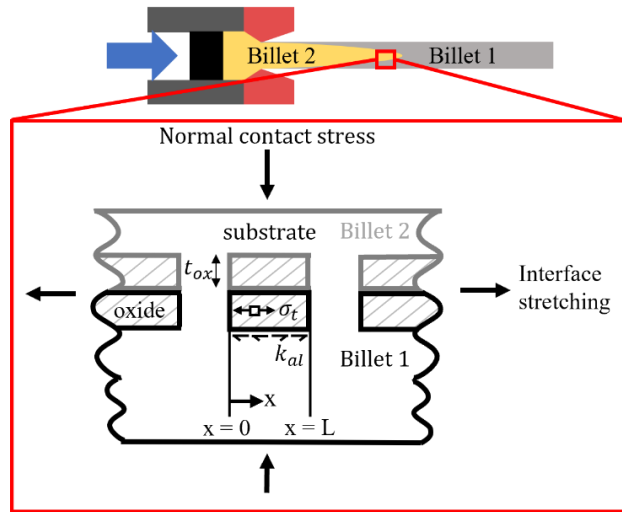
$$\lambda_1 = \sigma_{f,oxide} \cdot t_{oxide} / k_{aluminum} \quad (3.2)$$



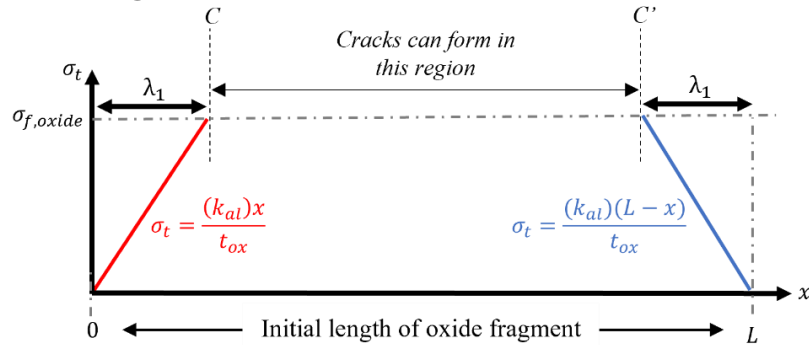
$$\lambda_{average} = \frac{3 \cdot \sigma_{f,oxide} \cdot t_{oxide}}{2 \cdot k_{aluminum}} \quad (3.3)$$

As shown in Figure 3c, the oxides may fragment coherently, where the oxides on opposite sides of the interface break-up together, or incoherently, where the oxides on opposite sides of the interface break-up at different locations. Coherent fragmentation should lead to greater weld strengths by increasing the area of the line-of-sight channels between the substrates on opposite sides of the interface, increasing the potential bonding area. We hypothesize a mix of coherent and incoherent oxide fragmentation modes occur in extrusion. Incoherent fragmentation is likely to be secondary because in that case oxide cracking on one side of the interface will be restrained by the frictional stresses acting from the neighboring uncracked oxide on the opposite side of the interface. This frictional restraint against cracking is not present if the oxides fragment coherently. Despite this, we still expect some incoherent fragmentation to occur due to oxides cracking before local interface contact and because any interface lubricity, which is difficult to eliminate in industrial settings, will reduce the frictional restraint against incoherent fragmentation.

a) Initial fragmentation at interface



b) Stretching of the interface induces tensile stresses within the oxide and further fragmentation



c) Oxide fragmentation configurations

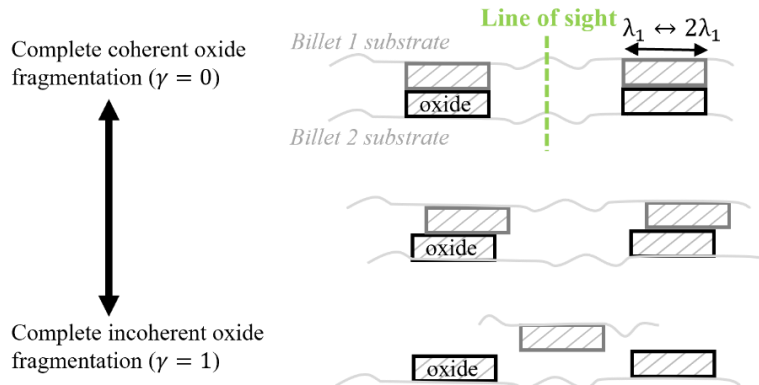


Figure 3.4: Shear lag modeling of oxide fragmentation at the billet-billet interface. Final oxide fragment lengths are expected to vary from  $\lambda_1$  to  $2\lambda_1$ .

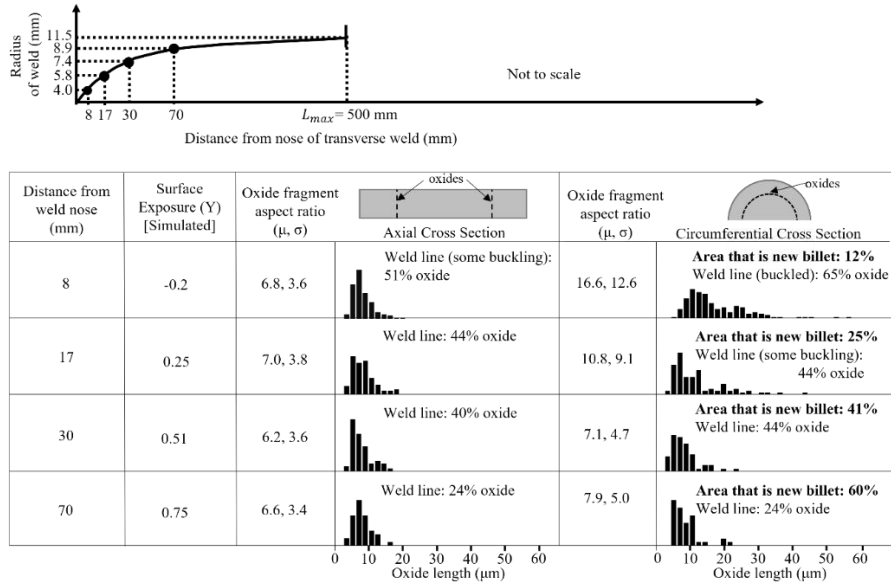
As shown in Figure 3c, the oxides may fragment coherently, where the oxides on opposite sides of the interface break-up together, or incoherently, where the oxides on opposite sides of the interface break-up at different locations. Coherent fragmentation should lead to greater weld strengths by increasing the area of the line-of-sight channels between the substrates on opposite sides of the interface, increasing the potential bonding area. We hypothesize a mix of coherent and incoherent oxide fragmentation modes occur in extrusion. Incoherent fragmentation is likely to be secondary because in that case oxide cracking on one side of the interface will be restrained by the frictional stresses acting from the neighboring uncracked oxide on the opposite side of the interface. This frictional restraint against cracking is not present if the oxides fragment coherently. Despite this, we still expect some incoherent fragmentation to occur due to oxides cracking before local interface contact and because any interface lubricity, which is difficult to eliminate in industrial settings, will reduce the frictional restraint against incoherent fragmentation.

### **3.2.1.2 Oxide fragmentation using anodized billets**

Assumptions A-D are tested by observing oxide fragmentation at the billet-billet interface; however, native oxide fragmentation cannot be easily observed given that the native amorphous alumina layer is only around 2-10 nm thick (Evertsson et al., 2015) and that aluminum surfaces quickly reoxidize. Previously, Le et al. (2004) showed similar aspect ratios (oxide fragment length to thickness) are achieved in fragmentation of anodized and native-grown oxide, concluding that anodized surfaces can be used to help study native oxide fragmentation. We therefore extrude single-piece and two-piece billets with anodized interfaces and observe the oxide fragmentation using optical microscopy in the final profiles. To anodize, the billets were faced-off on a lathe, polished, and chemically cleaned. The billets were then suspended in a sulfuric acid solution and charged with a current density of 160 A/m<sup>2</sup> for 2 minutes to grow an oxide thickness of 0.9 μm. Axisymmetric extrusion was performed using Ø3.5" (89 mm), 8" (203 mm) long anodized AA6061 billets at 425°C at an extrusion ratio of 15. Two anodized 4" (101 mm) long billets were used in the same set-up for the two-piece billet test.

Figure 3.5 shows the measured oxide size distributions at eight different locations examined across the two profiles. Figure 3.6 shows representative microscopy images of the oxide fragmentation patterns.

a) Transverse weld formed in single-piece billet extrusion



b) Transverse weld formed in two-piece billet extrusion

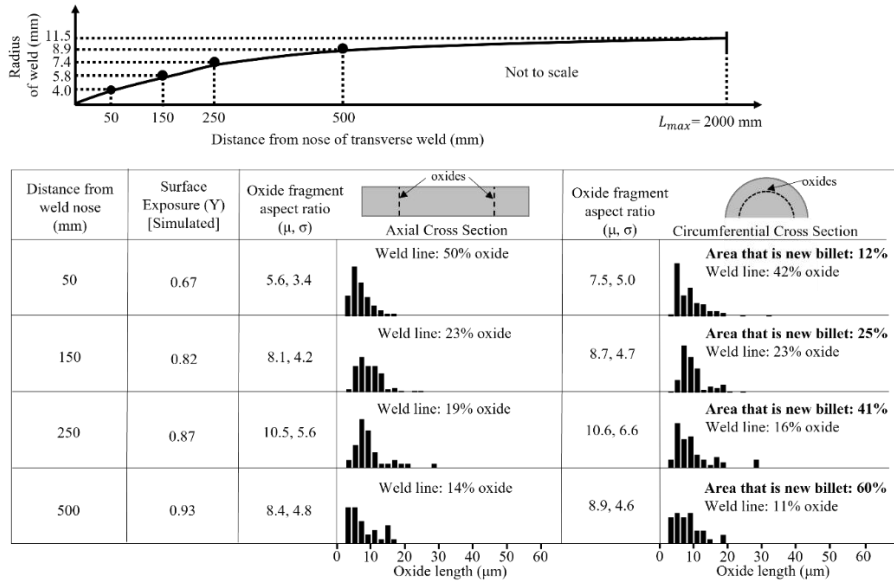


Figure 3.5: Experimentally observed oxide fragmentation of 0.9  $\mu\text{m}$  anodized billets in (a) single-piece and (b) two-piece billet extrusion. Weld line % oxide is total length of observed oxide along weld line (irrespective of fragmentation mode) divided by the straight line or circular weld length. It is not indicative of weld area % oxide in cases of interface buckling.

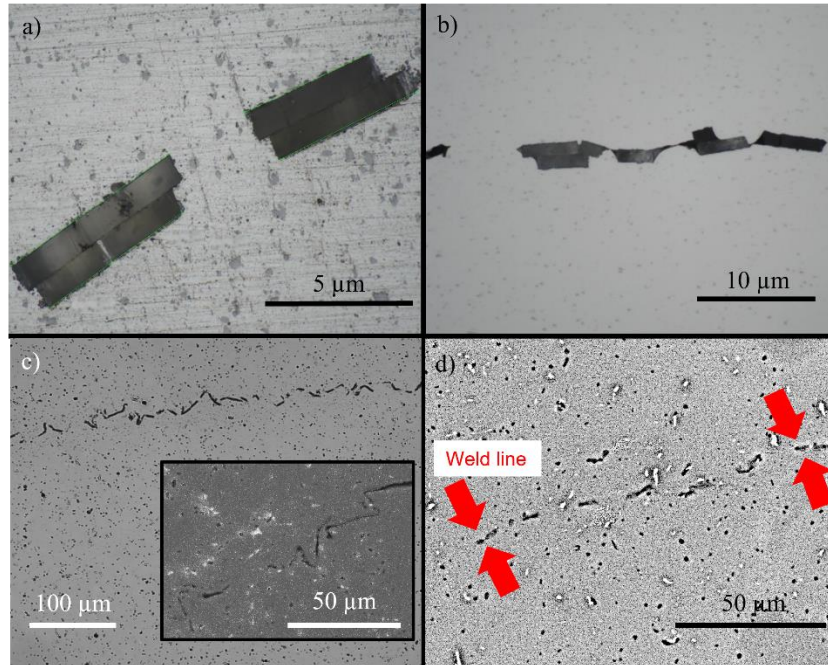


Figure 3.6: Microscopy of circumferential oxide fragmentation for single-piece billet extrusion. (a) Optical microscopy showing (near complete) coherent oxide fragmentation. (b) Optical microscopy showing incoherent oxide fragmentation. (c) Optical and SEM (inset) of the weld nose (12% new billet). (d) SEM of oxides at 41% new billet.

Shear lag modeling (equation 3.2, with  $k_{al} \approx 40 \text{ MPa}$  and  $t_{\text{oxide}}=0.9 \mu\text{m}$ ) predicts an oxide fragment aspect ratio of 5.4-10.8 and oxide fragment length of 4.8-9.7  $\mu\text{m}$ . The experimental oxide size distributions in Figure 3.5 are wider than the 1:2 minimum to maximum ratio implied by the shear lag modeling. This is likely due to varying experimental oxide thicknesses and fracture strengths. Even so, the mean oxide fragment aspect ratio (and length) is within the size distribution predicted by shear lag modeling for fifteen out of the sixteen location-orientation pairings shown in Figure 3.5. The measured oxide size distributions in the axial and circumferential directions are also similar for all seven locations that correspond to local contact area expansion. Therefore, it is deemed reasonable that the length and width of the broken oxide fragments are modeled as equal and predictable using shear lag modeling, justifying assumption A.

Figure 3.5 shows that the percentage of the weld line occupied by oxides is consistent in the axial and circumferential direction for all seven locations that correspond to local contact area expansion. Therefore, it is reasonable to assume that the broken oxide fragments are evenly spaced (locally) across the interface, justifying assumption B.

Optical microscopy of the weld lines shows that (near) complete coherent oxide fragmentation (Figure 3.6a) was the primary fragmentation mode in the anodized billet trials, accounting for  $\approx 75\%$  of all observed oxide fragmentation. Incoherent fragmentation (Figure 3.6b) was found scattered across the welds,

accounting for the remaining 25%. These observations justify assumption C that oxide break-up occurs with a mix of fragmentation modes.

The outlier in Figure 3.5 is the circumferential distribution of oxides at the nose of the single-piece billet extrusion (12% new billet area). This corresponds to the only location in Figure 3.5 to have experienced local contact area contraction during extrusion. Figure 3.6c shows severe local buckling of the interface at this location, more oxide along the weld line than at any other tested location, and by far the highest mean oxide aspect ratio at 17. The weld in this location also possessed only handling strength, justifying assumption D. Further back in the single-piece billet weld, mean oxide fragment lengths are still longer in the circumferential than axial direction at 25% new billet area; however, by 41% new billet area there is not an appreciable difference between the oxide fragment size in the two directions.

### 3.2.2 Updating the C-A model

The anodized billet experiments validate the assumptions described in the Section 3.2 introduction. Using these assumptions, we revise the calculation of the C-A model inputs.

#### 3.2.2.1 Calculating the exposed aluminum substrate area fraction ( $\nu$ )

The exposed substrate area ( $A_{\text{exposed}}$ ) is equal to the interface area ( $A_{\text{nominal}}$ ), less the original area covered by oxides ( $A_{\text{original}}$ ), less the area of exposed substrate oxidized by entrapped air ( $\eta A_{\text{original}}$ ), and less the increase in interface area needed to create line-of-sight substrate-to-substrate channels through the cracks in the oxide layers ( $\gamma A_{\text{original}}$ ). The fraction ( $\nu$ ) of the interface area that is exposed substrate is therefore given by equation 3.4, which can be rewritten as equation 3.5, eliminating the area terms by introducing the surface exposure,  $Y$ .

$$\nu = A_{\text{exposed}}/A_{\text{nominal}} \rightarrow \nu = [A_{\text{nominal}} - A_{\text{original}}(1 + \eta + \gamma)]/A_{\text{nominal}} \quad (3.4)$$

$$\therefore \nu_{\text{weld}}^{\text{transverse}} = Y + (\eta + \gamma)(Y - 1) \quad (3.5)$$

where  $Y$  is the interface surface exposure,  $\eta$  is the fractional surface area expansion that is oxidized due to entrapped air, and  $\gamma$  is the fractional increase in the original interface area needed to create line-of-sight substrate-to-substrate channels through the cracks in the oxides. Each parameter is described below.

The surface exposure ( $Y$ ) has been used previously in the roll bonding literature (e.g., Bay (1983)) and is defined as the difference between the current interface area ( $A_{\text{nominal}}$ ) and the original interface area ( $A_{\text{original}}$ ) divided by the current interface area (equation 3.6).

$$Y = \frac{A_{nominal} - A_{original}}{A_{nominal}} \quad (3.6)$$

For uniaxial stretching of the interface (as in rolling),  $Y_{plane} = \frac{\varepsilon^{eng}}{1+\varepsilon^{eng}}$ . In equation 3.7, we rewrite the calculation for the case of a biaxial strain state as exists in transverse weld formation. Equation 3.7 is derived by considering the deformation of an infinitesimal square on the interface that is subjected to perpendicular in-plane strains,  $\varepsilon_1$  and  $\varepsilon_2$ .

$$Y_{weld}^{transverse} = 1 - 1/[(1 + \varepsilon_1^{eng})(1 + \varepsilon_2^{eng})] = 1 - \exp[-(\varepsilon_1^{true} + \varepsilon_2^{true})] \quad (3.7)$$

Cooper and Allwood (2014) argue that the significant threshold deformation needed for welding to occur in roll bonding is due to entrapped air oxidizing initially exposed substrate. They estimate the moles of entrapped oxygen at the interface by considering the air temperature and interface surface roughness. They then estimate the area of exposed substrate aluminum these moles of oxygen will oxidize; thus, deriving an estimate for the fractional increase in interface area ( $\eta$ , equation 8) needed before any further expansion of the interface occurs in an inert atmosphere.

$$\eta = \frac{A_{oxidation\ limit} - A_{original}}{A_{original}} \approx 50000 \times \sqrt{2}r \times \cosine(\sqrt{2}\psi) \times \frac{298}{T} \quad (3.8)$$

where  $r$  is the surface root mean square asperity height, in meters,  $\psi$  is the asperity inclination angle, and  $T$  is the bonding temperature, in Kelvin. The calculation of  $\eta$  for transverse weld formation remains unchanged from the original C-A model.

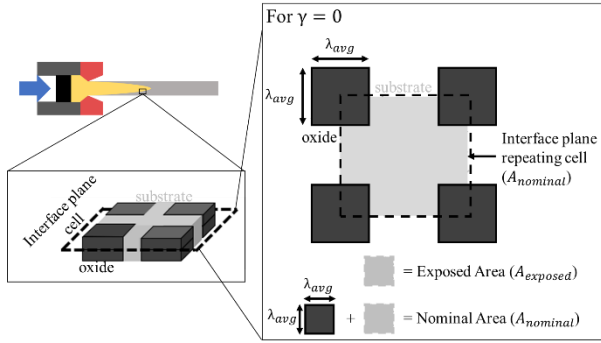
We introduce the  $\gamma$  parameter to model the effect of coherent versus incoherent oxide fragmentation (Figure 3.4c).  $\gamma=0$  for complete coherent fragmentation, as the layers of broken oxide on opposite sides of the interface cover the same regions of substrate.  $\gamma=1$  for complete incoherent fragmentation, as at the limit the original interface area doubles and misalignment of the oxide layers still prevents line-of-sight substrate-to-substrate channels across the interface. A mix of fragmentation modes occur in extrusion (Assumption C). The problem is bounded by using  $\gamma = 0 \leftrightarrow 1$ .

For any welding to occur, the local contact area must expand (Assumption D) and substrate-to-substrate channels across the interface be created,  $\nu > 0$ . Therefore, a threshold minimum surface exposure,  $Y'$ , is required.  $Y'$  is defined in equation 3.9 and derived by setting equation 3.5 to zero.

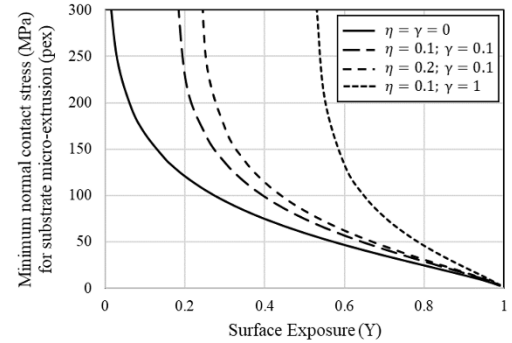
$$Y' = (\eta + \gamma)/(1 + \eta + \gamma) \quad (3.9)$$

### 3.2.2.2 Calculating the minimum micro-extrusion normal contact stress ( $p_{ex}$ )

The minimum normal contact stress needed to micro-extrude substrate aluminum through cracks in the billet-billet oxide layers depends on the geometry of the exposed substrate and oxide fragments. We consider an idealized repeating unit cell (Figure 3.7a) at the billet-billet interface. The unit cell contains exposed substrate and the corners of four equally spaced, equally sized, oxide fragments (Assumptions A and B).



a) Schematic of the modeled repeating unit cell at the local billet-billet interface



b)  $P_{ex}$  results using equation 12. Modeled for  $\sigma_{flow} = 70$  Mpa,  $t_{oxide} = 4$  nm, and  $\lambda_{Average} = 24$  nm

Figure 3.7: Calculating the minimum micro-extrusion pressure ( $p_{ex}$ )

The mean oxide fragment length ( $\lambda_{Average}$ ) for native oxides ( $t_{oxide} \approx 4$  nm) is approximated using shear lag modeling (Assumption A). For example, using equation 3.3, for AA6061 extruded at 425°C ( $k_{Al} \approx 40$  MPa),  $\lambda_{Average} \approx 24$  nm. Equation 3.10 defines the area of the unit cell ( $A_{unit\ cell}$ ). The  $(1 + \eta)$  term accounts for the oxides observed in the unit cell being the result of both the original oxide film and newly oxidized exposed substrate. Inclusion of the surface exposure ( $Y$ ) in equation 3.10 comes from  $A_{unit\ cell}$  being equivalent to  $A_{nominal}$  in equation 3.6.

$$A_{unit\ cell} = A_{original}/(1 - Y) \approx \frac{\lambda_{Avg}^2}{(1 + \eta)(1 - Y)} \quad (3.10)$$

The area of exposed substrate in the unit cell ( $A_{exposed, unit\ cell}$ ) is given by equation 11 and is equal to the area of the unit cell (equation 3.10) less the projected area of oxide in the unit cell. For  $\gamma=0$ , this area of oxide is  $\lambda_{Avg}^2$ . Equation 3.11 can be used to calculate the minimum surface exposure needed for the exposed substrate area in the unit cell to be positive. This results in the same threshold minimum surface exposure as calculated in equation 3.9, confirming model consistency across the new calculations of  $v$  and  $p_{ex}$ .



$$A_{exposed, unit\ cell} \approx \max\left(\frac{\lambda_{Avg}^2}{(1 + \eta)(1 - Y)} - \frac{\lambda_{Avg}^2(1 + \eta + \gamma)}{(1 + \eta)}, 0\right) \quad (3.11)$$

Using equations 3.10 and 3.11, an expression for the micro-extrusion pressure,  $p_{ex}$ , is derived using classic equilibrium extrusion analysis (Saha, 2000).  $p_{ex}$  is assumed equal to the extrusion pressure needed in axisymmetric extrusion of a round billet of cross-sectional area,  $A_{unit\ cell}$ , into a round rod of cross-sectional area,  $A_{exposed, unit\ cell}$ , using dies with a land length of  $t_{oxide}$  and a dead zone angle of  $90^\circ$ . While a crude assumption, the results in Section 3.4 show that in hot extrusion the modeled transverse weld strength results are likely insensitive to small variations in the estimate of  $p_{ex}$ . Equation 3.12 shows the new expression for the micro-extrusion pressure,  $p_{ex}$ . The first term derives from the pressure needed to deform the substrate through the gap in the oxides and the second term derives from the pressure needed to overcome the sticking friction shear stresses along the walls of the oxide fragments. ER is the micro-extrusion ratio for the unit cell (equation 3.14), calculated using equations 3.10 and 3.11. Figure 3.7b shows some typical results for  $p_{ex}$  using equation 3.12. Figure 3.7b shows that the initially high values of  $p_{ex}$  are sharply reduced as the surface exposure increases.

$$p_{ex, transverse\ weld} \approx \sigma_{flow} \ln(ER) + 2 \cdot t_{oxide} \cdot \sigma_{flow} \cdot \left(\frac{\pi}{3 \cdot ER \cdot A_{unit\ cell}}\right)^{0.5} \quad (3.12)$$

$$ER = A_{unit\ cell} / A_{exposed, unit\ cell} \quad (3.13)$$

$$\therefore ER = 1/[Y(1 + \eta + \gamma) - (\gamma + \eta)] \quad (3.14)$$

### 3.3.3 Calculating the local transverse weld strength

In summary, the following calculation updates have been made to the C-A model:

- The fraction of the interface that is exposed substrate ( $v$ ) has been revised (equation 3.5) to include an oxide fragmentation coherency parameter ( $\gamma$ ).
- The surface exposure ( $Y$ ) has been defined (equation 7) for an in-welding-plane biaxial strain state.
- The minimum micro-extrusion normal contact stress ( $p_{ex}$ ) has been revised (equation 3.12) to account for biaxial oxide fragmentation at the welding interface.

With these updates to the C-A model inputs, equation 3.1 can be used to predict the local transverse weld strength. This is achieved by tracing the deformation conditions experienced at points on the original planar billet-billet interface along streamlines through the extrusion die to their final position in the extruded

profile.  $\tau_b$  (equation 3.1) is evaluated along the streamlines for each point (see Figure 3.8). As no regions of hydrostatic tension exist along the evolving interface, it is assumed that the local weld strength can only increase and is equal to the maximum realization of equation 3.1 anywhere along the streamline.

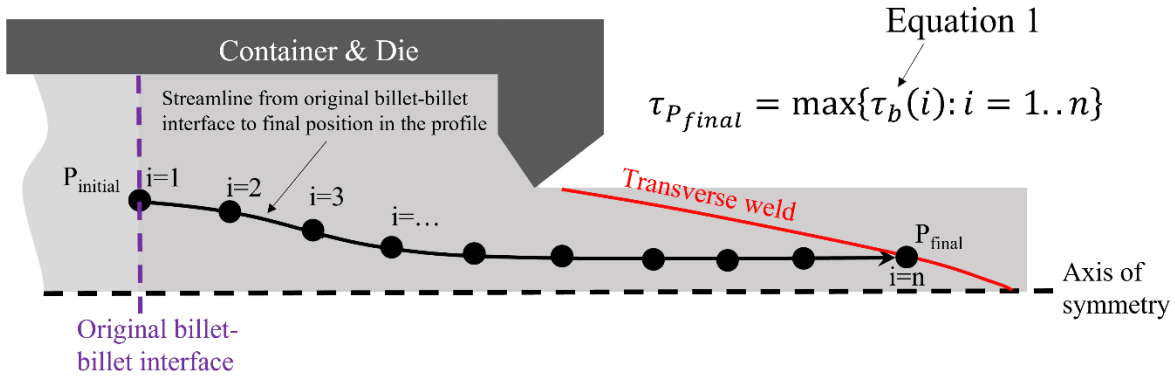


Figure 3.8: Implementation of the new transverse weld strength model.

### 3.3 Methodology for evaluating transverse weld strengths

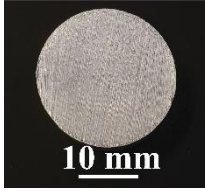


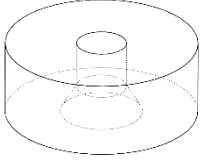
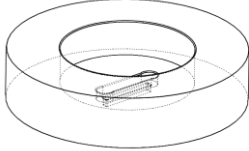
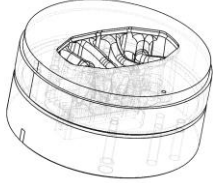
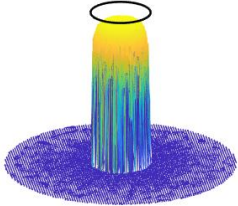
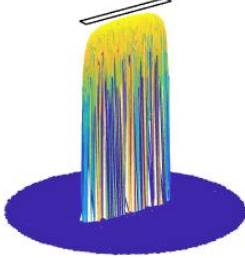
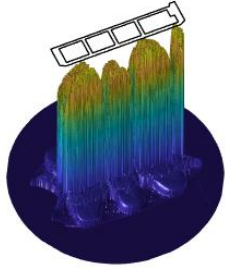
A series of extrusion trials are conducted (Section 3.3.1) and the strength of the generated transverse welds evaluated using shear tests (Section 3.3.2). The experimental weld strengths are then compared to predictions made using the new model. The model inputs are extracted from finite element models (FEM) of the extrusion trials (Section 3.3.3).

#### 3.3.1 Extrusion trials and alloys

Three profiles are extruded using different alloys and presses to test model flexibility. Table 3.1 presents the profiles, die geometries, and extrusion settings. Figure 3.9 presents the flow curves ( $\sigma_{flow}$ ) for the aluminum alloys; a high-resolution AA6082 flow curve model is provided by DEFORM (sourced from Heinemann (1961)), and the AA6061 flow curves are sourced from Ding et al. (2021).

Table 3.1: Details of the experimental extrusion trials performed in this work. Note: One set of axisymmetric single-piece billet experiments tested continuous extrusion without use of the butt shear.

Profile	Round bar	Rectangular bar	Hollow
---------	-----------	-----------------	--------

Profile image			
Profile dimensions (mm)	Ø23.08	6.06 x 60.6	26 x 142 outer dimensions
Alloy	AA6061	AA6061	AA6082
Die image	Container side  Exit side	Container side  Exit side	Container side (8 die)  Exit side
Tongue-shaped weld geometry (generated from FEM; colors are for visualization purposes only)			
Billet diameter (mm)	Ø88.9 (3.5")	Ø152.4 (6")	Ø228.6 (9")
Billet length (mm)	1x203.2 (8") for single-piece billet extrusion 2x101.6 (4") for two-piece billet extrusion	800 (31.5") Single-piece billet extrusion	1120 (44") Single-piece billet extrusion
Extrusion ratio	15	50	26
Billet temperature (°C)	425	450	493

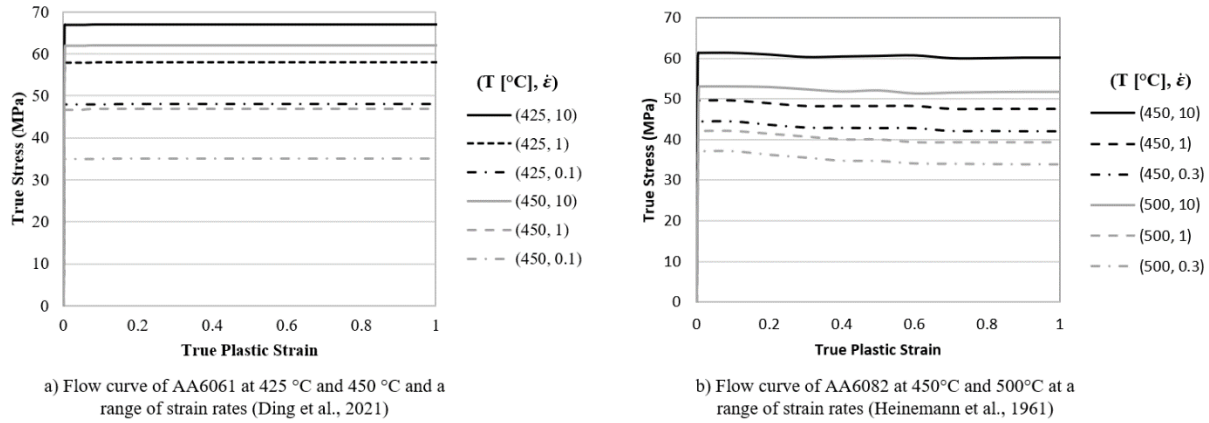


Figure 3.9: Flow curves for the aluminum alloys used in the extrusion trials.

### 3.3.2 Evaluating the experimental weld strengths

Room temperature shear tests (1 mm/minute crosshead displacement) were conducted on samples extracted from the axisymmetric and rectangular profiles. In all cases, wire electrical discharge machining (EDM) was used to produce shear test geometries that isolate the weld in the test region (see Figure 3.10).

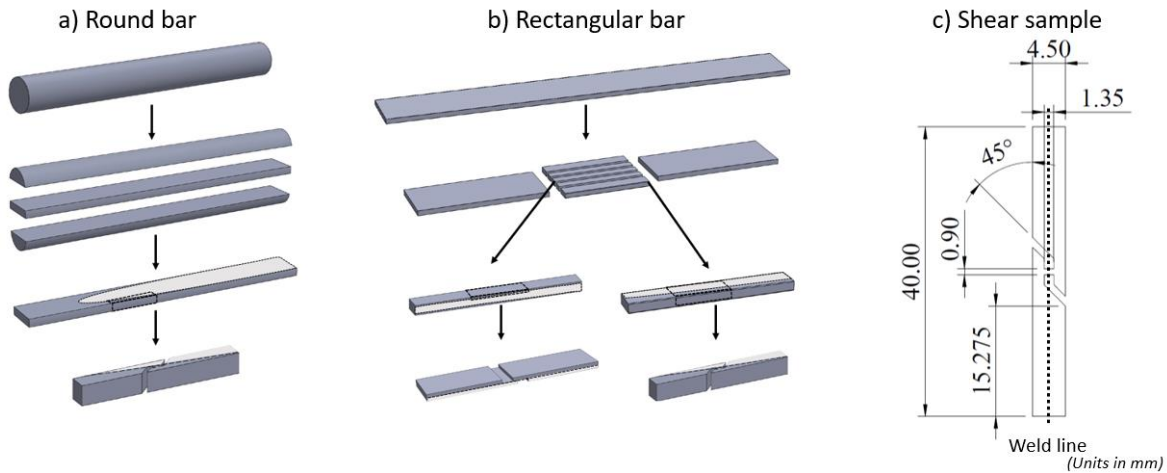


Figure 3.10: Shear test sample machining process using wire EDM.

The shear test sample geometries (Figure 3.10c) are modified from the ASTM B831-05 standard (ASTM, 2010) to have a wider test region so as to reliably incorporate the transverse weld. The modified shape is similar to the shear test sample geometry suggested by Merklein and Biasutti (2011) to facilitate fatigue shear testing and shown by Yin et al. (2014) to experience a similar strain distribution to the ASTM standard. Reductions in sample geometry were necessary to test the strength of welds at the rear of the

profile. In all cases, shear testing of the bulk profile using identical shear test geometries was performed to calibrate the results.

For non-axisymmetric profiles, local deformation conditions at the weld vary across as well as along the profile. For the rectangular bar, test samples were extracted from both the major and minor axis of the ellipsoid shaped weld. It was impractical to test directly the strength of the multi-nose weld created in the hollow profile. Therefore, the visibility of the weld across etched cross-sections was used instead as a proxy for the strength, as used in other aluminum extrusion weld studies (e.g., Kolpak et al. (2019)).

### 3.3.3 Determining model inputs

#### 3.3.3.1 Finite element models of the extrusion process

The extrusion trials listed in Table 3.1 were simulated using DEFORM® software. The FEMs were run using the multifrontal massively parallel sparse direct solver and the Newton-Raphson iteration method. The billets were modeled as von Mises materials with isotropic hardening and different flow curves used for different temperatures and strain rates (Figure 3.9). The die, container, and dummy block were modeled as rigid bodies. Contact between the billet-die and billet-container were modeled using sticking friction (a friction coefficient of  $m = 1$  where the frictional shear stress,  $\tau = mk$ , and  $k$  is the aluminum billet shear yield stress), and between the billet-dummy block as frictionless ( $m = 0$ ), reflecting the use of boron nitride lubricant on the dummy block. The typical element size was  $\approx 0.75$  mm in the die region and  $\approx 1.5$  mm elsewhere. Remeshing occurred when the billet-tooling interference exceeded 0.25 mm. An axisymmetric model was used to simulate extrusion of the round rod. A quarter-size symmetric 3D model was used to simulate extrusion of the rectangular bar, and a full 3D model was used to simulate extrusion of the complex asymmetric hollow profile. The accuracy of the simulations was ensured by performing several checks. A mesh refinement study ensured sufficient mesh density for accurate prediction of the ram force and the weld geometry. The ram force and new billet area predictions were within  $\pm 10\%$  of the experimentally measured forces and new billet areas (determined by sectioning and etching the profiles). Figure 3.11 shows a comparison between the simulated and measured weld geometries. Note that to produce Figure 3.11e, the velocity field from the DEFORM post-processor was extracted and then a simple MATLAB script used to track a plane of points corresponding to the original billet-billet interface through the die. This results in a 3d point cloud with the points positioned across and along the weld shape within the profile. To produce a cross-sectional view of the weld at any given axial position from the nose, the point cloud between that position and the nose is projected onto the 2d cross-section.

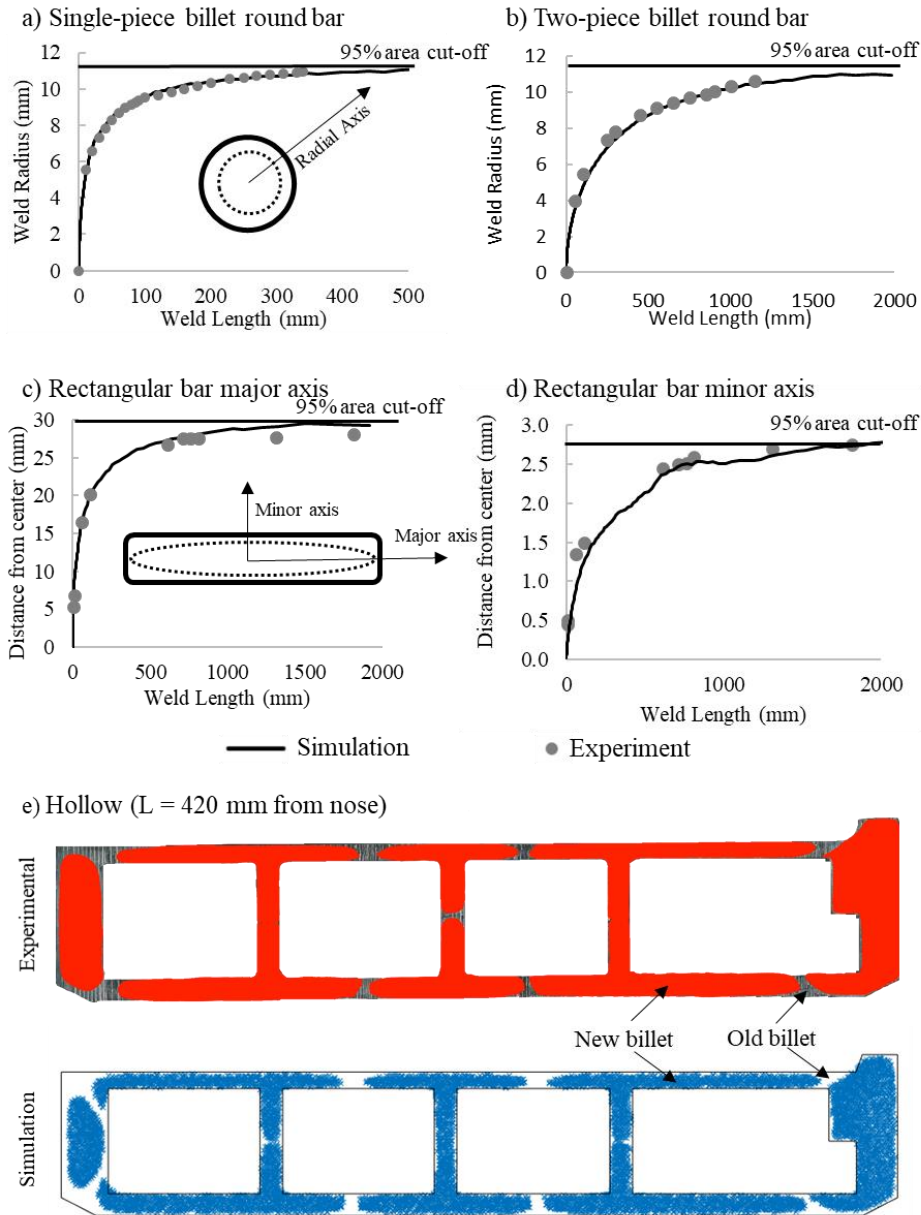


Figure 3.11: Comparison of experimental and simulated weld geometries.

### 3.3.3.2 Model inputs: Evolving deformation conditions at the billet-billet interface ( $\sigma_n$ , $\tau$ , $\epsilon_1$ , $\epsilon_2$ )

To implement the new model (Figure 3.8), the normal contact stress, shear stress, and surface strains must be determined along streamlines of material from the initially planar billet-billet interface through the die to the final point on the profile weld. We use DEFORM®'s point tracking feature to track the displacement and global stress tensor ( $\sigma_t$ ) of a particle as it flows along its streamline. For a given particle of interest ( $c_1$ ) on the initial planar billet-billet interface, we also track the displacement of two adjacent

particles ( $c_2$  and  $c_3$ ) that also lie on the interface, initially a small distance from  $c_1$  such that the vector  $c_{1 \rightarrow 2}$  is perpendicular to  $c_{1 \rightarrow 3}$ . The local unit normal ( $\hat{\mathbf{n}}_t$ ) to the interface at any time,  $t$ , is determined by normalizing the cross product of  $c_{1 \rightarrow 2,t}$  and  $c_{1 \rightarrow 3,t}$ . We calculate the evolving local traction vector along the streamline ( $\mathbf{T}_t$ , equation 3.15, Figure 3.12) by taking the dot product of the unit normal and global stress tensor.

$$\mathbf{T}_t = \hat{\mathbf{n}}_t \cdot \boldsymbol{\sigma}_t \quad (3.15)$$

The local normal contact stress ( $\sigma_n$ , equation 3.16) and shear stress ( $\tau$ , equation 3.17) are then defined using the axioms of stress analysis.

$$\sigma_{n,t} = \mathbf{T}_t \cdot \hat{\mathbf{n}}_t \quad (3.16)$$

$$\tau_t = \mathbf{T}_t \cdot \hat{\mathbf{s}}_t \text{ where } \hat{\mathbf{s}}_t = [\mathbf{T}_t - \sigma_n \hat{\mathbf{n}}_t] / [\|\mathbf{T}_t - \sigma_n \hat{\mathbf{n}}_t\|] \quad (3.17)$$

Equations 3.18 and 3.19 define the perpendicular surface strains experienced in the small region around the particle of interest. These strains are estimated by tracking the relative displacement of the adjacent particles and applying the definition of engineering strain as change in length divided by original length.

$$\varepsilon_{1,t}^{eng} \approx [\|c_{1 \rightarrow 2,t}\| - \|c_{1 \rightarrow 2,t=0}\|] / [\|c_{1 \rightarrow 2,t=0}\|] \quad (3.18)$$

$$\varepsilon_{2,\perp 1,t}^{eng} \approx \left[ \left\| c_{1 \rightarrow 3,t} \times \frac{c_{1 \rightarrow 2,t}}{\|c_{1 \rightarrow 2,t}\|} \right\| - \|c_{1 \rightarrow 3,t=0}\| \right] / [\|c_{1 \rightarrow 3,t=0}\|] \quad (3.19)$$

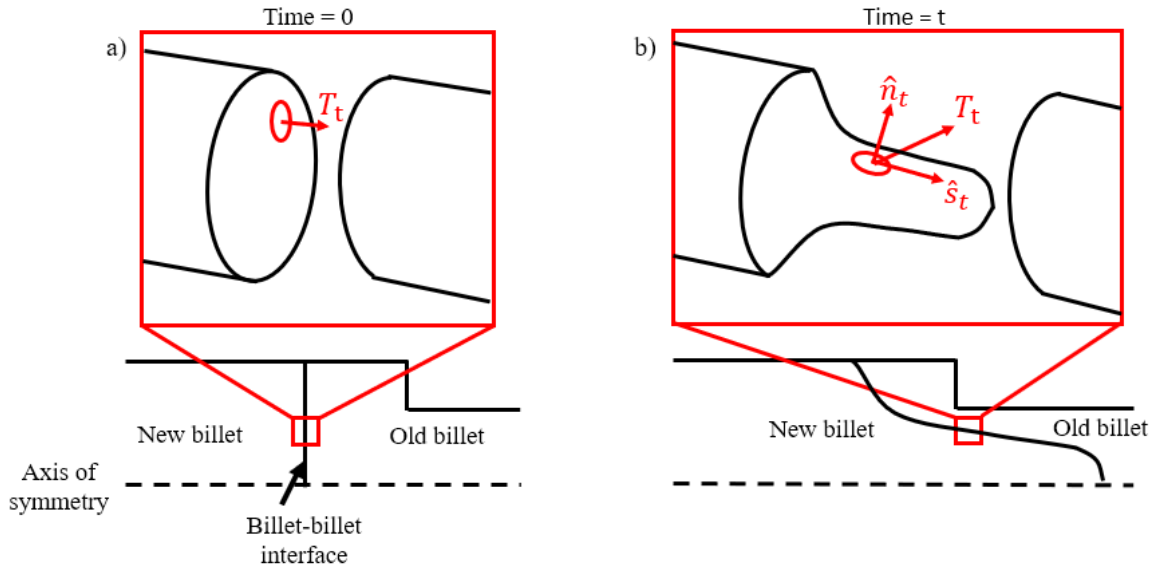


Figure 3.12: DEFORM<sup>®</sup> simulation output is used to calculate the local traction vector ( $T_t$ ) and unit normal vector ( $\hat{n}_t$ ).

### 3.3.3.3 Other model inputs ( $\eta$ and $Y'$ )

Equation 3.8 is used to calculate the fractional increase in interface area ( $\eta$ ) needed for further expansion to occur in an inert atmosphere. The root mean square asperity height,  $r$ , was determined using an AMTAST portable surface roughness tester for the billets used in the round profile ( $r=0.3 \mu\text{m}$ ), rectangular bar ( $r=7.5 \mu\text{m}$ ), and complex hollow profiles ( $r=7.5 \mu\text{m}$ ). A typical asperity inclination angle ( $\psi \approx 6^\circ$ ) for machined surfaces was also used (Grigoriev, 2015), resulting in  $\eta$  values ranging from 0.01 (round bar profile) to 0.20 (rectangular bar profile). Using equation 3.9, these  $\eta$  values translate into threshold minimum surface exposure,  $Y'$ , values ranging from 0.01 for the round bar to 0.17 for the rectangular bar profile (evaluated for  $\gamma = 0$ ).

### 3.3.4 Model implementation

Figure 3.13 shows how the key deformation conditions are tracked across streamlines of material for two points on the mid-plane of the rectangular bar profile. Figure 3.13 (top) shows how the surface exposures and normal contact stresses vary from the initial planar billet-billet interface to die exit. It shows that points near the weld nose (e.g., RA) experience negative surface exposures ( $v=0$ ) and are therefore predicted to have a zero weld strength. For point RB, Figure 3.13 shows the normal contact stress is highest at the start when the interface unit normal is parallel with the extrusion direction. However, the local surface



exposure at the start is lower than the threshold value ( $Y'$ ) needed to expose reactive substrate aluminum; therefore, no welding can occur initially. Once the surface exposures exceed the threshold (at  $Z \approx 12$  mm), the pressure needed for substrate micro-extrusion through the oxide cracks ( $p_{ex}$ ) quickly drops to below the actual normal contact stress,  $\sigma_n$ . Thus, welding can occur between  $Z \approx 12$  mm and  $Z \approx 48$  mm, which corresponds to the die exit when  $\sigma_n$  drops below  $p_{ex}$ . For point RB, the maximum realization of equation 3.1 occurs just before the die exit, at  $\tau_b = 0.71 \times \tau_o$ .

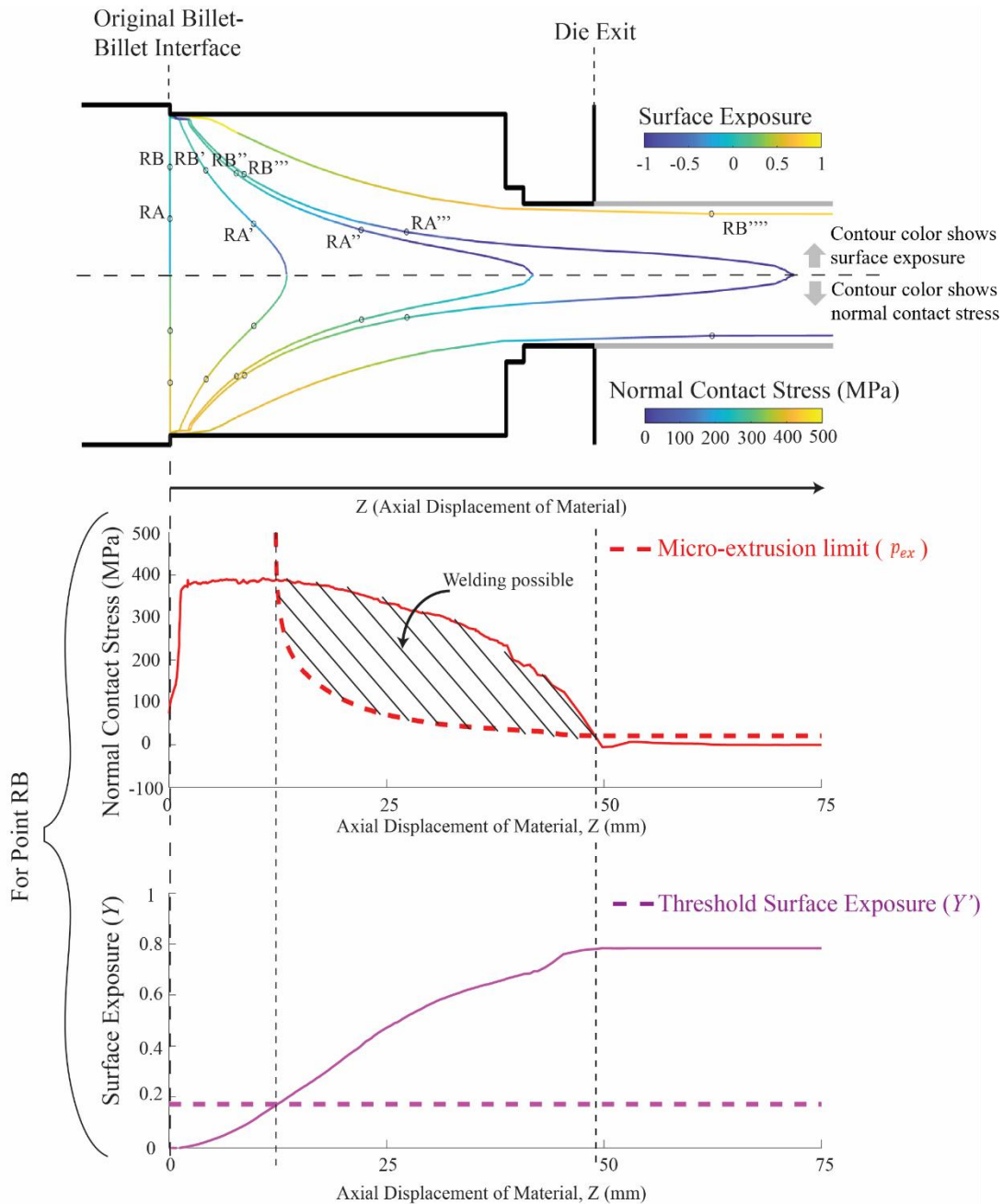


Figure 3.13: Tracking the deformation conditions across the major axis plane on the billet-billet interface during extrusion of the rectangular bar. Modeled for  $\gamma=0$ .

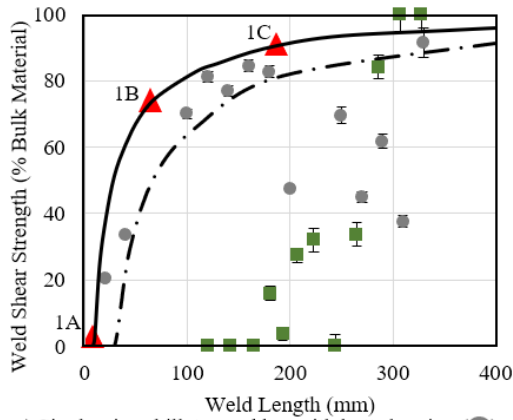
### 3.4 Results: Experimental and modeled weld strengths

#### 3.4.1 Weld strength in the round rod and rectangular bar

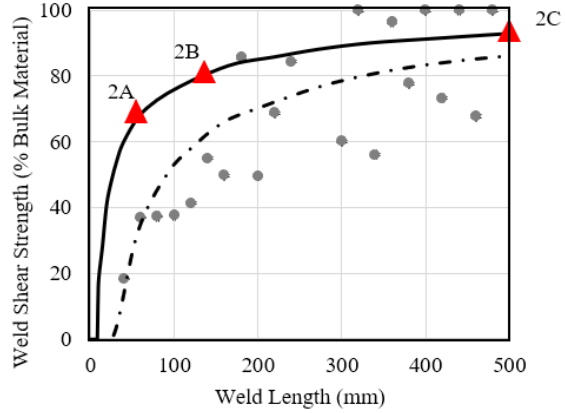
Figure 3.14 presents experimental and predicted transverse weld strengths (y-axis) as a function of the axial distance from the weld nose (x-axis). The weld shear strengths are expressed as a percentage of the bulk material shear strength.

The experimental results show several trends including a positive correlation between increasing distance from the nose and the weld strength. Figures 3.14a and 3.14b show that two-piece billet welds, despite being longer than single-piece equivalents, experience a similar rise in weld strength with distance from the weld nose. Many two-piece billet transverse weld samples reach bulk metal strength long before the end of the 2 m weld. Figure 3.14a also shows that consecutive extrusion of single-piece billets without the use of a butt shear has a deleterious effect on the weld strength. The front 10 cm of these welds break apart on attempts to machine a sample. This weakness is likely due to lubricant on the back of the previously extruded billet (transferred from the dummy block) and potentially contaminants in the (unremoved) back-end defect. Lubricants minimize the frictional restraint against incoherent oxide cracking. More importantly, lubricants themselves wet the interface and form a physical barrier to substrate-on-substrate contact. The lubricant was likely squeezed towards the billet center as normal contact stresses are highest on the outside of the billet-billet interface (Figure 3.13). Consistently, Figure 3.14a shows negligible strength for the first 200 mm from the nose and then a sudden increase to close to 100% of the bulk strength at the weld rear, corresponding to the outside of the billet. Figures 3.14c and 3.14d show that for the rectangular bar, the weld strength of samples extracted from along the minor axis of the ellipsoid shaped weld are greater than those of samples extracted from along the major axis. One tested sample from along the minor axis displays bulk metal shear strength.

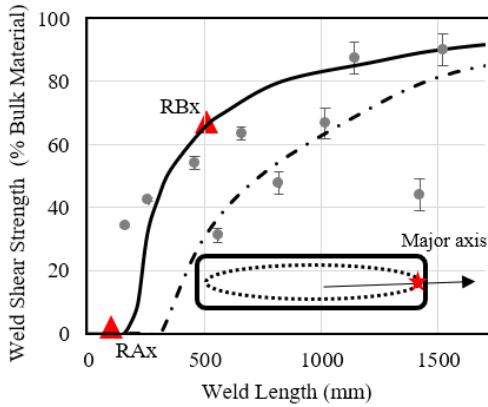
- - Experimental results (butt shear unless otherwise specified)
- ▲ - Highlighted sample locations (Fig. 13, 14)
- - - Modeled results (complete coherent oxide fragmentation)
- - - Modeled results (complete incoherent oxide fragmentation)



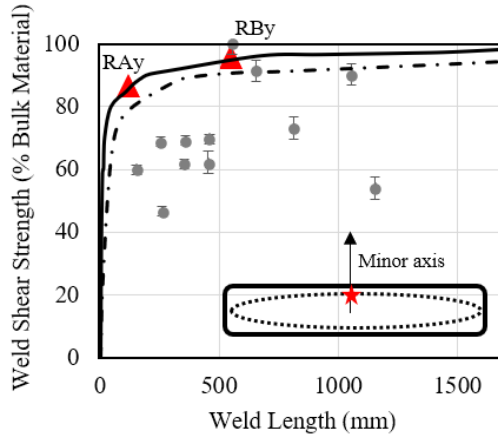
a) Single-piece billet round bar with butt shearing (●) and without butt shearing (■)



b) Two-piece billet round bar



c) Rectangular bar major axis  
(shear test samples extracted from (★))



d) Rectangular bar minor axis  
(shear test samples extracted from (★))

Figure 3.14: Experimental and modeled aluminum extrusion transverse weld strengths for the AA6061 round bar and rectangular bar profiles.

The model predictions in Figure 3.14 are shown bound by assumptions of complete coherent and incoherent oxide fragmentation ( $\gamma=0-1$ ). There are areas of disagreement between the predictions and experimental results; for example, the model over-predicts the weld strength near the nose axis along the minor axis of the ellipsoid shaped transverse weld in the rectangular bar profile (Figure 3.14d). Nonetheless, the model can be used to help explain the experimental results. Figure 3.15 shows the surface exposure and stress histories along material streamlines for points on the round rod and rectangular bar transverse welds. Figures 3.15a and b show that the size of the region where welding is possible gets smaller towards the nose of the weld as does the final value of the surface exposure. For the case of point 1A, located near the center of a single-piece billet, surface exposures are negative and no welding is predicted. In contrast, for

point 2A, located near the center of a two-piece billet, surface exposures are significant by die exit ( $Y \approx 0.4$ ) and welding is predicted. In Figure 3.15, whenever  $Y > Y'$ , the normal contact stress ( $\sigma_n$ ) quickly exceeds the minimum micro-extrusion pressure needed for substrate-on-substrate contact ( $p_{ex}$ ) and bonding is predicted to occur. Figure 3.15c shows that at the same axial position in the rectangular bar profile, a point placed on the minor axis (RBy) experiences a greater surface exposure (and therefore a higher predicted weld strength) than a point placed on the major axis (RBx).

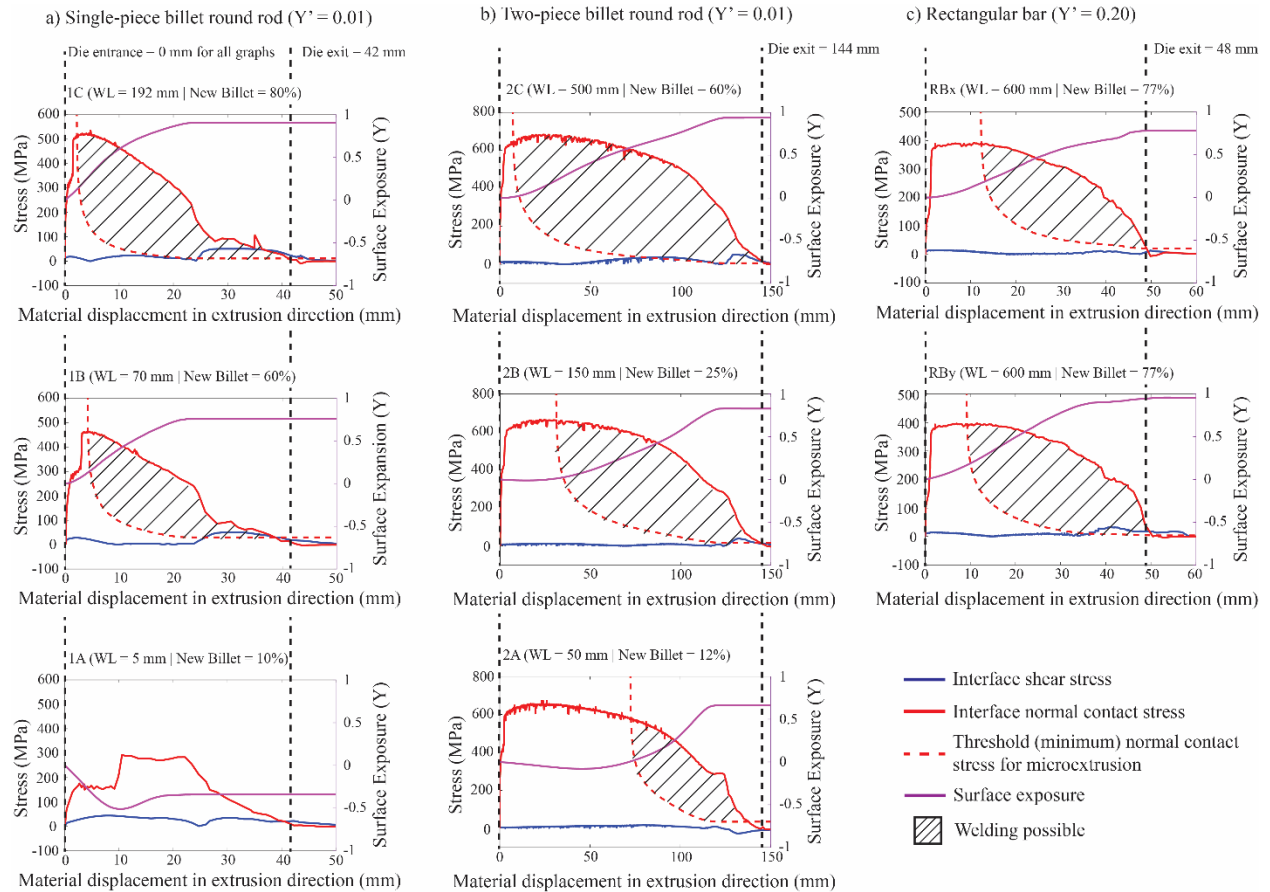


Figure 3.15: Surface exposures and stresses along material streamlines from the die entrance to exit. Welding can occur when the normal contact stress exceeds the threshold (minimum). Modeled for  $\gamma=0$ .

### 3.4.2 Weld strengths in the complex hollow extrusion

Figure 3.16 shows the model weld strength predictions and the experimental weld visibility across cross-sections near the front, middle, and rear of the weld. This profile contains eight tongue-shaped welds corresponding to each die port. The weld noses are not aligned axially: the weld nose corresponding to the right-hand side of the cross-section (as viewed in Figure 3.16) is  $\approx 200$  mm further forward into the profile than the weld nose on the left-hand side. Figure 3.16 (right) shows high weld visibility around the nose of each weld. In addition, the weld is most visible in high curvature regions of the weld line (disappearing in

the flatter portions), which is consistent with the weaker weld strengths seen along the major (high curvature) axis in the rectangular bar (Figure 3.14c). Figure 3.16 (left) shows the modeled weld shear strength evaluated over the complex 8-tongue weld geometry. Using weld visibility as a proxy for strength, the model correctly predicts high visibility near each of the weld noses, the higher visibility around high curvature regions of the weld, and lower visibility on flat regions both near and far from the nose.

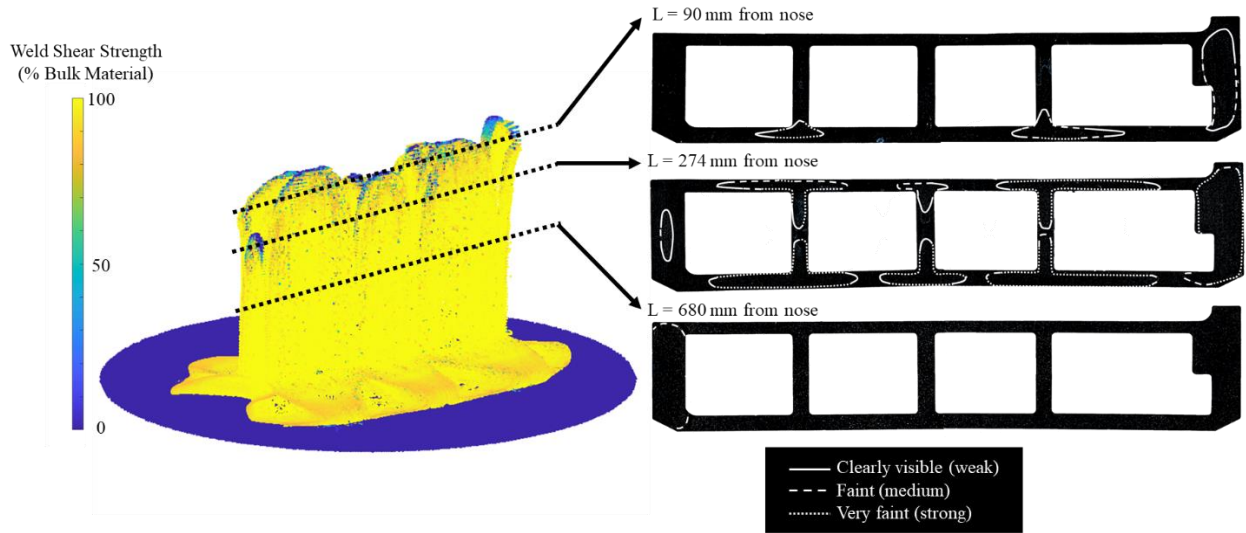
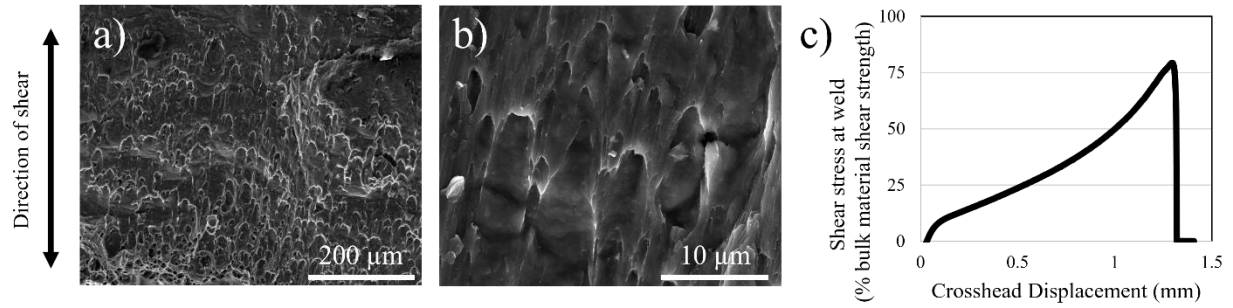


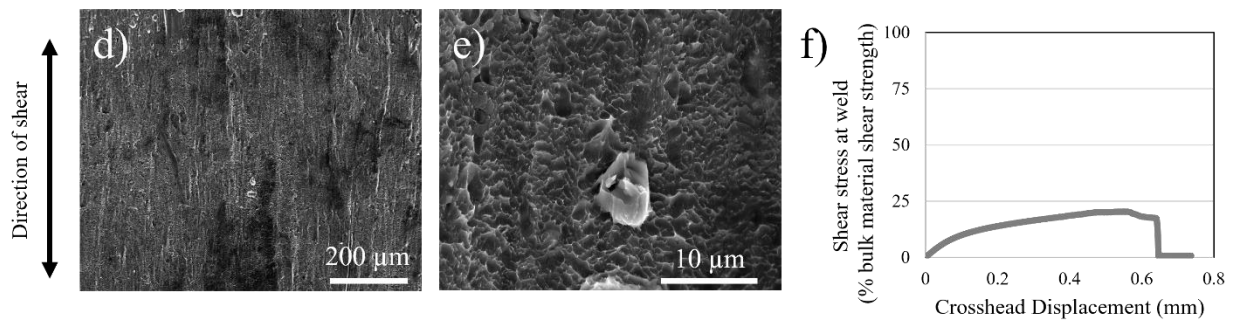
Figure 3.16: Predicted (left,  $\gamma=0$ ) transverse weld strengths versus experimental weld visibility (right) for the complex multi-hollow profile.

### 3.4.3 Weld fracture morphology

Figure 3.17 shows fracture surfaces for samples extracted from weak and strong welds. These images are representative of the fracture surfaces found across the profiles. The fracture surface created by breaking the strong weld shows long, drawn out tongue-shaped fragments around  $10\ \mu\text{m}$  in length, which were likely formed as the weld plastically deformed in the shear test direction. In contrast, the fracture surface created by breaking the weak weld is relatively planar with small thorn-shaped fragments orientated in the shear test direction which are less than  $1\ \mu\text{m}$  in length, suggesting brittle failure.



Samples (a-c) were extracted 180 mm from the nose (77% new billet area)



Samples (d-f) were extracted 20 mm from the nose (30% new billet area)

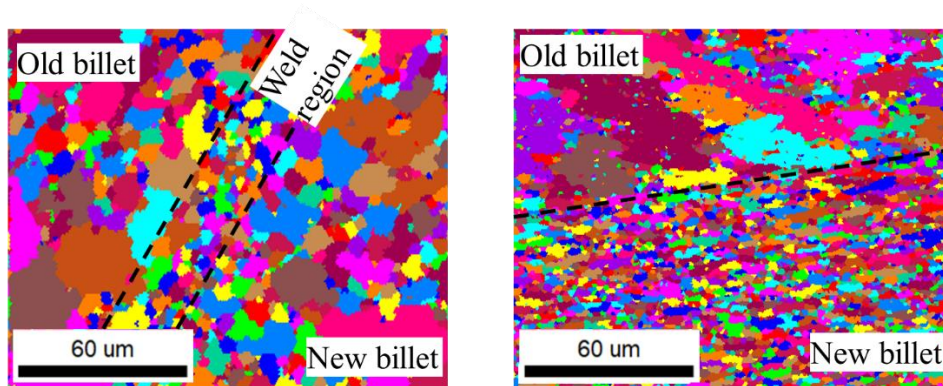
Sample (g) shows the nose of weld extruded without use of a butt shear, which disintegrated on machining



Figure 3.17: Shear test fracture morphology. The samples were extracted from the AA6061 round bar, single-piece billet extrusion, with butt shear (except where specified otherwise).

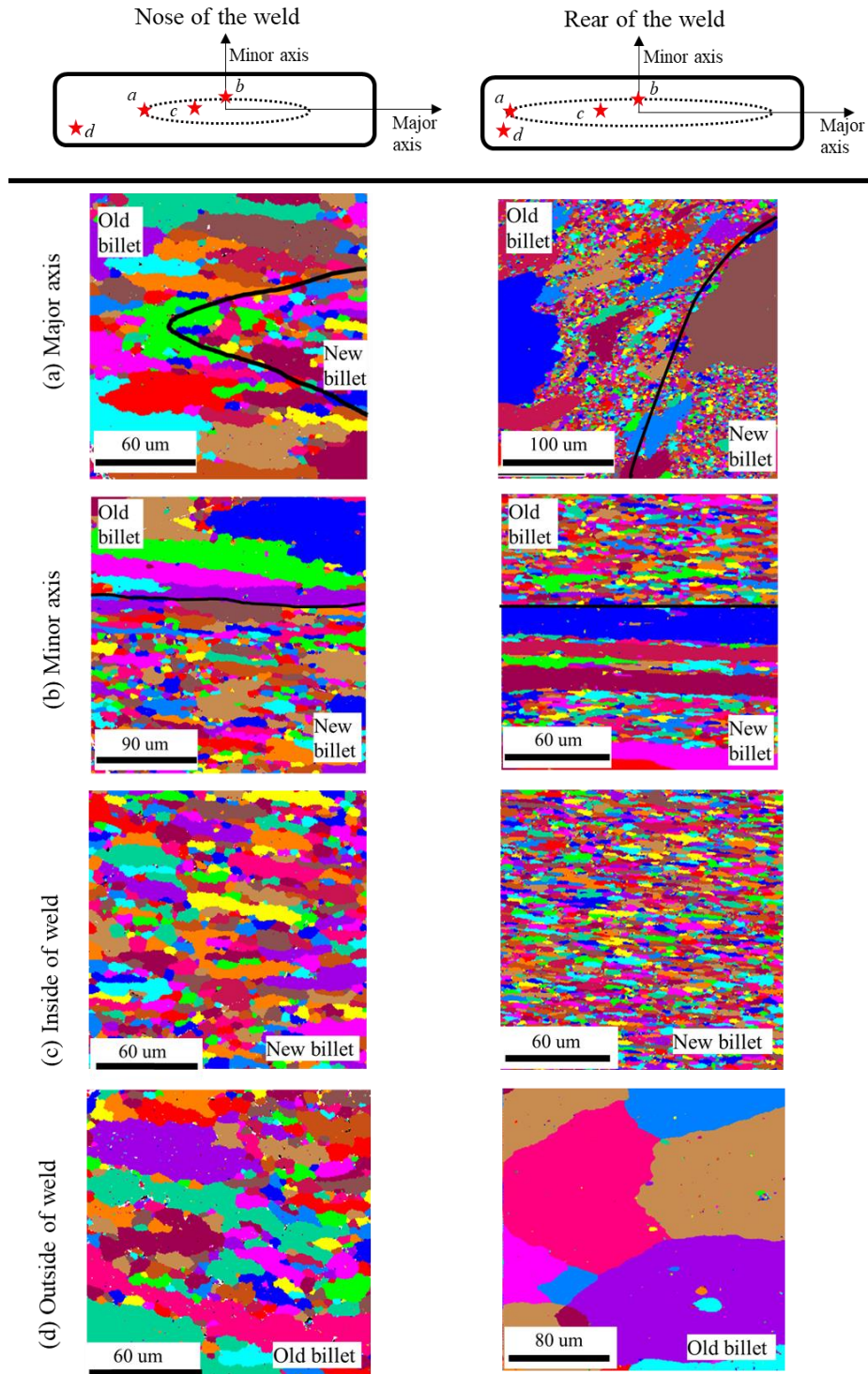
Figure 3.18a shows a relatively wide weld region of finer grains near the nose of the round bar profile (12% new billet area), corresponding to weak welding where the surface has buckled/crumpled. This welding region becomes narrow towards the rear of the round bar transverse weld with a distinct change in grain size from new (fine grain) to old (larger grain) billet. Figure 3.18b shows that for the rectangular bar then, even at the front of the weld, the grain structure is finer in the new billet and the grains have been flattened in the extrusion direction. Towards the rear of the rectangular bar transverse weld, there is a fine microstructure in the new billet. There is an emerging peripheral grain structure around the outside of the profile (old billet), with large, recrystallized grains on the major but not minor axis. The weld on the minor axis appears to consist of recrystallized grains, indicating additional deformation/heat from

interface shearing in this weld region to prompt recrystallization. The authors caution against drawing a direct causal relationship between the grain structure and welding quality. As the weld progresses, the weld's position in the cross-section changes and moves towards the outside of the profile. This shift towards the outside of the profile could alone prompt a switch from fine, elongated grains near the center of the profiles to recrystallized grains near the edge that have undergone greater shearing.



(a) Grain structure in the AA6061 round bar profile: 12% new billet area and negligible strength (left), and 41% new billet area and 50% bulk strength (right)





(b) Grain structure in the AA6061 rectangular bar profile. The nose corresponds to 30% new billet area (major axis strength $\approx$ 34% bulk; minor axis strength $\approx$  60% bulk) and the rear corresponds to 73% new billet area (major axis strength $\approx$ 48% bulk; minor axis strength $\approx$ 73% bulk).

Figure 3.18: Electron Backscatter Diffraction (EBSD) images of the grain structure at the transverse weld and in the bulk of the profile. All quoted weld strengths are experimental (not modeled).

#### **3.4.4 Sources of error**

The main error in the experimental determination of the weld shear strength is uncertainty in the fracture area measurement. The thicknesses of the shear test samples were measured using a micrometer and the length of the fracture region measured using a low-zoom microscope. For each measurement, we assign a  $\pm 0.1$  mm uncertainty. This translates to a strength calculation error of  $\pm 0.6\%$  for the largest test geometries (near the weld nose) and  $\pm 5\%$  for the smallest test geometries needed towards the weld rear. Potential damage to the welds caused by the EDM process is another potential source of error.

Parametric uncertainty is estimated to translate to  $\pm 10\%$  uncertainty in the modeled strength predictions. This uncertainty originates from imperfect material specifications (e.g., billet flow curves), an experimental uncertainty of  $\pm 2$  mm in the original position of the planar billet-billet interface (affecting the FEM point tracking), and stress tensors extracted from imperfect simulations. Additional model-form uncertainty includes whether isolated pockets of lubricant were present on the billet-billet interface. The billet faces were nominally clean; however, eliminating the presence of all lubricant in metal forming processes is challenging.

### **3.5 Section discussion**

#### **3.5.1 Accuracy of the new model**

Figure 3.14 shows the experimental results are dispersed. There is poor reliability regarding the experimental strength obtained at points along or across the welds. Dispersed weld strength results are common in the literature on planar solid-state welding; e.g., in Bay's (1983) and Cooper and Allwood's (2014a) work. However, some trends are clearly visible from Figures 3.14 and 3.16, such as increasing strength towards the rear of the weld, the poor weld strength associated with lubricated surfaces (e.g., when the billet butt is not removed), the increased weld length and strength of two-piece billet welds, and the varying weld strengths along and across the cross-section of non-axisymmetric profiles. The proposed model predicts these experimental trends. However, given the dispersed experimental results, the model should be seen as indicative rather than an accurate predictor of the weld strength. The model results were open-loop predictions for a range of alloys, shapes, and extrusion parameters. Accuracy might be improved with tuning of parameters (e.g., the threshold surface exposure) based on experimental results from similar profiles.

### 3.5.2 Industry implications

For traditional extrusion, the new model can be used to help determine whether a weld needs to be removed, to judge the minimum length of profile from the weld nose that must be scrapped, and to help optimize die design for maximum transverse weld strength. The model can also be used to predict weld strengths in novel extrusion processes being studied by researchers. For example, in Lv et al.'s (2023) multi-container extrusion method for manufacturing wide aluminum profiles where multiple billets with oxide-covered surfaces are welded in the die orifice, or in Oberhausen and Cooper's (2023) profiled dummy block method for reducing process scrap and starting with a non-planar billet-billet interface.

#### 3.5.2.1 Surface exposure as the key determinant of transverse weld strength

Figure 3.15 shows that even for points that form weak welds (e.g., 1A), the normal contact stress is at least three times greater than the yield strength of the hot billet material. Therefore, the pressures in hot extrusion are likely always sufficient to establish close contact between the billet-billet surfaces and exceed the minimum micro-extrusion pressure (shown in Figure 3.7b) needed to micro-extrude the substrate through any oxide cracks. The Figure 3.6 microscopy also indicates that substrate-to-substrate contact is achieved wherever there are oxide cracks. Subsequently, the fraction of the final contact area that is exposed aluminum,  $v$  in equation 3.1, is the key determinant of hot extrusion transverse weld strength.  $v$  is largely determined by the surface exposure. The importance of the surface exposure is illustrated in Figure 3.18 by plotting the strain history of points that formed strong and weak welds in the experiments. At one extreme there are locations near the nose of the round bar profiles that experience a net negative surface exposure, as observed in Figure 3.6c, and possess only handling strength. At the other extreme, several shear test samples display bulk metal strength if extracted from a point that experienced a surface exposure of around 0.95.

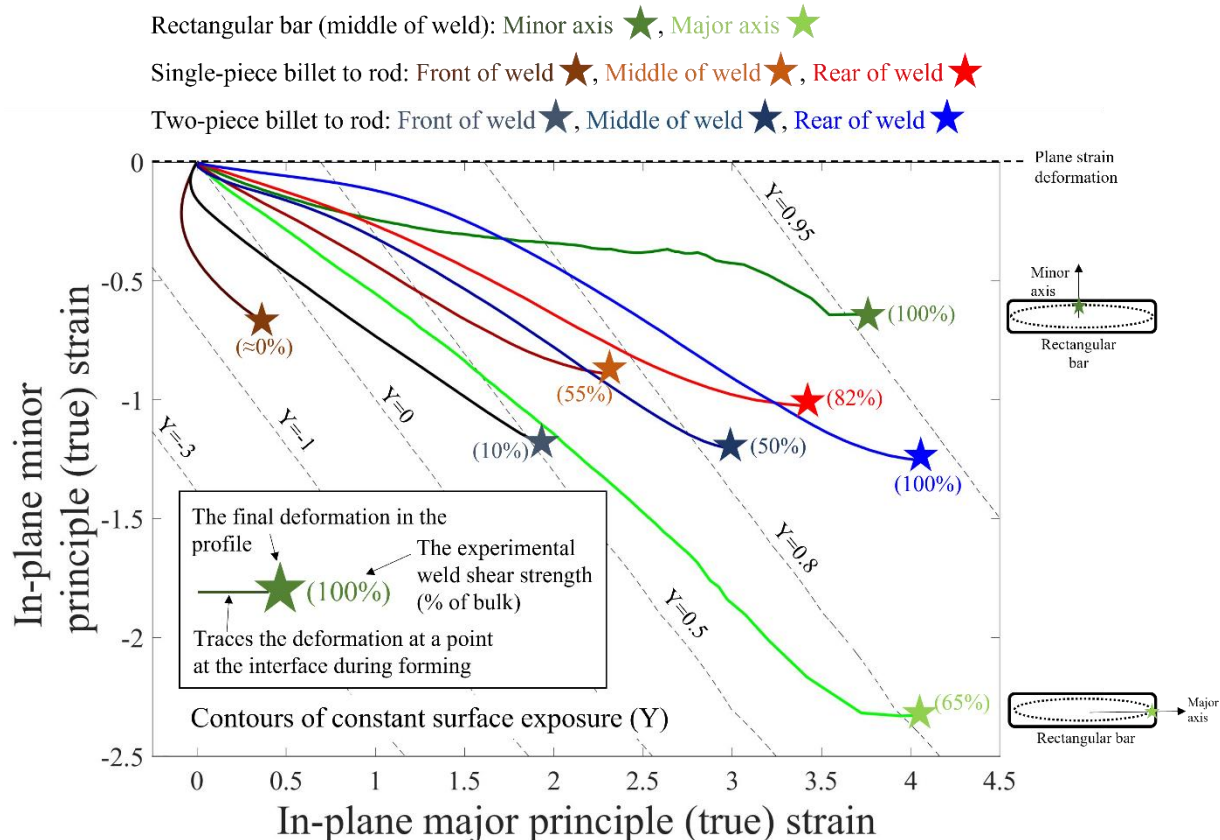


Figure 3.19: Plot of principal in-plane strain histories for points along the bonding interface.

Surface exposures vary across as well as along profiles. Figure 3.18 highlights that at the same axial distance from the weld nose, a point on the minor axis of the rectangular bar weld experiences a greater surface exposure than a point on the major axis. Both points experience a similar tensile strain but varying perpendicular compressive strains. These compressive strains reduce the surface exposure and correspond to high curvature portions of the weld cross-section. Similarly, Figure 3.16 shows regions of greatest weld visibility and lowest strength in areas of high weld line curvatures. This knowledge might be used to inform extrusion profile and die design and, for those cases where the weld is not removed, inform the likelihood of failure if adding fasteners around the outside of the profile.

### 3.5.2.2 Reusing process scrap using two-piece billets

For the two-piece billet round rod extrusion, the weld was four times longer than in the single-piece billet case (2000 mm versus 500 mm). Despite this, the two-piece billet weld possesses similar weld strengths to the single-piece billet weld at the same distance from the weld nose (Figures 3.14a and b) and exhibits bulk strength long before the weld rear. This is because, for the same percentage area of new billet at the cross-section, the two-piece billet weld experiences greater surface exposures (Figure 3.18) and greater oxide spacings (Figure 3.6) than the single-piece equivalent. This suggests that the two-piece billet

extrusions could be used for more critical components, providing more opportunities for billet scrap reuse, especially if the front section of the elongated weld is removed.

### **3.5.2.3 Lubrication and the billet butt shear**

The effect of lubrication at the interface is severe. The transverse weld section in profiles produced without use of a butt shear (profiles produced by a minority of extruders using old presses and as explored in some new tooling concepts) is likely unusable even in non-safety critical applications. More generally, every effort should be made to minimize the lubricity of the billet surfaces by minimizing lubricant transfer from billet cutting saws or the butt shear; e.g., using minimum quantity lubrication methods such as supercritical CO<sub>2</sub> for cutting (Cai et al., 2021).

## **3.6. Section conclusions**

Concern regarding transverse weld strength is the greatest source of material inefficiency in aluminum extrusion. The main contribution of this work has been to conduct a study on the fragmentation of oxides at the billet-billet interface and to use the findings to update a plane strain film theory model of solid-state welding to non-plane strain conditions, applying it to predict local transverse weld strengths. The oxide fragmentation study showed that local surface contraction results in interface buckling, limited oxide cracking, and weak resulting welds. In contrast, local surface expansion results in oxide fragments that are equally spaced (locally) in the axial and circumferential directions with dimensions predictable using shear lag modeling. To evaluate the new weld strength model, transverse weld strengths along and across simple and complex profiles were measured experimentally. Unlike in previous work, the weld strengths were determined using sample geometries that isolate the transverse weld and provide a direct measure of weld strength. The experiments show the sensitivity of the weld strength to the starting position of the billet-billet interface (e.g., single-piece vs. two-piece billets) and to the position on the weld across as well as along a profile. Weld strengths are lower in higher curvature portions of the weld.

The model predicts the experimental trends and indicates that the weld strength in hot extrusion is not limited by the normal contact stresses at the billet-billet interface. The die pressures are sufficient to ensure intimate contact and micro-extrusion of substrate through any cracks in the interface oxides. The strength is instead limited by the ability to generate large positive surface expansions across the billet-billet interface, exposing reactive substrate for bonding. Any lubricant at the interface has a deleterious effect. The new model can be used to help determine whether a weld needs to be removed for a given application, to help estimate the minimum length of profile that must be scrapped to ensure the remaining profile contains only strong welds, and as part of a profile and die geometry optimization for increased weld strengths. These developments can help decarbonize the extrusion industry through increasing manufacturing process yields.

## **Chapter 4. Reducing the Aluminum Extrusion Transverse Weld Length**

The poor reliability of the transverse weld strengths observed in Chapter 3 suggests that efforts to reduce the weld length, rather than increase the weld strength, might be a more fruitful avenue of research directed at reducing the process scrap created. We develop a novel aluminum extrusion process, utilizing concave, profiled dummy block designs to produce near-flat transverse welds. Section 4.1 will introduce an analytical design method for the concave dummy blocks and present preliminary results in comparison to traditional means of transverse weld length reduction in literature and industry (e.g., process parameter and die geometry optimization). Section 4.2 will introduce a numerical design method and more extensive experimental results including lab- and industry-scale extrusion trials on profiles of increasing complexity (round bar, rectangular bar, and square hollow).

### **4.1 Reducing aluminum extrusion transverse weld process scrap**

Nearly 20% of aluminum produced globally is extruded. Up to one quarter of this aluminum is scrapped in the form of extrusion butts and segments of extruded profile that contain weak solid-state “transverse” welds that are created between consecutively extruded billets in direct extrusion. In this article, extrusion of different color clay billets is used to conduct a parametric study on the effect of extrusion ratio, die angle, friction coefficient, profile shape and dummy block profile on transverse weld length. Shorter transverse weld lengths require smaller lengths of the extruded profile to be extracted and scrapped. The results show that the transverse weld length can be reduced by decreasing the extrusion ratio, die angle or friction coefficient. The profile shape also has a strong influence; the transverse weld length was found to scale

with the cross-sectional perimeter to area ratio of the extruded profile. Additionally, it is shown that the dummy block profile (a previously unexplored design variable) can be modified to decrease the weld length. A concave dummy block was designed using an estimated velocity field for axisymmetric extrusion of solid rods, decreasing the weld length by 44%. The industry implications of this work and the need for further research is discussed.

#### **4.1.1 Section background**

Aluminum is one of the five materials (steel, cement, paper, plastic, aluminum) whose production is responsible for over half of all annual greenhouse gas emissions released by industry globally (IEA, 2017). The energy efficiency of the primary aluminum production process is reaching the thermodynamic limit (Gutowski et al., 2013); therefore, significant emission reductions must be delivered through electricity grid decarbonization and/or material efficiency (Cullen and Allwood, 2013). Global material flow analyses (MFAs) of the aluminum sector reveal significant ostensible opportunities to increase material efficiency by reducing manufacturing scrap generation. Cullen and Allwood (2013) found that 40% of all liquid aluminum is scrapped before reaching a final product, and that billets destined for extrusion account for 20% of all semi-finished aluminum. In their mass balanced MFA, Cullen and Allwood calculate that 25% of the extrusion billet is scrapped during the metal forming process. Elsewhere, the European Aluminum Association (EAA) (2013, 2018) survey 69 extruders (894 kt of product; 32% of European production) and find that between 22 and 24% of the extrusion billet volume is scrapped during the metal forming process.

There are many sources of scrap in the aluminum extrusion process. Sheppard (1999), in his seminal textbook on aluminum extrusion, identifies many of these sources as insignificant because they each account for less than 2% of the total initial billet volume. These insignificant scrap sources include the material deformed by the grippers during the stretching process as well as material remaining in the die after a tool changeover. Sheppard identifies the two most significant sources of scrap: removal of the billet butt and the transverse weld. The approximate locations of the billet butt and the transverse weld within the extrusion process are shown in Fig. 4.1.

The billet butt is scrapped because it contains a concentration of impurities which would reduce the aesthetic, mechanical and electrical properties of the final profile if it were to be extruded through the die (Saha, 2000). To prevent this effect, it is standard industry practice to not press the whole length of the billet through the die; thus, allowing the billet butt to be sheared off between strokes of the main hydraulic ram (Sheppard, 1999). The source of the impurities in the billet butt is the billet skin, which contains oxides and solid-phase inclusions, such as spinels ( $MgAl_2O_4$ ), carbides, nitrides and intermetallics, developed during billet casting (Saha, 2000). The billet skin impurities concentrate in the billet butt during the extrusion process due to the material flow inside the billet. While the center of the billet flows through the

die, the billet skin has a tendency to stick to the container walls due to friction (Sheppard, 1999; Sano et al., 2008), forming a conglomeration of billet skin in the

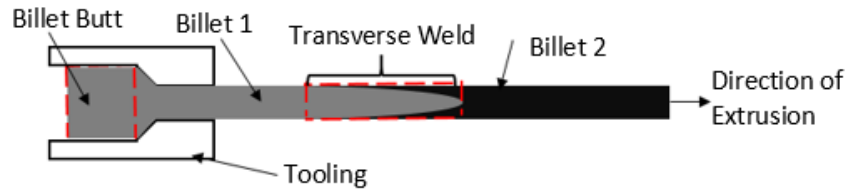


Figure 4.1: Major sources of scrap in consecutively extruded billets.

last 5-20% of the initial billet length (Sheppard, 1999). To the authors' knowledge, the shearing of billet butts is commonplace in industry (Oberhausen and Cooper, 2019). An alternative to butt shearing is "Dick's extrusion method" (Sheppard, 1999) which utilizes a dummy block with a diameter smaller than that of the container walls. After the initial stroke of the press, the billet skin is left intact on the container walls and a second press-stroke is then used to remove the skin in the form of a "skull". Dick's method is less prevalent in current industry practice (Oberhausen and Cooper, 2019), which is probably because of the extra time that results from the second press-stroke for each billet.

Transverse weld scrap is the segment of the extruded profile that contains the interface between two consecutively extruded billets. This interface forms a solid-state weld that elongates over a significant length of the extruded material and is typically removed from the extruded profile due to concerns of it having lower strength than surrounding material (Sheppard, 1999). Reviewing the literature however, the authors have found only one recorded instance of the transverse weld strength being experimentally tested. Den Bakker et al. (2017) test the transverse weld tensile strength of a series of dog-bone samples extracted from a hollow AA6082 extrusion. They find that the weld strength varies by position with respect to length along the weld; dropping to around 75% of the strength of the parent metal. Sheppard (1999) does not quantify the contribution of transverse weld removal to total extrusion scrap rates; however, Mahmoodkhani et al. (2013) and Hatzenbichler and Buchmayr (2010) found that the transverse weld length (TWL) accounted for 20% and 15% of the initial billet volume in profiles for which the billet butt accounted for 12% and 10% of the initial billet volume respectively. The rest of this article will focus on existing and novel methods of reducing the TWL, as this is the largest source of scrap identified in the extrusion process.

#### 4.1.1.1 Previous work on reducing the length of the transverse weld scrap

Parametric studies that use a finite element model (FEM) are often used to investigate methods of reducing the billet butt volume and TWL (Oberhausen and Cooper, 2019; Mahmoodkhani et al., 2013; Hatzenbichler and Buchmayr, 2010; Chen et al., 2015; Sano et al., 2008b; Zhang et al., 2017). Extensive experiments are probably avoided due to their high cost and the significant time expended in processing and measuring the TWL. However, it is common for a single extrusion to be performed on the simplest set of parameters, from which the extrusion pressure and experimentally measured billet butt or TWL are used to validate the FEM (Sano et al., 2008a; Mahmoodkhani et al., 2013; Hatzenbichler and Buchmayr, 2010;



Sano et al., 2008b; Zhang et al., 2017). The parameters which have been studied by previous researchers include: die angle, extrusion ratio, ram velocity, ram-billet friction coefficient, billet length, temperature, and bearing length for solid profiles, in addition to port bridge diameter, welding chamber radius and baffle plate height of the specialty porthole die used in hollow extrusions (Sano et al., 2008a; Mahmoodkhani et al., 2013; Hatzenbichler and Buchmayr, 2010; Chen et al., 2015; Sano et al., 2008b; Zhang et al., 2017). The finite element software packages used in these studies are DEFORM<sup>TM</sup> (Sano et al., 2008a; Mahmoodkhani et al., 2013; Hatzenbichler and Buchmayr, 2010; Sano et al., 2008b) and HyperXtrude<sup>TM</sup> (Chen et al., 2015; Zhang et al., 2017). The alloys studied are AA3003 (Mahmoodkhani et al., 2013), AA6005 (Chen et al., 2015), AA6063 (Sano et al., 2008a; Sano et al., 2008b), AA6082 (Hatzenbichler and Buchmayr, 2010) and AA7N01 (Zhang et al., 2017).

The parametric studies found in the literature were performed by making slight alterations to validated finite element simulations, such that the effect of individual parameter changes on the TWL could be isolated and measured. Studies on solid, axisymmetric profiles have looked at the effects of die angle, extrusion ratio, ram velocity, ram-billet friction coefficient, bearing length and billet length on TWL (Mahmoodkhani et al., 2013; Hatzenbichler and Buchmayr, 2010). Decreasing the extrusion ratio was found to have the largest effect of reducing the TWL (Hatzenbichler and Buchmayr, 2010). The use of a smaller die angle (Mahmoodkhani et al., 2013), increasing billet length or increasing temperature (Hatzenbichler and Buchmayr, 2010) was also found to have a significant effect in reducing the TWL. Bearing length, ram velocity and ram-billet friction coefficient were found to have an insignificant effect on the TWL (Hatzenbichler and Buchmayr, 2010). No studies on non-axisymmetric solid profiles have been found in the literature. The hollow profile studies (Mahmoodkhani et al., 2013; Zhang et al., 2017) examined non-axisymmetric profiles (no studies on hollow axisymmetric profiles were found) and also looked at extrusion ratio, temperature and ram speed, as well as porthole die dimensions, including the port bridge diameter, welding chamber radius and baffle plate height. It again was found that decreasing the extrusion ratio had a significant impact in reducing TWL (Zhang et al., 2017). Increasing the port bridge diameter, welding chamber radius and baffle plate height were all found to have a significant effect in decreasing the TWL as well (Zhang et al., 2017). Contrary to in solid profiles, however, it was found that an increase in the ram speed could actually decrease the TWL (Mahmoodkhani et al., 2013; Zhang et al., 2017), and that temperature no longer had a significant impact (Zhang et al., 2017). Although Zhang et al. (2017) suggests that the ram speed would affect the material flow velocity through the die and therefore affect the transverse weld formation, neither they nor Chen et al. (2015) have offered an explanation for the varying impacts they observed between solid and hollow profiles.

Previous research on reducing the TWL has examined neither the effect of the profile shape nor the effect of the dummy block profile geometry. In addition, previous work has been focused primarily on FEM

studies. This work will examine the effect of common and novel extrusion design variables on the TWL using a multi-colored clay extrusion technique before discussing the significance of the results and the implications for industry.

## 4.1.2 Section methodology

### 4.1.2.1 Equipment

The experiments in this study were conducted on a hydraulic press extrusion set-up developed for this research, shown in Fig. 4.2. The press container is made from aluminum and is 127 mm long with an internal diameter of  $\text{Ø}25.4$  mm. The interchangeable dummy block is made from steel and was turned on a lathe to produce a sliding fit with the container. Several sets of dies were also produced for use with this press, Fig. 4.3. Die sets were machined and polished from a  $\text{Ø}42$  mm aluminum rod. The first set is designed for axisymmetric solid rod extrusions of varying diameters corresponding to extrusion ratios of 4, 6.67, 10 and 25. The next set was produced for rectangular profiles of the same extrusion ratios. The third and final set of dies are more complex geometries, one cross and one with dual-circles, both of an extrusion ratio of 4. Each die in these three sets has one side with a flat face (a die angle of  $90^\circ$ ) and one side with a tapered,  $45^\circ$ , die angle.

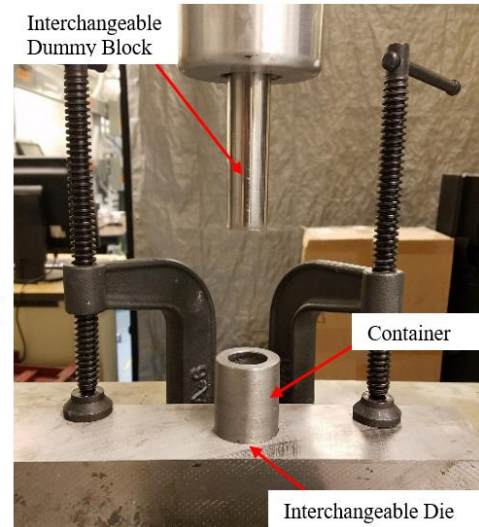


Figure 4.2: Experimental, plasticine clay direct extrusion press used in this study.



Figure 4.3: From left to right: Axisymmetric die set; rectangular die set; complex dies with dual-circle die on top, cross die on bottom.

#### 4.1.2.2 Billet material

The billets used in the experiments were made from plasticine clay, which is a low-cost material that can be used to adequately model hot-metal deformation (Sofuoglu and Rasty, 2000). In addition, the use of differently colored plasticine for consecutive billets enables the transverse

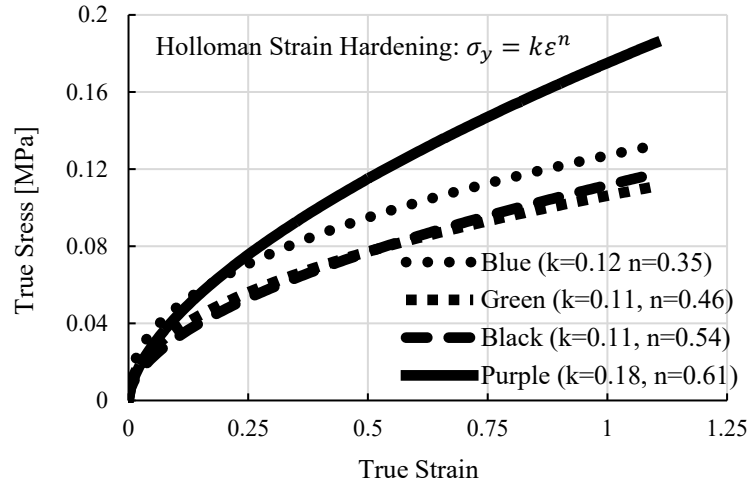


Figure 4.4: Flow curves of four different colors of plasticine.

weld in an extruded profile to be easily located using a scalpel to section the profiles, as opposed to the lengthy and expensive sectioning, polishing and etching process that is required for aluminum extrusions.

The elastoplastic properties of plasticine are dependent on its color (Sofuoglu and Rasty, 2000), which is indicative of the additives in the clay. The two colors of plasticine used in this work must have similar mechanical behavior to maintain a consistent material flow through the die, as would be the case in real industrial extrusion of aluminum billets. The flow curve of differently colored plasticine was determined using a uniaxial compression test (Sofuoglu and Rasty, 2000), and fitted to a power-law Hollomon strain hardening model (Hosford and Caddell, 2007), as shown in Fig. 4.4. Based on these results, the green and black were chosen for the experiments. In each extrusion trial the green billet was extruded first, followed by the black billet.

Plasticine extrusions were conducted using different lubricants to examine the effect of friction on the TWL. Friction ring compression tests were conducted in order to determine the Coulomb friction coefficient ( $\mu$ ) under different lubrication conditions (Hosford and Caddell, 2007; Sofuoglu and Rasty, 1999).

During a friction test, a ring of plasticine (initially of height  $h_0=25.4$  mm, inner radius  $r_0=12.7$  mm, and thickness  $t_0=9.5$  mm) was covered in lubricant and axially compressed between two platens, reducing the height ( $h$ ). The test was intermittently paused in order to measure the inner radius ( $r$ ) of the ring at the mid-plane at different levels of compression. The changing inner radius is indicative of the friction conditions; e.g., if there were zero friction the radius would increase; whereas, with sticking friction it would decrease (Hosford and Caddell, 2007; Sofuoglu and Rasty, 1999). Green plasticine and aluminum platens of the same surface finish as the extrusion container were used in the friction tests. Additional trials tested the effect of using Vaseline<sup>®</sup>, Teflon<sup>®</sup> spray, and talcum powder as lubricants as well as the use of no lubricants at all. An Abaqus FEM was produced to simulate the change of the inner radius during compression for different contact friction conditions. These FEM results were compared to the experimental results (see Fig. 4.5) in order to estimate the friction coefficient ( $\mu$ ) associated with each of the different lubricants. The axisymmetric, quarter-sized Abaqus model was meshed using 1,000 linear CAX4 elements with reduced integration and enhanced hourglass control. The validity of the model was confirmed by comparing the

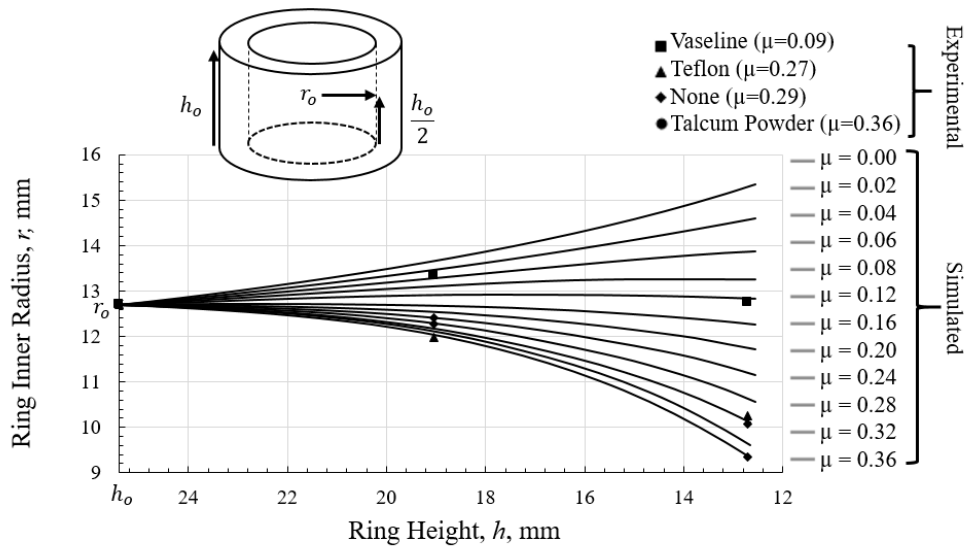


Figure 4.5: Axisymmetric solid rod ring compression test results: experimental data points for different lubricants, and simulated curves for different modeled friction levels.

simulated and actual compression loads and ensuring that the energy dissipated due to contact stabilization was less than 1% of the internal energy of the model. The interfaces between the billet and the bottom and top plates were modeled using penalty tangential behavior at a range of friction coefficients from 0 to 0.36.

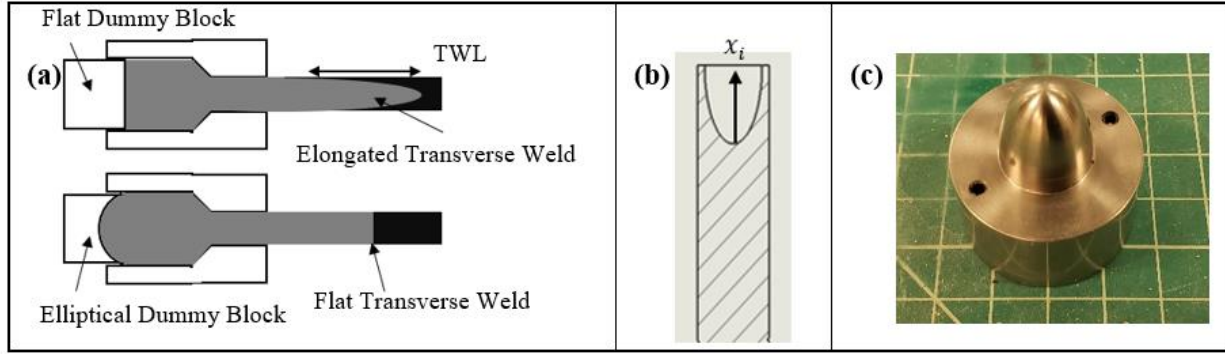


Figure 4.6: (a) Transverse weld geometry formed in conventional extrusion (top) and profiled dummy block and billet extrusion (bottom). (b) Section view of elliptical concave ram used in profiled dummy block and billet experiments. (c) The convex forming element used as part of the profiled billet mold.

#### 4.1.2.3 Dummy block geometry

The majority of experiments conducted in this work use a conventional flat-faced dummy block; however, an attempt was also made to adjust the TWL by changing the geometry of the dummy block face in order to alter the material flow through the die. Material at the center of the billet-on-billet interface travels through the die quicker than material on the interface periphery, which causes the elongation of the “bullet-shaped” weld. It was hypothesized that the TWL could be reduced by changing to an initially concave billet-on-billet interface geometry (see Fig. 4.6a). A trial dummy block and billet geometry were designed using analytical velocity field analysis, as described below.

For axisymmetric profiles, the flow of metal through the die can be estimated using a velocity field first proposed by Avitzur (1963), where velocity discontinuities appear at spherical-“caps” at the die entry and exit, see Fig. 4.7. To understand the difference in material flow between the center and outside of the billet, consider two particles ( $A$  and  $O$ , Fig. 4.7) both situated at the end of a billet (on the interface with a previously extruded billet) but at different radial positions.  $A$  is located near the edge of the billet (next to the container wall) and  $O$  is located on the billet center axis. During the extrusion process both particles enter the velocity field with speed  $v_i$  (the ram speed).  $O$  then passes through the spherical-cap velocity discontinuity before  $A$ . Both particles exit the die at speed  $v_o$ , where  $v_o$  is equal to the product of  $v_i$  and the extrusion ratio ( $R_i^2/R_o^2$ ). The TWL can be estimated as the difference in the axial positions of  $A$  and  $O$  once they emerge from the die ( $A''$  and  $O''$ ).

The velocity field is broken into three regions. The first region, I, contains material traveling at the same speed as the ram,  $v_i$ . This region ends at the first spherical-cap velocity discontinuity,

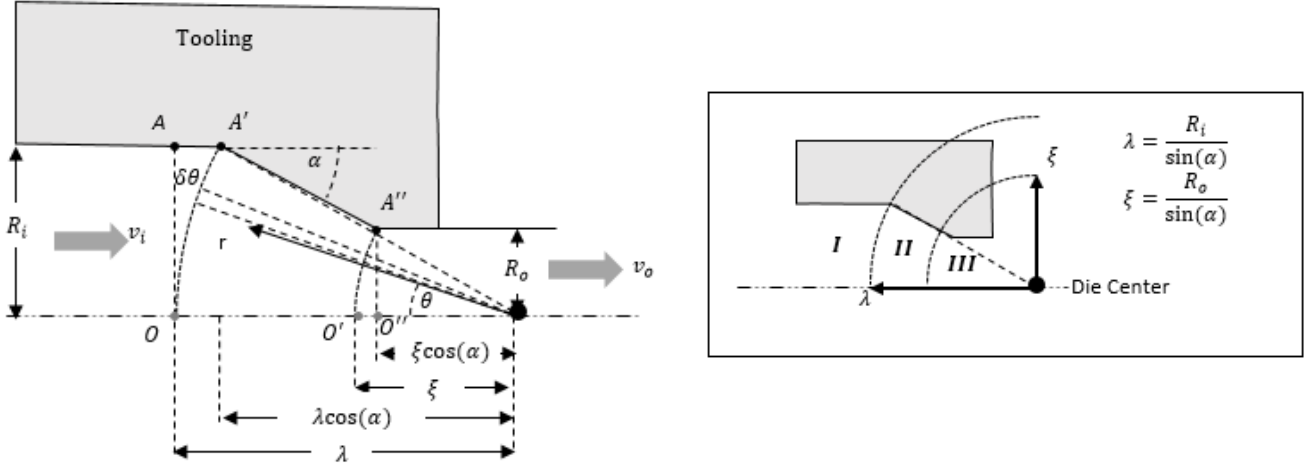


Figure 4.7: Estimated velocity field for solid axisymmetric extrusion. Velocity discontinuities are seen as circular arcs on this 2D image.

along which points  $A'$  and  $O$  are found. The field line at this first spherical-cap velocity discontinuity indicates the start of region II, with material traveling at increasing speed in the direction of the die center, labelled on Fig. 4.7. Region II ends at the second spherical-cap velocity discontinuity, with a smaller radius (on which lie points  $A''$  and  $O'$ ). The material then enters region III in which all material (irrespective of its radial position) travels in the extrusion direction at speed  $v_o$ . Point  $A''$  is located at the end of the conical die taper, marking the exit of particle  $A$  from the forming region. Point  $O''$  is found within region III, traveling at the velocity of the exiting profile,  $v_o$ .

The time taken by particle  $A$  to travel through region I, from point  $A$  to  $A'$ , is shown in equation 4.1.

$$t_{AA'} = \frac{\lambda(1-\cos\alpha)}{v_i} \quad (4.1)$$

On entry to region II, material flows towards the die center at  $v_i \cos \theta$ , ensuring that the normal component of velocity is continuous on the velocity discontinuity surface; however the parallel component of the velocity is discontinuous in this kinematically admissible velocity field (Hosford and Caddell, 2007). Next, to find the changing velocity in region II, consider a small area of material traced out by  $\delta\theta$  at a distance  $r$  from the die center, Fig 4.7. The area of this strip is  $2\pi r^2 \sin\theta \delta\theta$ . Volume conservation, therefore, dictates that the velocity towards the die center at any point along the length,  $r$ , from the entrance to exit of region II is given by equation 4.2.

$$v(r, \theta) = \frac{v_i \lambda^2 \cos \theta}{r^2} \quad (4.2)$$

It follows that the time taken by particle  $A$  to travel through region II, from  $A'$  to  $A''$ , is given by equation 4.3.

$$dt = \frac{dr}{v(r, \alpha)} \rightarrow t_{A'A''} = \int_{\xi}^{\lambda} \frac{r^2 dr}{v_i \lambda^2 \cos \alpha} \rightarrow t_{A'A''} = \frac{1}{3v_i \cos \alpha} \left( \frac{\lambda^3 - \xi^3}{\lambda^2} \right) \text{ for } \theta = \alpha \quad (4.3)$$

Similarly, the time taken for particle  $O$  to travel through region II, from  $O$  to  $O'$ , is given by equation 4.4.

$$t_{OO'} = \frac{1}{3v_i} \left( \frac{\lambda^3 - \xi^3}{\lambda^2} \right) \quad (4.4)$$

Lastly, the time taken for particle  $O$  to travel through region III, from  $O'$  to  $O''$ , is given by equation 4.5.

$$t_{O'O''} = \frac{\xi (1 - \cos \alpha)}{v_o} \quad (4.5)$$

The difference in the time taken for particles  $A$  and  $O$  to travel from initial to final positions ( $A''$  and  $O''$ ) can then be used to solve for the total extra distance traveled by particle  $O$  into the profile, the TWL, shown in equation 4.6.

$$\text{Transverse weld length (TWL)} = v_o \times (t_{AA'} + t_{A'A''} - t_{OO'} - t_{O'O''}) \quad (4.6)$$

The difference in distance particles  $A$  and  $O$  travel into the profile can be reduced by using a billet with a leading concave and trailing convex face, extruded with a concave dummy block. This offsets the initial axial position of  $A$  and  $O$ ; particle  $O$  being shifted further back a distance,  $x_i$ , towards the ram in region I, Fig. 4.6b. The offset distance ( $x_i$ ), which according to the stylized velocity field model above will result in axial alignment of  $A''$  and  $O''$  (TWL=0), is shown in equation 4.7.

$$x_i = v_i \times (t_{AA'} + t_{A'A''} - t_{OO'} - t_{O'O''}) = \frac{\text{Transverse weld length (flat billet scenario: eqn 6)}}{\text{Extrusion ratio}} \quad (4.7)$$

Using the above analysis, a concave dummy block geometry was designed for axisymmetric extrusion of a solid rod with a die angle of  $\alpha=45^\circ$  (see Fig. 4.6b). A mold with a convex forming element of identical geometry, shown in Fig. 4.6c, was machined and used in conjunction with the concave ram to make billets with a concave recess at one end and a convex protrusion at the other end. These profiled billets were then loaded into the extrusion press with the convex end of the billet nested into the concave ram. Multiple billets were then consecutively extruded and the TWLs measured.

Table 4.1: The values of the parameters studied in each of the sets of experiments.

<b>Trials</b>	<b>Extrusion Ratio</b>	<b>Die angle</b>	<b>Friction Coefficient</b>	<b>Profile Shape</b>	<b>Dummy Block &amp; Billet Geometry</b>
<b>Set 1</b>	4, 6.67, 10, 25	Tapered ( $45^\circ$ ), Flat ( $90^\circ$ )	Unlubricated ( $\mu = 0.29$ ), Vaseline ( $\mu = 0.09$ )	Axisymmetric, rectangular	Conventional (flat)
<b>Set 2</b>	4	Tapered ( $45^\circ$ )	Unlubricated	Axisymmetric, rectangular, cross, dual-circle	Conventional (flat)
<b>Set 3</b>	4	Tapered ( $45^\circ$ )	Unlubricated	Axisymmetric	Conventional (flat), Profiled (concave)

#### 4.1.2.4 Experiments

A parametric study was performed on the TWL. The factors studied were the extrusion ratio, die angle, friction coefficient, profile shape and dummy block profile. Table 4.1 summarizes the 35 different experiments conducted. Each experiment was performed three times in order to increase the reliability of the results. The resulting TWLs were measured using high-resolution photography input into IC Measure computer software (The Imaging Source, 2019). The length of the weld was measured from the tip to the point at which the cross sectional area of the old billet was just 5% of the total cross sectional area of the profile. This criteria of 5% area is used in industry as a standard point at which the effect that the transverse weld has on lowering profile strength is deemed to be no longer significant (Mahmoodkhani et al., 2013). For the axisymmetric profiles, longitudinal scalpel cuts along the length of the extruded profile revealed the complete weld geometry. For non-axisymmetric shapes, however, a salami-slicing approach was used to determine the weld geometry (see Fig. 4.8).



Figure 4.8: Incremental cross-sectional “salami-slicing” cuts of the cross profile.



### 4.1.3 Section results

The TWLs measured in this study ranged from 55 mm to 570 mm, increasing over 1000% from a Vaseline® lubricated tapered axisymmetric die with an extrusion ratio of 4, to an unlubricated, flat rectangular die with an extrusion ratio of 25. The effects of the extrusion ratio, die angle and friction coefficient on the TWL are shown in Fig. 4.9. The effect of the profile shape on the TWL is presented in Fig. 10.

The effect of the extrusion ratio was studied on both lubricated and non-lubricated, axisymmetric, tapered and flat die faces. The results from axisymmetric trials in Fig. 4.9 show that as extrusion ratio increases, the weld length increases significantly. The TWL from unlubricated, flat dies increased over 550% from 73 mm on an extrusion ratio of 4 to 430 mm on an extrusion ratio of 25.

The results in Fig. 4.9 also show that the use of the tapered die reduced the TWL in nearly all scenarios. Similarly, the TWL decreased in nearly all the trials where Vaseline® was used to lower the friction coefficient. The influence of lubrication on the TWL was greatest in the case of the tapered dies at higher extrusion ratios. For example, the Vaseline® decreased the TWL associated with the tapered die by an insignificant amount at an extrusion ratio of 4, increasing to a 30% reduction at an extrusion ratio of 25. In contrast, the percent reduction in the TWL caused by using lubrication was relatively constant across different extrusion ratios in the case of the flat dies.

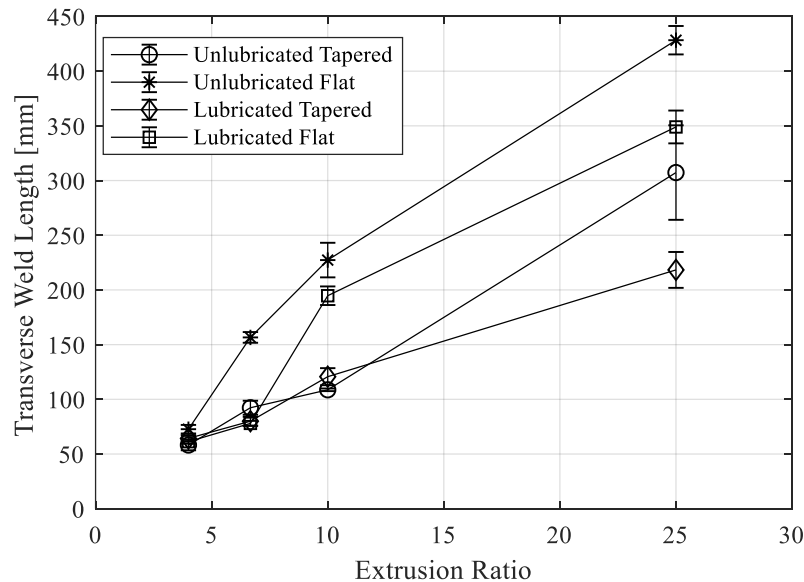


Figure 4.9: Transverse weld lengths in axisymmetric solid profiles at varying extrusion ratios, die angles, and friction coefficients.

The results in Fig. 4.10 show that extruding the rectangular profiles produced longer TWLs than extruding the corresponding axisymmetric profiles of the same extrusion ratio. The amount the TWL increased varied by scenario, from 8% in the case of flat dies at an extrusion ratio of 6.67, to a 110% increase in the case of tapered dies at an extrusion ratio of 10. The second set of profile shape trials included two, more complex profiles at an extrusion ratio of 4; one cross shaped, one dual-circle, as shown in Fig. 4.3. Fig. 4.11 shows the measured TWLs for the various extruded profile shapes when plotted against (a) the ratio of profile perimeter to area, and (b) the minimum section thickness of each profile. These plots

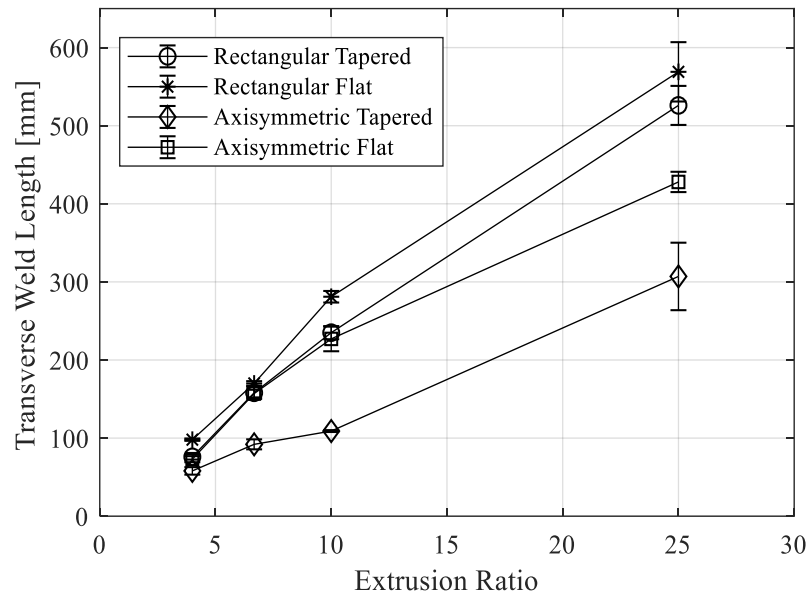


Figure 4.11: Transverse weld lengths in axisymmetric solid profiles and rectangular solid profiles at varying extrusion ratios and die angles.

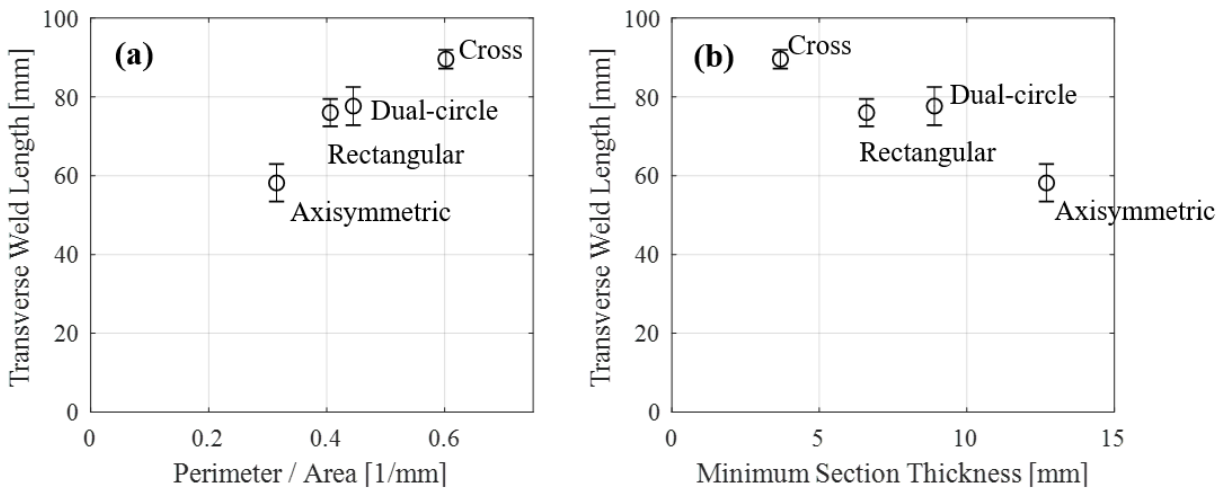


Figure 4.10: Transverse weld lengths against (a) the ratio of profile cross sectional perimeter to area and (b) the profile minimum section thickness. All profiles represent an extrusion ratio of 4.

show that, for the shapes chosen in this research, the TWL increases as the ratio of the perimeter to area increases.

Fig. 4.12 shows that the concave-profiled dummy block and profiled billets produced a TWL of 31 mm, which represents a 44% reduction in weld length from the 55 mm weld that was produced using a flat dummy block and conventional billet geometry. The resultant weld profile is shown to have changed drastically, inverting at the tip.

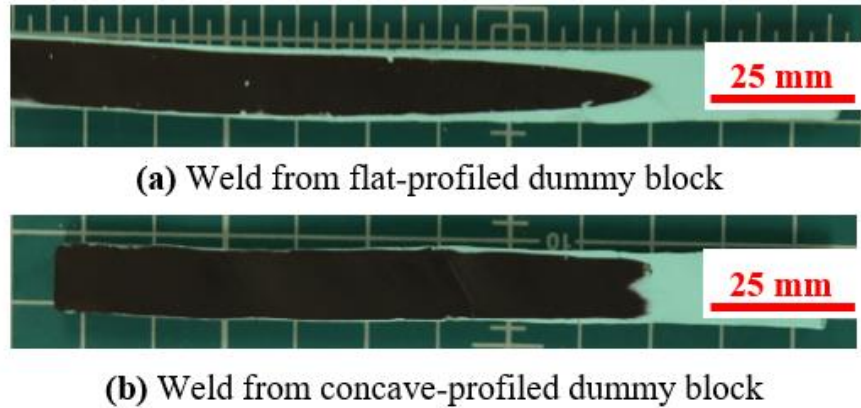


Figure 4.12: Transverse weld profiles produced from (a) flat and (b) concave profiled dummy blocks.

#### 4.1.4 Section discussion

In this section, we discuss the physical reasons behind the experimental trends and the implications for reducing process scrap in industry.

##### 4.1.4.1 Extrusion ratio

The extrusion ratio is a term that equals the cross-sectional area of the press container divided by the cross-sectional area of the extruded profile. A smaller extrusion ratio reduces the TWL by reducing the relative velocity difference between the material flowing at the interior and exterior of the profile (Fig. 4.7). An extruder has limited flexibility for changing the profile geometry requested by a customer; therefore, the extruder can only reduce the extrusion ratio by using a press with a smaller container diameter. Reduced container and therefore billet diameters would, however, reduce plant throughput without a concurrent increase in billet length in order to maintain overall billet volume. A smaller extrusion ratio also reduces the ram force required to push material through the die; however, longer billets would increase the ram force through higher billet-container frictional forces. Chien et al. (2018) recently showed that for AA6063 extrusions at 454°C, decreasing the billet diameter from 254 mm to 203 mm and simultaneously increasing the length of the billet to maintain a constant volume of aluminum resulted in a 1.9% decrease in extrusion load. This would allow for the length of the billet to be increased even further before the maximum load

rating of the press is reached. Chien et al. show that a marginal increase in throughput could be achieved while also decreasing the extrusion ratio and from this research it can be reasoned that the transverse weld scrap amount would also be decreased.

#### 4.1.4.2 Die angle and friction

In industry and the literature, it is often assumed that a flat die forms a dead metal zone (DMZ) with a DMZ angle (equivalent in function to the die angle) of close to  $45^\circ$ . The DMZ is a volume of stationary material at the face of the die over which the billet material shears, allowing it to flow through the die. If it were the case that a flat die forms a  $45^\circ$  DMZ angle, then we would expect that the TWL results of the flat and  $45^\circ$  tapered dies might be similar. However, our results show that using a tapered die significantly reduces the TWL, particularly at higher extrusion ratios. Sectioning partially extruded billets from this work (Fig. 4.13) revealed that the DMZ angle formed on an unlubricated, flat die of extrusion ratio 4 was close to  $45^\circ$  (Fig. 4.13a) but that this DMZ angle greatly increased at higher extrusion ratios (Fig. 4.13b) becoming much closer to a truly square/flat material flow. Elsewhere, Sluzalec (1991) found that the relationship between the DMZ angle and extrusion ratio changes based on the aspect ratio of the billet used (billet length to diameter). He found that for an aspect ratio of 1 (the ratio used in this research), the DMZ angle increases with extrusion ratio. However, as the aspect ratio is increased through an increase in billet length, the DMZ was found to decrease as extrusion ratio increases.

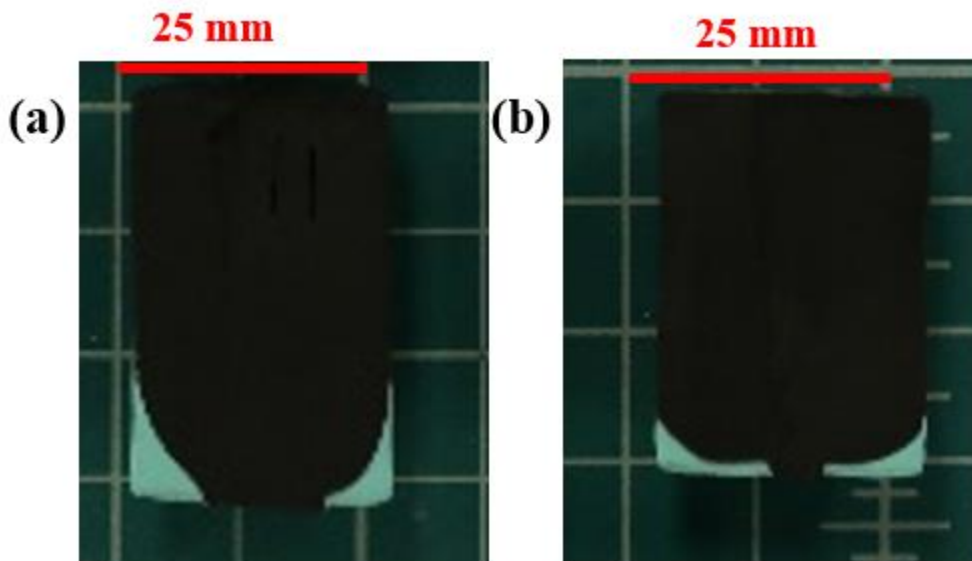


Figure 4.13: Longitudinal cross sectional cut after partial extrusion of second billet to show DMZ of (a) Extrusion ratio = 4, and (b) Extrusion ratio = 25. DMZ is in green. Aspect ratio of billets (diameter : initial length) = 1.

When using flat dies, the effect that reducing the friction has on the TWL is relatively constant across the extrusion ratios; whereas, the effect that reducing the friction has on the TWL when using tapered dies appears to grow with the extrusion ratio (Fig. 4.9). One explanation for this observation, is that the DMZ angle formed behind the flat die increases as friction is lowered, as observed by Sluzalec (1991) for billet aspect ratios of 1. An increasing DMZ angle would act to increase the TWL (analogous to increasing the die angle), and therefore counteracts some of the positive effects of decreasing the TWL through reduced friction. To isolate the effect of friction on TWL (independent of DMZ/die angle) it is therefore recommended to observe the changes in TWL on the tapered dies. This research suggests that adding a lubricant to lower the friction coefficient can significantly reduce TWLs at higher extrusion ratios. However, many extruders are reluctant to use lubricant between the billet and container wall for fear that this could cause surface defects on the extruded profile, including blistering (Shepard, 1999).

#### **4.1.4.3 Profile shape**

The effect of the profile shape on the TWL has not been previously studied. Fig. 4.11 suggests that (for a given cross-sectional area), the TWL scales with the perimeter of the extruded profile cross-section. This may be because a larger perimeter suggests a thinner average section thickness and, locally, this manifests itself as a more extreme material flow; equivalent to a local increase in the extrusion ratio. For example, in the extrusion of the cross profile the old (green) billet can be seen further along the profile in the thin extremities of the cross rather than in the thicker central portion (see Fig. 8). A larger perimeter also causes greater frictional forces, which, as discussed elsewhere, will lead to a higher TWL.

An extruder may have limited opportunities to influence the shape of the extruded profile requested by a customer. However, designers should be fully aware of the material efficiency and environmental implications of their component designs. There is probably some scope for improved profile shapes that reduce the TWL, which can be found through greater awareness of the process scrap ramifications.

#### **4.1.4.4 Dummy block profile**

This article has presented a simple case study that highlights the potential of using profiled dummy blocks and billets to control material flow through the die and to subsequently reduce the TWL. The TWL decreased by 44% in the case study (Fig. 4.12). The reason the TWL did not decrease to zero is because the velocity field used to design the profiled block and billets is an idealization of extrusion and drawing flow through conical dies, neglecting, for example, the effect of friction along the container walls.

Further studies must address the technical feasibility of the profiled dummy block concept across a wider variety of profile shapes as well as the use of real aluminum material rather than a clay proxy. The benefits from reduced scrap generation will have to be reconciled against barriers to industry take-up that

may include the costs of the new dummy blocks and new casting molds or forming apparatus that are needed to make the profiled billets.

#### **4.1.5 Section conclusions**

The removal of transverse welds between consecutively extruded billets is a key material inefficiency in the aluminum extrusion industry. This study has shown the potential to reduce the TWL through reduced extrusion ratios, die angles, friction coefficients, and profile perimeter to area ratios. Additionally, it has been demonstrated that adjustments to the dummy block profile (a previously unexplored design variable) might be an option to further decrease the weld length. Future work will include defining a process window for the profiled dummy block concept considering more realistic extrusion profiles (e.g., hollow non-axisymmetric shapes) and exploring the potential to reduce the TWL while constraining dummy block stresses to the elastic region and minimizing the costs of any new profile-specific dummy blocks and casting molds or forming apparatus.

#### **4.2 Exploring a novel process for reducing aluminum extrusion process scrap using profiled dummy blocks and billets**

Extruded aluminum supply chains are materially inefficient with around 40% of the billet material likely to be scrapped before the profile is embedded in a product. One of the largest sources of process scrap is the removal due to weld integrity concerns of the tongue-shaped transverse weld(s) that forms between consecutively extruded billets (front-end defect). Process setting and die geometry optimization can decrease the weld length (and hence scrapped material) but only by  $\approx 15\%$ . We explore a novel process for significant scrap savings using profiled dummy blocks to generate shorter welds by compensating for the differential metal flow velocities across the billet cross-section as the billet flows through the die ports. We develop a design process for defining the profiled dummy block shape. For a given part and press, we first define an ideal dummy block shape by extracting the velocity field from finite element simulations of the conventional process and assuming perfectly rigid tooling. Next, we rationalize the tool shape using stress and deflection limits for the dummy block (preventing plastic deformation and interference with the container wall) and ductile damage limits for the billet to prevent cracking. We then simulate the likely effect of the rationalized dummy block design on back-end defect removal. The methodology is demonstrated for four profiles of increasing complexity: solid round and rectangular bars, a square-tube hollow, and a complex multi-hollow profile. The process' potential is evaluated experimentally using billets machined to match the ideal dummy block shape. The results show that dummy blocks with a profile-specific design can achieve weld length reductions  $>50\%$ . We also demonstrate that multi-profile tooling can deliver scrap savings across a family of similar profiles.

### **4.2.1 Section introduction**

The transverse weld is a metallurgical defect that forms between consecutively extruded billets in the direct extrusion process. It can be the most significant source of extrusion scrap, representing an average loss of 20% in standard extruded profiles (Oberhausen et al., 2022). It is formed because the initially planar billet-billet interface in the extrusion container elongates as the material passes through the die (Figure 4.15a). In complex, multi-hollow profiles, as are common in the fast-growing automotive extrusion market (Aluminum Extruders Council, 2023), the interface will form multiple tongue-shaped welds, with one tongue-shaped weld for each die port. The elongated interface must be removed for many applications due to its weak mechanical properties (den Bakker et al., 2016; Oberhausen and Cooper, 2023; Ford Motor Company, 2013). Removal of the weld occurs after billet extrusion (Superior Extrusion, 2022), effectively reducing the productivity of the capital intensive press (Can Art, 2021). A reduction in the transverse weld length could, therefore, reduce environmental impacts and save time and money (Oberhausen et al., 2021).

The length of profile containing the transverse weld has traditionally been estimated in industry using heuristics. Most common is the ‘1.5 rule’, whereby the volume of the profile containing the weld is conservatively estimated at 150% of the volume of billet contained within the filled die minus the volume of the die’s dead metal zones (Jowett et al., 2008; Reggiani et al., 2020). Academics and some industry extruders have more recently used finite element models (FEMs) for weld length prediction. Reggiani and Donati (2018) performed a study on hollow extruded profiles to compare the accuracy of these competing methods and concluded that numerical methods offer more accurate prediction of the weld length with an average error of 9.8% versus 13.1% for the 1.5 rule, but at the cost of significant computational time of up to a week. FEMs have then been used to predict the reduction of the transverse weld length from process parameter (e.g., temperature, ram speed, friction conditions) and die geometry optimization. Oberhausen et al. (2021) report that the weld length reductions achieved by such optimizations do not exceed 15%. Oberhausen et al. then show that additional savings might be achieved by changing the geometry of the initial billet-billet interface in the press container (Figure 4.15b); however, they only demonstrate it for a round bar profile using plasticine clay billets. The goal of this current study is to further evaluate the profiled dummy block concept.

#### **4.2.1.1 Traditional dummy block design**

The dummy block is a sacrificial tool between the hydraulic ram (stem) and billet. It is subjected to the wear and tear of friction during each extrusion stroke. Traditionally, “floating” dummy blocks were used. These steel blocks were pushed out of the container at the end of each stroke and recirculated (Robbins et al., 2016). “Fixed” dummy blocks, attached firmly to the stem, were developed in the 1980s and have

become the industry standard ( Figure 4.14). They have led to increased press productivity by avoiding the need to cycle the dummy block from the front to the back of the press after each stroke. Further improvements led to the “expanding” dummy block, featuring an outer ring that intentionally expands during the extrusion stroke due to a pressure activated bevel (Thumb Tool and Engineering, 2021). This expansion reduces the gap between the outer radius of the dummy block and the inside of the container from around 1 mm to around 0.1 mm (Dyla, 2019; Thumb Tool and Engineering, 2021). The expansion of the dummy block has the benefit of avoiding backward extrusion when pushing against the billet, while the contraction has the effect of reducing friction and therefore also forces during ram retraction (Robbins et al., 2016; Thumb Tool and Engineering, 2021). These advanced dummy blocks do, however, introduce new failure modes. For example, the contact point on the expanding joint is subject to very high stresses leading to fatigue and plastic deformation (Dyla, 2019; Thumb Tool and Engineering, 2021). The blocks often deform after the first few extrusion strokes and then require some machining of the outer radius of the expanding face to maintain the specified gap with the container (Thumb Tool and Engineering, 2021; Robbins et al., 2016).

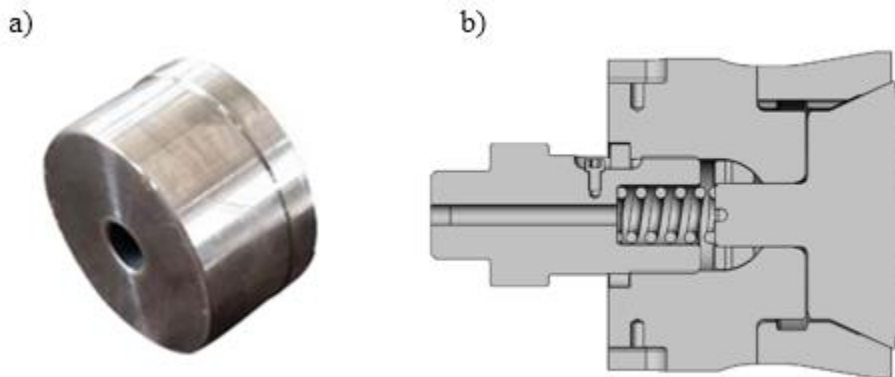


Figure 4.14: A (a) floating and (b) fixed dummy block (Robbins et al., 2016).

Dummy block designers must contend with the desire from the extrusion industry to use higher ram forces, which can push larger billets and extrude increasingly complex profile designs from higher strength alloys (Aluminum Extruders Council, 2022). Currently, the same dummy block on a press is used to extrude a wide variety of different profiles. Robbins et al. (2016) have discussed the prospect of dummy blocks customized to families of profiles for further optimization of the container-dummy block clearance and structural design.

#### 4.2.1.2 The profiled dummy block and billet concept

Figure 4.15b shows the proposed extrusion process for a round bar profile. The profiled (fixed and solid) dummy block and billet is designed to generate shorter welds by compensating for the differential



metal flow velocities across the billet cross-section as the billet flows through the die. The result is a near-flat transverse weld, requiring a minimal length of profile to be scrapped. For more complex profiles, asymmetric dummy block concavities will be required, or multiple concavities for the case of hollow profiles extruded using porthole dies. In the latter case, the number of concavities on the dummy block surface will, at most, equal the number of die ports. A profiled dummy block designed for a specific profile and press would maximize scrap savings; however, the requirement to change the dummy block as well as die when extruding a new profile may add a significant burden to the extruder; therefore, we can also consider multi-profile dummy blocks that deliver scrap savings over a family of similarly shaped profiles. The profiled billets may be created by casting, ex-situ forging of conventional billets before being loaded into the extrusion chamber, or in-situ upsetting/forging as part of the initial extrusion stroke with additional gas escape channels in the dummy block/forging block concavities to prevent air entrapment. The profiled dummy block concept requires the absence of the butt shear (typically used to remove the last 10% of the billet that contains the back-end defect (Johannes et al, 1996; Lou et al., 2017)) to preserve the profiled billet-billet interface. Figure 4.15b depicts one method of then dealing with the back-end defect: extrusion of the back-end defect to a consolidated quantity of scrap in front of the transverse weld, which then requires scrapping of that section of profile. We hypothesize that profiled dummy blocks consolidate the back-end defect into a smaller volume of profile than would otherwise be the case. Alternatively, back-end defect removal can rely on using peeled billets or Dick’s method of extrusion (Sheppard, 1999), whereby a smaller diameter dummy block is used to form the oxide-rich billet skin into a “skull” in the container that must be removed using an additional ram stroke using a clean-out block.

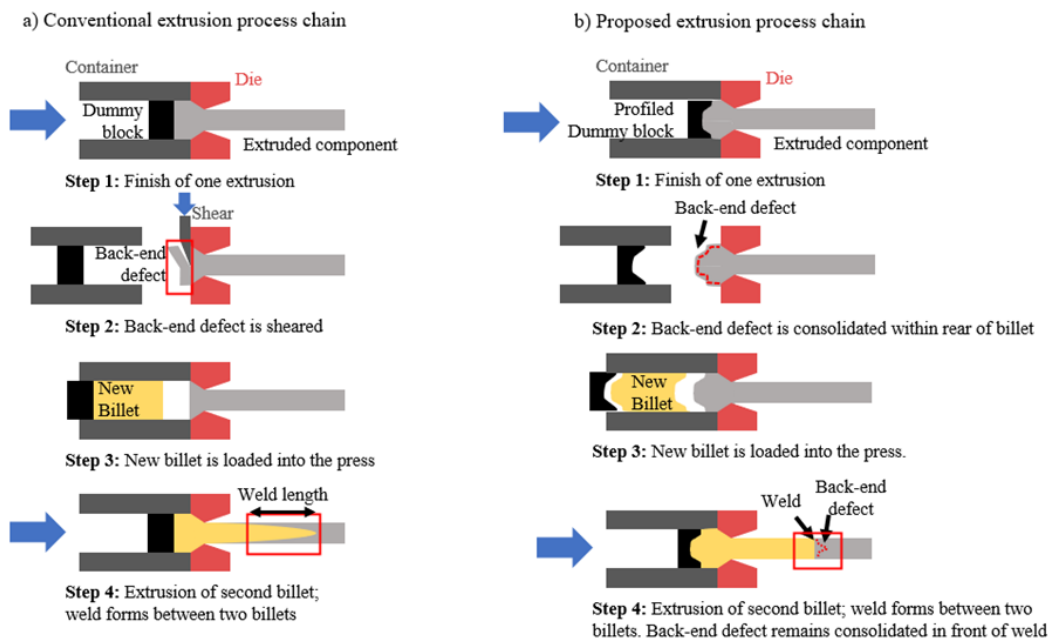


Figure 4.15: The (a) conventional and (b) proposed extrusion process chains.

#### **4.2.1.3 Scope of this article**

The goal is to develop a profiled dummy/forging block and billet design methodology (assuming the profiled billets are created using ex-situ hot forging) and then demonstrate the methodology by designing dummy blocks for profiles of increasing complexity: a round bar, rectangular bar, square hollow, and complex hollow profile. As a first step towards evaluating the design methodology, we then extrude billets that have been machined to the ideal profiled geometry to assess the potential transverse weld length reductions. We also assess the potential to use the same profiled dummy block and billet geometry to reduce the transverse weld across a family of similar profiles, avoiding the need to switch the dummy block with every die change.

#### **4.2.2 Design process for profiled dummy blocks that deliver front-end scrap savings**

Figure 4.16 shows the proposed design process, which relies on multiple rounds of FEM. First, the geometries of idealized (rigid) dummy blocks and profiled billets are determined that would deliver a desired transverse weld length reduction. Next, these idealized designs are rationalized through a series of steps, beginning with a geometric rationalization ensuring that the profiled dummy blocks and billets can mate during the extrusion stroke and then decouple during ram extraction. The dummy block geometry is then further adjusted to ensure no plastic and minimal elastic deformation of the profiled dummy block based on a revised FEM of the extrusion process that models the dummy block as a deformable body. Finally, a FEM of the ex-situ billet hot forging process ensures that the ductile damage endured by the billet will not cause billet cracking.

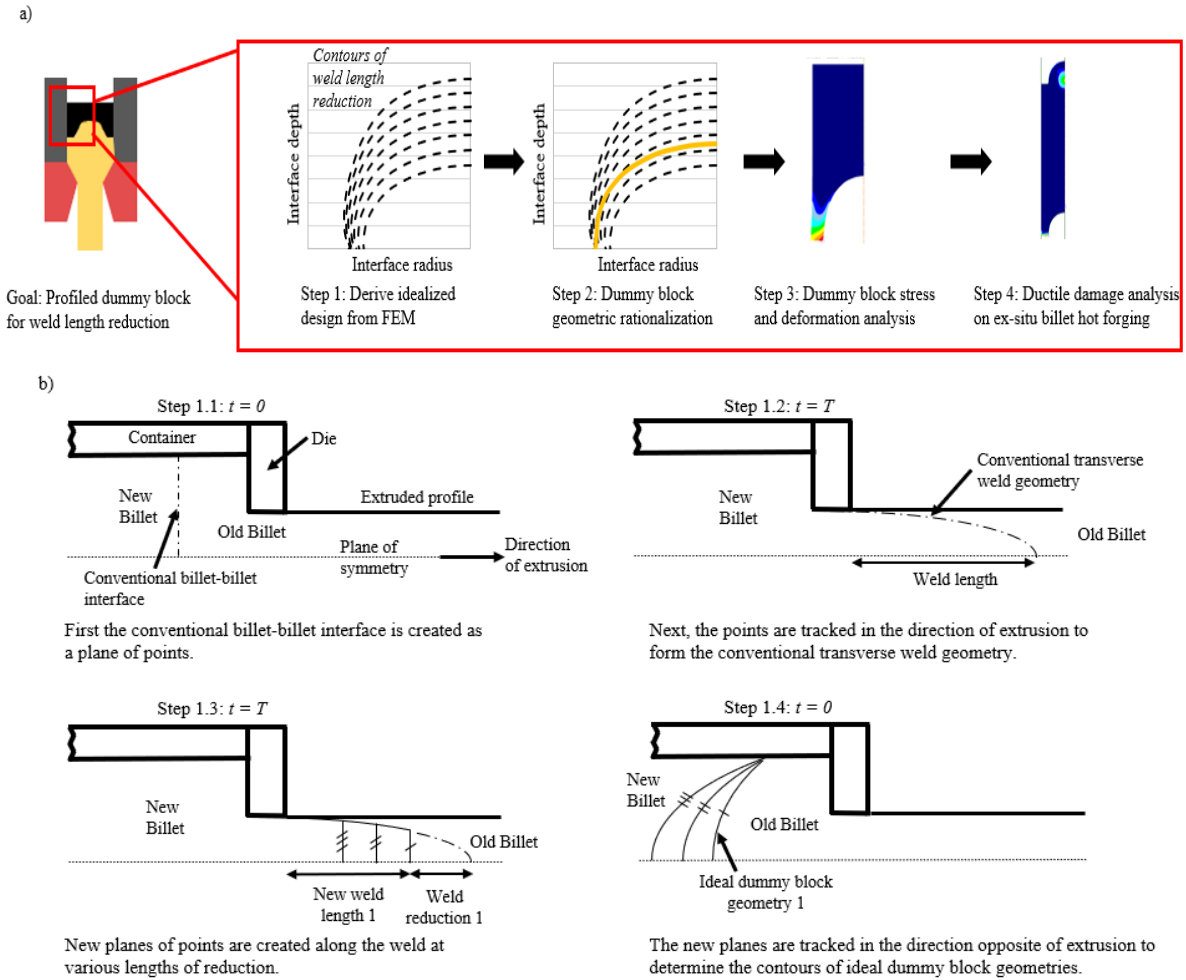


Figure 4.16: (a) Profiled dummy block and billet design process. (b) The velocity field method for generating the idealized profiled dummy block and billet geometry.

#### 4.2.2.1 Step 1: Deriving the geometry of an idealized (rigid) profiled dummy block

For a given profile and press, a FEM of the conventional extrusion process is used to generate the steady-state velocity field for points throughout the aluminum workpiece. Using MATLAB, a point in the workpiece ( $P$ ) can then be iteratively tracked through the extrusion process using Equation 4.8, where  $v_{P,old}$  is the velocity vector attributed to the initial position of the point during each increment and  $\Delta t$  is the modeled time increment. For every increment,  $v_{P,old}$  is calculated using linear interpolation from the velocity vectors defined for the four neighboring nodes in the relevant tetrahedral element.

$$P_{new} = P_{old} + v_{P,old}\Delta t \quad (4.8)$$

$$P_{old} = P_{new} - v_{P,new}\Delta t \quad (4.9)$$

This ability to easily track the position of points through the extrusion process is used to derive an ideal billet-billet interface geometry for minimizing the transverse weld length, as shown in Figure 4.16b. A plane of points corresponding to the conventional flat billet-billet interface in the container is tracked for time  $T$  to define the conventional weld geometry. Next, a new plane of points is defined corresponding to the flattened end of a shortened transverse weld. This new plane of points is then tracked for time  $T$  backward through the velocity field using Equation 4.9 to define the original shape of the billet-billet interface that results in the shortened transverse weld.

#### **4.2.2.2 Steps 2-4: Rationalizing the dummy block design**

*Step 2:* The idealized geometry generated using Step 1 will often be impractical to implement; therefore, the profiled dummy block and billet designs undergo a series of rationalizations. First, the shape is adjusted to ensure geometric compatibility for mating and decoupling between the dummy block and billet. This adjustment is aided by generating a design map showing how different geometry contours relate to different weld length reductions (see Step 2 in Figure 4.16a). By adjusting the dummy block design to cross these contours the final weld length reduction will correspond to the lowest weld length reduction contour touched by the adjusted design. In Figure 4.16a (Steps 3-4), there are multiple iterations of ideal dummy block derivation performed across a range of weld length reductions to create a map of potential design contours. The maps generated through these iterations are useful in understanding how changes to the geometry of the ideal profile will affect the performance of the dummy block in reducing the weld length. Increasing the cross-sectional area of the dummy block at the billet face will result in a region which does not follow the desired ideal curve. The design should be carried out carefully, as to not cross contours of lower reduction, or of elongation, as designs for reductions of  $>100\%$  will cause the location of critical radius marking the end of the weld to be relocated further back into the extruded profile.

*Step 3:* The next step is to ensure that the designed dummy block geometry does not experience plastic deformation or excessive elastic deformation under the pressure of the extrusion process. An elastic deformation limit is used equal to a maximum of 1 mm of radial expansion on the outside of the dummy block. This elastic deformation limit prevents significant interference between the dummy block and container wall and is based on interviews with extrusion tooling industry experts. The stresses and subsequent deformation on the dummy block can be reduced by adjusting to lower reduction designs (thickening the outer dummy block wall) guided by the contour map.

*Step 4:* In this article, we assume the profiled billets could be hot forged from conventional flat-end cylinders. To prevent cracking, the ductile damage imparted on the billet during forging must be less than

the critical value to cause a crack to form. Christiansen et al. (2017) find that the *Cockroth-Latham (1968)*, *Ayada (1987)*, and *Shear* (Christiansen et al., 2016) models of ductile damage (Equations 4.10-4.12) can predict the onset of cracking in cold aluminum samples with their relative accuracy determined by the predominant stress state in the metal. The Cockcroft-Latham and Ayada criteria predict damage accumulation from the relationship between the largest principal ( $\sigma_1$ ) and hydrostatic ( $\sigma_m$ ) stresses, respectively, with the effective stress ( $\bar{\sigma}$ ) and effective strain ( $\bar{\epsilon}$ ). The Shear criterion uses the shear stress ( $\tau$ ) and strain ( $\gamma$ ). Following on from Christiansen et al. (2017), we recommend finding the critical values for these criteria that cause cracking in the alloy of interest at the temperature of interest by conducting hot compression tests on a range of sample geometries and determining the corresponding criteria values at the onset of cracking via FEM of the process. Figure 4.17 below shows the onset of cracking that was observed by Christiansen et al.

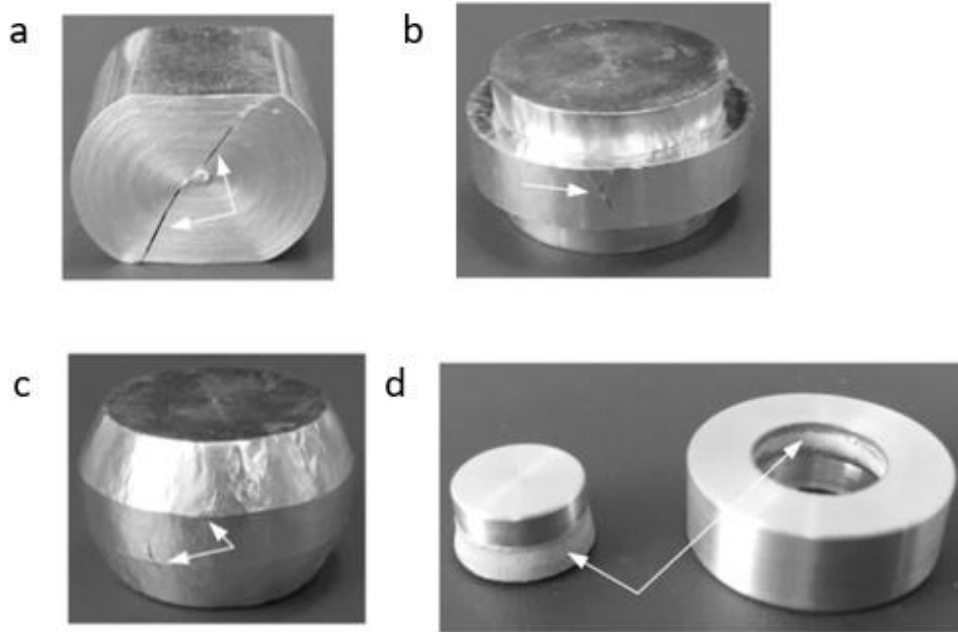


Figure 4.17 Onset of cracking observed on room temperatures (a) cylinder, (b) flange, (c) taper, and (d) shear samples in Christiansen et al. (2017).

These critical criteria limits for the onset of cracking can then be used to evaluate whether hot forging of the given profiled billets design would cause cracking by evaluating the criteria values during hot forging using a FEM of the process. If cracking is predicted to occur, a more modest reduction in weld length can be designed that will reduce the depth and width of the profiled dummy block concavities.

$$D_{Cockroth-Latham} = \int \frac{\sigma_1}{\bar{\sigma}} d\bar{\epsilon} \quad (4.10)$$

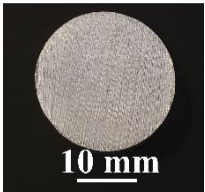

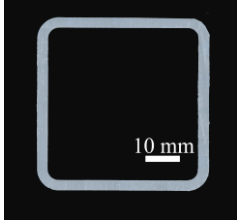

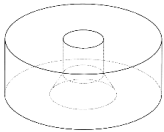
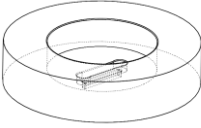

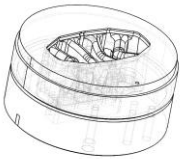
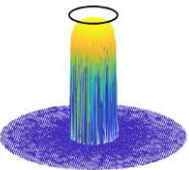
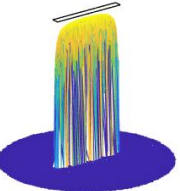
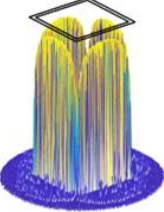
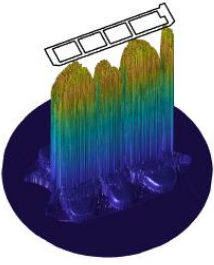
$$D_{Ayada} = \int \frac{\sigma_m}{\bar{\sigma}} d\bar{\epsilon} \quad (4.11)$$

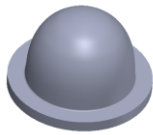

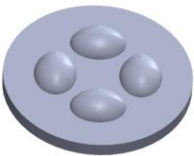
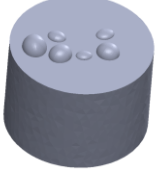
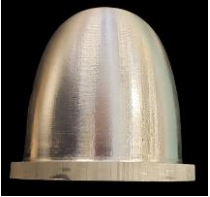

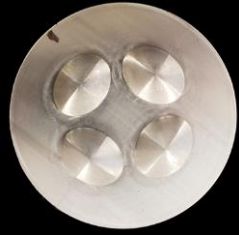
$$D_{Shear} = \int \frac{\tau}{\bar{\sigma}} d\gamma + \int \frac{3\sigma_m}{2\bar{\sigma}} d\gamma \quad (4.12)$$

### 4.2.3 Testing the design method

As part of the evaluation, we follow the methodology outlined in Section 4.2.2 to design profiled dummy blocks and billets for both a simple round bar profile and a complex, multi-hollow profile. We then experimentally test the first two steps of the design methodology (Figure 4.16a) by extruding profiled billets (in this case machined rather than hot forged) for round bar, rectangular bars, and a square hollow tube. Table 4.2 presents the profiles and billet sizes examined in this study.

Table 4.2: Profiles and billet sizes examined in this study

Profile	AA6061 Round bar	AA6061 Rectangular bar	AA6061 Square hollow	AA6082 Multi-hollow profile
Profile image				
Die image	Die entrance  Die exit	Die entrance  Die exit	Die entrance  Die exit	Die entrance  Die exit
# of die ports	1	1	4	7
Tongue-shaped weld geometry (generated from FEM)				

Conventional weld length (mm)	500	5250	1000	1000
Billet diameter (mm)	Ø88.9 (3.5")	Ø152.4 (6")	Ø88.9 (3.5")	Ø228.6 (9")
Billet length (mm)	203.2 (8")	800 (31.5")	203.2 (8")	1120 (44")
Profile dimensions (mm) & Extrusion ratio	Base case: Ø23.08 & 15 Small: Ø 16.18 & 30 Large: Ø27.94 & 10	(6.06 x 60.6) & 50	(41 x 41 outer dimensions) & 15	(26 x 142 outer dimensions) & 26
Billet temperature (°C)	425	530	425	493
Profiled billet design (3D model)	 Round bar profile-specific design 2			
Profiled billet design (experiment)	 Round bar design 2			Not tested experimentally due to unavailability of the press & die for testing

#### 4.2.3.1 Step 1: The geometry of an idealized (rigid) profiled dummy block

For each profile shown in Table 4.2, a FEM was produced using Altair Inspire Extrude Metals (Altair Engineering, Inc., 2023) and the velocity field was then extracted from the FEM results. The model was run using an Augmented Lagrangian Eulerian (ALE) solver, combining the Updated Lagrangian and Eulerian methods through a two mesh system (Walters et al., 2012). A non-distorting computational reference mesh fixed only in the extrusion direction facilitates the FEM calculations and is updated according to the Lagrangian method in the plane perpendicular to the extruding direction. A second, material reference mesh follows the material more closely, distorting as the material is deformed through the extrusion die. The models were created with a ‘fine’ billet mesh, equating to a tetrahedral element density ranging from approximately a 1 mm spacing in the die region up to 15 mm at the back of the billet. A time step of 0.1 seconds was used for all simulations. The accuracy of the FEMs was validated by comparing the measured ram forces and weld geometries to the simulated ram forces from Altair and the simulated weld geometry via the velocity method outlined in Section 4.2.2.1. All measured and simulated ram forces and weld geometries for conventional extrusion were within  $\pm 10\%$  and  $\pm 5\%$  respectively. The weld length is determined in this work to be from the weld nose to the length that the new billet area exceeds 95% of the cross-sectional area (Oberhausen et al., 2021).

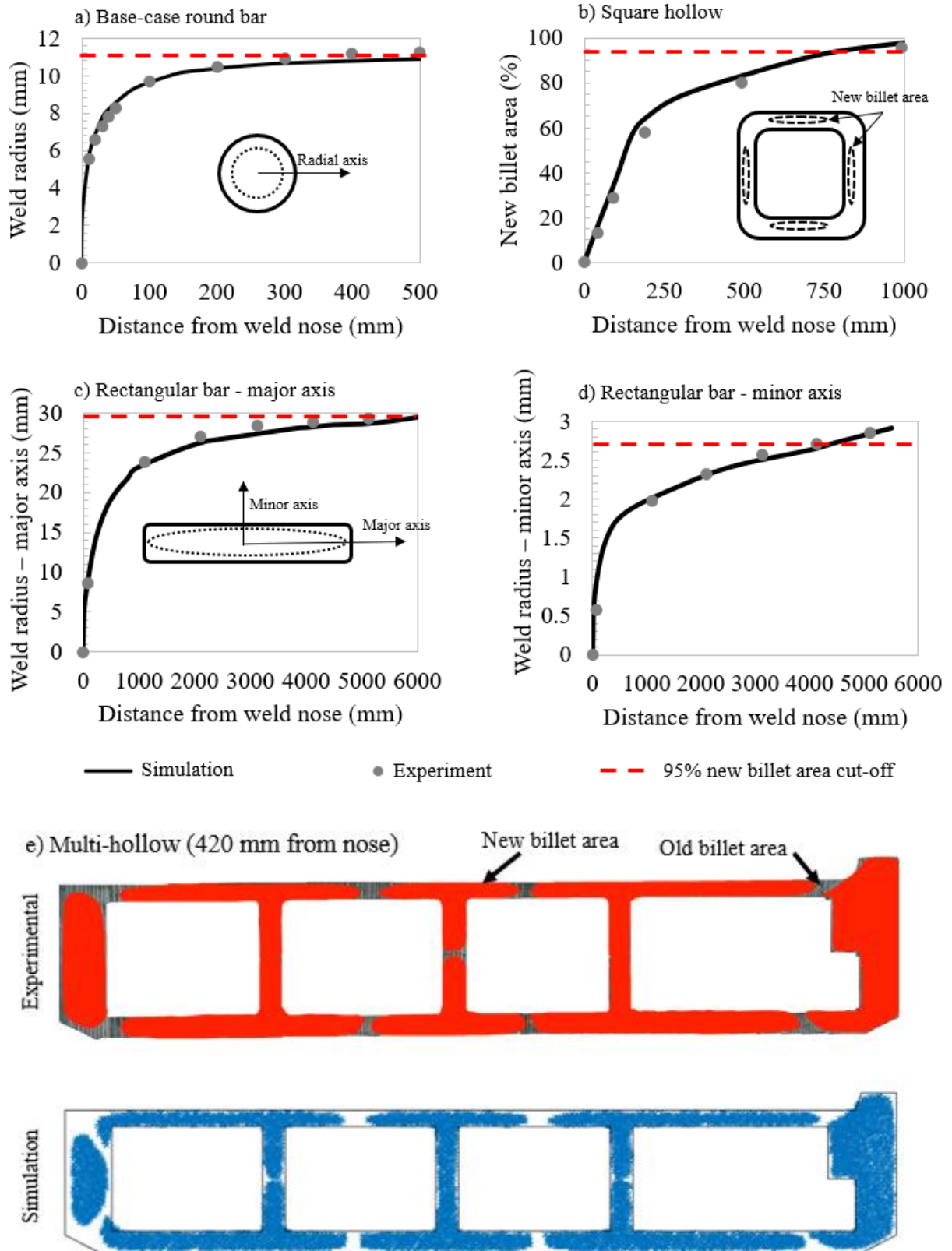
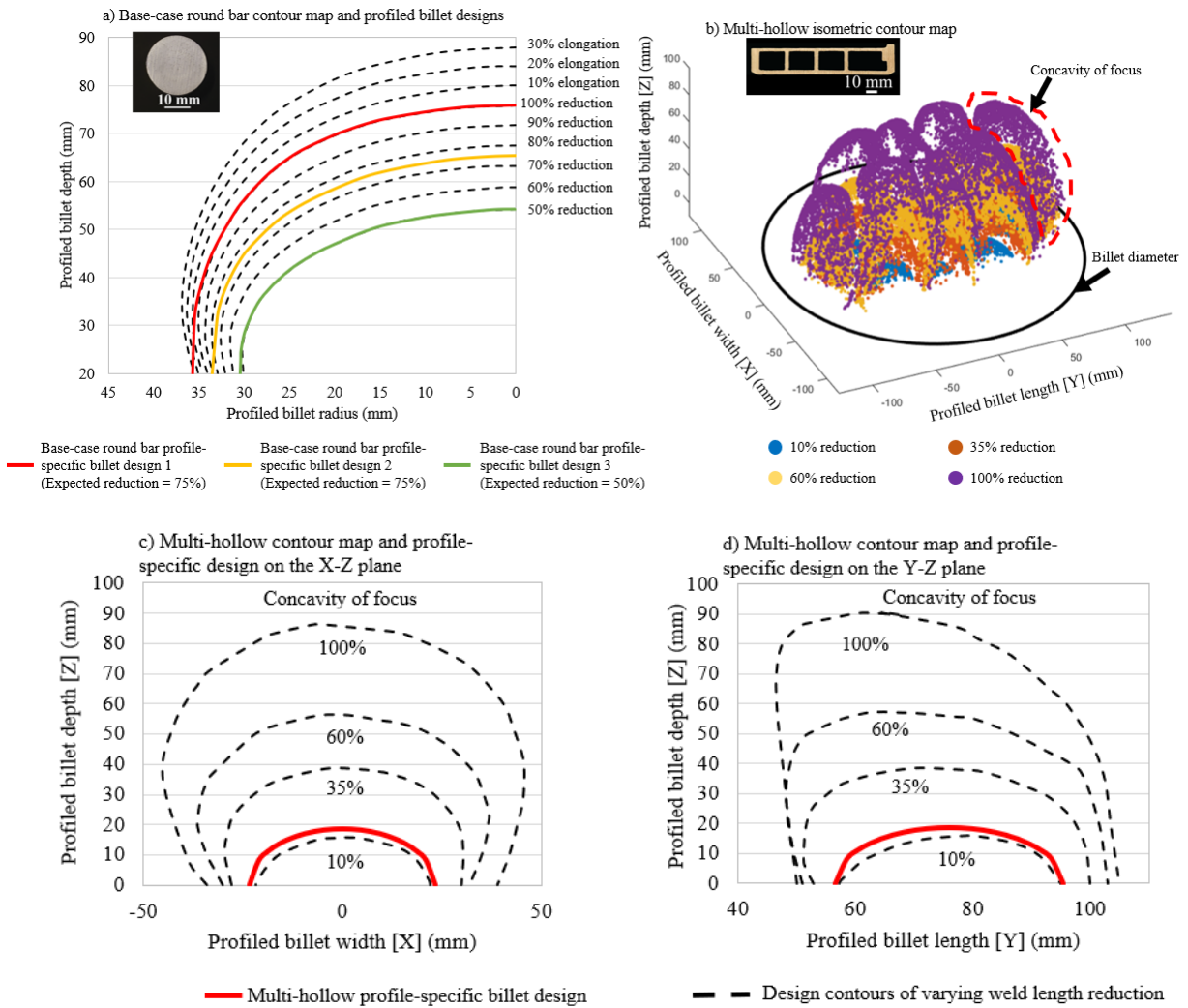


Figure 4.18: Comparison of experimental and simulated weld geometries on the (a) base-case round bar, (b) square hollow, (c and d) rectangular bar, and (e) multi-hollow profiles.



Extracting the velocity fields from these FEMs, and using the approach outlined in Section 2.1, design contour maps were created that relate the geometry of the profiled dummy blocks and billets to the expected weld length reduction. Figure 4.19 shows the design maps for the base-case round bar profile (requiring a single large axisymmetric cavity), the multi-hollow, where 7 separate concavities are required, the rectangular bar and the square hollow profiles.



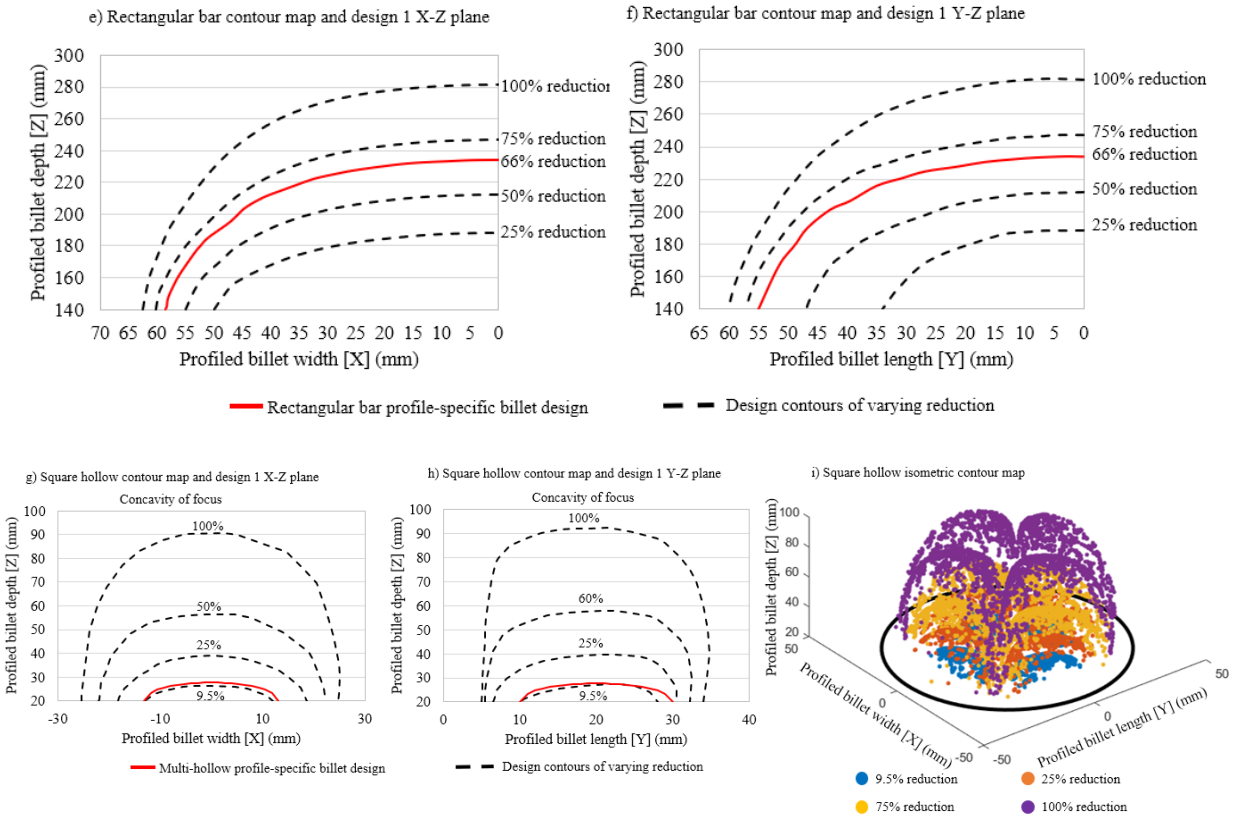


Figure 4.19: Contour maps with plotted profile-specific billet designs for the (a) base-case round bar, (b, c, and d) multi-hollow, (e and f) rectangular bar, and (g, h and i) square hollow profiles.

#### 4.2.3.2 Step 2: Geometric feasibility

The profiled dummy block and billet geometry is adjusted to ensure geometric compatibility for mating and decoupling between the dummy block and billet. The colored lines on Figure 4.19 show the rationalized profiles. For the base-case round bar profile (Figure 4.19a), a curve following the contour of 100% reduction is chosen as profile-specific billet design 1. The curve is adapted with a fillet which spans the 25% elongation line, to open the entrance to the concavity. Profile-specific billet design 1 is therefore expected to result in a 75% reduction of the weld length; 100% reduction – 25% elongation. Profile-specific billet design 2 is created which begins on the 75% reduction contour and has a fillet which ends at the 90% reduction contour. Profile-specific billet design 2 is therefore expected to result in a 75% reduction. For the multi-hollow profile, designs near and above a reduction of 35% interfere with neighboring concavities, leading to impractically thin walls in the profiled dummy block and billet. Therefore, a mild reduction of 10% is chosen for its relative geometric simplicity.

#### Experimental trials using profiled billets

The geometrically feasible designs created at this point were chosen to be used for the experimental trials. At this stage of development, the experiments are run with pre-machined profiled billets which act

as a proxy for the dummy block profile (Figure 4.20). In this manner, the results of this work were focused on the evaluation of the weld length reduction of the profiled dummy block design, rather than the production of functional dummy blocks. The rectangular bar profile-specific billet design was created for a reduction in weld length of 66%, and the square hollow was designed for a 9.5% reduction. The pre-machined billets for all profiles were designed as two-piece billets. The front piece of each assembly is a flat cap containing the designed convex profile. The backpiece then has an identical concave profile machined out for the cap to mate into. Additionally, a two-piece billet pair with flat faces and identical billet lengths is extruded for each profile to create a baseline weld geometry. The round bar and hollow square profile billets were produced with a 7 mm cap (Figure 4.20b). Combined with shortened butt length of 13 mm left from the previous billet, this created a billet-billet interface that began at the standard 20 mm length from the die entrance. The rectangular bar profile was made with a 140 mm cap (Figure 4.20d). These billets were extruded on a side loading press, and required the two-piece billet assembly to rest centered on a 330 mm billet with a minimum total billet length of 460 mm. A length of 140 mm was the minimum that satisfied these center of gravity requirements.

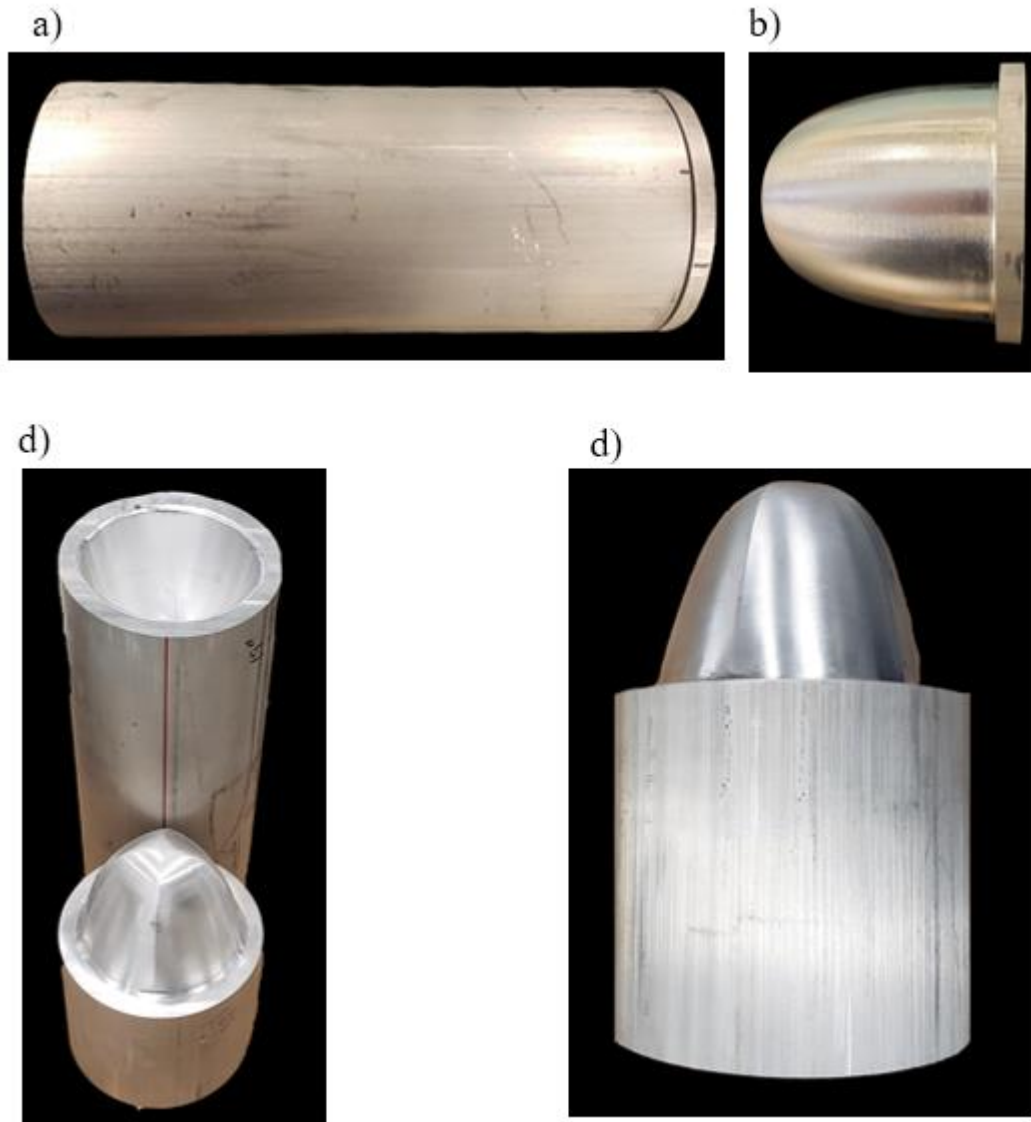


Figure 4.20: The two-piece billet assemblies for the (a and b) round bar and (c and d) rectangular bar profiles.

#### Experiments on a multi-profile tooling concept

To understand the effect of profile-specific designs across a family of profiles, the base-case round bar profile-specific billet design 2 can be plotted against the design contours of a small and large round bar profile. Figure 4.21 shows that the profile-specific billet design 2 for the base case round bar profile should produce weld length reductions of 54% in the smaller round bar, and 47% in the larger round bar (from an 82% reduction at the nose and a 35% elongation at the cut-off).

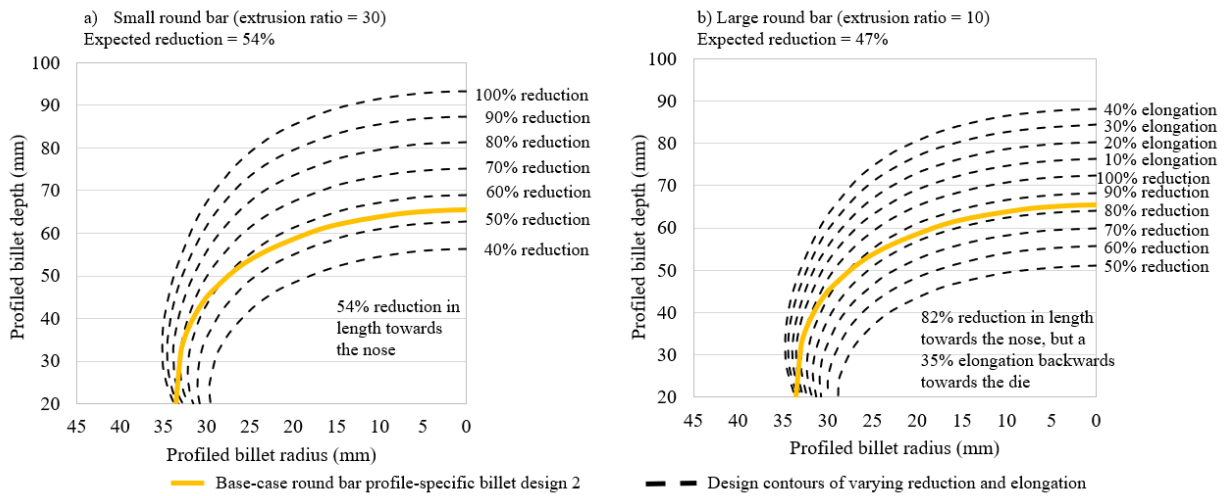


Figure 4.21: The base-case round bar profile-specific billet design 2 plotted against the contour maps of the (a) small and (b) large round bar profiles.

#### 4.2.3.3 Step 3: Preventing Dummy block plastic deformation and limiting elastic deformation

Using the profiled dummy block design that results from Step 2, de-coupled FEM analyses using DEFORM® (2023) were used to assess the stresses and strains present on the dummy blocks for the base-case round bar and multi-hollow profile under extrusion loads. A de-coupled analysis was chosen in place of a single, coupled simulation with both deformable billet and tool to decrease the simulation time. The de-coupled model is first run with the dummy block, container and die as rigid solids, and the extrusion billet as a plastically deformable object. The simulation is run to die-break through, and then the step with the peak ram forces is extracted. Next, this step is used to create a new simulation in which the dummy block is converted to an elasto-plastic body and the forces experienced by the back of the billet are interpolated onto the dummy block's face. Then, all objects except the dummy block are removed and the simulation is run until equilibrium to analyze the response of the tool to the interpolated forces. The billet mesh is generated utilizing the mesh-window function to create a mesh with several different regions of density. The regions within the die, experiencing significant deformation, have a fine mesh (tetrahedral elements with a length roughly equal to 1% of the billet radius) and the areas undergoing minimal deformation, such as the middle of the billet (by length) in the container, have a coarse mesh (3-10% of the billet radius). This meshing strategy maintains accuracy, while reducing the total number of necessary elements and therefore also simulation time. The back face of the billet is meshed with fine elements (1-2% of the billet radius) for greater resolution in dummy block force interpolation. The total number of elements is approximately 10,000 for the round bar profile, and 2 million for the multi-hollow profile. In the model used to assess the dummy block response, the block is meshed with a region of fine (1-2% of the

billet diameter) elements on the billet facing third, and a region of coarser elements (5% of the billet diameter) on the remaining two-thirds, resulting in approximately 2,000 and 500,000 elements on the round bar and multi-hollow dummy block respectively.

Each step in the simulation represents a maximum dummy block displacement of 0.0005% of the billet’s length. This step size is reduced in cases where the simulation cannot be reconciled with a jump of this size, or when significant distortion of the mesh occurs as a result of the deformation experienced within the die. Distortion is considered significant at a threshold of 70% element penetration into any of the present rigid bodies. This typically occurs in the die region due to the smaller element length.

Contact interactions are generated on the billet with the dummy block, container and die. The container and die contacts are assumed to be sticking friction (a friction coefficient of  $m = 1$  where the frictional shear stress  $\tau = mk$ , and  $k$  is the aluminum billet shear yield stress), and the ram contact is assumed to be frictionless as lubricant is used on the dummy block – billet interface (Can Art, 2021). The simulation is run as isothermal and the material properties of the billet at the respective extrusion temperature are selected from a list built into DEFORM®: AA6061 (Ding et al., 2021) for the round bar and AA6082 (Heinemann, 1961) for the multi-hollow profile. The boundary conditions include just the restriction of the tri-axial velocities on the back face of the dummy block to prevent movement of the block. The dummy block is given elasto-plastic material property data for TQ1 steel at the desired temperature (TopSteel, 2023).

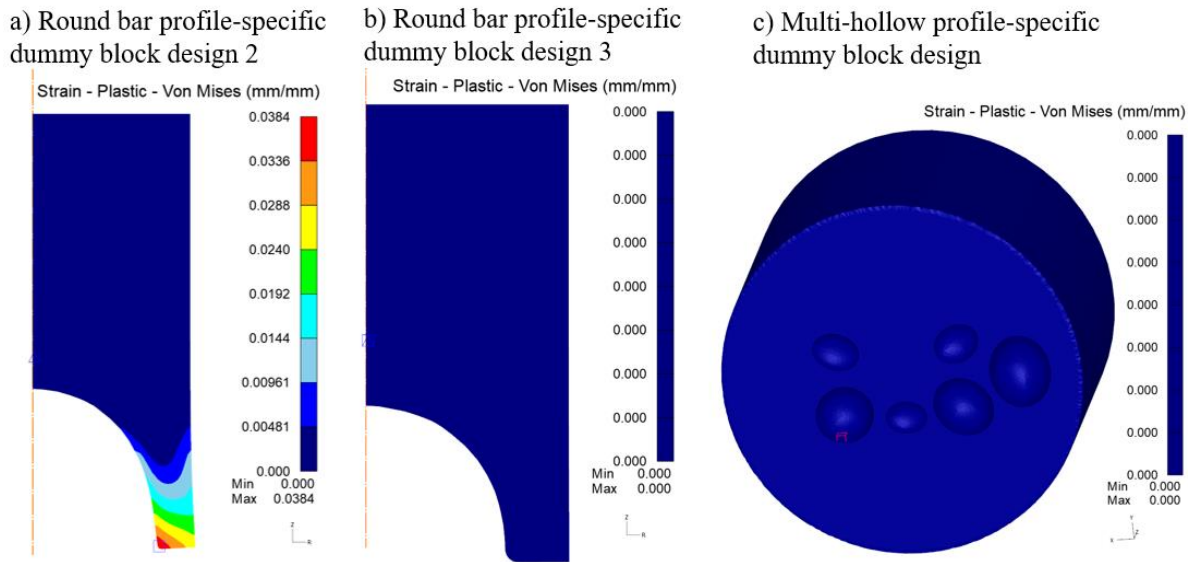


Figure 4.22: The simulated plastic strain expected on the (a) base-case round bar profile-specific dummy block design 2 and (b) base-case round bar profile-specific dummy block design 3, as well as the (c) the multi-hollow profile-specific dummy block design.

Figure 4.22 shows the plastic strains expected on the round bar and multi-hollow designs. The plastic strain expected on the base-case round bar profile-specific dummy block design 2 is non-zero (Figure 4.22a); 3.8% radial plastic strain is expected on the thin dummy block edge, exhibiting about 1.6 mm radial

displacement. We therefore iterate on the round bar design, lowering the reduction to 50% of the conventional weld length, adapted to be geometrically feasible. After this iteration the base-case round bar profile-specific dummy block design 3 experiences zero plastic strain (Figure 4.22b) and just 0.1 mm of elastic radial displacement. The multi-hollow design also achieves zero plastic deformation (Figure 4.22c) with only 0.2 mm of elastic radial deflection for the 10% reduction design and is therefore left unchanged.

#### **4.2.3.4 Step 4: Preventing billet cracking in hot forging of the profiled billet**

First, it is necessary to determine the value of damage that would occur during billet forming. Simulations were run to model a traditionally flat, full-length, AA6061 billet being forged at the extrusion temperature (425°C) such that the top platen was identical to the dummy block geometry and was pressing the billet into the negative (convex) shape on the bottom platen. The contact interaction between the billet and container wall was modeled as sticking friction. The contact interactions between the billet and the dummy block and bottom platen were modeled as frictionless due to the use of lubricant already being typical on the dummy block-billet interface (Can Art, 2021). Friction forces could be reduced by using a double-action forging process that pushes on the material simultaneously from the top and bottom. Figure 4.23 below shows the maximum damage values that occur during profile billet hot forging from a flat-end cylinder for the base-case round bar profile-specific billet design 3. Both the Cockrath-Latham, as well as the Ayada criteria predict maximum damage (0.22 and 0.55 respectively) on the corner of the bottom flat edge just before the billet forming is complete, where the material will have undergone the greatest hydrostatic stresses and strains. The Shear criteria (maximum damage: 1.52) predicts the damage will concentrate on the outer diameter of the bottom length of the billet due to the frictional shear stresses between the container wall and the billet.

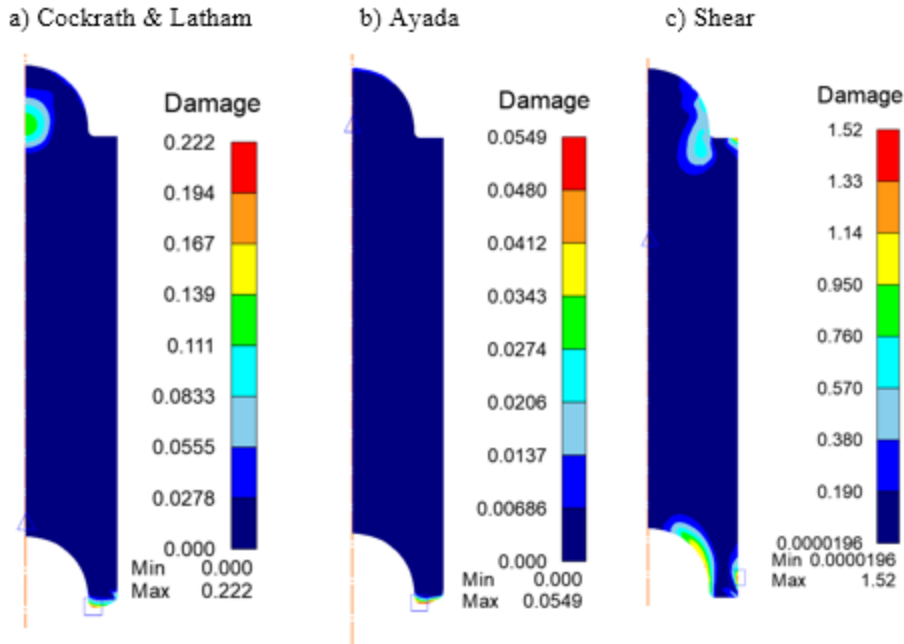


Figure 4.23: Simulated damage values across four explored damage models during billet forging for the base-case round bar profile-specific billet design 3, for 50% weld length reduction. The billet is AA6061 with an initial diameter of  $\varnothing 88.9\text{mm}$ , a length of 200 mm, and was heated to a temperature of  $425^{\circ}\text{C}$  prior to forging.

Next, simulations of compression tests were run on four different sample geometries (Figure 4.23) at near-extrusion conditions (AA6061 samples at a temperature of  $500^{\circ}\text{C}$ ) to determine the height reduction necessary to replicate the value of damage present in billet forming. Table 4.3 shows the geometries tested, the damage values during billet forming, and the necessary compression value tested.



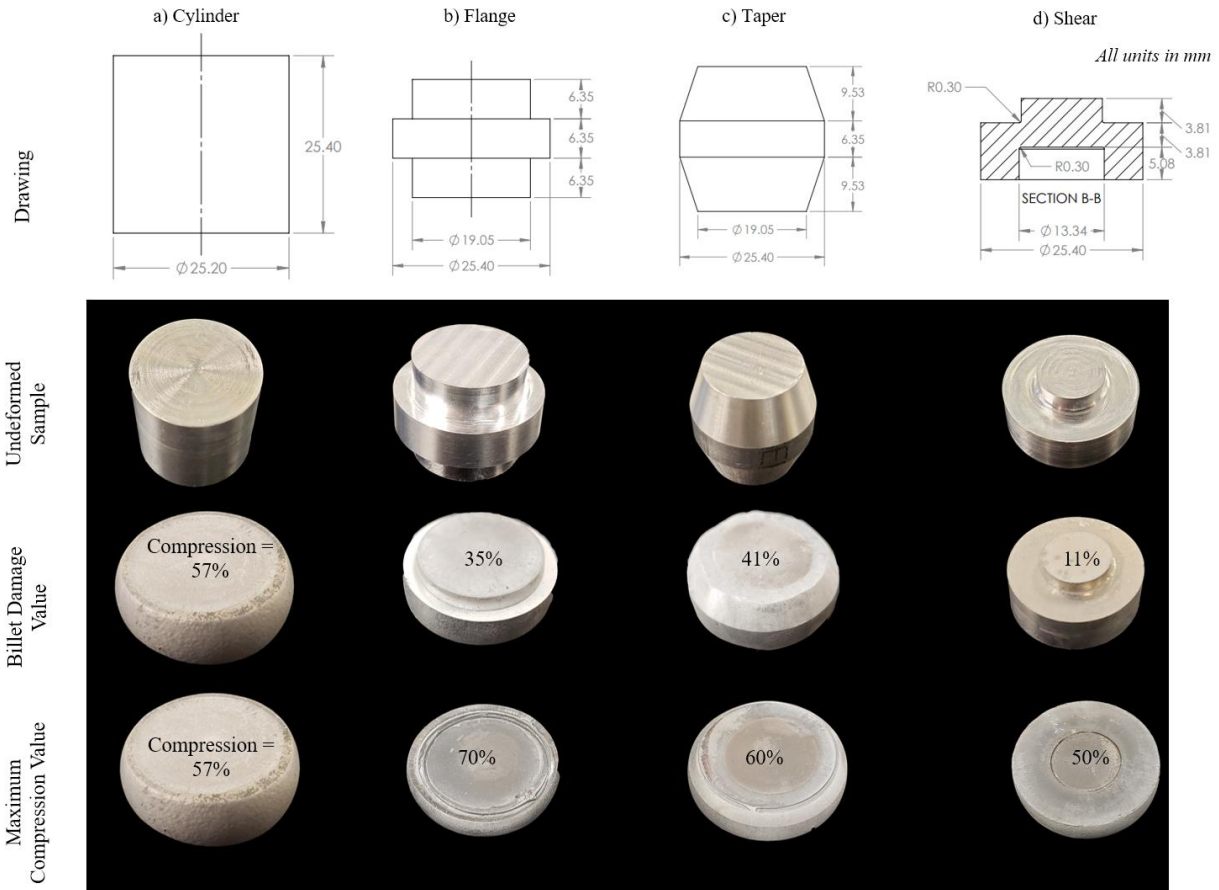


Figure 4.24: Experimental samples tested in the ductile damage derivation procedure.

Table 4.3: Critical damage values from ductile damage criterion derivation.

Damage criteria	Cockrath & Latham	Ayada	Shear
Maximum damage value from hot forging FEM	0.22	0.055	1.52
Sample geometry	Corresponding compression value for upsetting between two flat platens (%)		
Cylinder	44	57	N/A*
Taper	43	39	N/A*
Flange	37	27	N/A*
Shear	11	6	5

Note 1: The cylindrical, tapered, and flanged test samples could not be tested to the maximum shear value due to force limits on the testing equipment. The samples were AA6061 at a temperature of 500°C.

Hot compression tests to 57% compression on the cylinder, 41% on the taper, 35% on the flange, and 11% compression on the shear sample confirmed that no cracking was present after this level of deformation; therefore, the billet damage incurred during hot forging of conventional billets to create profiled billets for the base-case round bar profile-specific billet design 3 would be insufficient to cause billet cracking.

A more thorough ductile damage procedure followed, which included the derivation of the critical damage values which would result in cracking. This procedure was carried out specifically for the extrusion conditions of this particular case: AA6061, at 500°C. This means that the results cannot be extrapolated to all extrusion cases, but this is meant to act as a guide for how to approach new cases. The added benefit of determining these critical values is to enable the application of one set of test data to all extruded profiles with the same alloy and temperature.

To determine the critical value, compression on the samples is increased until visible cracks begin to form on the surface. Then, the simulated damage values are cross-referenced for this compression value. However, the equipment used for this experiment limited the compression ratios that could be achieved on the samples due to the 38.1 mm platen diameter. The bottom row of Figure 4.24 shows the compression ratios that were achieved on each sample before the platen diameter was exceeded: 57% on the cylinder, 60% on the taper, 70% on the flange, and 50% on the shear sample. The damage values for these compression values are shown in Table 4.4 below.

<b>Sample geometry</b>	<b>Compression Value</b>	<b>Cockrath &amp; Latham</b>	<b>Ayada</b>	<b>Shear</b>
<b>Cylinder</b>	57%	0.34	0.054	0.40
<b>Taper</b>	60%	0.39	0.12	0.36
<b>Flange</b>	70%	0.64	0.26	0.55
<b>Shear</b>	50%	2.7	0.88	6.4

#### 4.2.4 Section experimental results and discussion

Figure 4.25 shows the results of the profiled billet extrusion trials with the expected (designed) and achieved (experimental) weld lengths shown as a percentage of the conventional weld length. Figure 4.26 shows the experimental weld geometries.

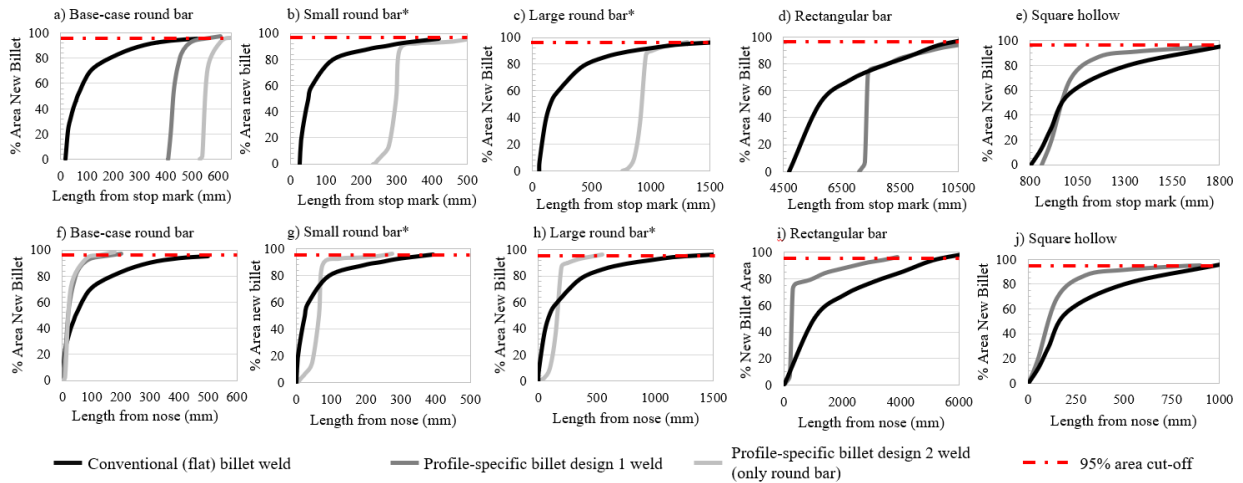


Figure 4.25: Experimental conventional and profiled billet transverse weld geometries. \*The small and large round bar profile billet designs were not profile-specific, and instead were designed for the base-case round bar (extrusion ratio = 15).

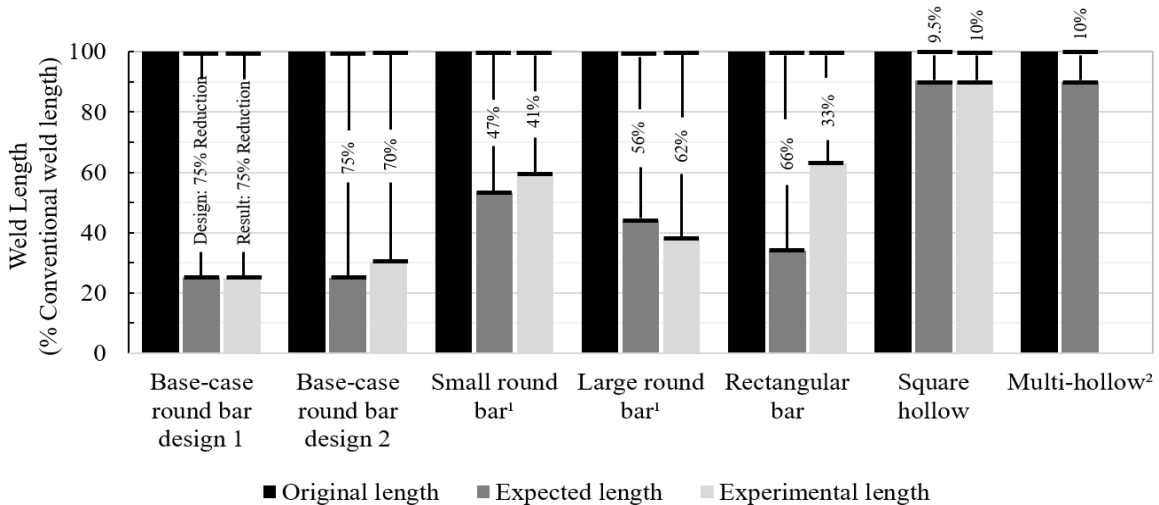


Figure 4.26: Expected and achieved weld length reductions using profiled billets. The base-case profile-specific billet designs 1 and 2 were different designs intended to achieve a 75% weld length reduction in the base case (mid-sized) round bar. 1: This same design was then also used during extrusion of the smaller and larger diameter round bars. 2: The multi-hollow profile was not evaluated experimentally due to unavailability of the press and die.

Figures 4.25 and 4.26 show that weld length reductions were achieved across the different profiles (ranging from 10% to 75% reductions) but weld length reductions were much smaller for the hollow profiles

(around 10%) compared to the solid profiles. This was largely because neighboring concavities begin to interfere with each other, resulting in asymmetric and difficult to model shapes given our current ellipsoidal approach.

In Figure 4.26a-f, the expected experimental results local to the nose and cut-off point of the weld can be observed. The welds produced using the round bar and square hollow profiled billets were as expected. For example, the base-case round bar profile-specific billet design 1 was expected to reduce the nose of the weld by 100%, and elongate the cut-off by 25%, and the experimental weld had a 105% reduction and 30% elongation. The weld for the rectangular bar profile-specific billet, however, was very far out from the expected result. The design was for a 66% reduction at the nose. The profile-specific billet weld was found to have a reduction at the nose of only 43%, and an elongation at the cut-off of roughly 10%.

#### 4.2.4.1 Discrepancies between the expected and achieved changes in weld geometry

For the round bar and square hollow profiles, the expected and achieved weld lengths were within 20%; however, the discrepancy for the rectangular bar reached 50%. One potential origin of the discrepancies is that (for the round bar profiles) the lab-scale press used for experiments does not align the center of the billet with the center of the die. Instead, the  $\text{Ø}88.9$  mm billets rest on the bottom of a  $\text{Ø}94$  mm container. This results in the designed profiles being extruded slightly off-center through the die. The material at the top of the billet will enter the velocity field more quickly, while material at the base of the billet will enter more slowly, creating an asymmetric weld and shifting the nose and cut-off of the weld (shown in Figure 4.27).

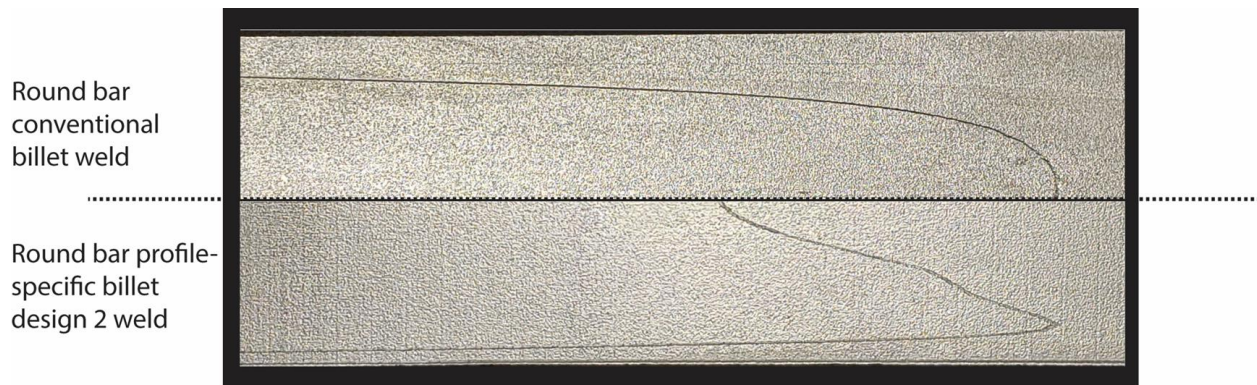


Figure 4.27: Longitudinal cross section of the conventional billet and profile-specific billet design 2 welds for the base-case round bar profile produced experimentally.

The largest discrepancies between theory and experiment were for the rectangular bar profile. The profiled billet geometries were designed by using the velocity field method to create the profile-specific billet contours along the major and minor axis of symmetry. These boundary curves were then lofted

(interpolated), along a third boundary curve along the billet-billet interface, using SolidWorks (Dassault Systemes, 2023) to create a full 3D-design. The billet designed in this manner produced a weld with an inverted radial center. This means that the radial center was not the furthest forward point in the extruded profile, and was therefore not used in the measure of the weld length. If the weld length was instead measured from the radial center of the weld, the achieved reduction would be 63%, nearly identical to the designed 66% reduction. This indicates that the designed depth of the profile-specific billet design had a similarly small discrepancy to the other profiles, however the interpolation between the design boundary curves had flaws which resulted in significant alterations to the weld geometry and an increase in the weld length.

For the square hollow and multi-hollow profiles, the profiled billets were designed using semi-ellipsoid shapes that encapsulate all the back-tracked points from the velocity field method. This method guarantees a weld length reduction and does not introduce the interpolation problems that reduced the savings for the rectangular bar profile.

#### **4.2.4.2 Effect of using profiled dummy blocks and billets on the back-end defect scrap**

The back-end defect contains a conglomeration of oxides and other contaminants from the billet skin (Saha, 2000; Oberhausen et al., 2022). The billet skin ranges from roughly 0.05 mm to 0.5 mm in thickness (Hydro, 2022) depending on the billet quality resulting from the composition and casting process. Point tracking in the extrusion FEMs is used to determine the potential effect on scrap savings from extruding the back-end defect through the die in order to preserve the profiled billet-billet interface. It is hypothesized that the concave dummy block will further conglomerate the billet skin leading to a small volume of material in front of the transverse weld needing to be removed to eliminate the back-end defect and further improvement of the process yield. To simulate the back-end defect in the profiled billet concept, we focused on the case of the profiled dummy block and billet design for a 50% reduction in weld length for the base-case round bar profile (design 3 in Figure 4.19a). The FEMs first simulated hot forging of a flat-faced billet and then extrusion of these profiled billets using the profiled dummy block. The length of the billet skin in front of the nose of the transverse weld (shown in Figure 4.28), is used to calculate the volume of material necessary to be removed as part of the back-end defect. Conventional butt shearing would remove the last 10% of the billet length (20 mm) (scrap: 124,000 mm<sup>3</sup>). If instead, the conventional butt was extruded through, with the next billet, the back-end defect would infiltrate the profile in front of the transverse weld according to Figure 4.28a: an average billet skin thickness would result in roughly 350 mm of profile length, for a volume 125,500 mm<sup>3</sup>, roughly equal to the volume of the billet butt.

The FEM results shown in Figure 4.28b show that a 0.05 mm thick billet skin would contribute to a volume of 17,220 mm<sup>3</sup> of profile scrap (41 mm removed), and a billet skin thickness of 0.5 mm would contribute a volume of 98,250 mm<sup>3</sup> of profile scrap (235 mm removed), for a reduction of the back-end defect scrap of between 20-85%.

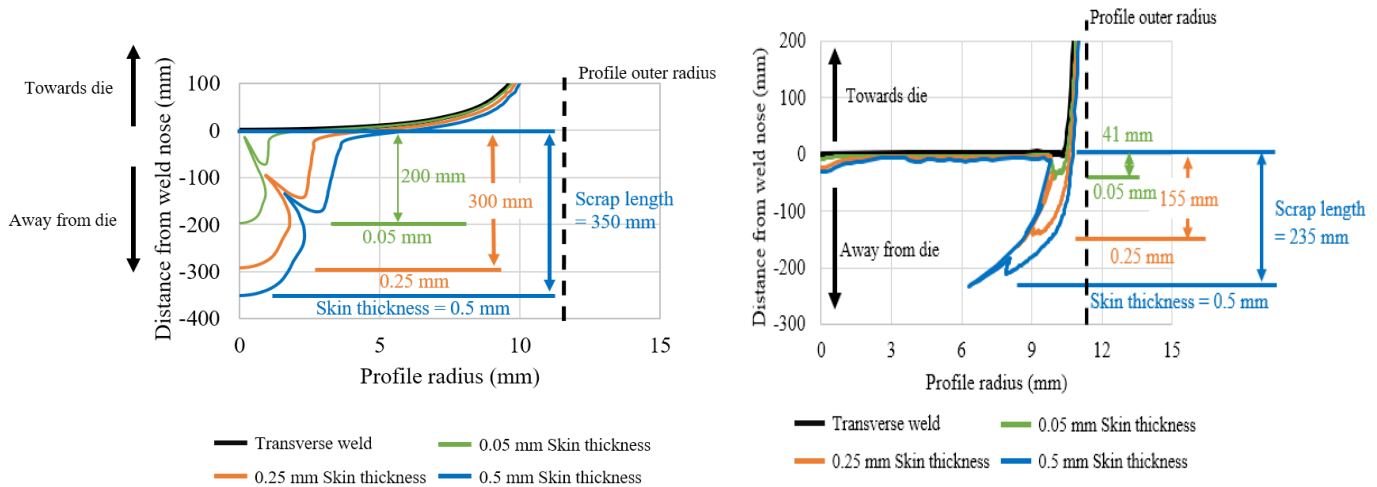


Figure 4.28: (a) The location of the back-end defect in the conventional and (b) base-case round bar profile-specific design 3, aimed at a 50% weld length reduction, given varying billet skin thicknesses.

#### 4.2.4.3 The potential benefits of multi-profile tooling

Current industry practice is to replace the dummy block every week for maintenance (Superior Extrusion, 2022); however, profiled dummy blocks may need to be changed with every change of die (and therefore profile extruded) unless profiled tooling can be designed that delivers savings across a family of similar profiles. The current dummy block changeover time is roughly 15 minutes (Can Art, 2021). With each change in profile extruded, it is also necessary to change the die. Die changeover requires approximately 3 minutes, and can be overlapped with part of the dummy block changeover time (Can Art, 2021). This 12 minute loss equates to approximately a 10% production loss, based on an average profile run length of 2 hours (Can Art, 2021). This loss will be offset to some extent by the production gained through a reduction of scrap generation. A greater frequency and importance of dummy block changeover could inspire innovation in dummy block design which allows for quick installation and release. Alternatively, longer production runs could be scheduled to amortize the lost time over a greater volume of product. This effect is also achieved through multi-profile tooling, allowing multiple, related profiles to be extruded back to back using the same dummy block.

The concept of multi-profile tools, or tools which can be used to achieve savings across a family of similar profiles could prove critical to reducing the cost of dummy block design, production, and

changeover. The rod and bar market represents the best candidate for multi-profile tooling. Figure 4.25 shows that a profile-specific billet design for achieving a 75% weld length reduction for a mid-sized round bar (extrusion ratio (ER) = 15) also achieves a 42% and 62% reduction in the weld length for larger (ER=10) and smaller (ER=30) bars respectively. In industry, there are presses dedicated exclusively to the production of rod and bar profiles (Hydro, 2023). This creates a concentration of similar profiles, and therefore also a concentration of the need for additional tooling, equipment, and labor to fewer locations.

The rod and bar markets alone represent 11% of the total extrusion market, totaling over 0.3 million metric tons of extruded product per year in just North America (Oberhausen et al., 2021). Within the rod and bar market, this work focuses on round bar, the most immediately applicable case for multi-profile tooling due to differences between profiles being limited to a single dimension, the radius. Extrapolation to rectangular bar and other markets will largely depend on the similarity within profile families. For the rectangular bar market, as an example, we hypothesize that the products would best be grouped by the aspect ratio (length / width) to create distinct families of shapes. The design contour maps have been shown to allow for accurate prediction of expected reductions and could be used to plan these production families. Another 7% of the extrusion market, or roughly 0.2 million tons of product, is captured within the tube market. We would expect that grouping of these shapes would be more complicated to group than rectangular bar, given the addition of wall thickness as a dimensional-variable beyond just the shape. The remaining 82% of the extrusion market is complex shapes. It is our assumption that these are shapes that cannot be neatly split into near-shape families and would require one-to-one customization of the dummy block to extruded profile.

#### **4.2.5 Section conclusions and future work**

This work has presented a new methodology for designing profiled dummy blocks and billets that can be used to reduce the transverse weld length and subsequently the scrap created during direct extrusion. The experimental trials present promising results in the potential of the technique across a range of profiles, and particularly for solid profiles where a family of similarly shaped profiles might be able to use the same profiled dummy block and billet design. Furthermore, initial simulations suggest that this new concept could also reduce the scrap removed to eliminate the back-end defect.

Future work will include an extrusion trial using a profiled dummy block for the base case round bar profile analyzed in this work. The dummy block will be used to hot forge profiled billets from conventional cylinders and then extrude the profiled billets to form a shortened transverse weld. The analysis presented in this article has shown that a dummy block designed for a 50% reduction in transverse weld length can withstand the extrusion pressures without plastic or significant elastic deformation, as well as avoid causing ductile damage in the billet during forming.

## **Chapter 5. Conclusions and Future Work**

In this thesis, the opportunities within the aluminum extrusion industry for significant cost-effective and environmental impact savings have been identified and explored. This chapter will summarize the major contributions of this work and will outline potential future work.

### **5.1 Contributions of this thesis**

Chapter 2 presents cradle-to-gate models for quantifying the cumulative energy demand, greenhouse gas emissions and costs for the direct aluminum extrusion process using aggregated data from extrusion companies, semi-structured interviews with industry experts, electrical power measurements from case studies, and physics-based extrapolations. The models show that an increase in material efficiency is the greatest opportunity to reduce both the costs and environmental impacts associated with the extrusion process. Next, a material flow analysis of the 2018 North American extrusion industry is conducted with separated flows for extrudate alloy, shape, and application. The data input into the MFA was collected from existing literature, semi-structured interviews with extrusion experts and from industry reports. The developed MFA is used to identify opportunities for increased material efficiency in the extrusion supply chain. It is revealed that approximately 40% of raw extrusion billet is scrapped before it reaches a fabricated product and that the single greatest form of scrap is the transverse weld.

The work in Chapter 3 seeks to bring understanding to transverse weld formation, as greater control of weld geometry and strength could lead to reduced scrap rates and a more competitive and environmentally benign extrusion industry. The transverse weld is a solid-state-weld (SSW) which forms at the interface between consecutively extruded billets and is elongated due to material flow through the die. The weld forms as the deformation experienced by the billets in the extrusion process causes the surface oxides to fragment and the substrate material to perforate through the cracks and form metallurgical bonds. The weld exhibits weaker mechanical properties than surrounding material and therefore must be removed in structural applications. We adapt the film theory of solid-state bonding to non-plane strain conditions to derive a mechanistic SSW strength model which uses deformation conditions from finite element analysis (FEA) to predict the strength along the transverse weld and perform novel material failure tests to measure the mechanical performance of the transverse weld isolated from the bulk material. To guide derivation of the model, we first investigate oxide fragmentation behavior under complex deformation conditions through microscopy on the outputs of anodized extrusion and novel-geometry roll bonding trials. We then perform



a series of identical non-anodized trials to analyze the microstructure and strength of the bonding interface. Through this work we reveal that the surface exposure experienced by the interface is the driving factor for weld strength, rather than the pressure as suggested by previous literature. This is because the normal contact stresses across the bonding interface are found to be sufficient for microextrusion of substrate aluminum through cracks that are formed. We find that the strength of the transverse weld increases towards the rear of the weld, however the reliability of the weld remains low, with low strength samples found at equivalent lengths to high strength samples. The poor reliability of the weld strengths achieved suggests that efforts to reduce the weld length, rather than increase the weld strength, might be a more fruitful avenue of research directed at reducing the process scrap created.

In Chapter 4, we investigate the use of novel extrusion tooling to reduce the length of the transverse weld. The elongation of the transverse weld interface occurs due to the velocity field present in the extrusion container and die, causing the initially flat consecutive-billet interface to be present in up to 20% of the length of the extrudate. In the case of axisymmetric extrusion, material in the radial center of the billet travels quickly through the die, while the friction on the container and the dead metal zone present at the die entrance causes the radial edges to travel much more slowly. We develop a design methodology which creates dummy block profiles to offset this velocity differential and significantly flatten the weld. The methodology first incorporates FEA and MATLAB solutions which models the flow of material for a given extruded profile and die. The numerical solutions output an ideal dummy block profile geometry. Next, the ideal tool shape is rationalized to meet maximum stress and deflection specifications for the dummy block (preventing plastic deformation and interference with the container wall), as well as ductile damage limits for the billet to prevent cracking during formation of the billet into the dummy block concavity. We then simulate the likely effect of the rationalized dummy block design on back-end defect removal. A series of lab- and industry-scale trials are performed to test the efficacy of the design methods on extruded profiles of varying complexity. The results show that dummy blocks with a profile-specific design can achieve weld length reductions >75%. We also demonstrate that multi-profile tooling can deliver scrap savings across a family of similar profiles. Finally, we discuss the industry implications and the commercialization challenges.

## **5.2 Future work**

Through this work, several opportunities for further research have been identified. These opportunities are outlined in the sections below.

### **5.2.1 Reducing the effects of quench distortion in extruded profiles**

*The preliminary work shown in this section represents collaborative work with post-doctoral scholar, Ala'aldin Alafaghani, and undergraduate student Lily Adams.*

Semi-structured interviews with industry experts revealed that a key source of scrap in the extrusion industry, which is becoming more important as the automotive market grows, is profile reject scrap due to lack of quench distortion control. For example, Hydro (2020), the largest extruder in North America, cited some profiles suffering reject rates higher than 40%.

Quenching is the cooling process used to improve mechanical properties (via age hardening) in the final product. Figure 5.1 shows the phase diagram of an aluminum alloy. As the heat treatable aluminum billet passes through the extrusion die, the aluminum material is in the alpha phase, in which all precipitates are dissolved into a solid solution. For heat treatable aluminum alloys, the profile will often be water quenched as it leaves the extrusion die. Quenching, or the rapid cooling of the part, causes the material to quickly cool, traveling through the alpha and theta phase without allowing any of the dissolved precipitates to solidify out of solution (Assaad, 2016). Through this process, the solid solution microstructure is maintained and little or no precipitates are formed. Any precipitates that are formed will result in detrimental effects to the mechanical properties after the subsequent aging process (Techno, 2018).

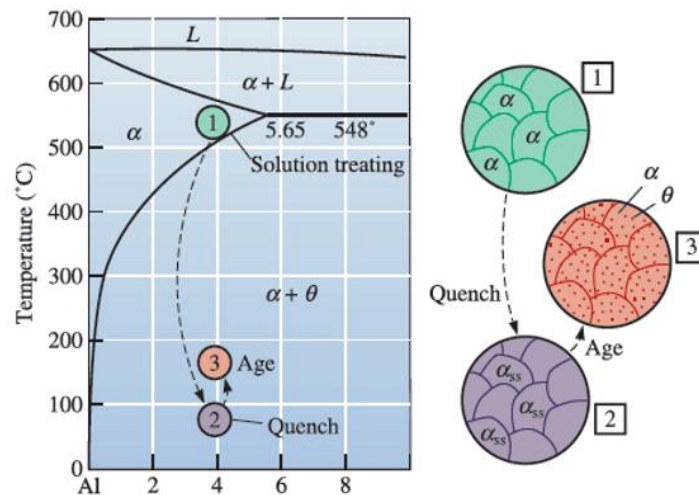


Figure 5.1: Aluminum phase diagram showing the typical route from (1) post-extrusion temperatures through the (2) quench and (3) aging processes (Techno, 2018).

The quench process is primarily used on high-performance parts such as in the automotive, aerospace and construction industries (Magnode, 2020; Granco Clark, 2022). The minimum quench cooling rate for AA6082, a common high-strength alloy used for automotive profiles (e.g., the F-150 roof rail), is 2500°C/min between the temperatures of 500 and 300°C (Parsons et al., 2020). Quench distortion is in part caused by the complex multi-hollow extrusion profiles commonly found in these industries (Can Art, 2021). The water from the quenching process rapidly cools the outside profile (left side of Figure 5.2), while the inner webs of the profile are reliant on conduction through the outer walls to release their heat (Granco Clark, 2022). This causes a temperature differential between the outer walls and the inner webs, resulting in plastic strain on the profile as the now cooled outer profile contracts around the still hot inner webs.

Figure 5.2 also shows an example of the effects of quench distortion, where even relatively small amounts of plastic strain in the profile can cause it to fail dimensional tolerance checks (Ford, 2021). Reduction of the overall quench rate can help to reduce the quench distortion, however, this change will result in unsatisfactory microstructure and therefore performance in the overall profile.

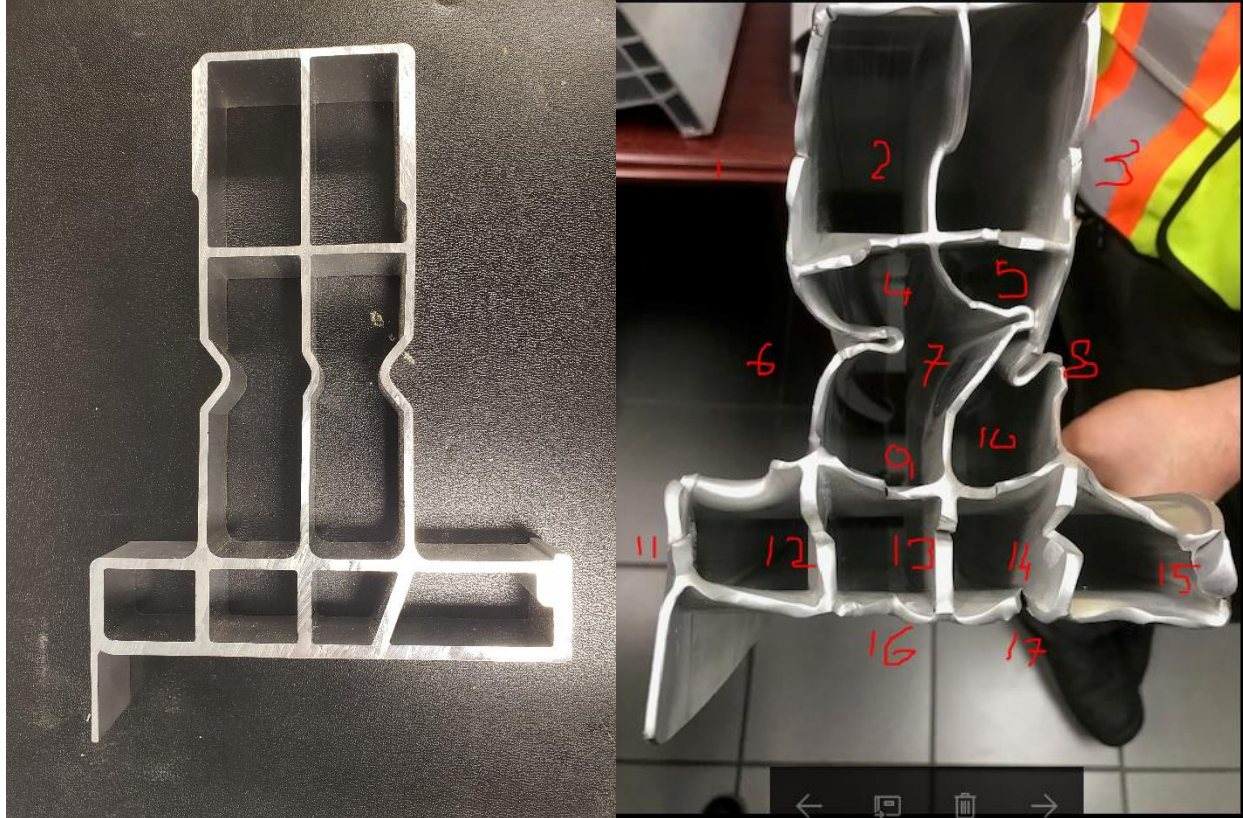


Figure 5.2: Example of significant plastic strain on quench cooled Ford F150 battery tray side rail profile (Ford, 2021). Left: Normal, Right: Quench distorted.

The slow, conductive cooling of the inner webs also results in a change in microstructure in this region. We explored the effect of the varied cooling rates across the Ford F150 battery tray side rail, shown in Figure 5.3. Six key locations were selected to represent exterior and interior regions of the profile that have identical wall thicknesses and are relatively near to each other.

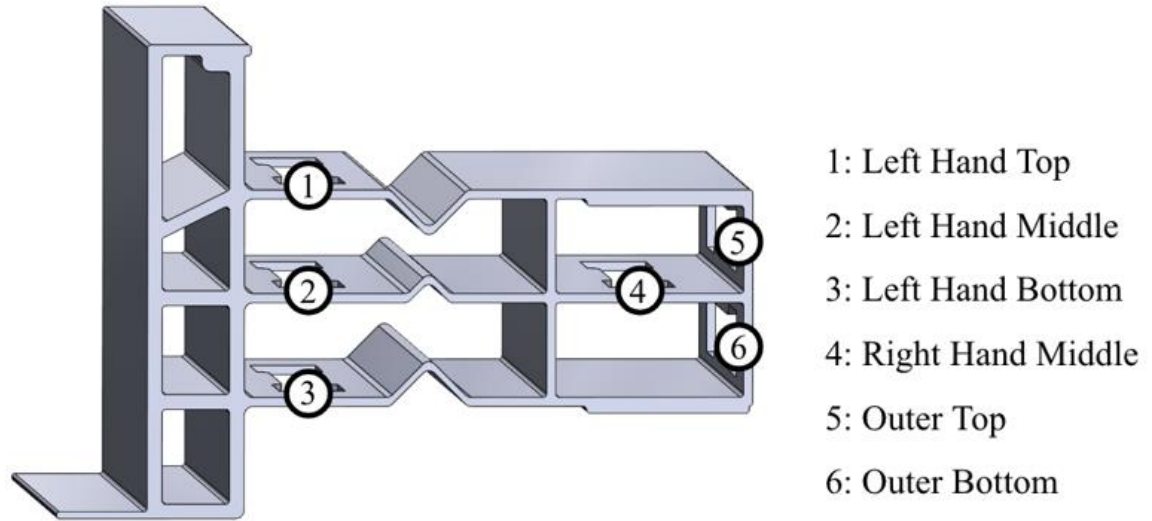


Figure 5.3: Ford F150 side rail profile, and the six locations that tensile test samples were taken.

First, a finite element analysis (FEA) using Abaqus software was performed to understand how the quench differs quantitatively across the profile. The test was done on a 2D model of the cross section beginning at the post-extrusion temperature of 500°C. A convection surface film interaction with ambient temperature at 25°C on the exterior walls is then applied to recreate a water spray hitting the exterior of the extrusion. This model was run with film coefficients defining the ambient interaction from a range of 500 to 5000 W/m<sup>2</sup>K to represent the feasible span of real world film coefficients (Granco Clark, 2022).

Figure 5.4 below depicts the cooling of the six locations within the profile at three selected film coefficients (500, 2000, and 4000 W/m<sup>2</sup>K). It is seen that in all cases the internal samples cooled significantly slower than the external samples, having an insufficient cooling rate for satisfactory quench at even the most extreme film coefficients.

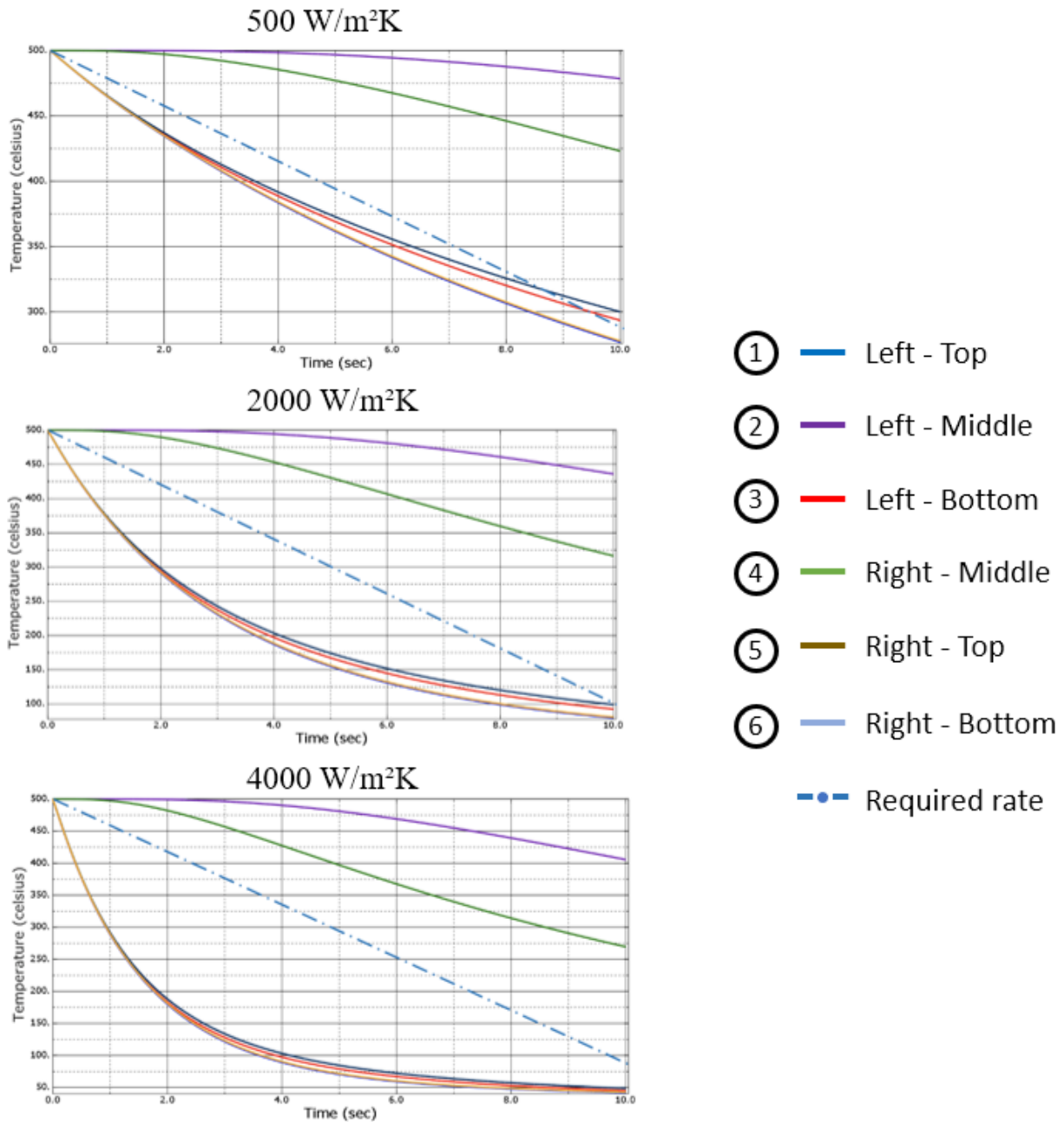


Figure 5.4: Cooling rate of the six sample locations on the Ford F150 battery tray side rail profile across a range of quench film coefficients.

To measure the impact on the mechanical performance caused by the different cooling rates, tensile specimens from post age hardened profiles were extracted and tested to failure at the six sample locations. Figure 5.5 shows that both the ductility and strength were found to be consistently lower in the inner webs (samples 2, 4). One inconsistency that is seen in these results is the relatively low ductility of the Left – Top sample. A preliminary explanation for this difference, is that our FEA model idealizes the interaction

between the quench and the exterior of the profile. There is an assumption that the water is applied uniformly across the entire exterior, however we have not been granted access to the participating company's extrusion sites to learn if this is the case. Future work could include a more precise modeling of the quench processes used in real life, including both nozzle locations, sizes, and spray patterns.

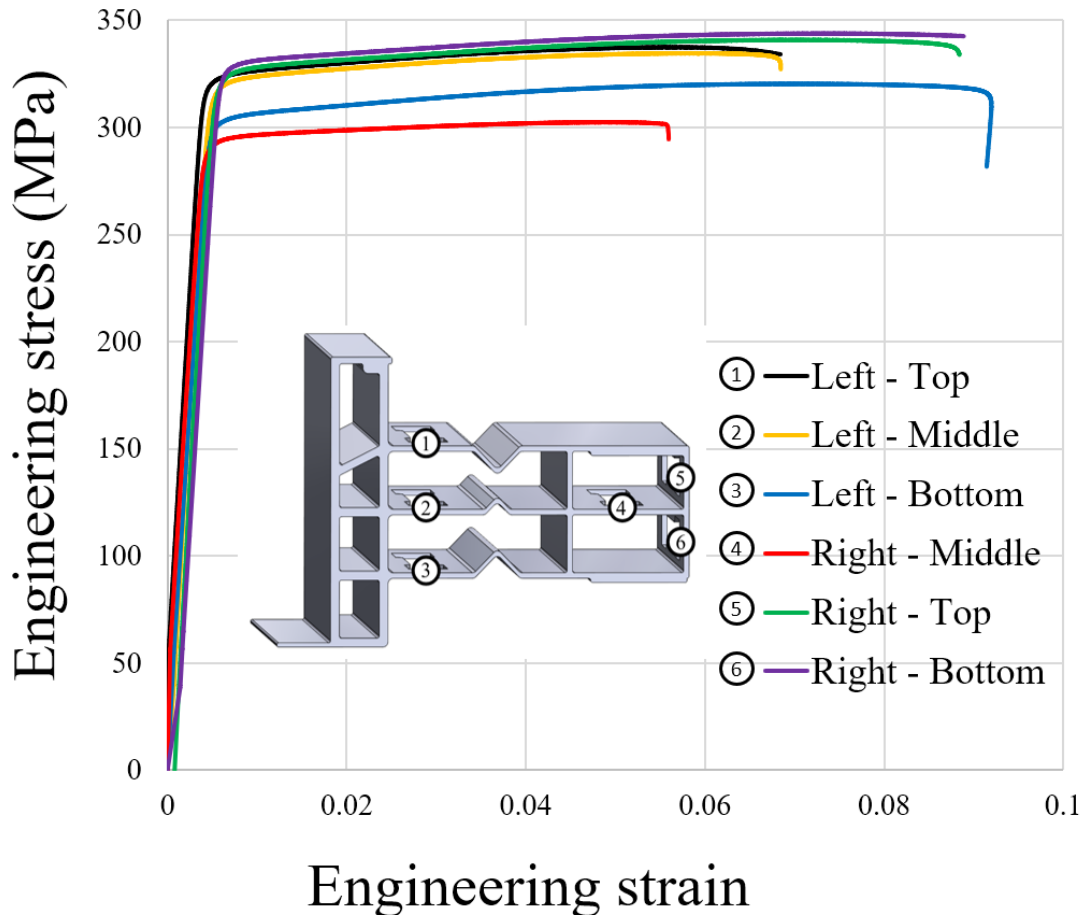


Figure 5.5: Stress-strain curves from tensile tests at the six sample locations on the Ford F150 side wall.

In part testing for compliance with demanded specifications, the inner webs are not chosen for testing due to the geometric difficulty in sample removal (Hydro, 2021; Superior Aluminum, 2021). The result is that the problem is often overlooked, and parts are produced with regions that do not meet the specified requirements. To overcome the problem of poor inner mechanical properties and profile distortion, we propose a die with cooling channels be produced and used to deliver quench water directly to the middle cavities of the extruded profile (Figure 5.6). Preliminary simulations show that the channels can produce quench rates that bring inner walls within cooling specifications. Future work is now focused on evaluating

the dies for industrial feasibility, including whether plastic deformation can be prevented in the dies once cooling channels have been added.

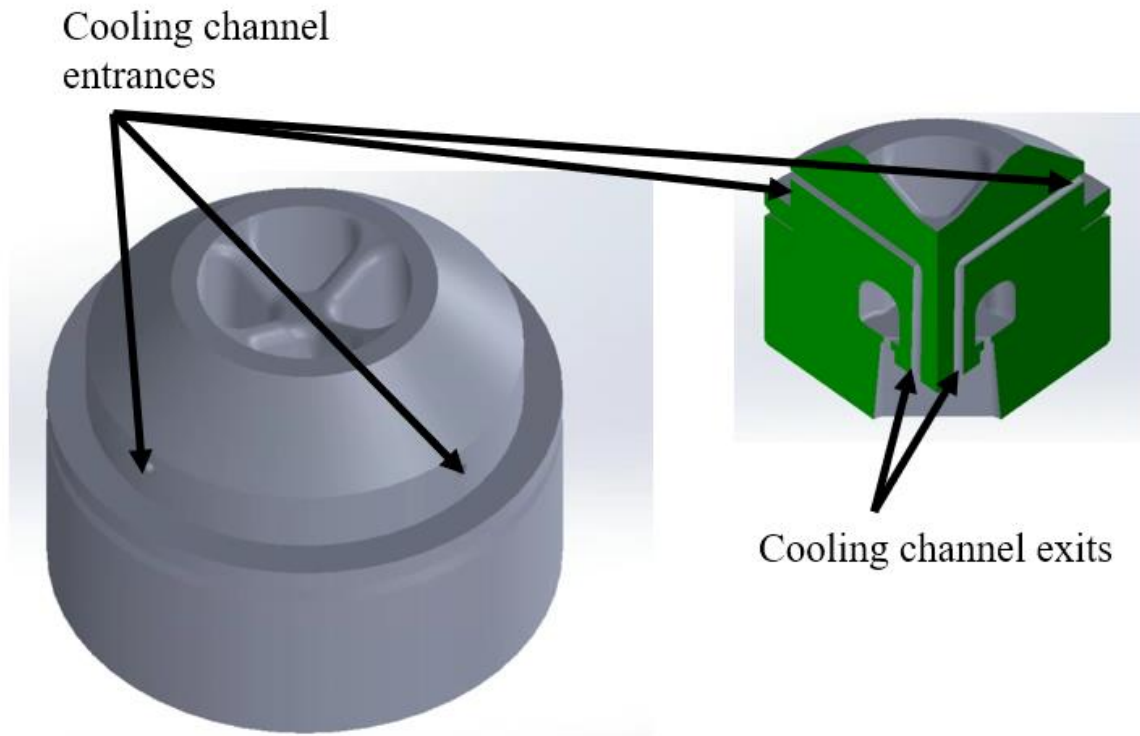


Figure 5.6: Example of conformal channel die, with channels carrying quench solution from the outside of the die through the die bridges and down through the mandrel into the profile's hollows.

### 5.2.2 The potential benefits of improved transverse weld strength modeling

Removal of the transverse weld is rooted in its sub-standard mechanical performance (Oberhausen et al., 2022; den Bakker et al., 2016; Tang et al., 2022). Greater control of weld strength may offer the greatest opportunity for transverse weld reduction in the complex profiles for which the concave-profiled dummy blocks will likely achieve only a modest reduction in weld length. In Chapter 2 of this work, a proposed weld strength model correctly predicts the experimental trends in weld shear strength testing and suggests the surface exposure of the welding interface to reveal substrate aluminum is the driving mechanism for bonding of the billet-billet interface.

However, the approach of transverse weld mitigation through strength improvements will require significant additional research. There are several means by which industry could seek to control surface exposure and therefore strength; die design, and beginning billet-billet interface location are the two main options. In today's approach to mitigation of weld scrap through weld length reduction, a large number of studies on the relationship between weld length and extrusion parameters such as billet and container

temperature, ram speed, and friction conditions on the dummy block and container (Mahmoodkhani et al., 2014; Chen et al., 2015; Zhang et al., 2017; Hatzenbichler and Buchmayr, 2009) as well as die geometry (Zhang et al., 2017; Reggiani and Donati, 2018; Hatzenbichler and Buchmayr, 2009; Crosio et al., 2018) were performed. A similar framework of studies could be performed with a focus on die design to show that surface exposure and strength can be controlled. In Chapter 4, the impact of billet-billet interface geometry on the transverse weld length is explored through use of concave dummy block geometry. A similar extension could be made to determine the design of dummy blocks with a convex design for increasing the local surface exposure and therefore strength of the transverse weld. Greater control of the transverse weld strength could enable the production of profiles containing welds which meet specifications and do not require removal. However, for this style of approach the reliability of the transverse weld strength will become essential, as otherwise the elongation of the weld would only contribute to increased scrap quantities.

There are several potential improvements which can be made to the transverse weld strength model presented in Chapter 3 in order to increase its accuracy. The experimental results presented in the included proposed weld strength model are dispersed and show poor reliability at any point along or across the studied welds. The model does, however, reveal some experimental trends in the transverse weld strength such as increasing strength towards the rear of the weld, the poor weld strength associated with lubricated surfaces (when the billet butt is not removed), the varying weld strengths for single versus two-piece billets and across the cross-section of non-axisymmetric profiles, as well as higher local surface exposures resulting in higher local weld strengths.

Validation, through microscopy, of the oxide fragmentation width as a foundation for the required normal contact stress for microextrusion ( $p_{ex}$ ) was performed on a round bar profile in both a single- and two-piece billet configuration. The round bar case provides a wide range of surface biaxial strain conditions which covers the design space, from compressive-compressive to compressive-tensile; however, material limitations led to a low number of experimental samples. Additional anodized billet trials could be conducted on round bar samples to further populate the design space, as well as on multi-hollow complex profiles to ensure that the relationship between deformation conditions and oxide fragmentation continues in a more complex design space. The results of these trials will also add depth to the understanding of the balance between coherent and incoherent oxide fragmentation. In the presentation of the results the two scenarios were used as a lower and upper bound respectively. Studies could show that there is a consistent average percentage of coherency, identification of which would yield a more accurate model of strength.

An additional benefit of further study of the relationship between surface strains and oxide fragmentation would be an improved understanding of the re-oxidation of the exposed substrate. In its current implementation, the re-oxidation is estimated as a fraction of the initial surface,  $\eta$ , calculated from



the approximate volume of oxygen entrapped between the contacting surfaces, as introduced by Cooper and Allwood (2014). A refined definition of  $\eta$  could be achieved in two major ways. One would be the expensive and time intensive use of transmission electron microscopy (TEM) to measure re-oxidation between anodized pre-extrusion oxides. Care would have to have taken to ensure no re-oxidation occurs between the times of extrusion and TEM analysis. Alternatively, the value of  $\eta$  could be parametrically studied to determine the best fit using measured strength data. Variation across profile types could be moderately controlled by investigating the term independently on profiles of varied complexity (solid, semi-hollow, and hollow) to identify different trends.

### **5.2.3 Overcoming the hurdles for implementation of novel profiled dummy blocks into industry**

In Section 4.2 the challenges in developing a dummy block for reduction of transverse weld length were highlighted. There is significant potential for continued work towards the goal of implementing these novel tools into industry.

A potential barrier to industrial implementation is the danger of air entrapment between the flat-end billet loaded into the container and the profiled dummy block at one end of the extrusion container, and between the previous billet butt/hard tooling at the other. We hypothesize two potential solutions for this problem. First, we hypothesize a small diameter air vent in the hard tooling can allow air to escape while preventing micro-extrusion of the metal through the vent (analogous to the air vents used in injection molding dies). This can be tested using simulation plus lab-scale compression tests on heated aluminum cylinders using concave air vent tools. Second, we hypothesize that entrapped air between the loaded billet and the previous billet butt can be eliminated by press burping (as is standard in the extrusion industry) and/or using profiled radial tapered preheating of the loaded billet. Modern billet heaters transport and heat the billet from room to extrusion temperature over 30 minutes and have gas-fired nozzles which can precisely control the temperature independently on every part of the billet (Granco Clark, 2022). Burping is the action of moving the billet out of the dummy block concavity, to give any pressurized air a chance to escape from the concavity if it is sealed in by the outer radius of the billet. This can again be tested for AA6082 test samples using lab-scale compression tests.

As introduced in Section 4.2.5, the use of a novel-profiled dummy block relies on the previously shaped billet-butt remaining in the container to alter the consecutive-billet interface shape. Current industry practices rely on shearing of the billet-butt for removal of back-end defect scrap. Introduction of novel-profiled dummy blocks, and the removal of the shearing step will therefore require an alternative method of removing back-end defect scrap.

Prior to industry's adoption of the back-end shear, Dick's method of extrusion was commonplace (Sheppard, 1999). Dick's method relied on the use of a dummy block that is roughly 2 mm smaller in

diameter than the container, such that the contaminant shell which evolves into the back-end defect remained stuck to the container wall. A secondary ram stroke was then required to remove this shell from the container using the clean-out block, a ring-shaped tool which scrapes all edges of the container as it is pushed through. Before even Dick's method was introduced, the original method of back-end defect removal was simply to extrude the contaminants through the die along with the next billet and then to remove the back-end defect as a section of extrudate. With conventionally flat billets, there is minimal difference in quantity of material scrapped between this original method and the shearing of the billet butt. There is, however, a significant loss in throughput with the original method, as the extra time to extrude the final section of the billet can be significant.

Preliminary results in this work show that the designed concave dummy blocks can be used to concentrate the back-end defect in simple, round bar geometries. The simulated effects on the back-end defect can be validated against lab-scale extrusion trials. Scanning electron microscopy (SEM) and electron backscatter diffraction (EBSD) can be used to locate the billet skin within the final extruded product to determine how it flows relative to the transverse weld. It is critical to understand how best to minimize the back-end defect in this technology variant, e.g., concentrating the coring defect and extruding it through the die or alternatively peeling the defects off of the surface of the billets prior to extrusion. Additionally, profiles of increasing complexity should be studied to determine whether the concentrating effect is localized the simple profiles.

The combination of the above two issues (air entrapment and back-end defect evolution) as well as the two preliminary issues addressed more fully in section 4.2 (no plastic deformation on tooling and no ductile damage on billet) could be combined into a process window. The process window will help to define the products for which the technology is most viable. Important parameters will include the press size and capacity, the extrudate geometry, the billet length and temperature, as well as current and predicted scrap rates. The process window can be split into three classes of profiles (solid symmetric, solid complex, and hollow) to be used following idealized design from FEA to narrow the design as we include the detailed constraints.

Experimental validation of the above issues can be performed through a set of trials at Michigan Technological University on their lab-scale, 3.5" diameter, 350-ton extrusion press. One of the profiles studied in Section 4.2 was the base-case round bar with an extrusion ratio of 15. A design was created for a 50% reduction in the transverse weld length and was shown through FEM to experience no plastic deformation, limited elastic deformation and cause no ductile damage to the billet during forming. A fixed, solid dummy block (see Figure 4.14a) will be produced to this design by leading North American extrusion tool maker, Thumb Tool & Engineering (TTE). Machined billet trials on the manufactured dummy block will be conducted to validate the absence of plastic deformation or significant elastic deformation (Figure

5.7a). First, a billet with a flat front face and profiled back face will be extruded to fill the die. Next, one or multiple billets with machined front and back faces should be extruded. The extruded profile produced in these trials should be evaluated for their transverse weld length, as well as the infiltration of the back-end defect. The butt of the last billet in the trial should be evaluated to understand the initial evolution of the back-end defect, before it enters the die.

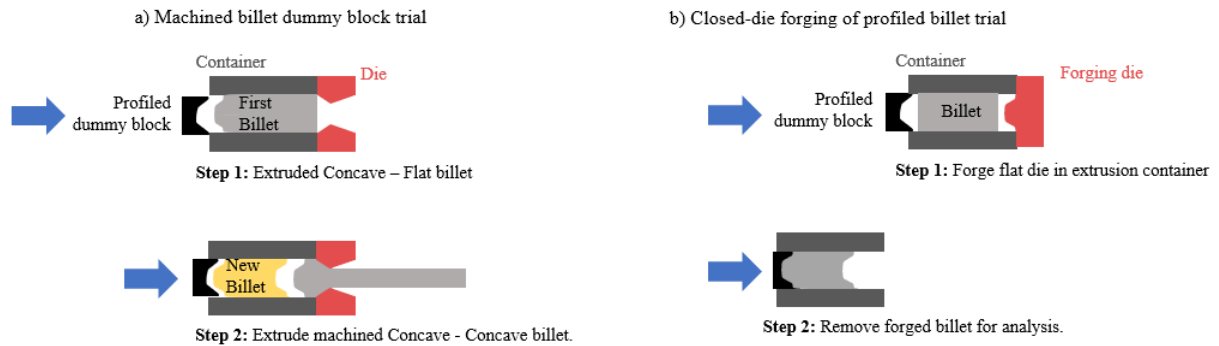


Figure 5.7: Outline of (a) machined billet dummy block trial, and (b) closed-die forging of profiled billet trial.

In a subsequent trial, the extrusion die can be replaced with a solid negative of the dummy block geometry to convert the extrusion press into a closed-die forging press (Figure 5.7b). A flat billet should be placed in the container and shaped using the new forging die, and profiled dummy block. The formed billet should then be removed from the container without being extruded. The billet should be evaluated for dimensional accuracy, ductile damage on the formed faces, as well as the evolution of the billet skin during forging.

After the dummy block's successful performance has been proven, implementation into industry will be dictated by the financial and environmental performance. One of the first steps towards building this understanding is to derive cost models that include tool purchasing, changeover, and storage costs, guided by advice from our industrial partners. For a single profile, we will first evaluate the breakeven point (production volume) for cost savings from the technology.

The greatest material savings and productivity gains in the new technology are achieved by customizing the dummy block to the individual profile; however, this results in increased upfront dummy block purchasing and inventory costs. In section 4.2 we also introduce and evaluate the performance of a single multi-profile dummy block designed to be used across extrusion ratios 10, 15, and 30 for round bar profiles. This concept can be further investigated in profiles of increasing complexity to better understand the most efficient way to serve the largest portion of the market.

## **Appendices**

Appendix A is the supporting information for Chapter 2. The data collection and reconciliation processes for derivation of the 2018 North American Aluminum Extrusion Material Flow Map are detailed.

Appendix B presents the weld shear strength from accumulative roll bonding experiments for comparison to Chapter 3's transverse weld strength results.

Appendix C details an initial study on design of profiled dummy blocks for a Ford electric vehicle

## Appendix A: Reducing the Environmental Impacts of Aluminum Extrusion – Supporting Information

This document contains information useful to understanding the themes, calculations, and numbers introduced in the main manuscript. This document is 43 pages long and contains 17 tables and 12 figures.

### A.1 Extrusion case study equipment and measuring the transverse weld length

#### A.1.1 Extrusion equipment

Table A1: Description of the machines used in the case studies.

Process	Machine Description
Billet and die preheating	The electric preheating furnace used in this case study has a maximum operating temperature of 530°C. The furnace chamber houses two shelves; the shelves can each fit either one die with a maximum diameter of Ø358 mm or two billets with a maximum length of 800 mm and diameter of Ø152.4 mm (Ø6”). In the case studies one shelf was used to preheat the die while the other was used to preheat two billets.
Heated billet and die transfer	A hydraulic and pneumatic device with an upper and lower arm driven by a carriage was used to transfer the heated billets from the oven to the press.
Extrusion of the billets	Danieli Breda 12MN (1,220 metric tons) extrusion press. The press is equipped with an Ø157 mm diameter container, which can be used to extrude Ø152.4 mm diameter billets up to a maximum length of 800 mm. The press has a main hydraulic cylinder which is used to push the billet, and two side cylinders which both aid the forward push of the main cylinder into the billet, but also work opposite the main cylinder on the press return-stroke to prevent the container from moving back with the ram. The cylinders are driven by four 3,000 rpm electrical pumps.
Press container heating	The container is outfitted with 12 thermal resistors which act to heat the container up to operational temperature (450°C in this study). The container also has three thermocouples spread over its length that help to regulate the temperature.

Shearing the billet butt	The 0.5 MN shear is powered by a separate hydraulic cylinder which operates by means of the main electric pumps. It is used after each billet extrusion to remove the butt (last 50.8 mm) of the billet in this study.
-----------------------------	------------------------------------------------------------------------------------------------------------------------------------------------------------------------------------------------------------------------

### A.1.2 Measuring the transverse weld length of the case study profiles

In order to determine the transverse weld scrap length in the case study extrusions a series of incremental cuts were taken from each extrudate cross section. The cross sections were then cold mounted in epoxy resin before being ground and polished in steps of decreased particle size until 1 micron diamond suspension. It is then finished with a final polishing step of colloidal silica. Next, the cross sections were etched in a 10% sodium hydroxide solution for 7.5 and 15 minutes for the solid rectangular, and 80-20 T-slot bar profiles respectively. Immediately after etching the samples were rinsed in deionized water, dipped in nitric acid and then rinsed in deionized water a second time. The resultant sample could then be imaged on a low-power microscope (1-4x) to produce an image from which the percentage area of the new and old billet could be measured. The transverse weld length is measured from the stop mark, to the cross-section of the extrudate at which the second billet area is 95% of the cross-sectional area.



Figure A1: Example cross sections of case study profiles (a) rectangular solid (70% billet 2 area) and (b) 80-20 T-slot bar (23% billet 2 area) used to measure the transverse weld length.

## A.2 European extruder dataset

The energy categories of the extrusion global impact and cost models are driven by an industry dataset provided by a leading European extruder on the condition of anonymity. Section 2.1 describes the context of the data, describing when it was collected, and what processes and products it represents. Section 2.2 describes how the data was then used to derive the inventory values found in Table 2.3 of the main article for use in the global models.

### A.2.1 Data representation

Table A2 below presents the data provided, representing the annual gas and electricity consumption for the European extruder in 2011, during which the extruder produced 8.71 kt of final extruded profile. The data broadly segregates the energy consumption by process and further divides the extrusion process specific energy data into 6-categories each representing a different profile. The data included is applicable to soft-alloy extrusion, which is assumed to be 6xxx series. The gas consumption during the extrusion process represents billet and die pre-heating, while the electricity consumption represents maintaining temperature in the container as well as powering the hydraulics required for the extrusion process.

Table A2: Annual energy consumption of European extruder for 2011 segregated by process and energy type.

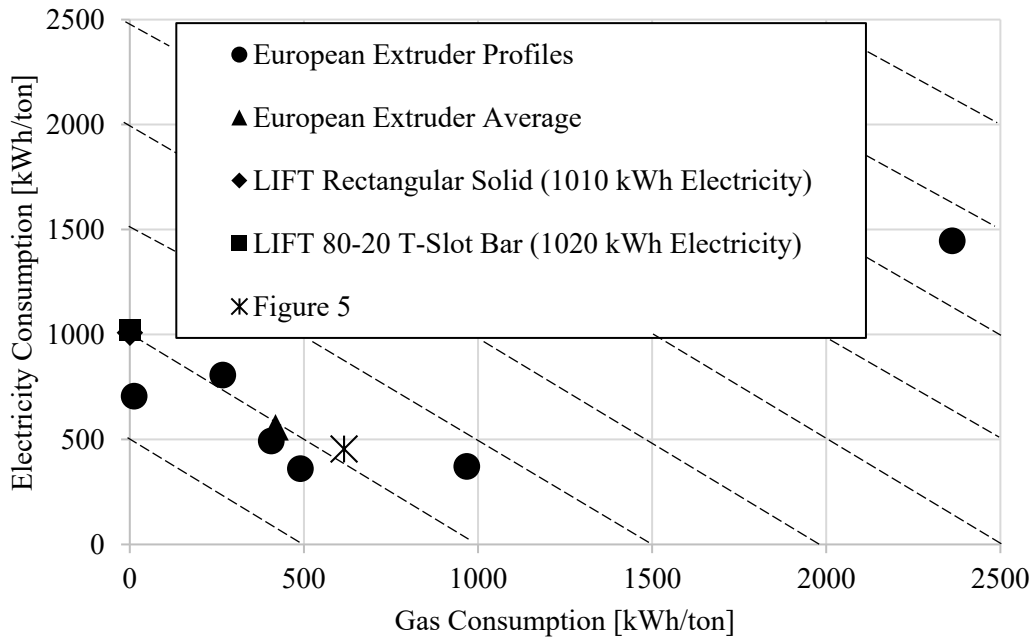
Average 2011		Gas			Electricity		
Process	Process ID	Consumption (MGW)	Output (kg)	specific cons. (kWh/ton <sub>out</sub> )	Consumption (MGW)	Output (kg)	specific cons. (kWh/ton <sub>out</sub> )
<b>Gas furnace melting</b>	60401	5478.4	6300000.0	869.6	366.5	6300000.0	58.2
	<b>Casting Homogenization</b>	60401	843.9	6300000.0	133.9	56.5	6300000.0
	60421	1277.5	6236000.0	204.9	405.0	6236000.0	64.9
<b>Extrusion - soft alloy</b>	60170	666.8	694748.0	959.8	252.7	694748.0	363.7
	60180	0.0	1101624.0	0.0	764.6	1101624.0	694.0
	60190	835.4	1776354.0	470.3	604.9	1776354.0	340.5
	60220	1103.6	2876463.0	383.7	1281.5	2876463.0	445.5
	60130	491.8	208247.0	2361.6	301.3	208247.0	1446.6
	60860	547.6	2053041.0	266.7	1657.8	2053041.0	807.5
	<b>total</b>	<b>3645.2</b>	<b>8710477.0</b>	<b>418.5</b>	<b>4862.7</b>	<b>8710477.0</b>	<b>558.3</b>
<b>Age hardening</b>	60140	0.0	1819688.0	0.0	170.2	1819688.0	93.5
	60210	63.3	2876463.0	22.0	138.6	2876463.0	48.2
	60240	138.4	3572726.0	38.7	151.7	3572726.0	42.5
	<b>total</b>	<b>201.7</b>	<b>6449189.0</b>	<b>31.3</b>	<b>290.3</b>	<b>6449189.0</b>	<b>45.0</b>



<b>Anodizing</b>	33170	2005.3	3052764.0	656.9	2931.2	3052764.0	960.2
	EAKS9352						
<b>Polishing</b>	80	0.0	3052764.0	0.0	387.0	3052764.0	126.8

The age hardening data represents the required energy for the different profiles, grouped by the process that is required. The row labeled 60210 shows the age hardening energy consumption for the extrusion of the 2.87 million kg of the profile in row labeled 60220. Similarly, age hardening row 60240 is the sum of the profiles in extrusion rows 60170-60190, which all undergo the same age hardening process.

We can also compare the energy consumption of the 6 presented profiles to the energy consumption of the two case study profiles in order to validate the case study measurements. Figure S2 below shows the plotted gas and electricity consumption of the case study, industry profiles, and the profile modeled in the sensitivity study (Table A4). The case study profiles utilized an electric billet heating furnace and did not have any gas consumption, therefore we compare the profiles using contours of constant total direct energy consumption. We can see that the case study profiles have energy consumption values that fall slightly above the average (LIFT Rectangular Solid: 1010 kWh/ton; LIFT 80-20 T-Slot Bar: 1020 kWh/ton; European extruder Average: 980 kWh/ton), but well below the European extruder's most energy intensive



profile (3810 kWh/ton).

Figure A2: Comparison of energy consumption for case study and European extruder profiles.

### A.2.2 Derivation of inventory values for Table 3 of main article

To convert the consumption values from Table A2 to the per kg values presented in Table A3 necessary for our global models we simply apply a unit mass conversion. The values provided by the European extruder are already in units of energy per mass unit produced, and therefore already account for the production of scrap material. Table A3 below shows the values produced for Table 2.3 in the main text. We do not include the process data provided for the billet casting process (gas furnace melting, casting, homogenization) as these are represented in the global model by data from the ecoinvent database (Wernet et al., 2016).

Table A3: Derived inventory values for Table 2.3 of main text.

<b>Average 2011</b>	<b>Gas</b>		<b>Electricity</b>	
<b>Process</b>	specific cons. (kWh/ton)	specific cons. (therm/kg)	specific cons. (kWh/ton)	specific cons. (kWh/kg)
Gas furnace melting	869.59	-	58.18	-
Casting	133.95	-	8.96	-
Homogenization	204.86	-	64.94	-
Extrusion - soft alloy	418.00	1.43E-02	558.25	5.58E-01
Age hardening	31.00	1.06E-03	45.00	4.50E-02
Anodizing	656.87	2.24E-02	960.18	9.60E-01
Polishing	0.00	-	126.76	-

Additionally we do not include the European extruder's data for the electricity consumption of the extrusion process, as we represent this in the global model through use of the ideal energy expected for the given profile and the energy efficiency of the extrusion press derived in the case study. Also assumed to be included in the extrusion electricity consumption value provided by the European extruder is the electricity consumed in pre-heating the billets, maintaining the heat of the press container, as well as the billet shear and other supporting processes. In our global model we represent these, with the exception of pre-heating electricity, using values measured in our case study. We can then compare this total estimated electricity consumption in the extrusion process to the data provided by the European extruder in order to validate the accuracy of our method.

At the industry average yield of 75.5%, our modeled profile is estimated to consume 0.42 kWh/kg profile. This is approximately 25% lower than the industry provided 0.56 kWh/kg profile, a difference that can be explained mostly by the missing data in our model of preheat furnace electricity. We include both the industry-reported value as well as our derived value of electricity consumption to allow the reader their own choice of estimate.

### A.3 Global parametric model and uncertainty analysis

### A.3.1 Mechanical energy required for extrusion

The theoretically required energy to deform the billet can be estimated by summing the area under a force displacement curve (Figure A3), with force decreasing from starting force,  $F_{start}$  to ending force,  $F_{end}$ , over length of billet,  $L_{billet}$ , as seen in equation A2 (Groover, 2010).

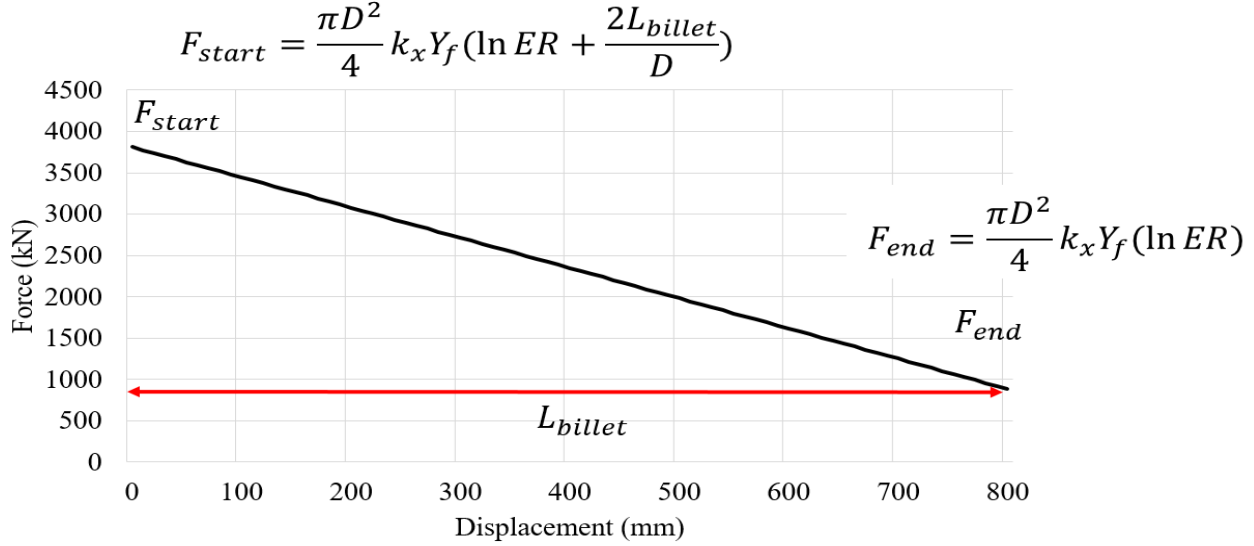


Figure A3: Ideal force vs displacement graph for extrusion of one billet.

$$E_{mech} = \frac{F_{start} + F_{end}}{2} L_{billet} \quad (A1)$$

The force is estimated based on the area of the billet and the extrusion pressure (Groover, 2010). The equation uses the billet length, billet diameter ( $D_{billet}$ ), billet material yield stress ( $Y_f$ ), the shape factor of the profile ( $K_x$ ), and the extrusion ratio ( $ER$ ). The starting force and ending force can then be derived (equations A2 and A3). The term in equation A2 dependent on the extrusion ratio describes the energy required for deformation of the extruded material, while the term dependent on the geometry of the billet ( $L_{billet}$  and  $D_{billet}$ ) describes the force required to overcome the friction between the billet and container walls and is therefore not present in the ending force.

$$F_{start} = \frac{D_{billet}^2}{4} K_x Y_f \left( \ln (ER) + \frac{2L_{billet}}{D_{billet}} \right) \quad (A2)$$

$$F_{end} = \frac{D_{billet}^2}{4} K_x Y_f \ln (ER) \quad (A3)$$

The shape factor is an empirically determined correction factor that accounts for differences in profile shape and its effect on the extrusion force by a comparison of the actual perimeter of the profile ( $P_{tot}$ ), and the ideal perimeter if the profile was a circle of the same area ( $C_{eq}$ ) (Equation A4).

$$K_x = 0.98 + 0.02 \left( \frac{P_{tot}}{C_{eq}} \right)^{2.25} \quad (A4)$$

Using these equations, we predict an ideal energy of deformation of 1.97 MJ and 1.56 MJ for the first and second profile respectively.

### A.3.2 Example profile inputs

Table A4: Example profile inputs used to perform sensitivity analysis in main text (Figure 2.5)

Profile parameter	Value
Alloy	6082
Yield Strength, $Y_f$ MPa	17.5
Process Yield, $\alpha$ %	76.3
Speed of extrudate, $V$ m/min	14.5
Extrusion press energy efficiency, $\eta_{press}$ %	7.25
Billet preheat energy efficiency, $\eta_{preheat}$ %	21
Mass produced, $M_{produced}$ kg	63,000
Linear density, $\lambda$ kg/m	1
Mass billet, $M_{billet}$ kg	124.4
Length billet, $L_{billet}$ mm	1117.6
Diameter billet, $D_{billet}$ mm	228.6
Diameter Container, $D_{container}$ mm	228.6
Profile perimeter, $P_{tot}$	729
Equivalent circumference, $C_{eq}$ mm	140.28
Circumscribing circle diameter, $CCD$ mm	146
Shape factor, $S$	5
Extrusion ratio, $ER$	26.2
Heat treatment	Yes
Surface finish	None
Recycled Content, $R$ %	54

Billet Temperature, $T_{billet}$ °C	494
Container Temperature, $T_{container}$ °C	426
Die Temperature, $T_{die}$ °C	454
Die Mass, $M_{die}$ kg	86.6
Die Mass Removed, $M_{removed}$ kg	26.0
Die Lifespan, $L_{die}$ kg <sub>profile</sub>	63,000
Minimum mechanical energy to extrude the billet per kg of billet, $e_{mech}$ MJ/kg	11.8

Table A5: Yield strengths of common extrusion alloys at extrusion temperatures.

Alloy	Yield Strength, $Y_f$ (MPa)
6061	15
6063	11
6082	17.5
7005	35
7075	80

### A.3.3 Uncertainty analysis

Figure A4 below shows the results of the uncertainty analysis for the profile described in A.3.2 plotted on the graph of the mean costs and impacts using industry average values. The error bars represent one standard deviation above and below the mean of the current industry standard conditions for AA6082 (76.3% forming yield, 54% recycled content, 21% billet preheat efficiency, 7.25% press efficiency, 14.5 m/min extrusion rate).

The uncertainty is equal to \$0.40 in costs (11.4%), 1.03 kg CO<sub>2</sub>eq / kg profile (10.9%) and 12.1 MJ / kg profile (10.5%) at the average industry values. The source of the majority of uncertainty comes from the intrinsic billet environmental impacts as well as the billet and wage costs.

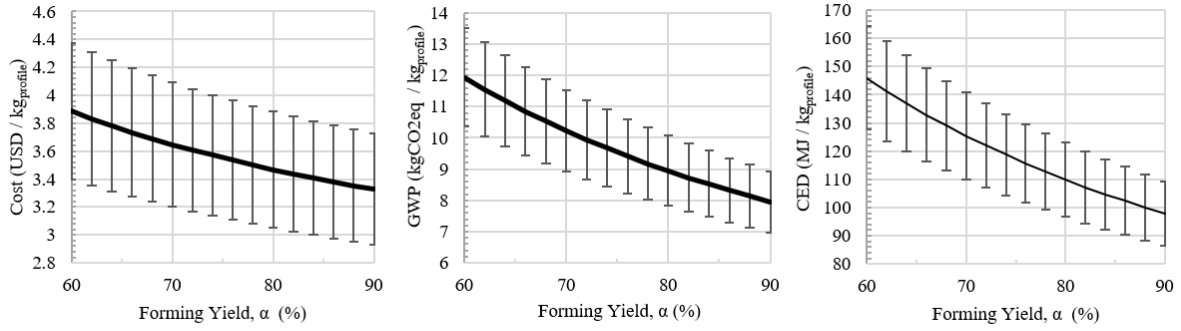


Figure A4: Uncertainty in Cost, GWP and CED for the modeled profile.

#### A.4 Data Reconciliation

This section will present the initial values used in the reconciliation optimization, as well as the results of the optimization and analysis of the residuals that were found. The methods used for reconciliation optimization and cataloging are presented in Zhu et al. (2019) and adapted here. Table A6 shows the node coordinate system used in this analysis.

Table A6: Node coordinate system used in this analysis.

Node in MFA	Coordinate
Primary Aluminum Production	1
Primary Ingot Production	2
End-of-life Scrap	3
Primary Billet Production	4
Secondary Billet Production	5
North American Extrusion	6
North American Fabrication	7
Construction	8
Transportation	9
Consumer Durables	10
Electricity and Energy	11
Machinery	12
North American Consumption	13
Imports	14
Exports	15
Scrap	16

### A.4.1 Wire frame map

Figure A5 below depicts the wireframe map that was used as a guide in material flow analysis of the extrusion industry. The wireframe map was built from discussion with industry experts. The nodes are labeled with their coordinate, and the flows are labeled to represent which coordinates they connect (on the basis of From.To). Note that an MFA variable that refers to either the scrap generated, or the associated yield is designated by a third index, “x.x.2” for scrap flows, and “x.x.3” for yields.

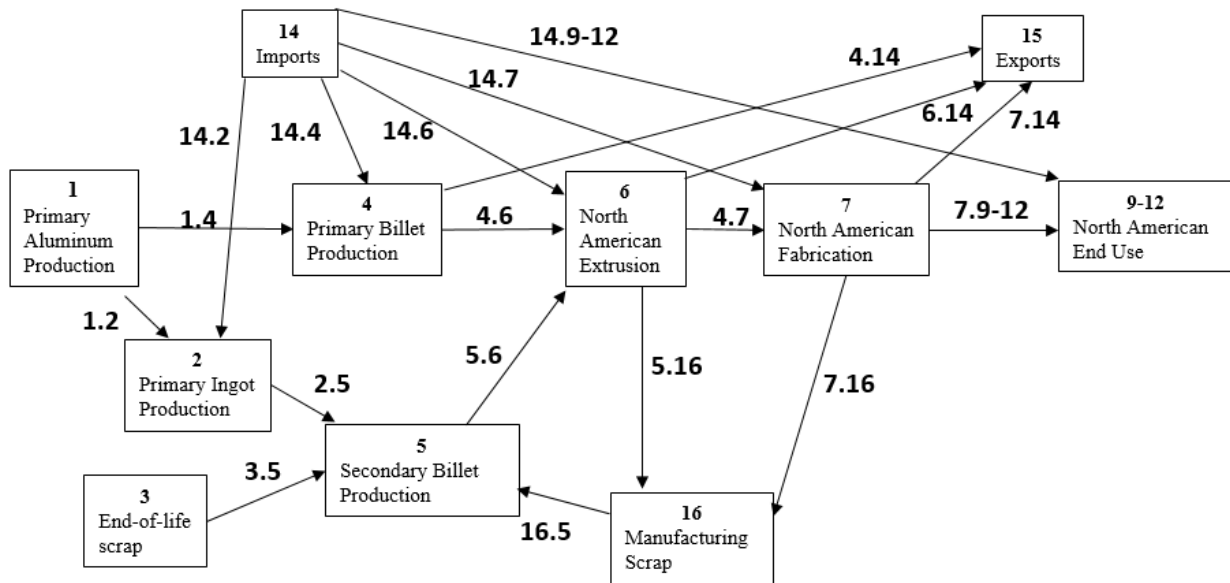


Figure A5: Wireframe map of aluminum extrusion industry.

### A.4.2 Initial values

Table A7 below lists the flows present in the construction of the extrusion industry MFA. The source of the initial value data is also shown, with the list of sources included in Table A16. The initial values used are derived from the data gathered, presented in Section A.5. In the case of mass balanced initial values, the exact calculations used to derive the values is included in Table A17.

Table A7: Initial values and reconciled results of all data points in MFA.

Flow Coordinate	Description	Initial Value (Mt unless a yield)	Reconciled Result (Mt unless a yield)	Source for initial value
1.2	Primary Aluminum to Primary Ingots	0.456	0.440	Mass Balance

Flow Coordinate	Description	Initial Value (Mt unless a yield)	Reconciled Result (Mt unless a yield)	Source for initial value
1.4	Primary Aluminum to Primary Billet Production	0.654	0.650	Mass Balance
1.18	Primary Aluminum Production Node In	1.110	1.090	Mass Balance
1.19	Primary Aluminum Production Node Out	1.110	1.090	Mass Balance
1.20	Primary Aluminum Yield <sup>1</sup>	1.000	1.000	2
2.2	Primary Aluminum Ingots to Primary Aluminum Ingots	0.037	0.035	Mass Balance
2.5	Primary Aluminum Ingot to Secondary Billet Production	0.764	0.740	Mass Balance
2.17	Primary Aluminum Ingot to Losses	0.021	0.020	Mass Balance
2.18	Primary Aluminum Ingot Node In	0.821	0.800	Mass Balance
2.19	Primary Aluminum Ingot Node Out	0.764	0.740	Mass Balance
2.20	Primary Aluminum Ingot Yield <sup>1</sup>	0.930	0.930	2
2.21	Primary Aluminum Ingot Unconventional	0.288	0.280	1,9
2.21.2	Primary Aluminum Ingot Unconventional (2)	0.045	0.045	14
3.5	End of Life Scrap to Secondary Billet Production	0.263	0.261	Mass Balance
3.18	End of Life Scrap Node In	0.263	0.261	Mass Balance
3.19	End of Life Scrap Node Out	0.263	0.261	Mass Balance
3.20	End of Life Scrap Yield <sup>1</sup>	1.000	1.000	Mass Balance
3.21	End of Life Scrap Unconventional	0.100	0.100	1
4.4	Primary Billet Production to Primary Billet Production	0.031	0.031	Mass Balance
4.6	Primary Billet Production to Extrusion	0.600	0.596	4
4.15	Primary Billet Production to Exports	0.040	0.040	4
4.17	Primary Billet Production to Losses	0.014	0.015	Mass Balance
4.18	Primary Billet Production Node In	0.685	0.682	Mass Balance
4.19	Primary Billet Production Node Out	0.640	0.636	Mass Balance
4.20	Primary Billet Production Yield <sup>1</sup>	0.934	0.933	2,3
4.21	Primary Billet Production Unconventional	0.045	0.045	14



Flow Coordinate	Description	Initial Value (Mt unless a yield)	Reconciled Result (Mt unless a yield)	Source for initial value
5.5	Secondary Billet Production to Secondary Billet Production	0.119	0.118	Mass Balance
5.6	Secondary Billet Production to Extrusion	2.460	2.440	4
5.17	Secondary Billet Production to Losses	0.055	0.080	Mass Balance
5.18	Secondary Billet Production Node In	0.266	2.640	Mass Balance
5.19	Secondary Billet Production Node Out	0.246	2.444	Mass Balance
5.20	Secondary Billet Production Yield <sup>1</sup>	0.934	0.926	2,3
5.21	Secondary Billet Production Unconventional	0.045	0.045	14
6.7	Extrusion to Fabrication	3.000	2.735	4
6.15	Extrusion to Exports	0.169	0.169	4
6.16	Extrusion to Scrap	1.172	0.895	Mass Balance
6.18	Extrusion Node In	3.825	3.800	Mass Balance
6.19	Extrusion Node Out	3.169	2.904	Mass Balance
6.20	Extrusion Yield <sup>1</sup>	0.730	0.764	6,5
6.21	Extrusion Unconventional	0.758	0.760	8
6.21.2	Extrusion Unconventional	2.490	2.490	8
7.8	Fabrication to Construction	0.948	0.987	4
7.8.2	Fabrication to Construction Scrap	0.117	0.172	4
7.8.3	Fabrication to Construction Yield <sup>1</sup>	0.890	0.852	4
7.9	Fabrication to Transportation	0.727	0.752	4
7.9.2	Fabrication to Transportation Scrap	0.187	0.239	4
7.9.3	Fabrication to Transportation Yield <sup>1</sup>	0.795	0.758	4
7.10	Fabrication to Consumer Durables	0.204	0.206	4
7.10.2	Fabrication to Consumer Durables Scrap	0.068	0.072	4
7.10.3	Fabrication to Consumer Durables Yield <sup>1</sup>	0.750	0.741	4
7.11	Fabrication to Electrical and Energy	0.228	0.230	4
7.11.2	Fabrication to Electrical and Energy Scrap	0.050	0.055	4

Flow Coordinate	Description	Initial Value (Mt unless a yield)	Reconciled Result (Mt unless a yield)	Source for initial value
7.11.3	Fabrication to Electrical and Energy Yield <sup>1</sup>	0.818	0.807	4
7.12	Fabrication to Machinery	0.168	0.169	4
7.12.2	Fabrication to Machinery Scrap	0.080	0.084	4
7.12.3	Fabrication to Machinery Yield <sup>1</sup>	0.670	0.662	4
7.16	Fabrication to Scrap	0.589	0.625	Mass Balance
7.18	Fabrication Node In	3.236	2.969	Mass Balance
7.19	Fabrication Node out	2.647	2.344	Mass Balance
7.20	Fabrication Yield <sup>1</sup>	0.818	0.790	4,7,13,15
8.13	Construction to North American Consumption	1.076	1.115	Mass Balance
8.15	Construction to Exports	0.007	0.007	4,7,13,15
8.18	Construction Node In	1.083	1.121	Mass Balance
8.19	Construction Node Out	1.083	1.121	Mass Balance
9.13	Transportation to North American Consumption	0.838	0.863	Mass Balance
9.15	Transportation to Exports	0.077	0.077	4,7,13,15
9.18	Transportation Node In	0.915	0.940	Mass Balance
9.19	Transportation Node Out	0.915	0.940	Mass Balance
10.13	Consumer Durables to North American Consumption	0.23	0.232	Mass Balance
10.15	Consumer Durables to Exports	0.003	0.003	4,10
10.18	Consumer Durables Node In	0.233	0.232	Mass Balance
10.19	Consumer Durables Node Out	0.233	0.232	Mass Balance
11.13	Electrical and Energy to North American Consumption	0.258	0.260	Mass Balance
11.15	Electrical and Energy to Exports	0.011	0.011	4,10
11.18	Electrical and Energy Node In	0.269	0.271	Mass Balance
11.19	Electrical and Energy Node Out	0.269	0.271	Mass Balance
12.13	Machinery to North American Consumption	0.171	0.172	Mass Balance
12.15	Machinery to Exports	0.010	0.010	4,10

Flow Coordinate	Description	Initial Value (Mt unless a yield)	Reconciled Result (Mt unless a yield)	Source for initial value
12.18	Machinery Node In	0.181	0.182	Mass Balance
12.19	Machinery Node Out	0.181	0.182	Mass Balance
14.2	Imports to Primary Aluminum Ingots	0.328	0.319	Mass Balance
14.6	Imports to Extrusion	0.765	0.759	4
14.7	Imports to Fabrication	0.236	0.234	4
14.8	Imports to Construction	0.135	0.135	4,7,13,15
14.9	Imports to Transportation	0.188	0.188	4,7,10,11,12
14.10	Imports to Consumer Durables	0.029	0.029	4,10
14.11	Imports to Electrical and Energy	0.041	0.041	4,10
14.12	Imports to Machinery	0.013	0.013	4,10
14.18	Imports Node In	1.707	1.718	Mass Balance
14.19	Imports Node Out	1.707	1.718	Mass Balance
14.21	Imports Unconventional	0.400	0.400	9
16.5	Scrap to Secondary Billet Production	1.580	1.520	Mass Balance
16.21	Scrap Unconventional	0.760	0.760	8
16.21.2	Scrap Unconventional (2)	0.600	0.576	1

1: Unit for yield is a fraction of 1, not Mt.

#### A.4.3: Methods for calculating residuals in the least squares optimization

In Kopec et al. (2016) and Zhu et al. (2019)'s analysis, the normalized residual  $r_{ij}$  between the final MFA variable  $x_i$  and a data record  $\hat{x}_{i,j}$  is calculated using Equation A5.

$$r_{i,j,original} = \frac{(x_i - \hat{x}_{i,j})}{\hat{x}_{i,j}} \quad (A5)$$

While in this analysis, a new equation for the residual calculation is used (Equation A6). In the new residual calculation, the difference between  $x_i$  and  $x_{i,j}$  is normalized to the average of all corresponding data records for variable  $x_i$  (from  $j=1$  to  $J$ ). This is to prevent the bias due to uneven distribution of data records.

$$r_{i,j,avg} = \frac{J_i(x_i - \hat{x}_{i,j})}{\sum_{j=1}^J \hat{x}_{i,j}} \quad (A6)$$

Here we demonstrate the advantage of using the average data records normalization method (Equation A6) compared to the original method. Assume for an MFA variable  $x_1$ , three data record values are collected equal to **5 kt, 10 kt, and 15 kt** are collected. In this example, we will assume that each of the data

records has the same confidence score weighting, equal to 1. The weighted sum of residuals for different potential values of the MFA variable,  $x_1$ , is shown in Figure S6. The optimized MFA variable,  $x_1$ , calculated using the two residual calculation methods are marked as dashed lines in Figure A6.

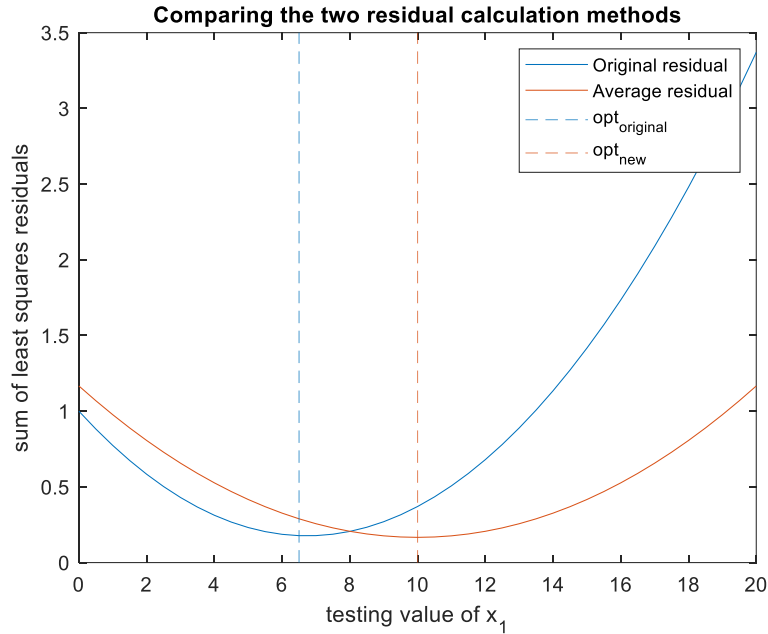


Figure A6: Optimization result for different  $x_i$  values (in kt) for equation 5 (original residual calculation from Kopec et al. and Zhu et al.) and equation A6 (new, average, residual calculation used in this work).

The optimized  $x_i$  value equals 6.5 kt using the original residual calculation methods (blue dashed line) and 10 kt using the new average residual calculation methods (orange dashed line). As can be seen by considering the data records collected were equal to 5 kt, 10 kt, and 15 kt, the original residual calculation method is biased towards calculating smaller MFA variables. On the contrary, the new average residual normalization method avoids this bias.

#### A.4.4 Optimization results

Zhu et al.’s (2019) nonlinear least squares regression model, adapted from Kopec et al.’s (2016) earlier work, and further adapted by using a non-biased normalized residual calculation (Equation A6) was used to determine a set of mass-balanced flows from these original values. Figure A7 shows the path of the feasibility and objective function over the 201 iterations the optimization required to converge on a mass balanced solution. Through the optimization process, the objective function was increased by 3500% from 0.0004 to 0.014. The optimization was implemented with Matlab’s fmincon algorithm using the “interior-point” method. It took 201 iterations for the objective function to converge (Figure A7): 20 minutes on an AMD Ryzen 5 2600 CPU, 3.40GHz with 16 GB of 3200 MHz RAM. The optimization achieved mass

balance after an initial maximum constraint violation of 0.51 Mt (corresponding to a discrepancy between reported billet consumption, extrusion production and yield rate) and reduced the objective function by 42% from a maximum of 0.024 during mass balancing to 0.014 at convergence (Figure A7). The code and data used for this MFA reconciliation is available for download (see A.6.3).

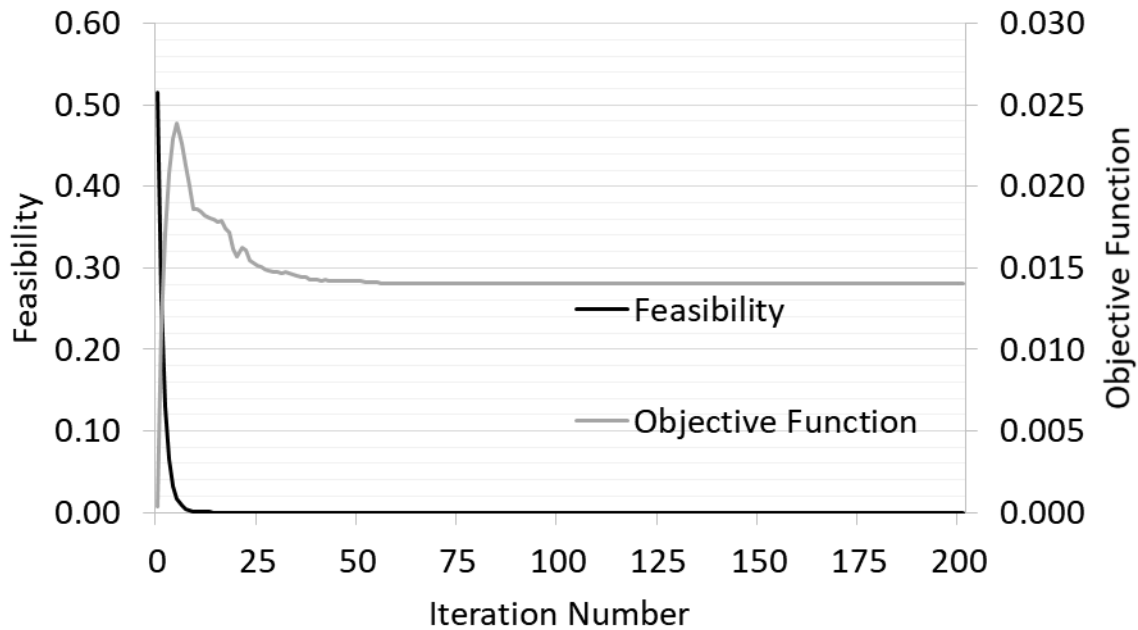


Figure A7: The feasibility and objective function value of the optimization as it converged to the final solution.

## A.5 Flow estimate sources and derivations

This section describes the source, and where necessary the derivation, of the empirical data records on the North American 2018 extrusion mass flow used in the reconciliation described in section A4. A summary of all the data records (and sources) used is provided in Table A15, in Section A6.3.

### A.5.1 Summary of aluminum processing and extrusion billet making process yields

The production of primary aluminum is derived from the volume and metallurgical composition of primary and secondary extrusion billet production. The breakdown of the extrusion billet ecosystem in North America (U.S. and Canada) is shown in the table below (Sattlethight, 2019).

Table A8: North American Extrusion Billet Ecosystem.

<b>Supply</b>	<b>Quantity [Mt]</b>	<b>Quantity (%)</b>
Primary Billet	0.60	15.5
Secondary Billet	2.46	63.7
Billet Imports	0.77	19.8
Billet Exports	0.04	1.0

It is assumed that all billet imports and exports are primary billets. Therefore, the North American production of primary billets is equal to the sum of the primary billets extruded and the billets exported, and the North American production of secondary billet is equal to the secondary billets extruded.

It is assumed that all primary billets are produced directly by primary aluminum producers and therefore no primary aluminum ingots are used in the production of primary aluminum billets. An environmental product declaration (EPD) (Mulholland, 2016) performed on extrusions made by members of the Aluminum Extruders Council (AEC) in 2015 shows that 27.5% of secondary billet volume is sourced from primary aluminum, 40.6% of which was imported from international producers. Similarly, Michigan Extruded (2020) report that 30% of secondary billet is sourced from primary aluminum, in addition to 60% coming from post-industrial scrap, and 10% coming from post-consumer, or end-of-life, scrap. It is assumed that all primary aluminum used in casting secondary billet is from primary aluminum ingot, and not directly from the molten primary production flows.

Primary billet production is found to have an internal recycling rate of 4.5%, and a loss of 1.5% (Rio Tinto, 2020). These rates are assumed to be equal for secondary billet production and primary ingot production.

### **A.5.2 Extrusion to fabrication**

Each year the AEC collects data on the extrusion production of their members, including the end-use category destination of the extrudate. In this extrusion stage the billets are extruded into semi-finished goods, which will be shipped to fabricators that apply final changes before being assembled into end-use goods. The AEC's (Sattlethight, 2019) 2018 survey finds that 2.95 Mt of extrudate was produced domestically. 0.17 Mt of domestic production was exported at this stage as semi-finished extrusions, while 0.24 Mt of extrusion profiles were imported to be fabricated.

Table A9: North American Extrusion

<b>Supply</b>	<b>Quantity [Mt]</b>	<b>Quantity (%)</b>
Construction	1.065	33.4
Transport	0.915	28.7

Consumer Durables	0.273	8.6
Electronic and Energy	0.279	8.8
Machinery	0.252	7.9
Export	0.168	5.3
Import	0.236	7.4

The supply of extrusion is listed by end-use category destinations, however, the data is treated homogeneously at this stage, and the segregation will have no effect within the extrusion process in this model. Imported goods to the fabrication node include extruded profiles that are not yet fabricated, or assembled into final goods or systems. Goods exported directly after extrusion are assumed to be the same.

The total material lost to scrap during the extrusion process in this model is comprised of several different sources of scrap described in section 3.3 (see Figure 6). However, the model treats the scrap flow homogeneously, instead using the yield reported by the AEC (Mulholland, 2016) and the EAA (European Aluminum Association, 2018): 68% and 78% respectively.

### **A.5.3 Shape and alloy of extruded goods**

Extruded aluminum profiles can be described as one of three different categories; rod and bar, tube, or shaped (anything that isn't one of the other two categories). The profiles can also be formed from any of the several dozen different aluminum extrusion alloys (Misiolek and Kelly, 2005). It is important to differentiate the production volume of each of these shape and alloy categories due to their drastically different metal flows during the extrusion process. Understanding the weighted importance of each profile-type and alloy will allow research to be primarily focused on the profiles and materials which will have the greatest impact.

The AEC (Consulting Collaborative, 2017) in their 2016 end-use survey report the percentage of North American aluminum extrusion consumption that is represented by each of these shape categories. According to the AEC the consumption is dominated by 82.3% of shaped components, with 9.2% and 8.5% being rod and bar, and tube respectively. In this same report, the AEC also breaks down the shape and average mass of extruded parts used in the auto industry. Rod and bar extrusions used in cars is comprised of just the transmission, weighing in at an average 1.9 kg, or 14.2% of the 13.2 kg of extrusions used. Tube extrusions include parts of the drive shaft and heat exchangers, for a combined 2.6 kg, or 19.9% of total extrusions mass. The remaining 8.7 kg, or 65.9%, of extrusions fall into the shape category, including components of the interior, seats, trim, bumper, etc. Machinery is the category that the AEC lists as including general components such as warehoused tubes and bar-stock. Therefore we assume that the category is segregated by shape evenly, with one-third comprised of each shape-type.

The AEC (2020) also lists the alloys that the majority of these automotive parts are most commonly made of. Bumpers and body structures are a combination of 6xxx and 7xxx series alloys, while the remaining parts excluding the heat exchanger are fully 6xxx series alloys. Sources in literature (Cooper and Allwood, 2012) and extrusion company documentation (Gabrian International, 2021; Tri-State Aluminum, 2020) state that 1xxx and 3xxx series alloys are predominantly used for heat exchangers in all applications. For parts with reported mixed compositions, it is assumed to be an even split unless otherwise stated. This results in the automotive industry having a representation of 8.4% 1xxx and 3xxx series alloys each, 15% 7xxx, and 68.3% 6xxx.

Figure A8 below shows the resulting flow of various alloy extrusions to the construction and transportation end-use categories.

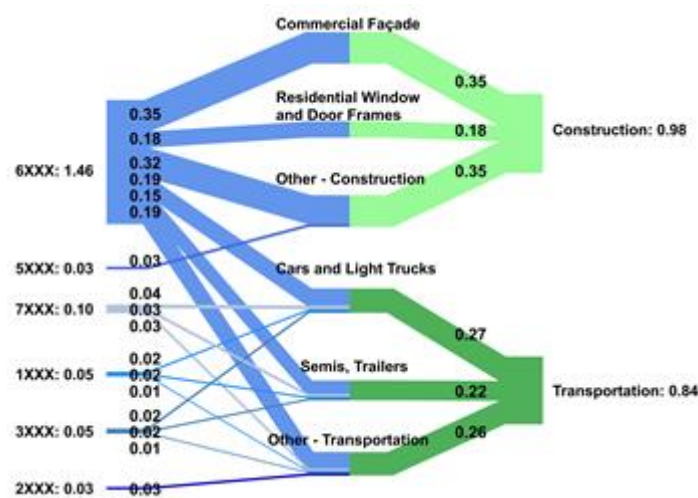


Figure A8: The flow of extrusions to end-use categories, by alloy.

#### A.5.4 Fabrication to end-use goods

The fabrication yield rates and production quantities of the different extrusion flows accounting for the various end-use categories are listed Table A10. These are then weight-averaged to determine the overall fabrication yield rate.

Table A10: North American Fabrication.

Type	Yield Rate [%]	Pre-Fab [Mt]	Post-Fab [Mt]
Construction	89	1.065	0.959
Transport	79.5	0.915	0.824
Consumer Durables	75	0.273	0.246
Electrical and Energy	81.8	0.279	0.251
Machinery	67	0.252	0.227



Table A11: North American fabrication by end use product.

<b>Construction</b>	
Product	% of end-use category
Commercial Façade	40
Residential windows and doors	20
<b>Transportation</b>	
Product	% of end-use category
Trailers, semis	29.0
cars, light trucks	36.0
truck/bus	8.0
RV	13.0
<b>Electrical and Energy</b>	
Product	% of end-use category
Alternative Energy	22.0
Power Transmission	17.0
Lighting	11.0
Electronics, Communication	10.0
Bus Bar	10.0
Electrical Equipment	9.0
<b>Consumer Durables</b>	
Product	% of end-use category
Boating	25.0
Furniture	25.0
Sporting Goods	10.0
Air Conditioning	21.0
<b>Machinery</b>	
Product	% of end-use category
Industrial, Ag, Mining	18.0
Process Industries	16.0
Ladders, Scaffolds	15.0
General Components	13.0
Professional	6

These fabrication yield rates are used in Cullen and Allwood's (2013) global flow of aluminum, for their flows of fabricated extrusions, however, the end-use categories were slightly adapted for use in this MFA. Table A11 shows the product types that contribute to each end-use category in this extrusion MFA, as reported by the AEC annual survey (Sattlethight, 2019). Table A11 shows only the product types that accounted for greater than 5% of their respective end-use category.

Cullen and Allwood separated their building and construction flows into three different categories (structural, non-structural, and infrastructure), however, the fabrication yield rate was the same for all three, 89%, and so it was directly applied to the above construction category.

In the transport sector, Cullen and Allwood list just two categories: cars & light trucks, and trucks, buses, train, planes and ships, with fabrication yield rates of 81 and 73% respectively. Cars & light trucks is the largest sector of the transportation industry flows in the AEC’s end use survey (Sattlethight, 2019), with trucks and busses being the closest match to Cullen and Allwood’s second category. Ships are not included in transportation in the AEC’s segregation of extrusion flows, but instead are a large part of consumer durables. To adapt Cullen and Allwood’s data, the fabrication yield rate for the two sectors were averaged based on the weighting of the AEC’s end-use categories. This weighted yield rate, 79.5%, was applied to the remainder of the transport industry.

As was mentioned earlier, consumer durables included boating products in the AEC’s report, however with no way to exclude it from Cullen and Allwood’s data the reported value of 75% fabrication yield was used for the category. The fabrication yield for machinery was also directly applied, for a rate of 67%. There was no reported extrusion flowing to electricity and energy in Cullen and Allwood’s MFA, so the weighted average fabrication yield of the other four categories was applied in this sector of the MFA.

#### A.5.4 End-use products indirect trade

The estimated import and export of post-fabrication end-use goods by category are shown in the table below.

Table A12: North American End-use Indirect Trade.

Type	Import [kt]	Export [kt]
Construction	134.93	6.98
Transport	188.28	76.58
Consumer Durables	28.77	3.08
Electrical and Energy	40.84	10.63
Machinery	12.69	10.47

The category values for imported and exported end-use mass are estimated using the import and export value of known extruded products. The table below shows the products derived from Comtrade (UN, 2018), and their estimated aluminum extrusion content derived in sections A5.4.1-A5.4.5.

Table A13: Comtrade North American Extrusion Data.

<b>Construction</b>
---------------------

Comtrade Label	Data	Import [kt]	Export [kt]	Quantity Extrusion [%]	Extrusion Import {kt}	Extrusion Export [kt]
Aluminum Doors, windows, frames and thresholds		84.32	4.36	32.0	26.99	1.40
Other		-	-	-	107.95	5.58
<b>Transportation</b>						
Comtrade Label	Data	Import [kt]	Export [kt]	% Extrusion	Extrusion Import [kt]	Extrusion Export [kt]
Trailers, semis		129.46	296.44	1.0	1.29	2.96
Cars and Light Trucks		9951.26	3718.73	1.2	119.42	44.62
Heavy Truck		351.33	480.81	0.7	2.46	3.37
Other		-	-	-	65.11	25.62
<b>Electrical and Energy</b>						
Product		Import [kt]	Export [kt]	% Extrusion	Extrusion Import {kt}	Extrusion Export [kt]
Other		-	-	-	40.84	10.63
<b>Consumer Durables</b>						
Comtrade Label	Data	Import [kt]	Export [kt]	% Extrusion	Extrusion Import {kt}	Extrusion Export [kt]
People and Cargo Moving Vessels		448.52	59.79	1.0	4.49	0.60
Pleasure craft		127.66	38.86	1.0	1.28	0.39
Air Conditioning		747.40	43.23	1.0	7.47	0.43
Other		-	-	-	15.54	1.67
<b>Machinery</b>						
Comtrade Label	Data	Import [kt]	Export [kt]	% Extrusion	Extrusion Import {kt}	Extrusion Export [kt]
Agricultural Machinery		82.57	68.13	0.7	0.58	0.48
Other		-	-	-	12.11	9.99

#### A5.4.1 Construction quantity extrusion estimates

For data taken from Comtrade (UN, 2018), it is often difficult to assess how the product types align with the categories listed in the AEC end-use survey (Sattlethight, 2019). For example, in the construction sector Comtrade has data for aluminum doors, windows, frames and thresholds. This is likely residential windows and doors, however it is probable that this category also includes the glass of the windows and may even include the other AEC product type of commercial façade. Because of their high level of

similarity, the process to determine the percentage of this data which refers to aluminum extrusions is the same regardless of the inclusion of commercial façade; both the façade and the windows and doors include a frame of aluminum with a glass insert. HGH Hardware (2021) has an aluminum sliding door frame that weighs 176 pounds for both the frame and the glass together. The glass has three .25" thick panels of 98.5"x 20" each, which Dulles Glass and Mirror (2021) estimates to weigh 40 lbs each. This would leave the weight of the aluminum to be 56 pounds, or 32% of the total weight. For this study it is assumed that 100% of the weight that is not accounted for in glass is aluminum, and that 100% of this aluminum is produced through extrusion; attachment hardware such as nuts and bolts are assumed to be insignificant in mass. Origin Windows (2021) has a 60" x 60" window that weighs 110 lbs, estimated to be approximately 32% of the weight as well. Based on this value of percentage extrusions, it is found that there are roughly 27 kt of imported extrusions as a part of aluminum doors, windows, frames and thresholds.

In order to check whether this category accounts for both residential windows & doors as well as commercial façade, the ratio of imported to domestically extruded aluminum extrusions is calculated and compared to known values of other categories. The 27 kt of imported doors, windows, frames and thresholds would be 13% of post-fabrication domestically extruded residential windows & doors, or just 4% of the quantity if commercial façade was included. The same ratio for the known transport quantities (trailers, cars & light trucks, and heavy trucks) is 22%. It is therefore assumed that the commercial façade is not included in this Comtrade data point. To account for commercial façade and the other unlisted product types the ratio of imported to domestically produced extrusions is used. The same process is used to estimate the quantity of exports based on the residential windows and doors which has just 0.7% exports.

#### **A.5.4.2 Transport quantity extrusion estimates**

Ducker Worldwide (2017a) found the average light vehicle mass in 2015 was 1743 kg, and was predicted to be 1698 kg by 2020. The average light vehicle mass would therefore be estimated to be 1716 kg in 2018. Ducker Worldwide also reports that the average mass of aluminum in a light vehicle was 180 kg in 2015 and will be a predicted 212 kg in 2020. This extrapolates to an estimated 200 kg of aluminum per light vehicle in 2018. More specifically, extruded aluminum in a light vehicle reported in 2015 and predicted for 2020 is 16.4 and 22.3 kg respectively, for an estimated 20 kg extruded aluminum per light vehicle in 2018. This indicates that 10% of the aluminum mass in a light vehicle is from the extrusion process, and that close to 1.2% of all light vehicle mass is made up of extruded aluminum profiles. Autosteel (Schnatterly, 2010) reports that the average mass of a heavy truck is 6333 kilograms. The AEC (2021) finds that of this mass, heavy trucks have 456 kg of aluminum. If it is assumed that heavy trucks have the same portion of aluminum that is produced through extrusion as is found in light vehicles, they would contain 46 kg of extrusion per truck, or 0.7% of the total mass.

Comtrade (UN, 2018) has separate trade data for ‘trucks for the transport of goods’ and ‘trailers and semi-trailers’. It is assumed that the former refers to heavy trucks including the tractor portion of 18-wheelers, while the later refers to the trailer portion of these 18-wheelers and other trailers. These would both fall under the category of trailers, semis in AEC’s end-use survey (Sattlethight, 2019), however it is important to create a distinction as to what portion of this category and amount of domestic production each product type represents. The Comtrade import data for heavy truck is three times larger than the same for trailers and semi-trailers. Therefore it is assumed that the same ratio applies to the mass of extruded product, and so heavy truck accounts for  $\frac{3}{4}$  of the 29% of transport products that are allocated to semi-trailer/trailers in AEC’s survey (Sattlethight, 2019), or 22%, while the remaining 7% is the mass of the extrusions in the trailers.

The extruded mass of cars, light trucks, and heavy trucks, the three product types for which the extruded content is known, therefore accounts for 58% of transport extrusions. The amount of trailers and semi-trailers imported is known, but the quantity of extrusions within these products is not. It is therefore assumed that the weighted average extrusion quantity as a percentage of the imported mass of cars, light trucks and heavy trucks is applicable to trailers and semi-trailers. With trailers and semi-trailers included, the transportation sector is now 65% represented. For the remaining 35% it is assumed that the quantity of imports and exports are equal to the weighted average quantity of extrusions imported and exported of the known products as a percentage of the domestically post-fabrication extruded quantity. It is therefore estimated that 21.5% of the quantity of the remaining post-fabrication, domestically extruded transportation parts, including rail, bus and aircraft, are imported, and that 8.5% of the same quantity is exported.

#### **A5.4.3 Electrical and energy quantity extrusion estimates**

The Comtrade database (UN, 2018) has no data for products which the AEC’s end-use survey (Consulting Collaborative, 2017) identifies as Electrical and Energy sector. This sector only accounts for roughly 10% of the North American market, therefore, it is necessary to extrapolate trends found elsewhere in Comtrade data. It is assumed that the amount of imported and exported aluminum extrusions in this sector are proportional to the domestically post-fabrication extruded amounts at a rate equal to the weighted average of all other sectors. These rates are calculated to be 15% for imports and 3.9% for exports.

#### **A5.4.4 Consumer durables quantity extrusion estimates**

The boating products that are imported in the consumer durables end-use sector are most similar to the products found in the transport sector. While the build of a boat and various land vehicles is bound to be different, it is assumed in this study that the transport average percent aluminum extrusions is equal to the boat products, at 1% of the product’s mass. This results in an imported quantity equal to 8.5% of the

domestically post-fabrication extruded quantity. If this same percentage quantity of aluminum extrusions were assumed to apply to air conditioning, then the quantity of imported extrusions for air conditioning would be 11% of the quantity that is domestically extruded. These two ratios of domestic to imported extrusions are relatively in-line with the ratios seen in transportation and construction which together account for 70% of the total North American market. The boating and air conditioning products represent 46% of the consumer durable end-use sector according to AEC's end-use survey (Consulting Collaborative, 2017). Therefore the remaining 54% of this sector, including furniture and sporting goods, is assumed to have a quantity of imported and exported extrusions that match the weighted average import and export to post fabrication domestically extruded product ratio found in boating and air conditioning. The ratios are estimated to be 10.7% import and 1.1% export to post-fabrication domestically extruded product.

#### **A5.4.5 Machinery quantity extrusion estimates**

Comtrade (UN, 2018) does not have a large representation of the imports and exports of machinery end-use sector products identified by AEC's survey. The only category found was agricultural machinery, accounting for just 6% of the US domestically extruded profiles according to AEC's end use survey (Consulting Collaborative, 2017), assuming that the Industrial, Ag and Mining equipment each share an even split of the categories' 18%. Based on their likeness, it is assumed that the agricultural machinery shares a similar percentage of extruded material to the heavy truck found in the transport sector, 0.7%. The amount of imported extrusions in agricultural machinery is therefore found to be 5.7% of the total domestically produced agricultural machinery extrusions. This ratio is applied to the remaining 94% of the machinery sector that is unrepresented. Likewise, the ratio of exported to post-fabrication domestically extruded profiles is found to be 4.7%.

### **A.6 MFA structure**

#### **A.6.1 Full matrix**

The full matrix is shown in Figure A9 with each cell labelled using the cataloguing two-coordinate system.

Node	NodeT Row/Column	Primary Aluminum Production	Primary Aluminum Ingots	End-of-Life Scrap	Primary billet production	Secondary billet production	Extrusion	Fabrication	Construction	Transportation	Consumer Durables	Electricity and Energy
		1	2	3	4	5	6	7	8	9	10	11
Primary Aluminum Production	1	0	<b>1.2</b>	0	<b>1.4</b>	0	0	0	0	0	0	0
Primary Aluminum Ingots	2	0	<b>2.2</b>	0	0	<b>2.5</b>	0	0	0	0	0	0
End-of-Life Scrap	3	0	0	0	0	<b>3.5</b>	0	0	0	0	0	0
Primary billet production	4	0	0	0	<b>4.4</b>	0	<b>4.6</b>	0	0	0	0	0
secondary billet production	5	0	0	0	0	<b>5.5</b>	<b>5.6</b>	0	0	0	0	0
Extrusion	6	0	0	0	0	0	0	<b>6.7</b>	0	0	0	0
Fabrication	7	0	0	0	0	0	0	0	<b>7.8</b>	<b>7.9</b>	<b>7.10</b>	<b>7.11</b>
Construction	8	0	0	0	0	0	0	0	0	0	0	0
Transportation	9	0	0	0	0	0	0	0	0	0	0	0
Consumer Durables	10	0	0	0	0	0	0	0	0	0	0	0
Electricity and Energy	11	0	0	0	0	0	0	0	0	0	0	0
Machinery	12	0	0	0	0	0	0	0	0	0	0	0
Imports	14	0	<b>14.2</b>	0	0	0	<b>14.6</b>	<b>14.7</b>	<b>14.8</b>	<b>14.9</b>	<b>14.10</b>	<b>14.11</b>
Exports	15	0	0	0	0	0	0	0	0	0	0	0
Scrap	16	0	0	0	0	<b>16.5</b>	0	0	0	0	0	0

12 Machinery	13 North American Consumption	14 Imports	15 Exports	16 Scrap	17 Loss	18 Node In	19 Node Out	20 Yield Ratio	21 Unconventional
0	0	0	0	0	0	1.18	1.19	1.20	1.21
0	0	0	0	0	2.17	2.18	2.19	2.20	2.21
0	0	0	0	0	0	3.18	3.19	3.20	3.21
0	0	0	4.15	0	4.17	4.18	4.19	4.20	4.21
0	0	0	0	0	5.17	5.18	5.19	5.20	5.21
0	0	0	6.15	6.16	0	6.18	6.19	6.20	6.21
7.12	0	0	7.15	7.16	0	7.18	7.19	7.20	0
0	8.13	0	8.15	0	0	8.18	8.19	0	0
0	9.13	0	9.15	0	0	9.18	9.19	0	0
0	10.13	0	10.15	0	0	10.18	10.19	0	0
0	11.13	0	11.15	0	0	11.18	11.19	0	0
0	12.13	0	12.15	0	0	12.18	12.19	0	0
14.12	0	0	0	0	0	14.18	14.19	0	14.21
0	0	0	0	0	0	15.18	15.19	0	0
0	0	0	0	0	0	16.18	16.19	0	16.21

Figure A9: Network of nodes and flows represented in matrix form. Data entries represent the existence of flow between two nodes.



### A.6.2 Data confidence weighting

Table A14: Confidence weighting criteria for flow data sources.

Data quality criteria	Score range (1-4)	Weight
Coverage	4: >50% of industry	33%
	3: <50% of industry	
	2: Clusters of case studies	
	1: Single case study	
Frequency	4: Monthly	33%
	3: Annually	
	2: Infrequent	
	1: Lone data point	
Spatial boundary	4: <b>North America</b> only / Same process	33%
	3: US only / Parent process group	
	2: Other industrialized country/Similar process	
	1: Global/ Scaling from elsewhere in industry	
Weighted total score		
Confidence score (0-1)		

### A.6.3 Matrix node and flow data with weighting

Table A15 provides a list of all sources used in the reconciliation optimization method. Table A16 provides the confidence weighting of the data, and Table A16 shows the data as input into the MFA. The final 2018 North American extrusion flow (.xlsx file) and reconciliation Matlab code (.m file) can be downloaded from:

<http://remade.engin.umich.edu/extrusion.htm>

Table A15. The most important sources of material flow data used to create the aluminum extrusion MFA.

Type of Source	Sources	Types Of Data
Industry Associations	Aluminum Extruders Council (Consulting Collaborative, 2017; Mulholland, 2016; Sattlethight, 2019), International Aluminum Institute (IAI) (2021), European Aluminum Association (2018, 2013), International Energy Agency (2017)	Billet Production, end-use categories, secondary billet composition
International Trade Data	UN Comtrade (UN, 2018), USGS (2018)	Imports/Exports
Company Database	Norsk Hydro (Norsk Hydro, 2019, 2020a), Gabrian International (2020), Tri-state Aluminum (2020), Michigan Extruded Aluminum (2020)	End-use Categories, Alloy breakdown, Types and alloys of extruded products, secondary billet composition

Semi-structured Interviews	MI Metals (2019), Magnode Aluminum (2019), Superior Extrusion (2019), Rio Tinto (2020), Southern Aluminum Finishing Co. (2020), Ford Motor Company (2020), Norsk Hydro (2019, 2020a, 2020b), Kaiser Aluminum (2020), General Motors (2020), Mag Specialties (2020), Boeing (2020)	End-use Categories, Alloy Breakdown, Scrap flows
Industry Publications	Light Metal Age (Chien et al., 2018; Fielding, 2009; Grayson, 2017; Pinter, 2017), Ducker Analysis (Ducker Worldwide, 2017b, 2017a), Autosteel (Schnatterly, 2010)	Billet production, Import/Export, Scrap flows
Research Publications	Cooper and Allwood (2012), Cullen and Allwood (2013), Misiolek and Kelly (2015), Fourmann (2018), Bertram et al. (2017), Mahmoodkhani et al. (2014), Hatzenbichler and Buchmayr (2010), Sheppard (1999), Gesing and Wolanski (2001)	Extrusion yield, Fabrication yield, Internal recycling rates, Types and alloys of extruded products

Table A16: Sources used to form matrix node and flow data used as inputs for the data reconciliation process, and their confidence score (weight).

Source #	Name	Coverage	Frequency	Spatial Boundaries	Confidence Score (Weight)
1	Michigan Extruded (2020)	1	4	4	0.75
2	EAA 2013 & 2018 Report (2018, 2013)	4	2	2	0.67
3	MI Metals (2019)	1	3	2	0.50
4	Sattlethight (2019)	4	2	4	0.83
5	Mahmoodkhani et al. (2014)	1	1	4	0.50
6	Hatzenbichler and Buchmayr (2010)	1	1	4	0.50
7	Ducker Analysis (2017)	2	2	3	0.58
8	USGS 2016 Mineral Yearbook (Aluminum) (2018)	1	3	2	0.50
9	AEC EPD (Mulholland, 2016)	3	1	4	0.67
10	UN Comtrade (UN, 2018)	4	4	3	0.92
11	Autosteel (Schnatterly, 2010)	2	2	2	0.50
12	AEC Truck (2021)	2	1	2	0.42
13	Sheppard (1999)	1	1	2	0.33
14	Rio Tinto Interview (2020)	2	1	3	0.50
15	Cullen and Allwood (2013)	2	1	2	0.42
16	Consulting Collaborative (2017)	4	3	2	0.83
17	International Aluminum Institute (2021)	4	3	1	0.66
18	International Energy Agency (2017)	4	3	1	0.66

19	Norsk Hydro (Norsk Hydro, 2019, 2020a, 2020b)	3	1	3	0.58
20	Gabrian International (2020)	2	1	3	0.5
21	Tri-state aluminum (2020)	2	1	3	0.5
22	Michigan Extruded Aluminum (2020)	2	1	3	0.5
23	Magnode Aluminum (2019)	2	1	3	0.5
24	Superior Extrusion (2019)	2	1	3	0.5
25	Southern Aluminum Finishing Co. (2020)	2	1	3	0.5
26	Ford Motor Company (2020)	2	1	3	0.5
27	Kaiser Aluminum (2020)	2	1	3	0.5
28	General Motors (2020)	2	1	3	0.5
29	Boeing (2020)	2	1	3	0.5
30	Chien et al. (2018)	2	1	4	0.58
31	Fielding (2009)	3	2	3	0.66
32	Grayson (2017)	3	1	1	0.42
33	Pinter (2017)	2	1	4	0.58
34	Cooper and Allwood (2012)	3	1	2	0.5
35	Misiolek and Kelly (2005)	2	1	3	0.5
36	Fourmann (2018)	2	1	3	0.5
37	Bertram et al. (2017)	4	1	3	0.66
38	Gesing and Wolanski (2001)	2	1	3	0.5
39	Mag Specialties (2019)	2	1	3	0.5

Table A17: Matrix node and flow data used as inputs ( $\hat{x}_{i,j}$ ) to the data reconciliation with source and weighting factor. Note that an MFA data record that refers to either the scrap generated or the associated yield is designated by a third index, “x.x.2” for scrap flows, and “x.x.3” for yields.

Coord	Description	Type	Value (Mt)	Source	Weight
1.2	Primary Aluminum to Primary Ingots	Flow	See [1.21]		
1.4	Primary Aluminum to Primary Billet Production	Flow	See [1.21.2]		
1.17	Primary Aluminum to Losses	Flow	Based on Yield $\{[1.19]/[1.20]-[1.20]\}$	Mass Balance	
1.18	Primary Aluminum Production Node In	Node In	Greater than zero		
1.19	Primary Aluminum Production Node Out	Node Out	Greater than zero		
1.20	Primary Aluminum Yield	Yield	0.93	2	0.67
1.21	Primary Aluminum Ingot Unconventional	Unconventional	Mass of primary aluminum flowing to ingot production is equal to		

			node in of ingot production minus the internal melt scrap and imported ingot masses		
1.21	Primary Aluminum Ingot Unconventional	Unconventional	Mass of primary aluminum flowing to primary billet production is equal to node in of primary billet production minus internal melt scrap		
2.2	Primary Aluminum Internal Recycling	Internal	See [2.21.2]		
2.5	Primary Aluminum Ingot to Secondary Billet Production	Flow	See [2.21]		
2.17	Primary Aluminum Ingot to Losses	Flow	Based on Yield $\{[2.19]/[2.20]-2.20\}$	Mass Balance	
2.18	Primary Aluminum Ingot Node In	Node In	Greater than zero		
2.19	Primary Aluminum Ingot Node Out	Node Out	Greater than zero		
2.20	Primary Aluminum Ingot Yield	Yield	0.93	2	0.67
2.21	Primary Aluminum Ingot Unconventional	Unconventional	28.75% of Secondary Billet Production is Primary Aluminum Ingot	1,9	0.67
2.21.2	Primary Aluminum Ingot Unconventional	Unconventional	Internally recycled material equal to melt losses	14	0.5
3.5	End of Life Scrap to Secondary Billet Production	Flow	See [3.21]		
3.18	End of Life Scrap Node In	Node In	Greater than zero		
3.19	End of Life Scrap Node Out	Node Out	Greater than zero		
3.21	End of Life Scrap Unconventional	Unconventional	10% of secondary billet is Post Consumer Scrap	1	0.75
4.4	Primary Billet Production Internal Recycling	Internal	See [4.21]		
4.6	Primary Billet Production to Extrusion	Flow	0.6	4	0.83
4.15	Primary Billet Production to Exports	Flow	0.04	4	0.83
4.17	Primary Billet Production to Losses	Flow	Based on Yield $\{[4.19]/[4.20]-[4.20]\}$	Mass Balance	

4.18	Primary Billet Production Node In	Node In	Greater than zero		
4.19	Primary Billet Production Node Out	Node Out	Greater than zero		
4.20	Primary Billet Production Yield	Yield	0.94	2	0.67
4.20.2	Primary Billet Production Yield	Yield	0.93	3	0.5
4.21	Primary Billet Production Unconventional	Unconventional	Internally recycled material equal to melt losses	14	0.5
5.5	Secondary Billet Production Internal Recycling	Internal	See [5.21]		
5.6	Secondary Billet Production to Extrusion	Flow	2.46	4	0.83
5.17	Secondary Billet Production to Losses	Flow	Based on Yield {[5.19]/[5.20]-[5.20]}	Mass Balance	
5.18	Secondary Billet Production Node In	Node In	Greater than zero		
5.19	Secondary Billet Production Node Out	Node Out	Greater than zero		
5.20	Secondary Billet Production Yield Ratio	Yield	0.94	2	0.67
5.20.2	Secondary Billet Production Yield Ratio	Yield	0.93	3	0.5
5.21	Secondary Billet Production Unconventional	Unconventional	Internally recycled material equal to melt losses	14	0.5
6.7	Extrusion to North American Fabrication	Flow	3	4	0.83
6.15	Extrusion to Exports	Flow	0.1685	4	0.83
6.16	Extrusion to Scrap	Flow	Based on Yield: {[6.19]/[6.20]-[6.20]}	Mass Balance	
6.18	Extrusion Node In	Node In	Greater than zero		
6.19	Extrusion Node Out	Node Out	Greater than zero		
6.20	Extrusion Yield Ratio	Yield	0.78	6	0.5
6.20 (2)	Extrusion Yield Ratio	Yield	0.68	5	0.5
6.21	Extrusion Unconventional	Unconventional	Lowerbound for new extrusion scrap: 0.758	8	0.5

6.21.2	Extrusion Unconventional	Unconventional	Lowerbound for extrusion shipments: 2.49	8	0.5
7.8	Fabrication to Construction	Flow	0.9585	4	0.83
7.8.3	Fabrication to Construction Yield	Yield	0.89	15	0.42
7.9	Fabrication to Transportation	Flow	0.8235	4	0.83
7.9.3	Fabrication to Transportation Yield	Yield	0.795	15	0.42
7.10	Fabrication to Consumer Durables	Flow	0.2457	4	0.83
7.10.3	Fabrication to Consumer Durables Yield	Yield	0.75	15	0.42
7.11	Fabrication to and Electrical Energy	Flow	0.2511	4	0.83
7.11.3	Fabrication to and Electrical Energy Yield	Yield	0.818	15	0.42
7.12	Fabrication to Machinery	Flow	0.2268	4	0.83
7.12.3	Fabrication to Machinery Yield	Yield	0.67	15	0.42
7.16	Fabrication to Scrap	Flow	Based on Yield: {[7.19]/[7.20]-[7.20]}	Mass Balance	
7.18	Fabrication Node In	Node In	Greater than zero		
7.19	Fabrication Node out	Node Out	Greater than zero		
7.20	Fabrication Yield	Yield	0.818	4,7,13,15	0.33
8.15	Construction to Exports	Flow	0.007	4,7,13,15	0.25
8.18	Construction Node In	Node In	Greater than zero		
8.19	Construction Node Out	Node Out	Greater than zero		
9.15	Transportation to Exports	Flow	0.077	4,7,13,15	0.417
9.18	Transportation Node In	Node In	Greater than zero		
9.19	Transportation Node Out	Node Out	Greater than zero		
10.15	Consumer Durables to Exports	Flow	0.003	4,10	0.83
10.18	Consumer Durables Node In	Node In	Greater than zero		

10.19	Consumer Durables Node Out	Node Out	Greater than zero		
11.15	Electrical and Energy to Exports	Flow	0.011	4,10	0.83
11.8	Electrical and Energy Node In	Node In	Greater than zero		
11.19	Electrical and Energy Node Out	Node Out	Greater than zero		
12.15	Machinery to Exports	Flow	0.010	4,10	0.83
12.18	Machinery Node In	Node In	Greater than zero		
12.19	Machinery Node Out	Node Out	Greater than zero		
14.2	Imports to Primary Aluminum Ingots	Flow	See [13.21]		
14.6	Imports to Extrusion	Flow	0.765	4	0.83
14.7	Imports to Fabrication	Flow	0.236	4	0.83
14.8	Imports to Construction	Flow	0.135	4,7,13,15	0.25
14.9	Imports to Transportation	Flow	0.188	4,7,10,11,12	0.417
14.10	Imports to Consumer Durables	Flow	0.029	4,10	0.83
14.11	Imports to Electrical and Energy	Flow	0.041	4,10	0.83
14.12	Imports to Machinery	Flow	0.013	4,10	0.83
14.18	Imports Node In	Node In	Greater than zero		
14.19	Imports Node Out	Node Out	Greater than zero		
14.21	Imports Unconventional	Unconventional	Import of ingot is 40% total ingot node in: [13.2] = 0.4*[2.18]	9	0.67
16.5	Scrap to Secondary Billet Production	Flow	See [15.21.2]		
16.17	Scrap Node In	Node In	Greater than zero		
16.18	Scrap Node Out	Node Out	Greater than zero		
16.21	Scrap Unconventional	Unconventional	Lowerbound for new extrusion scrap: 0.758	8	0.5
16.21.2	Scrap Unconventional	Unconventional	60% of secondary billet production is Post Industrial Scrap	1	0.75

### A.6.4 MFA Data Uncertainty

The MFA is presented as a Sankey diagram without any error bands to represent uncertainty. Tables A15 and A16 show the sources of data, and the data records used as inputs to the MFA data reconciliation. The uncertainty is mitigated in this study, as much as is possible, through the use of multiple data points and the mass-balance reconciliation of the MFA at each intersection of nodes present. The final reconciliation result is presented to the nearest 100,000 tons, or 1 significant figure in the case of values below 100,000 tons. Figure A10 shows the average residual data discrepancy of the flows represented in the MFA, and indicates the level of discrepancy between the final MFA result and the initial data records (see equation A8). It can be seen that the largest residual is close to 0.1 (0.088), found in the flow of profiles from the extrusion process to shapes, tubes, bar & rod. The final reconciled value is 2.735 Mt (2.25+0.23+0.25) compared to a value of 3 Mt from Sattlethight (2019). Note that the average residual for flows where no data record was found is zero.

$$\text{Average residual data discrepancy}_i = \sum_{j=1}^J \frac{I_i(x - \hat{x}_{i,j})}{\sum_{j=1}^J \hat{x}_{i,j}} \quad (\text{A8})$$

Despite the uncertainty in the final results, the global MFA presents an estimate of the North American extrusion industry that can be used to inform decision making in industry and academia.

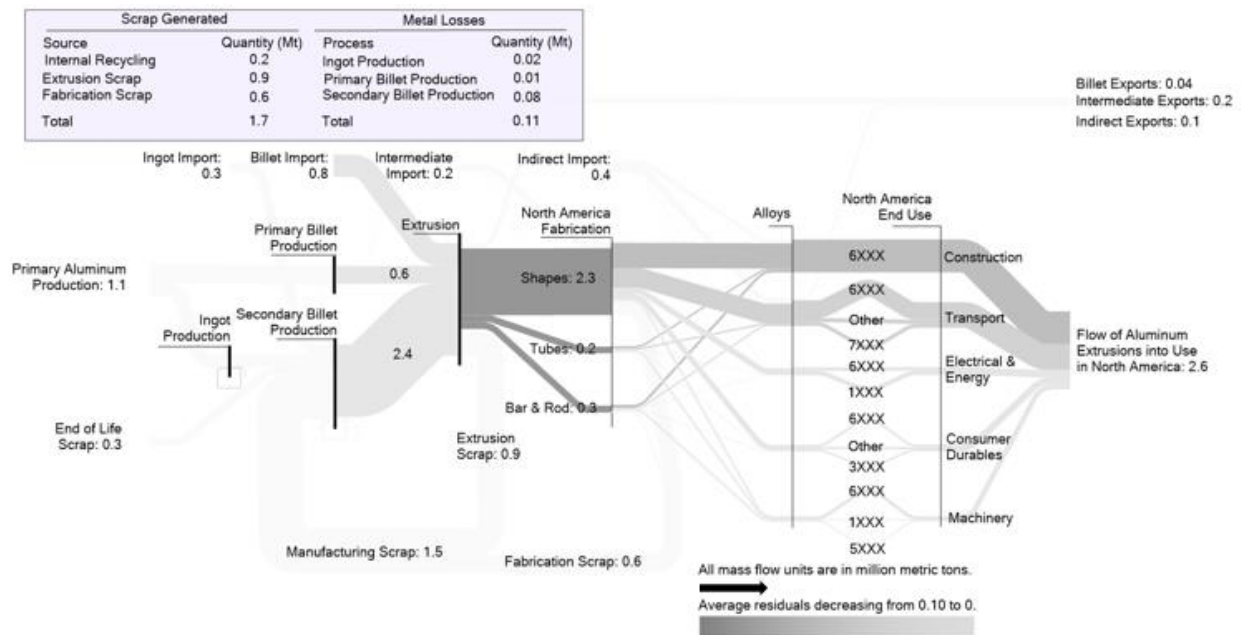


Figure A10: The average residuals of the flows representing the 2018 North American aluminum extrusion industry. The magnitude of the residuals is indicated by the darkness of the flow.

### A.7 Effect of billet geometry on the extrusion energy and force requirement



The extrusion mechanical energy requirement per kg of billet can be estimated analytically using equation A9 (see Section A.3.1).

$$e_{mech}(MJ) = \frac{1}{\rho} K_x Y_f \left( \ln(ER) + \frac{L_{billet}}{D_{billet}} \right) \text{ with } Y_f \text{ in MPa \& } \rho \text{ in } \frac{kg}{m^3} \quad (A9)$$

Therefore, the dependency of  $e_{mech}$  on billet geometry (for constant billet volume) scales as shown in equation A10.

$$e_{mech}(MJ) \propto \left[ \ln \left( \frac{0.25 \times \pi \times D_{billet}^2}{\text{Profile Cross - sectional Area}} \right) + \frac{V_{billet}}{\pi D_{billet}^3} \right] \quad (A10)$$

The maximum ram force,  $F_{max}$ , at the beginning of the extrusion stroke can be estimated analytically using equation A11 (see Section A.3.1).

$$F_{max}(MJ) = \frac{\pi D_{billet}^2}{4} K_x Y_f \left( \ln(ER) + \frac{2L_{billet}}{D_{billet}} \right) \quad (A11)$$

Therefore, the dependency of the maximum ram force,  $F_{max}$ , on billet geometry (for constant billet volume) scales as shown in equation A12.

$$F_{max}(MJ) \propto D_{billet}^2 \left( \ln \left( \frac{0.25 \times \pi \times D_{billet}^2}{\text{Profile Cross - sectional Area}} \right) + \frac{2 \cdot \text{Volume}_{billet}}{\pi D_{billet}^3} \right) \quad (A12)$$

Figure A11 shows the dependency of  $e_{mech}$  and  $F_{max}$  on the billet geometry when extruding a large versus small profile cross-sectional area (top row of Figure A11 versus bottom row) and when extruding using a large versus small billet volume (left side of Figure A11 versus right side). Figure A11 shows that increasing the billet diameter will decrease the mechanical energy needed to extrude the profile as well as increasing the extrusion ratio and decreasing the billet aspect ratio. Increasing the billet diameter has a more nuanced effect on the maximum ram force, decreasing the ram force when increasing the billet diameter from a small value and increasing the ram force when increasing the ram force from a higher value (see the ‘U’ shaped ram force shapes in Figure A11). As shown in Figure A11, the increase in ram force with billet diameter happens at smaller billet diameters when the billet volume is smaller.

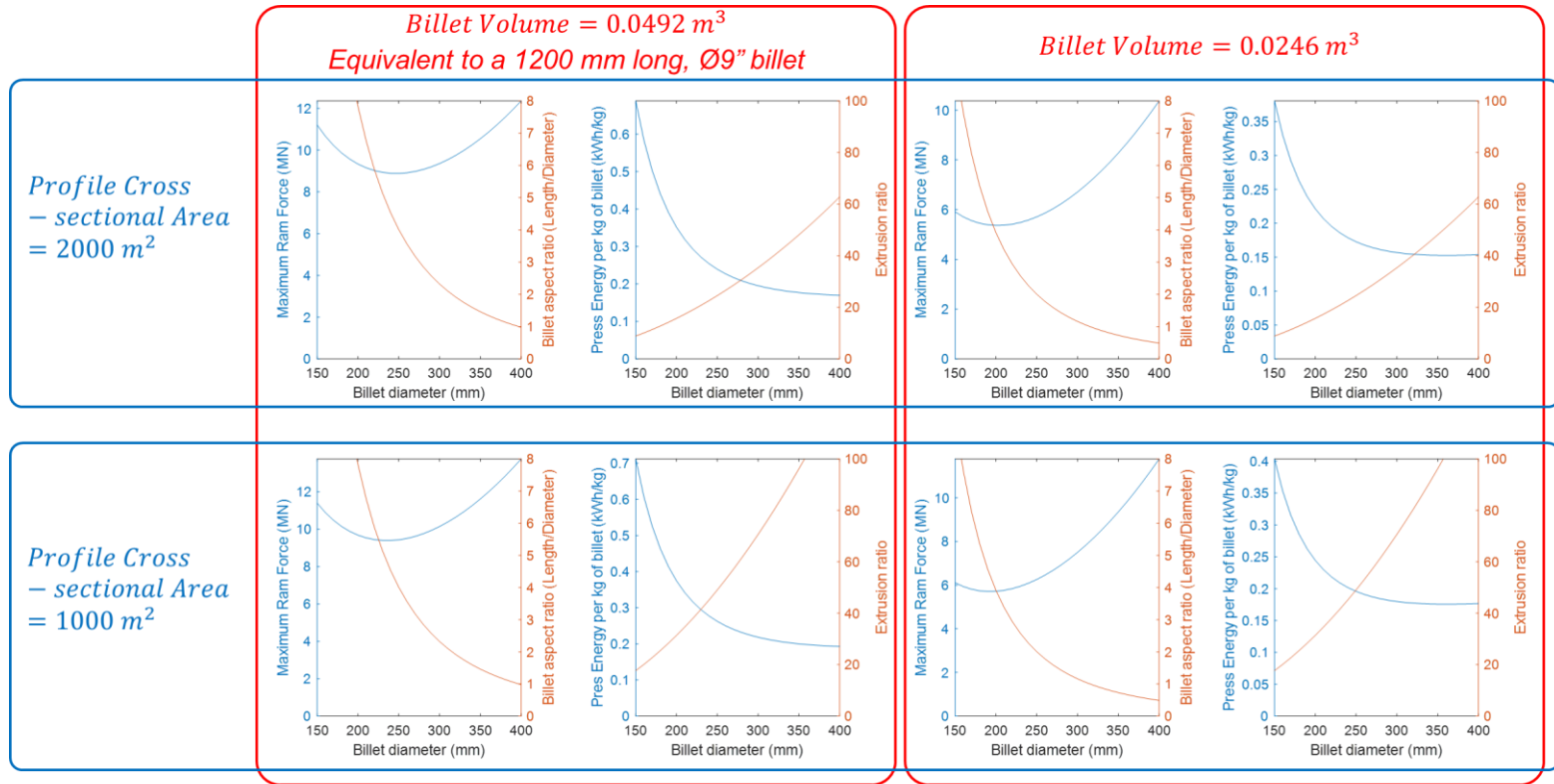


Figure A11: The effect of billet diameter (at a constant billet volume) on the mechanical energy and maximum ram force requirement. The various plots show how the relationships change for large versus small profile cross-sectional area (top versus bottom) and large versus small billet volumes (left versus right). The above plots were constructed for an aluminum material with  $Y_f=15$  MPa (at the extrusion temperature) and a profile geometry equivalent to  $K_x = 1.0751$ . In all cases, the press energy was calculated assuming that the mechanical energy accounted for 5% of the total press energy.

Experimental data consistent with these findings has been recording in a Light Metal Age magazine article by Chien et al. (2018). Figure A12 shows an image from their work showing the effect of increasing the billet diameter at a constant billet volume. The maximum ram force is relatively insensitive to this change but the mechanical energy needed to extrude the billets (the area under the force-displacement curves) decreases substantially by approximately 20%. It should be noted that the actual energy (electrical energy) needed to extrude the billets far exceeds the mechanical energy ( $e_{mech}$ ) due to inefficiencies in the press. Nonetheless, this analysis presents preliminary evidence that larger diameter billets reduce the mechanical energy needed to extrude billets and (without an accompanying drop in press efficiency) this should equate to a decrease in overall direct energy (electrical) energy requirements. Ultimately, an increasing billet diameter will be constrained by the force limit of the press and potentially by other problems that it could cause; e.g., dummy block functioning (Chien et al., 2018).

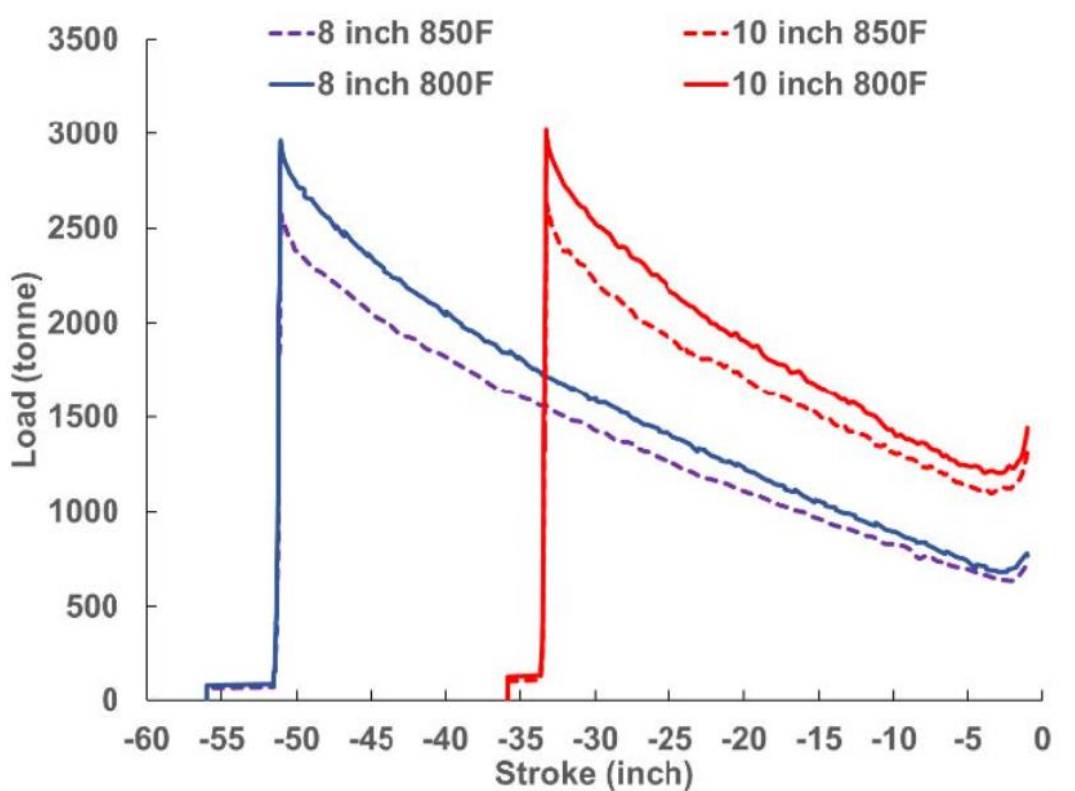


Figure A12: Ram force versus displacement graph for equal volume billets. Billets are Ø8” and Ø10” and extruded at 850F and 800F (Chien et al., 2018).

## A.8 References

AEC, 2021. Aluminum Extrusions are part of the Truck/Trailer Solution [WWW Document]. URL <https://www.aec.org/page/extrusion-applications-truck-trailer> (accessed 6.9.21).

- AEC, 2020. Aluminum Extrusion make important contributions in the Auto Industry [WWW Document]. URL <https://www.aec.org/page/extrusion-applications-auto-industry> (accessed 6.9.21).
- Bertram, M., Ramkumar, S., Rechberger, H., Rombach, G., Bayliss, C., Martchek, K.J., Müller, D.B., Liu, G., 2017. A regionally-linked, dynamic material flow modelling tool for rolled, extruded and cast aluminium products. *Resour. Conserv. Recycl.* 125, 48–69. <https://doi.org/10.1016/j.resconrec.2017.05.014>
- Boeing, 2020. Boeing roundtable discussion.
- Chien, K., Robbins, P., Jowett, C., Wang, Y., 2018. Extrusion Productivity, Part I – Billet Geometry. *Light Met. Age*.
- Consulting Collaborative, 2017. An Overview of the N.A. Aluminum Extrusion Market 2016 [WWW Document]. Consult. Collab. URL [https://cdn.ymaws.com/www.aec.org/resource/resmgr/2017\\_SMW/1\\_Extrusion\\_Overview\\_-\\_Brown.pdf](https://cdn.ymaws.com/www.aec.org/resource/resmgr/2017_SMW/1_Extrusion_Overview_-_Brown.pdf) (accessed 10.18.20).
- Cooper, D.R., Allwood, J., 2012. Reusing steel and aluminium components at end of product life. *Environ. Sci. Technol.* 46, 10334–10340. <https://doi.org/10.1021/es301093a>
- Cooper, D.R., Allwood, J.M., 2012. Supporting Information - Reusing steel and aluminium components at end of product life.
- Cullen, J.M., Allwood, J.M., 2013. Mapping the global flow of aluminum: From liquid aluminum to end-use goods. *Environ. Sci. Technol.* 47, 3057–3064. <https://doi.org/10.1021/es304256s>
- Ducker Worldwide, 2017a. Aluminum Content in North American Light Vehicles 2016 To 2028 [WWW Document]. Ducker Worldw. URL <https://www.drivealuminum.org/research-resources/ducker2017/> (accessed 6.9.21).
- Ducker Worldwide, 2017b. ALUMINUM CONTENT IN NORTH AMERICAN LIGHT VEHICLES.
- Dulles Glass and Mirror, 2021. Dulles Glass and Mirror Calculator [WWW Document]. URL <https://www.dullesglassandmirror.com/glass-weight-calculator> (accessed 6.9.21).
- European Aluminum Association, 2018. Environmental Profile Report [WWW Document]. URL <https://european-aluminium.eu/resource-hub/environmental-profile-report-2018/> (accessed 4.13.20).
- European Aluminum Association, 2013. Environmental Profile Report [WWW Document]. URL <https://european-aluminium.eu/media/1329/environmental-profile-report-for-the-european-aluminium-industry.pdf> (accessed 4.13.20).
- Fielding, R.A.P., 2009. Recycling Aluminum Extrusion Scrap. *Light Met. Age* 67, 32–35. <https://doi.org/10.1093/jpids/pix105/4823046>
- Ford Motor Company, 2020. Ford Motor Company roundtable discussion.
- Fourmann, J., 2018. AEC Webinar: Metal Flow Fundamentals.
- Gabrian International, 2021. What are the Characteristics of Different Aluminum Series? [WWW Document]. URL <https://www.gabrian.com/choose-the-right-alloy-for-your-aluminum-extrusions/> (accessed 6.9.21).
- Gabrian International, 2020. Extrusions for your industry [WWW Document]. URL <https://www.gabrian.com/aluminium-extrusions/industries/> (accessed 12.1.20).
- General Motors, 2020. General Motors roundtable discussion.
- Gesing, A., Wolanski, R., 2001. Recycling light metals from end-of-life vehicles. *Jom* 53, 21–23. <https://doi.org/10.1007/s11837-001-0188-3>
- Grayson, J., 2017. Reducing Melt Loss and Dross Generation - Light Metal Age Magazine. *Light Met. Age*.
- Groover, M.P., 2010. *Fundamentals of Modern Manufacturing: Materials, Processes, and Systems*, 4th ed. Wiley, Hoboken, New Jersey.
- HGH Hardware, 2021. HGH Hardware Catalogue [WWW Document]. URL [https://www.hghhardware.com/ASSETS/DOCUMENTS/ITEMS/EN/113285\\_brochure-catalog.pdf](https://www.hghhardware.com/ASSETS/DOCUMENTS/ITEMS/EN/113285_brochure-catalog.pdf) (accessed 6.9.21).
- International Aluminum Institute, 2021. IAI current statistics [WWW Document]. URL <https://www.world-aluminium.org/statistics/> (accessed 9.6.21).
- International Energy Agency, 2017. *Energy Technology Perspectives 2017 - Executive Summary* [WWW

Document]. [https://doi.org/10.1787/energy\\_tech-2014-en](https://doi.org/10.1787/energy_tech-2014-en)

Kaiser Aluminum, 2020. Kaiser Aluminum roundtable discussion.

Kopec, G.M., Allwood, J.M., Cullen, J.M., Ralph, D., 2016. A General Nonlinear Least Squares Data Reconciliation and Estimation Method for Material Flow Analysis. *J. Ind. Ecol.* 20, 1038–1049. <https://doi.org/10.1111/jiec.12344>

Mag Specialties, 2019. Mag Specialties roundtable discussion.

Magnode Aluminum, 2019. Magnode Aluminum roundtable discussion.

Mahmoodkhani, Y., Wells, M., Parson, N., Jowett, C., Poole, W., 2014. Modeling the Formation of Transverse Weld during Billet-on-Billet Extrusion 3470–3480. <https://doi.org/10.3390/ma7053470>

MI Metals, 2019. MI Metals roundtable discussion.

Michigan Extruded Aluminum, 2020. Michigan Extruded [WWW Document]. URL <https://www.michiganextruded.com/capabilities/aluminum-alloy/> (accessed 7.1.21).

Misiolek, W.Z., Kelly, R.M., 2005. Extrusion of Aluminum Alloys, in: Semiatin, S.L. (Ed.), *ASM Handbook Metalworking: Bulk Forming*. ASM International, pp. 522–527. <https://doi.org/10.1361/asmhba0004015>

Mulholland, E., 2016. Aluminum Extrusion EPD Background Report.

Norsk Hydro, 2020a. Extruded Aluminum Rod [WWW Document]. URL <https://www.hydro.com/en-US/products-and-services/extruded-profiles/north-america-resources/extruded-aluminum-products/aluminum-rod/extruded-aluminum-rod/> (accessed 6.9.21).

Norsk Hydro, 2020b. Norsk Hydro roundtable discussion.

Norsk Hydro, 2019. The Correct Alloy for You [WWW Document]. URL <https://www.hydro.com/en-US/aluminum/products/extruded-profiles/alloys-for-aluminum-extrusions/> (accessed 7.1.21).

Origin Windows, 2021. Origin Window Catalogue [WWW Document]. URL [https://irp-cdn.multiscreensite.com/577b3ad1/files/uploaded/Origin\\_windows\\_spec.pdf](https://irp-cdn.multiscreensite.com/577b3ad1/files/uploaded/Origin_windows_spec.pdf) (accessed 6.9.21).

Pinter, T., 2017. Recovery assessment in the extrusion of aluminum hollow shapes. *Light Met. Age* 75, 38–42.

Rio Tinto, 2020. Rio Tinto roundtable discussion.

Sattlethight, H., 2019. ARTICLE: North American Aluminum Extrusion Industry Hits Historic Record Shipment Highs [WWW Document]. *Light Met. Age*. URL <https://www.lightmetalage.com/news/industry-news/extrusion/north-american-aluminum-extrusion-industry-hits-historic-record-shipment-highs/> (accessed 6.9.21).

Schnatterly, J., 2010. Watching Our Weight: Steel Content of North American Auto [WWW Document]. Autosteel.

Sheppard, T., 1999. *Extrusion of Aluminium Alloys*, 1st ed, Extrusion of Aluminium Alloys. Springer Science + Business Media, Dordrecht. <https://doi.org/10.1007/978-1-4757-3001-2>

Southern Aluminum Finishing Co., 2020. Southern Aluminum Finishing Company roundtable discussion.

Superior Aluminum, 2019. Superior Aluminum roundtable discussion.

Tri-State Aluminum, 2020. Aluminum Extrusion Alloy Selection Guide [WWW Document]. URL <http://tri-stateal.com/alloys> (accessed 6.9.21).

UN, 2018. UN Comtrade Database 2018.

USGS, 2018. 2016 Minerals Yearbook - Niobium.

Wernet, G., Bauer, C., Steubing, B., Reinhard, J., Moreno-Ruiz, E., and Weidema, B., 2016. EcoInvent Version 3.

Zhu, Y., Syndergaard, K., Cooper, D.R., 2019. Mapping the Annual Flow of Steel in the United States. *Environ. Sci. Technol.* 53, 11260–11268. <https://doi.org/10.1021/acs.est.9b01016>

## Appendix B. Weld Shear Strengths in Accumulative Roll Bonding

Weld shear strengths achieved in ARB were evaluated in order to add data points to Figure 3.17 and place extrusion transverse weld formation in the context of other solid-state welding processes.

Experiments were conducted on bonding of two scratch brushed sheets of AA1100 aluminum alloy (each sheet initially 2.5 mm thick) on a two-high lab-scale rolling mill with Ø127 mm rolls. Experiments were conducted on both wide and narrow strips to induce plane strain and non-plane strain deformation respectively. The results are shown in Table B1.

Table B1: Plane strain and non-plane strain ARB results. The mean is from at least 3 tests.

Initial sample thickness	Initial sample width thickness (mm)	Pre-heat & Roll temperature (°C)	Rolling reduction (%)	Final sample width (mm)	True Longitudinal interface strain	True Lateral interface strain	Surface Exposure (Y)	Mean weld shear strength ( $\tau_b/\tau_o$ ) Mean
2 x 2.5 mm	50	200	75	52.2	1.34	0.04 [near plane strain]	0.75	0.61
2 x 2.5 mm	25	200	75	28.2	1.26	0.12 [non plane strain]	0.75	0.67

## **Appendix C. An Exploratory Study on Reducing Transverse Weld Scrap from Complex Extrusions Using Profiled Billets and Dummy Blocks**

One of the greatest sources of scrap in the aluminum extrusion industry is the removal of elongated solid-state welds at the interface between consecutively extruded billets. Design and implementation of concave, profiled extrusion dummy block tooling might yield significant reduction of this transverse weld scrap. In this report, an FEA-based velocity field methodology is derived and used for the design of a profiled dummy block for a multi-hollow, automotive extrusion profile. The derived dummy block profile design is then evaluated in terms of its mechanical response during the extrusion stroke: avoiding plastic deformation and minimizing radial elastic deformation. The potential savings of altering the extrusion process to use profiled dummy blocks are then explored to understand the block's full effect on the process chain. The results show that a dummy block can be created to reduce the transverse weld scrap quantity by 15%, reducing the per-unit costs of production by upwards of \$0.08 per kg. It is also found that ceasing the removal of the gap between the stop mark and the transverse weld nose might reduce transverse weld scrap by a further 33%, or an additional decrease of costs of \$0.18 per kg. Preliminary analysis suggests that profile-specific dummy blocks could decrease overall productivity when production runs are relatively short ( $\approx 2$  hours) and dummy block tool changeover times are prohibitively long ( $\approx 15$  mins); therefore, either production runs need to be lengthened, dummy block tool changeover times shortened, or multi-profile novel dummy blocks used that can deliver savings across a range of different profiles. The opportunities presented by the profile dummy block are then discussed, alongside the barriers and necessary next steps for implementation into the extrusion industry.

### **C.1 Section introduction**

Reduction of the greenhouse gas (GHG) emissions generated by the aluminum industry is a critical component of the path towards the IPCC's recommendation of halving all anthropogenic GHG emissions by 2050 to prevent  $2^{\circ}\text{C}$  of warming and the worst effects of climate change (Suhara, 2019). However, the energy efficiency of aluminum primary production is approaching thermodynamic limits (Allwood et al, 2010; Gutowski et al., 2013) and the demand for aluminum is only expected to grow with a projected increase in demand upwards of 125% by 2060 (IEA, 2017). Therefore, to achieve reductions in GHG emissions in the aluminum industry, it is necessary to pursue alternative means such as the decarbonization

of the grid, to reduce the impact of the baseline energy requirements, or an increase in material utilization, to decrease material consumption.

Aluminum production is energy and emissions-intensive when compared to other high volume materials (steel, cement, paper, and plastic) (Allwood et al., 2012). This problem has been exacerbated by a recent geographical shift of aluminum production to China, where 90% of the aluminum-making electricity is generated using emissions-intensive coal power plants (International Aluminum Institute, 2017; Cooper et al., 2017). The use of near-zero emissions energy (Liu et al., 2011; Pedneault et al., 2021) can reduce the GHG emission of primary aluminum production upwards of 83%. However, a shift to decarbonized energy sources will be limited by volume / supply of resources (Chen and Önal, 2016; Ryberg et al., 2019; Moreau et al., 2019) and will require a restructuring of the grid (Worighi et al., 2019). For these reasons, a transition to decarbonized energy will rely on factors upstream from the aluminum industry and require partnership with the energy sector (Pedneault et al., 2021).

There is significant scope for improvements to the material utilization in the aluminum industry; as of 2011, 40% of all aluminum produced each year is scrapped and internally recycled (Milford et al., 2011). Cullen and Allwood (2013) reveal that 20% of all aluminum is formed through extrusion, in their material flow analysis of the aluminum industry. Focusing on this high volume sector of the industry, Oberhausen et al. (2022) found that the greatest opportunity for impact and cost reduction in the extrusion process was through the increase of material efficiency through the reduction of process scrap. Specifically, Oberhausen et al. identified the transverse weld as one of the greatest sources of extrusion process scrap and therefore environmental impacts and costs.

The transverse weld is a solid state weld that is present along the interface between consecutively extruded billets (Sheppard, 1999) formed due to the fragmentation of oxides along this interface and the simultaneous micro-extrusion and metallurgical bonding of substrate aluminum within the cracks. The strength of the interface is weaker than the surrounding bulk material (Den Bakker et al., 2016), due to the oxides and other contaminants, therefore it must be removed in safety-critical applications where strength is a primary concern (e.g. transportation and structural construction).

There are several instances in literature of studies carried out to identify the parameters which present the most effective means of reducing transverse weld scrap length (Sano et al., 2008a; Mahmoodkhani et al., 2013; Hatzenbichler and Buchmayr, 2012; Chen et al., 2015; Sano et al., 2008b; Zhang et al., 2017; Oberhausen et al., 2021). These studies often heavily rely on finite element analysis (FEA) to quickly and inexpensively iterate across a parameter space, and might include a single experimental trial to calibrate the baseline FEA model. The parameters whose effects have been quantified in the literature include the die angle, extrusion ratio, ram velocity, ram-billet friction coefficient, billet length, temperature, and bearing



length for solid profiles, as well as the port bridge diameter, welding chamber radius, and baffle plate height of the specialty porthole die used in hollow extrusions.

Alongside their study of many of these typical parameters, Oberhausen et al. (2021) present preliminary experimental evidence, using a table-top plasticine extrusion set-up, showing that novel dummy block geometries can be used to reduce the length of the transverse weld significantly. They utilize an analytical model of the extrusion velocity field based on Avitzur's (1963) seminal work to design dummy block profiles which reduce the transverse weld length by upwards of 44% in a simple, axisymmetric extrusion profile. However, Oberhausen et al. note that the analytical model does not accurately account for the effect of friction within the container and die. Additionally, the analytical model will only function for axisymmetric extrusion profiles and therefore cannot accurately predict the flow of material through dies of increased complexity like those found in the automotive industry.

In this work a dummy block design process is proposed which uses FEA-driven methods to derive a dummy block profile to reduce transverse weld scrap length. Figure C1 shows the process of designing novel dummy block geometries which off-set material flow through the velocity field and result in flat transverse welds of reduced length.

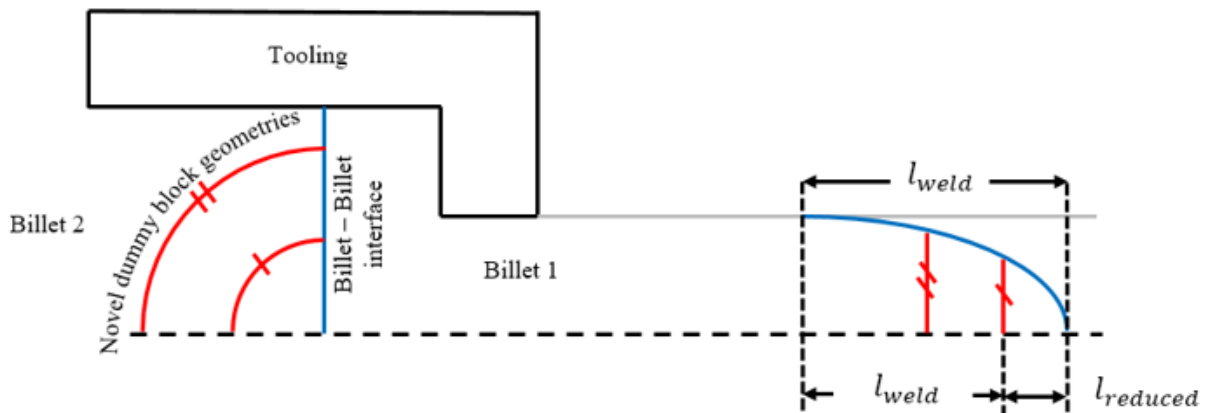


Figure C1: Flat, reduced length welds can be produced through concave, novel dummy block geometries.

The proposed methodology is used to generate a design for a complex, automotive extrusion profile. The mechanical performance of the designed block is evaluated under simulated extrusion conditions and the results compared with conventional dummy block performance. The benefits to environmental impact and costs are then calculated. Finally, the necessary changes to typical extrusion process flow, including the dummy block's effect on the back-end defect are discussed.

## C.2 Conventional tooling design

The dummy block is an interchangeable tool secured onto the billet-facing end of the hydraulic stem within the extrusion press. The dummy block is designed to be relatively inexpensive and to act as a sacrificial piece, allowing for cheap and easy tool changes when too much wear has occurred (compared to the alternative of replacing the entire hydraulic stem). With proper maintenance the dummy block has a production lifespan of around 650,000 kg (Superior Aluminum, 2021) and the stem is only changed every few years (average 2 years; 30,000,000 kg, (Thumb Tool & Engineering, 2018)).

The conventional dummy block in use throughout the extrusion industry is a multi-part assembly containing a central spine which connects to the stud and is topped with a mandrel surrounded by an expanding outer-ring (see Figure C2 (Robbins et al., 2016)).

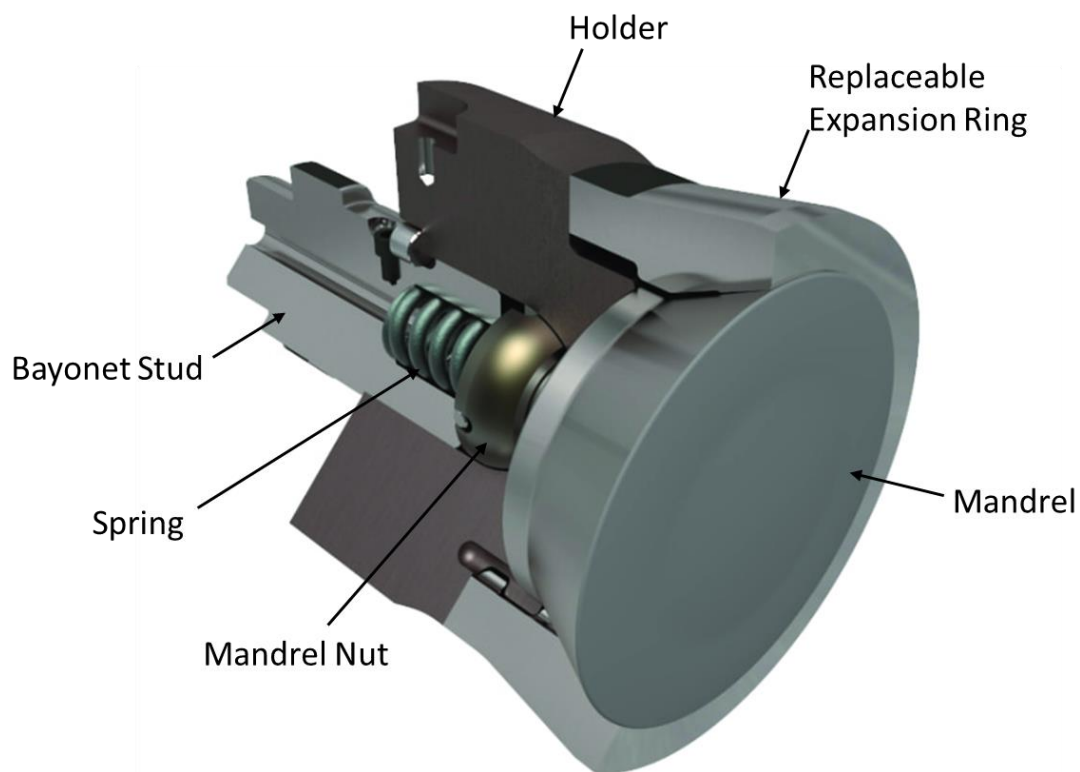


Figure C2: Dummy block cross section with parts labels. Adapted from Robbins et al. (2016).

The dummy block is designed such that the resting outer diameter of the expanding ring leaves approximately a 1 mm gap with the container wall (Thumb Tool & Engineering, 2021). Under compression the mandrel pushes on the expanding ring causing the ring to expand and the gap to narrow to just over 0.1 mm. A small gap is designed to remain even under compression to decrease wear on the ring by separating

the frictional interface, and also to allow for removal of the billet skin. The billet skin is a 0.05 mm layer on the outer radius of the billet containing contaminants such as oxides and solid-phase inclusions (spinels, carbides, nitrides and intermetallics) which are developed during casting (Saha, 2000). If the container is maintained at a temperature at least 50°C lower than the billet, this billet skin will stick to the container wall and pass through the gap left outside the dummy block's expanding outer radius. Similarly, as the stem and dummy block combo is retracted the outer ring relaxes and the gap re-widens to its original size, reducing the friction on any material stuck to the container wall allowing for easy return of the stem back out of the container.

The dummy block undergoes significant stresses through the extrusion process. The block is constructed using hardened H13 steel to prevent plastic deformation on the assembly during operation, however, some elastic deformation is still expected. Failure of the block typically occurs due to repetitive deformation at the joint between the mandrel and the expanding ring (Thumb Tool & Engineering, 2021; Robbins et al., 2016).

### **C.3 Section methodology**

The following section details the methods used to design the weld-length-reducing dummy block profiles. A pair of simulation packages, DEFORM®3D and Altair Inspire Extrude Metals, are used to model the extrusion process. The model outputs are compared to an experimental analysis of the extrudate and measured extrusion force to validate their likeness to reality. The Altair Inspire Extrude Metals model is then post-processed to determine the velocity field within the extrusion tooling, and then the necessary shape of the dummy block to reduce the length of the transverse weld. The dummy block geometry is then imported into the DEFORM®3D model to analyze the stresses and strains present on the tooling.

#### **C.3.1 Profile studied**

The profile studied in this work is an automotive battery tray component, produced from 228.6 mm (9") diameter, 1118 mm long AA6082 billets. The shape of the multi-hollow profile is shown in Figure C3, along with the shape of the die in Figure B3. The profile has a cross-sectional area of approximately 1550 mm<sup>2</sup>, for an extrusion ratio of 26. The velocity of the ram is approximately 4.66 mm/s, for an extrudate velocity of 121 mm/s. The billet temperature is 494°C, the die temperature is 454°C and the container temperature is 427 C.

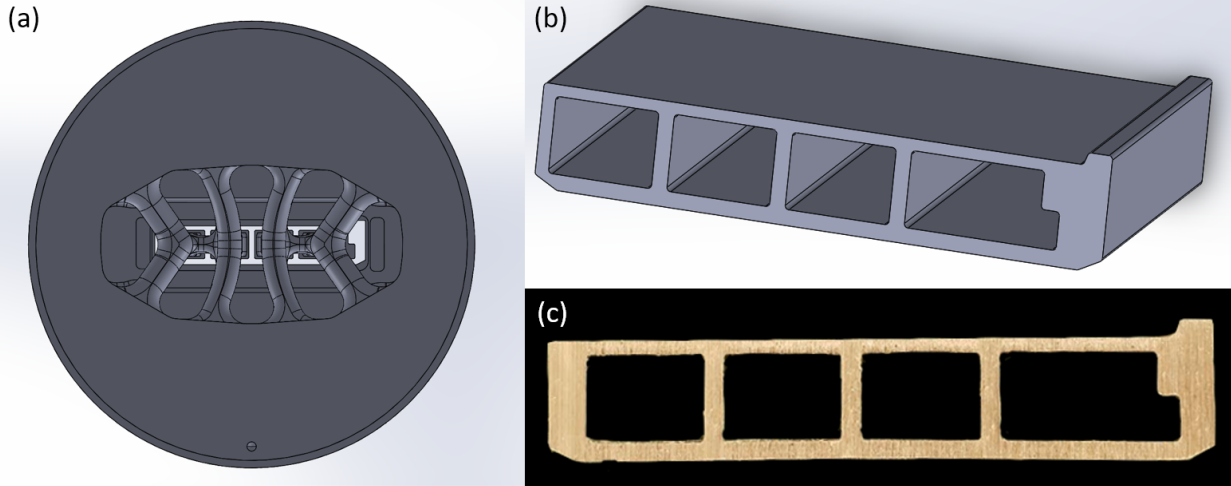


Figure C3: The (a) extrusion die used to create the (b,c) Ford battery tray profile studied.

### C.3.2 FEA

In this work both a DEFORM®3D and an Altair Inspire Extrude model are used to simulate extrusion of the profile. It was found to be necessary to use both simulations as they differed in capability and speed. DEFORM has the option of using an Updated Lagrangian or an Augmented Lagrangian Eulerian (ALE) solver. Altair offers just an ALE solver.

Walters et al. (2012) of the Scientific Forming Technologies Corporation (developers of DEFORM), describe in detail the various FEA methods as they apply to the aluminum extrusion process. The Updated Lagrangian (UL) method performs a full analysis of the process and outputs a complete load vs stroke curve as well as state variables for all discrete parts of the process (die fill, transverse weld formation, longitudinal weld formation). This increased resolution, however, is extremely computationally expensive, requiring many very small simulation steps and equally many remeshing operations in a high mesh distortion application such as extrusion. The DEFORM UL solver uses implicit analysis. Explicit analysis paired with mass or time scaling cannot be substituted to speed up the simulation due to the frequency and length of the remeshing steps.

The ALE method combines the Updated Lagrangian method with an Eulerian method. The Eulerian method is a steady-state solution in which the model part moves through a stationary mesh. Only a single step with maximum billet length is modeled, outputting an extremely fast solution that includes only a maximum load curve and does not include state variables. In the ALE method, both a steady state and transient analysis are performed simultaneously using a two mesh system. A non-distorting computational reference mesh (CRS) fixed only in the extrusion direction facilitates the FEA calculations and is updated according to the Lagrangian method in the plane perpendicular to the extruding direction. A second, material reference mesh (MRS) follows the material more closely, distorting as the material is deformed through the extrusion die. At the beginning of each simulation step the CRS and MRS are identical. As the

step is calculated and the deformation applied to the MRS, it diverges from the CRS. The difference in the form of the CRS and MRS at the end of each step is used to determine the step solution. The ALE method will yield both a load curve and state variables, however only in a steady state fashion; it does not include transient effects such as die fill or weld formation.

Separately from the methods offered, the DEFORM simulation package was found to be much more flexible in terms of both control over simulation settings, but also in terms of the geometry of the tooling and billet. Unlike the Altair simulation package, DEFORM allows simulation of a profiled dummy block. For this reason, as well as the Updated Lagrangian method's ability to output transient state variables, the DEFORM Updated Lagrangian method was chosen to simulate the dummy block response. However, as a consequence of this flexibility, and increased accuracy offered, the DEFORM model was found to run at a much slower rate than the Altair ALE method. A full model of the extrusion process in DEFORM would take many weeks to complete but could be run in just a day or two in Altair. Therefore, the Altair model was used to simulate the extrusion process from start to finish for the purpose of determining the velocity field present.

### **C.3.2.1 DEFORM**

A DEFORM<sup>®</sup>3D model was necessary to evaluate the deformation conditions on the transverse weld interface, as well as to model the effect of a change in dummy block geometry. It was necessary to simulate a conventional extrusion case, without profiled dummy blocks, to understand the baseline case and to act as a standard for comparison of the profiled models. The conventional model of the Ford / Can Art profile was created with three rigid bodies: the imported STL of the extrusion die, the dummy block, and the container. The dummy block is represented just as a solid, cylindrical block rather than the expanding dummy blocks used in industry (Figure C2) for simplicity of the simulation.

The multi-hollow profile is extruded using a port-hole die, which splits the billet into seven separate material streams. The rejoining of these streams in the welding chamber to form the final profile shape cannot be modeled from an empty die. The billet is therefore created using the Boolean addition of a cylindrical billet and the negative of the die geometry. This creates a starting billet of standard dimensions which also includes a section of material prefilling the die, avoiding the need to model the seam weld formation.

The billet mesh is generated utilizing the mesh-window function to create a mesh with several different regions of mesh density. The regions within the die experiencing significant deformation have a fine mesh (1 mm length tetrahedral elements) and the areas undergoing minimal deformation, such as the middle of the billet (by length) in the container, have a coarse mesh (5 – 15 mm elements). This meshing strategy reduces the total number of necessary elements and therefore simulation time, while maintaining accuracy

in the regions of importance. The back face of the billet is meshed with 2 mm elements for greater resolution in dummy block force interpolation. With this meshing strategy the total number of elements is approximately 2 million.

Each step in the simulation represents a maximum of 0.018 mm of dummy block displacement (0.004 seconds). This step size is reduced in cases where the simulation cannot be reconciled with a jump of this size, or when significant distortion of the mesh occurs as a result of the deformation experienced within the die. When significant distortion has occurred, the mesh is re-generated. This remeshing is triggered when a threshold element penetration of 0.7 is reached; in other words, when 70% of an element is overlapping one of the present rigid bodies. This typically occurs in the die region due to the 1 mm element length.

Contact interactions are generated on the billet with the dummy block, container and die. The container and die contacts are assumed to be sticking friction (a friction coefficient of  $m = 1$  where the frictional shear stress is equal to  $mk$  and  $k$  is the aluminum billet shear yield stress), and the ram contact is assumed to be frictionless (lubricant is used on the dummy block – billet interface, Can Art (2021)). The simulation is run as isothermal and the material properties of the billet are selected as the AA6082 properties at 493°C, built-in to DEFORM<sup>®</sup> (Figure C4) (Heinemann, 1961).

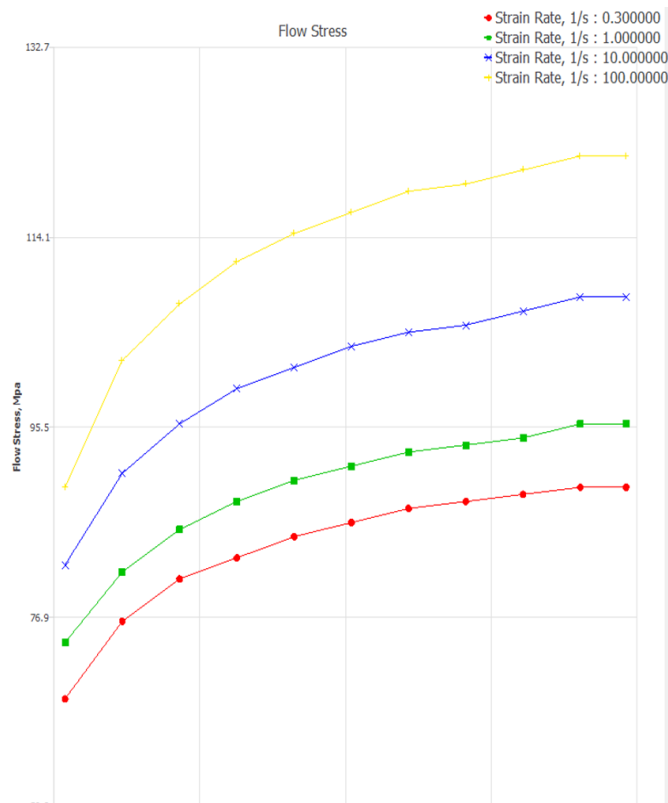


Figure C4: Billet material properties selected from DEFORM<sup>®</sup>. Data from Heinemann (1961).

### C.3.2.2 Altair Extrude Metals

The Altair Inspire Extrude Metals model has far fewer options and less flexibility compared to DEFORM. However, it does allow for easy export of the velocity field data cloud, and is therefore valuable in the design of profiled dummy blocks, as explained in section 1. The set-up follows the same basic principles as the DEFORM model. A simulation with deformable billet and rigid tooling is created. A mesh is generated using the ‘fine-mesh’ option, creating a mesh with small (approximately 1 mm) spacing in the die region, and large (approximately 15 mm) spacing in the rear billet. Differently from DEFORM, the step size in the Altair simulation is variable, separated into three time regions. The first and second regions represent the ram acceleration time and transverse weld formation respectively, and therefore have a small step size (0.1 seconds = 0.46 mm ram displacement), the third region includes the extrusion of the remaining billet length which will not be used for result analysis and has a large step size to increase simulation speed. Material properties are selected as AA6082 from the built-in Altair material data. The simulation is run as an adiabatic model; the final temperature of the extrudate is 647°C at the die exit.

A 3D velocity field point cloud (Figure C5) can then be exported from the Altair model to be used as a map of the material’s movement through the extrusion die. The data exported from Altair to a MATLAB script described in section 3.4.1, Velocity Field Method, includes the velocity vector for every node in 3-dimensional space represented by a set of x,y,z coordinates. The mentioned ‘fine’ mesh quality of the Altair model results in a velocity field with nodes spaced in an approximate 1 mm resolution in the die (the data points in the die are < 1 mm apart).

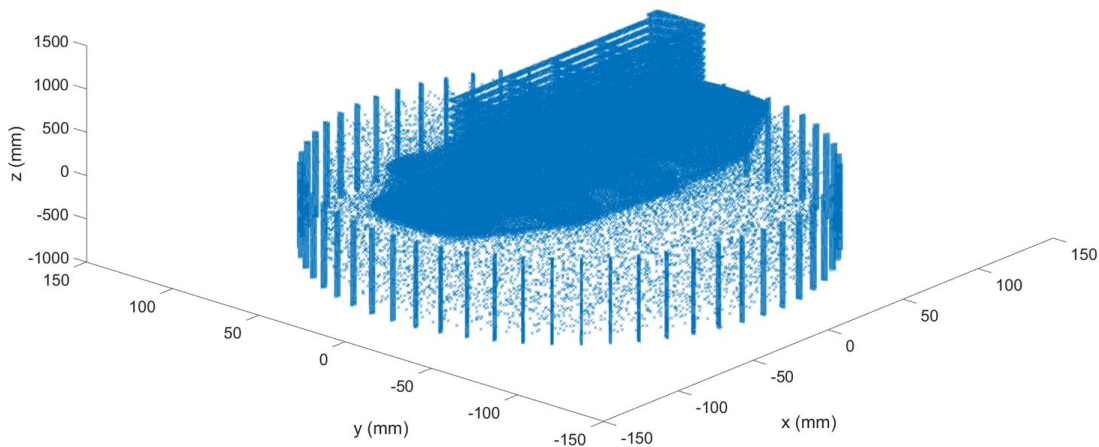


Figure C5: 3D velocity field point cloud exported from Altair Inspire Extrude model.

## **C.4 Section results**

The methodology used to evaluate the novel profiled dummy blocks allow for efficient iteration on design over a wide range of weld length reduction. The mechanical response of the considered dummy block designs is evaluated in the Technical Trade-offs section below. A design is chosen which satisfies a set of technical requirements. Then, the expected savings and costs of the chosen design is evaluated in the financial trade-offs section.

### **C.4.1 Technical Trade-offs**

A mechanically feasible dummy block design is defined by having no elastic deformation, as well as minimal plastic deformation and minimal radial displacement on the outer edge. Because the dummy block is simulated as a solid block and does not model the expanding assembly that exists in reality, the stresses extracted from the simulation cannot be taken at face value despite proper validation of the FEA models. Instead, a solid, flat dummy block without the assembly is first modeled and all profiled results are compared to this baseline value. The conventional dummy block was found to have peak stresses at 1,080 MPa and a radial displacement of 0.174 mm; all following designs will be represented as a flat stress value as well as a value relative to this conventional result (e.g. 1,620 MPa, 150% conventional stress). For this reason, the elastic dummy block models are preferable to the elasto-plastic, as the latter will include strain hardening that may not be present in reality. Use of the elastic model allows all results to be compared against the same baseline; the response of the dummy block will scale with the force, absent strain hardening.

Figure C16 below shows the relationship between the weld length reduction and the maximum stress present for each dummy block design evaluated. Over a range of reductions from 3 to 15.5%, maximum effective stresses were found to be directly correlated, increasing from roughly 100 to 200% of the conventional design stresses as the weld length reduction increased.



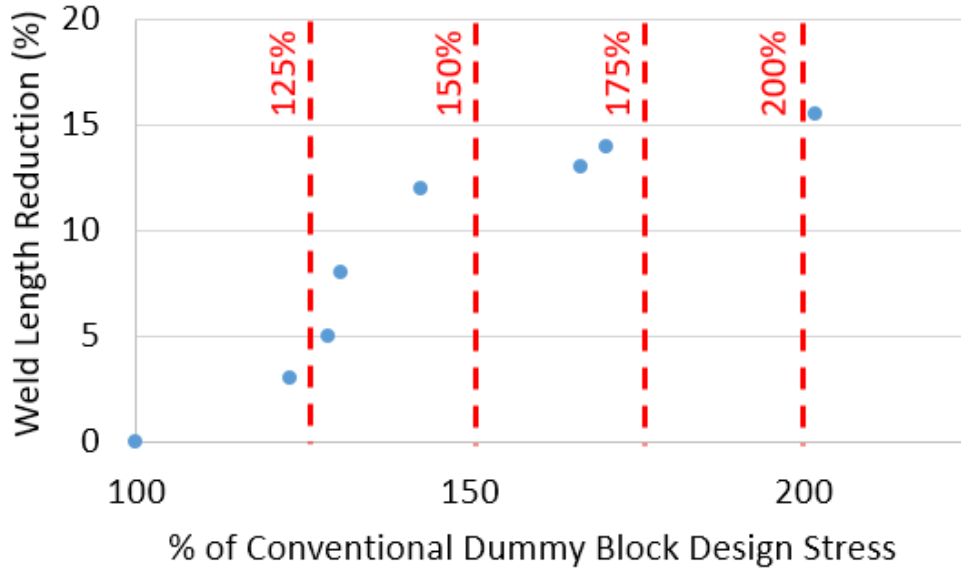


Figure C6: The maximum effective stress in dummy block profiles ranging from 3 to 15.5% weld length reduction.

Similarly, Figure C17 shows the direct relationship between radial displacement of the outer edge and the weld length reduction of the same seven dummy block profiles. The radial displacements found were in similar range to the maximum effective stresses when compared to the conventional design value; the radial displacements ranged from roughly 100 to 205%.

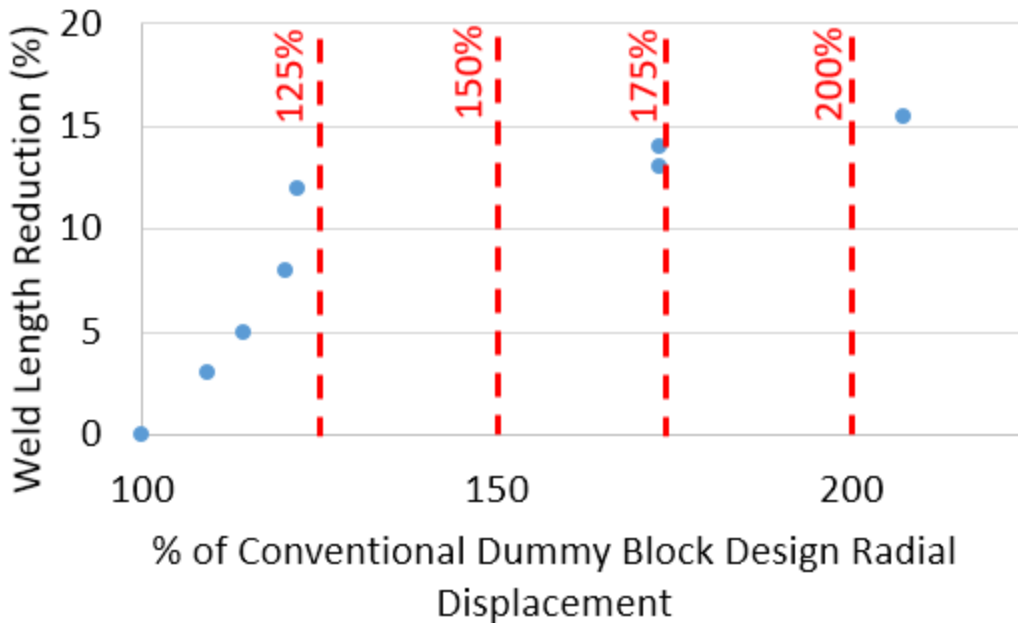


Figure C7: The maximum radial displacements of the outer edge in dummy block profiles ranging from 3 to 15.5% weld length reduction.

The results of Figure C16 and C17 show a maximum stress and radial displacement of approximately 200% and 210% of the conventional flat dummy block values respectively. These values correspond to roughly 2180 MPa and 0.361 mm, if the results of the simulation are to be taken at face value. The yield stress of H13 tool steel is roughly 950 MPa at extrusion temperature, which places the designed dummy block in excess of yield. However, the conventional flat dummy block simulation reported a maximum tool stress of approximately, 1080 MPa. In a case where the conventional design exceeds yield, it could only follow that the profile dummy blocks would as well. Figure C18 shows the stress and radial displacement on the conventional (C18a, C18c) and the profiled dummy block (C18b, C18d) respectively.

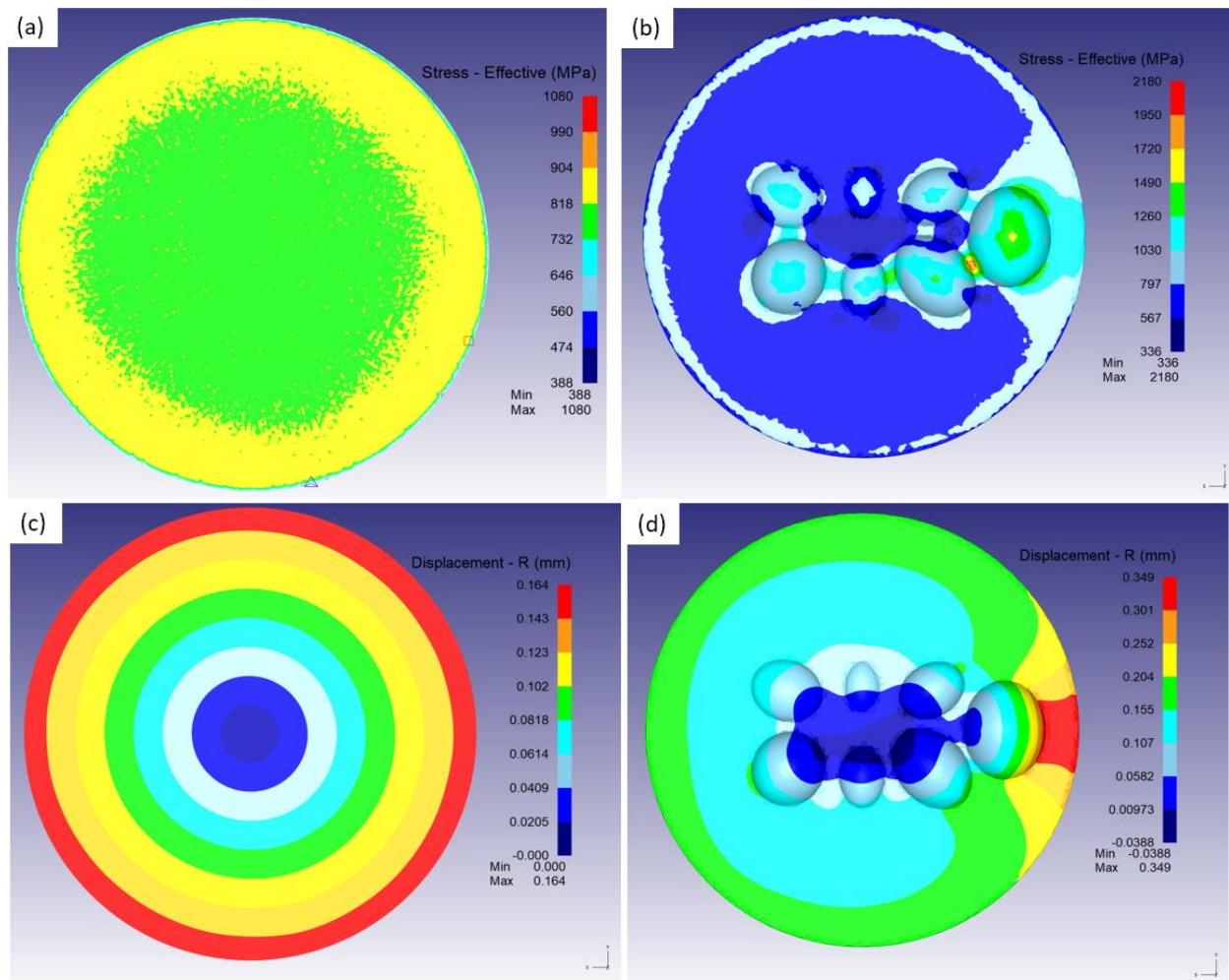


Figure C8: The stress and radial displacement on the conventional (a, c) and profiled dummy block (b, d).

#### C.4.2 Financial Trade-offs

The financial trade-offs were evaluated for the same set of seven dummy block profiles as explored in Figures C16 and C17. The model for extrusion costs, and all other necessary values (i.e. container, press, material and energy costs) were adapted from Oberhausen et al.'s (2022) extrusion cost model. The model

includes the costs of billet, die tooling, direct energy consumption and labor, with a rebate for scrap sold to recyclers (Equation C3). Additionally, the model assumes a billet recycled content equal to that of the industry as a whole, 54%. Press equipment and container costs are excluded as their relatively long lifespans result in a negligible inclusion to the total costs.

$$C_{per\ kg\ profile} = [(C_{log} - C_{scrap}) + C_{tooling} + C_{direct\ energy} + C_{labor}]_{per\ kg\ profile} \quad (C3)$$

The cost of a profiled dummy block ( $C_{dummy\ block}$ ) was evaluated in a range of 100 to 300% of the value of a conventional dummy block to account for increased costs in the initial design and repeated productions. Conventional, expanding dummy blocks costs approximately \$1000 (Thumb Tool & Engineering, 2021), so it follows that in our model the profiled dummy block would cost an additional \$0 to \$2000. No change was expected in the other tooling costs between dummy block profiles studied. The difference in machined volume for the dummy blocks from the lowest weld reduction (3%) to the highest (15.5%) was only 70,000 mm<sup>3</sup>, or 0.6 kg of material, and would not incur a significant additional dummy block manufacturing cost.

Additionally, it was assumed that the lifespan of a profiled dummy block ( $L_{dummy\ block}$ ) would be reduced by a lifespan reduction ratio ( $r_{lifespan}$ ) from its conventional value. The edges of each concavity of the profiled dummy block introduces a number of new critical edges which may experience higher than conventional maximum effective stresses and wear. It is unknown if failure will be expected to occur here before the typical location at the spreader hinge. Therefore, the assumption of decreased lifespan, tested over a range of 50-100% of the conventional lifespan, is included to provide a conservative estimate. Equation C4 below shows the additional tooling costs included in the adaptation of Oberhausen et al.'s model. The equation uses the mass of total production of the profile ( $m_{production}$ ), as well as the expected yield of the profile ( $\alpha$ ) to determine the number of tools needed.

$$C_{dummy\ block,per\ kg\ profile} = \frac{C_{dummy\ block}}{m_{production}} * \left[ \frac{m_{production}}{L_{dummy\ block} * r_{lifespan} * \alpha} \right] \quad (C4)$$

Additionally, an increased labor cost was included to account for changing the dummy block on a per-profile regularity, rather than it being a once-per-week maintenance routine (Can Art, 2022) as is conventionally the case when the dummy block is removed for caustic cleaning and inspection for wear (Dyla, 2019). If excessive wear is present the block is welded and remachined, before being reheat treated. The dummy block change process requires around 15 minutes ( $t_{dummy\ block}$ ), and would likely need to be repeated once every profile change ( $t_{run}$  : average profile run time = 2 hours (Can Art, 2022)). Equation

C5 applies this extra time as a simple proportion of the existing labor cost model (Oberhausen et al., 2022:  $P$  = number of workers,  $w$  = wage per worker,  $\lambda$  = linear density of profile,  $V$  = ram velocity).

$$C_{labor,per\ kg\ profile} = \frac{0.96 * P * w}{60 * \alpha * \lambda * V} * \left(1 + \frac{t_{dummy\ block}}{t_{run}}\right) \quad (C5)$$

At the average values from Can Art this increases the time to extrude and therefore the labor costs by 12.5%. To calculate the total savings generated by the change in dummy block tooling, the effect on the yield must be calculated. To find the new yield, the total scrap rate ( $S_{total}$ ) was altered according to Equation C6, based on the transverse weld reduction rate ( $r$ ) and the individual scrap rates ( $S_{scrap\ type}$ ) reported by Oberhausen et al. (2022). The transverse weld scrap rate ( $S_{transverse\ weld}$ ) was calculated based on the experimental weld findings and the known total billet mass. Table C3 below shows the average scrap rate by scrap type reported by Oberhausen et al. (2022), except for the Transverse weld scrap rate which has been adapted specifically for the Ford / Can Art profile.

$$S_{total} = S_{billet\ cutting} + S_{backend\ defect} + S_{quench} + S_{stretcher} + S_{die\ fill} + r * S_{transverse\ weld} \quad (C6)$$

Table C1: Estimated scrap rates for Ford extrusion profile. Adapted from Oberhausen et al., (2022)

Scrap type	Scrap rate (%)
Billet cutting	4
Backend defect	10
Quench curtain	1
Transverse weld	6.7
Stretcher	1
Die fill	0.7
<b>Total</b>	<b>23.4</b>

Figure C19 below shows the savings for the 15.5% weld length reduction dummy block, and how these savings change with the range of additional tooling costs considered. It is seen that the additional tooling costs have a minor effect on the total savings at higher production volumes, however the more expensive

tooling costs do have a noticeably offset in required production volume before profitability. The minimum production volume required for profitability scales with the additional tooling costs; a tool that is twice as expensive will require twice the minimum production volume.

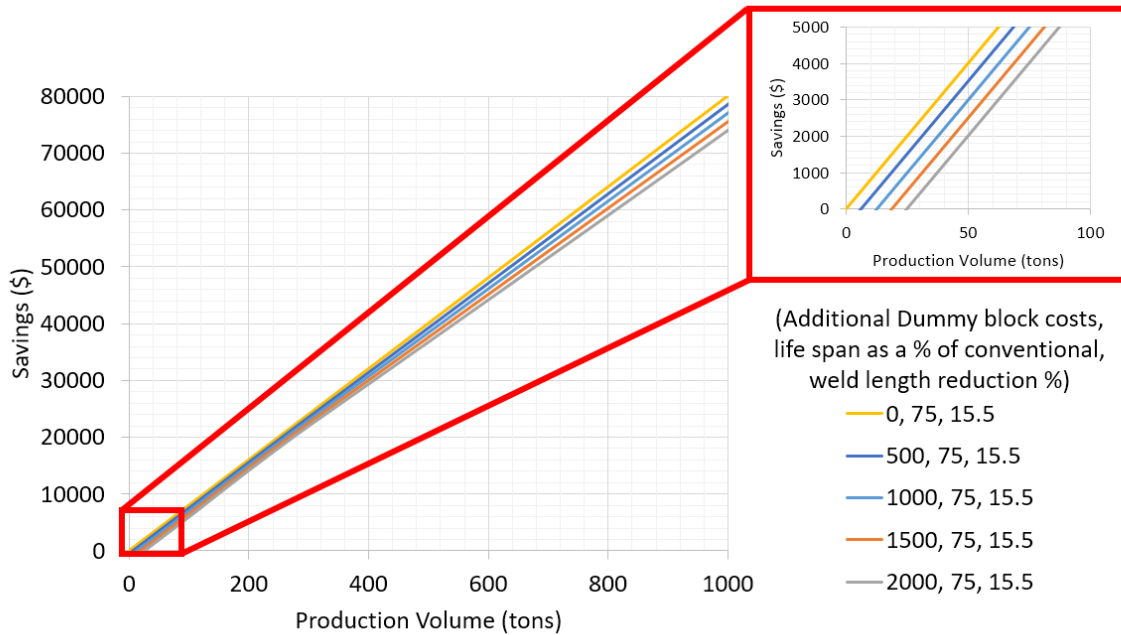


Figure C9: The savings of the 15.5% weld length reduction dummy block with additional tooling costs ranging from \$0 to 2000. Legend is labeled as the additional dummy block costs (\$), the lifespan as a % of the conventional block, and the % weld length reduction.

Similarly, Figure C20 shows that the dummy block lifespan has a marginal effect on total savings within the range studied (50 to 100% conventional dummy block lifespan).

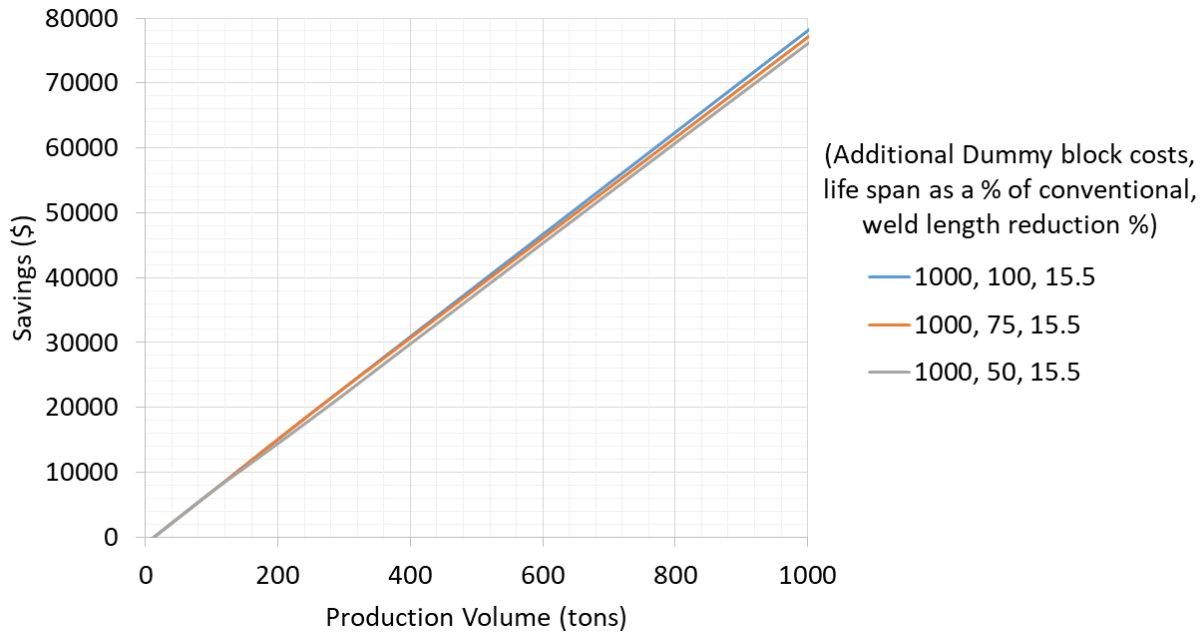


Figure C10: The savings of the 15.5% weld length reduction dummy block with dummy block lifespan ranging from 50 to 100% the conventional value.

Figure C21 below shows that the total savings scales proportionally to the weld length reduction. From an original modeled cost of \$3.61 per kg, the savings for weld length reductions of 5 to 15.5% were \$0.03 (0.8%) and \$0.085 (2.4%) respectively.

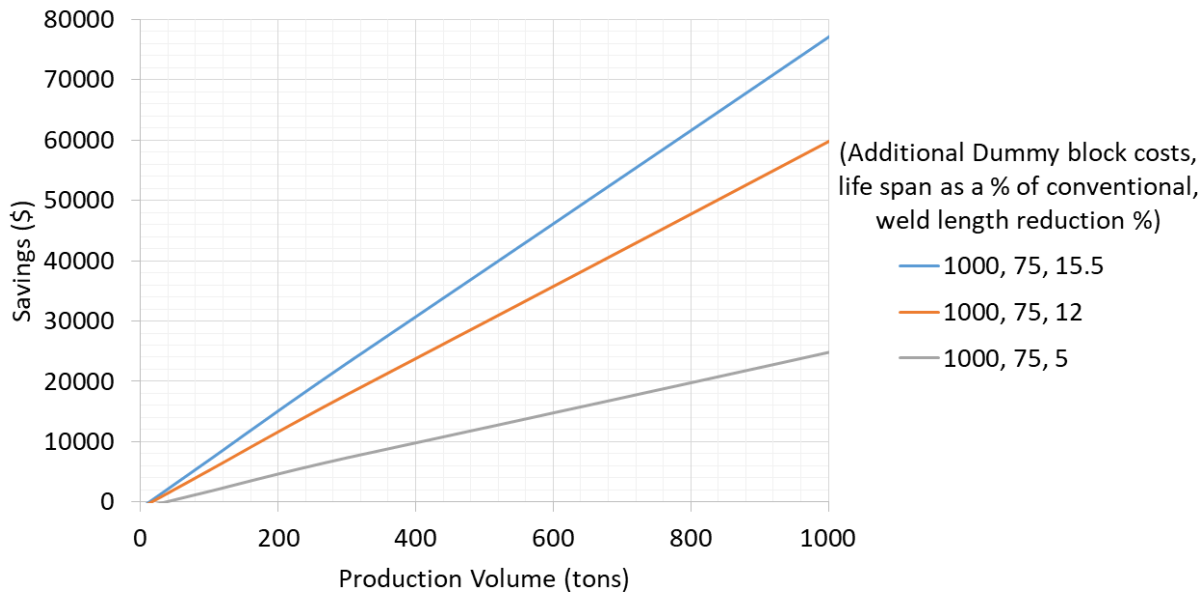


Figure C11: The savings associated with dummy block's of weld length reduction 5, 12 and 15.5% for a \$1,000 additional tooling cost with 75% tooling lifespan. Legend is labeled as the additional dummy block costs (\$), the lifespan as a % of the conventional block, and the % weld length reduction.

Separate from the effect on the unit economics, however, the effect on the press productivity must also be considered. An increase in the production yield results in an increase in the mass of extrudate produced per billet push, and therefore an increase in the productivity of the line. However, the implementation of a profile-specific dummy block requires additional press time to allow for tooling changes. In production of the Ford profile studied the dummy block is changed once per week, and is a process that requires 15 minutes of time (Can Art, 2022). However, it can overlap with the required 3 minutes of die change time, reducing the time lost specifically to dummy block change to 12 minutes. A profile specific dummy block would require the block to be changed for every profile run (an average of every 2 hours (Can Art, 2022)). A 12 minute tool change every 2 hours is a loss of 10% of productivity. The yield improvements gained through the dummy block design presented (15.5% weld length reduction), results in a productivity increase of 3.9%. If the production run duration is increased the loss of productivity due to dummy block changeover can be decreased. There can be found a minimum production time ( $P_{min}$ ) which must be exceeded for the profiled dummy block to increase production greater than the amount lost based on the conventional production rate (hours per kg extruded,  $t_{per\ kg\ profile}$ ) and improved production rate with novel dummy block ( $t'_{per\ kg\ profile}$ ) (Equation C7).

$$P_{min} = \frac{t_{dummy\ block}}{t_{per\ kg\ profile}} \left( t'^{-1}_{per\ kg\ profile} - t^{-1}_{per\ kg\ profile} \right)^{-1} \quad (C7)$$

The production rate can be found using Equation C8. The improved production rate is found by substituting the improved yield value.

$$t_{per\ kg} = \frac{1}{\lambda V \alpha} \quad (C8)$$

In the production studied, the minimum production time is found to be 16.6 hours. Therefore, it is a net loss of productivity to implement the dummy block described in a production run of 2 hours. However, there are several aspects of the profiled-dummy block implementation and production scheduling that can be altered to move the minimum production time towards a feasible value.

Firstly, the effect of the dummy block on productivity is heavily influenced by the scale of the weld length reduction. An increase in the weld length reduction can significantly decrease the minimum production time. If the achievable weld length reduction in this work was increased to 100% or a more reasonable 50%, with minimum production time would decrease to 2.6 or 5.2 hours respectively. This profile is a complex, multi-hollow profile, resulting in an equally complex dummy block design. In simpler profiles (e.g. bar and rod) feasible dummy blocks with much higher potential for weld length reduction can

be designed; Oberhausen et al. (2021) showed that even with rudimentary design methods, weld length reduction upwards of 40% can be achieved in round bar profiles.

Alongside adjusting scheduling of production runs, the discussed opportunity for multi-profile tooling can also be leveraged to adjust the length of production runs to be closer to the calculated minimum. Similarly, the length of time required for dummy block change-over could be studied. The increased frequency of dummy block change-overs places a higher importance on speed and may warrant a redesign of the hydraulic stem - dummy block joint. The minimum required production time will scale down directly with decreased change over time; a 10% reduction of the dummy block change-over time would decrease the minimum required production time by 10%.

### C.4.3 Environmental Impacts

The changes in generated environmental impacts through the process of extruding the studied profiled with the implementation of a profiled dummy block were also explored. In a similar fashion, the evaluation was performed using a model adapted from Oberhausen et al. (2022) (Equation C9). Included in this model are the impacts of the billet log ( $I_{log}$ ), the tooling ( $I_{tooling}$ ) and the direct energy ( $I_{direct\ energy}$ ). The equipment and container are again excluded due to their relatively long lifespans resulting in a negligible addition to the total impacts on a per kg of finished profile basis.

$$I_{per\ kg\ profile} = [I_{log} + I_{tooling} + I_{direct\ energy}]_{per\ kg\ profile} \quad (C9)$$

Figure C22 below shows the total savings, or reduction, of the global warming potential (GWP) measured in kg CO<sub>2</sub>-eq and the cumulative energy demand (CED) measured in MJ for weld length reductions of 5, 12 and 15.5%. The savings are equivalent to a 0.45%, 1% and 1.4% total reduction for the dummy blocks, respectively.

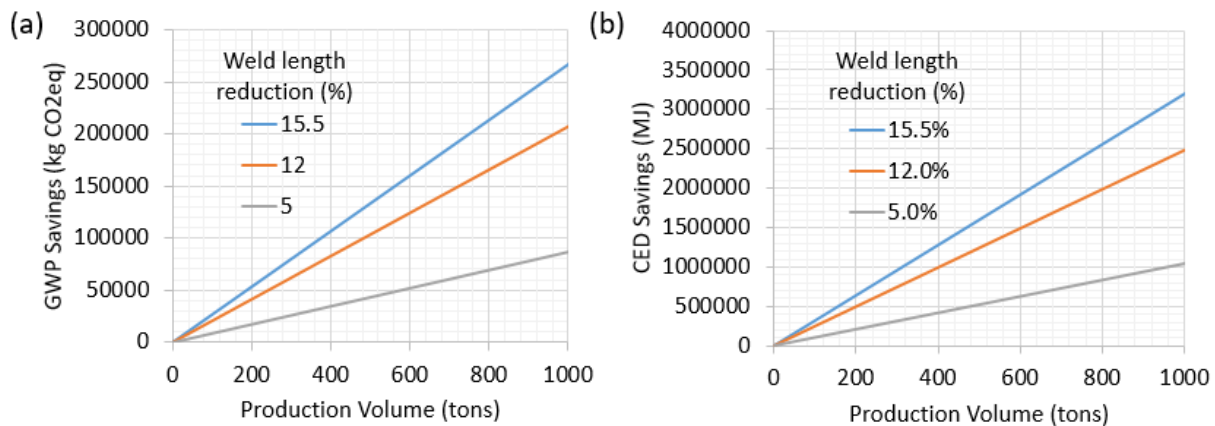


Figure C12: The reduction in (a) GWP and (b) CED for dummy blocks of weld length reduction 5, 12 and 15.5%.



### C.3.3 Experimental Validation of FEA

To ensure that the methods utilizing the above FEA models are accurate to reality, it is important to validate the models against experimental results. This validation is performed in two ways: the transverse weld progression (geometry) is validated to assess the FEA's use for the velocity field method, and secondly the maximum ram force value is compared to experimental data to assess the DEFORM model's use in the mechanical performance analysis of the dummy block.

The transverse weld in the Ford / Can Art profile is represented by a seven-nosed profile (one nose per porthole in the die). Validation of the weld progression is performed by comparing the order and distance at which these noses appear in the experimental and FEA modeled extrudate. Figure C6 below shows an example of the cross section with the seven weld regions labeled in their order of appearance in the sample (from A to G).

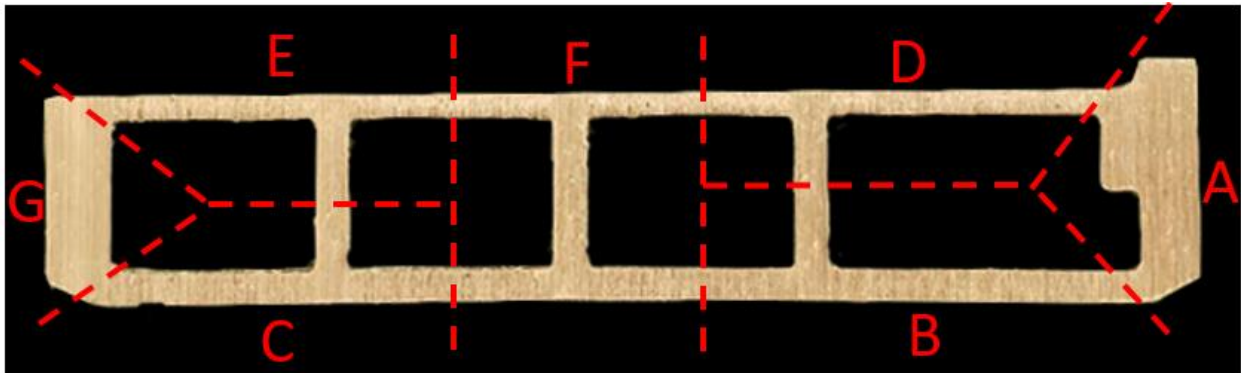


Figure C13: Profile cross section with the seven weld regions labeled A-G.

The experimental weld shape was analyzed through a series of cross-sectional cuts etched in a 10% NaOH solution heated to approximately 100°C for 15 minutes. The samples were then rinsed in deionized (DI) water, dipped in nitric acid to clean the etching residue, and then rinsed in DI water once more. The samples were imaged on a Nikon AZ100 microscope with a low optical zoom (1-4x) and then characterized using IC measure computer software (The Imaging Source, 2019). Figure C7 below shows an example of a set of cross-sectional images produced from each method (Experimental and Velocity Field) and how they may differ in shape.

L = 890 mm from SM; 492 mm from nose

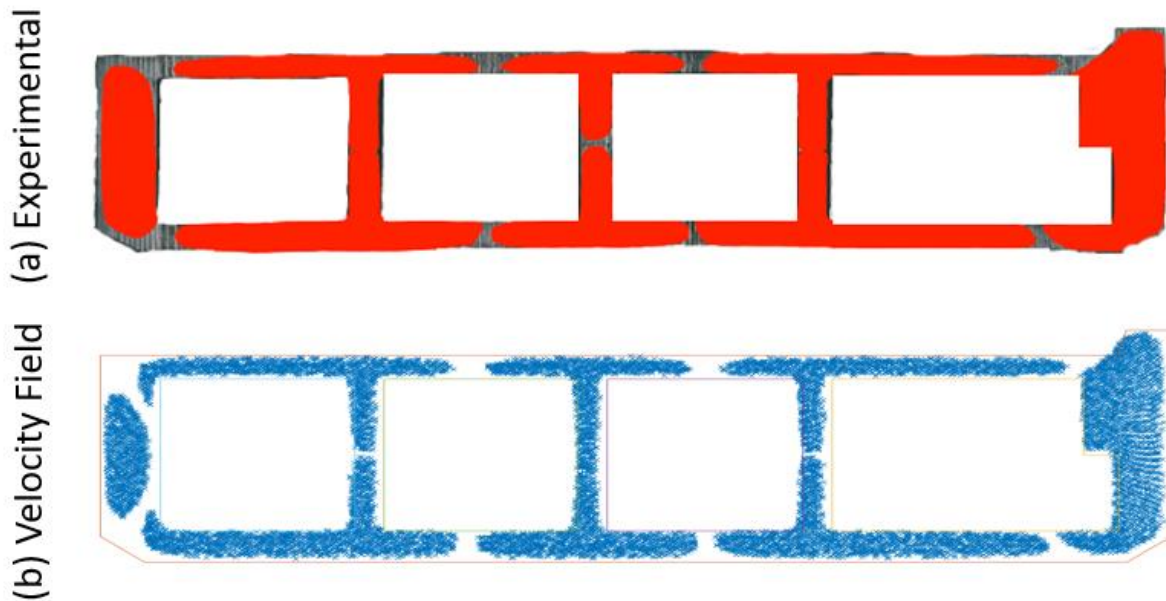


Figure C14: Comparison of (a) Experimental and (b) Velocity Field cross sections at 890 mm from the stop mark (SM) or 492 mm from the nose.

The tables below depicts the order and distance of appearance for the seven concavities across the different modeling methods.

Table C2: Order of appearance in various weld models compared to experimental results. SM = Stop Mark, Nose = Nose of furthestmost weld.

		Porthole						
Datum		A	B	C	D	E	F	G
Experimental	SM	1	2	3	4	6	5	7
Velocity Field	SM	1	2	2	4	5	6	7
Experimental	Nose	1	2	3	4	5	6	7
Velocity Field	Nose	1	2	2	4	5	6	7
DEFOR M	Nose	1	2	3	4	5	6	7

Altair Inspire Extrude	Nose	1	2	3	4	5	6	7
------------------------	------	---	---	---	---	---	---	---

Table C3: Distance of appearance in various weld models compared to experimental results.

		Porthole						
	Datum	A	B	C	D	E	F	G
Experimental	SM	455	490	505	535	545	530	685
Velocity Field	SM	421	444	444	505	515	525	713
Experimental	Nose	0	35	50	80	90	74	230
Velocity Field	Nose	0	23	23	84	94	104	292
DEFORM	Nose	0	14	15	16	59	68	160
Altair Inspire Extrude	Nose	0	18	30	66	78	90	198

It is seen that the order of appearance is nearly identical across the experimental and the different modeling methods; the E and F sections of the weld appear out of order; however, they are within a 15 mm difference when the distance of appearance is considered. Looking more closely, the distance of appearance has mild variability across the different methods. At the most extreme difference, the DEFORM model's D region appears much earlier (40 mm) than in the other methods.

The DEFORM model predicts the maximum ram force value to be 3,500 metric tons. This closely matches the approximate value provided by Can Art (2021) based on a maximum press load of 3,600 tons. With these two validation methods the FEA models can be confidently used in the design methodology.

### C.3.4 Dummy block design

In this section, the ideal weld-reducing dummy block design is derived and rationalized into a feasible geometry which is both geometrically and mechanically compatible with the extrusion process. First the velocity field derived from the Altair Inspire Extrude model (Section C.3.2.2) is utilized to determine the conventional transverse weld geometry. Then, it is again used to determine the ideal shape of the dummy

block for complete weld reduction. This shape is then checked against geometric constraints to ensure it is compatible with the extrusion process, before being translated into a CAD software. The profiled block is then imported into the previously described DEFORM simulation to model the stresses and strains experienced on the billet-contacting-face and to ensure it satisfies the mechanical constraints (limited elastic deformation and no plastic deformation).

### C.3.4.1 Velocity field method

The first step in deriving the ideal dummy block profile geometry in the Velocity Field method is to simulate the conventional transverse weld geometry. To start, a plane of points is created at the location of the billet-billet interface (in the Ford – Can Art profile this plane of points is located at the die entrance (Figure C8)). Also tracked simultaneously is the stop mark locator. The stop mark locator is a point positioned at the die exit which represents the movement and position of the stopmark and can be compared to the weld nose.

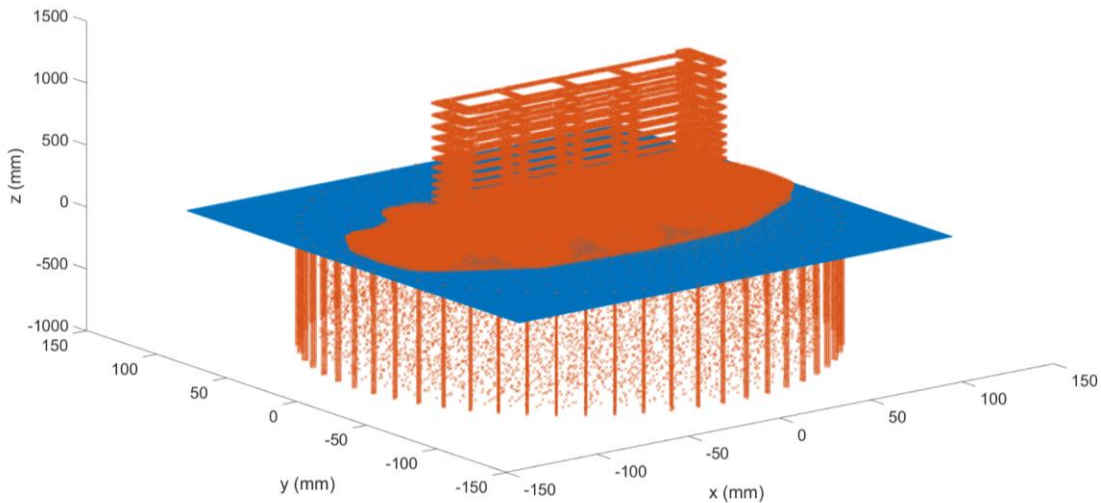


Figure C15: Plane of points (blue) generated at the die entrance to be traced through the velocity field (Orange). This represents tracking the billet-billet interface in conventional flat billet / flat dummy block extrusion.

The points are moved forward step-by-step from a current position ( $P_{old}$ ) to a new position ( $P_{new}$ ). The movement applied in each step is determined by checking the current position of the points ( $P_{old}$ ) against the velocity field map and extracting the velocity of the nearest node ( $V_{p,old}$ ). This velocity is applied to move the point to its new position ( $P_{new}$ ) (see Equation C1).

$$P_{new} = P_{old} + V_{p,old}\Delta t \quad (C1)$$

Figure C9 demonstrates the forward tracking of the original plane of points (depicted by the blue line on the left in the container) to find the conventional weld geometry (depicted by the curved blue weld line on the right).

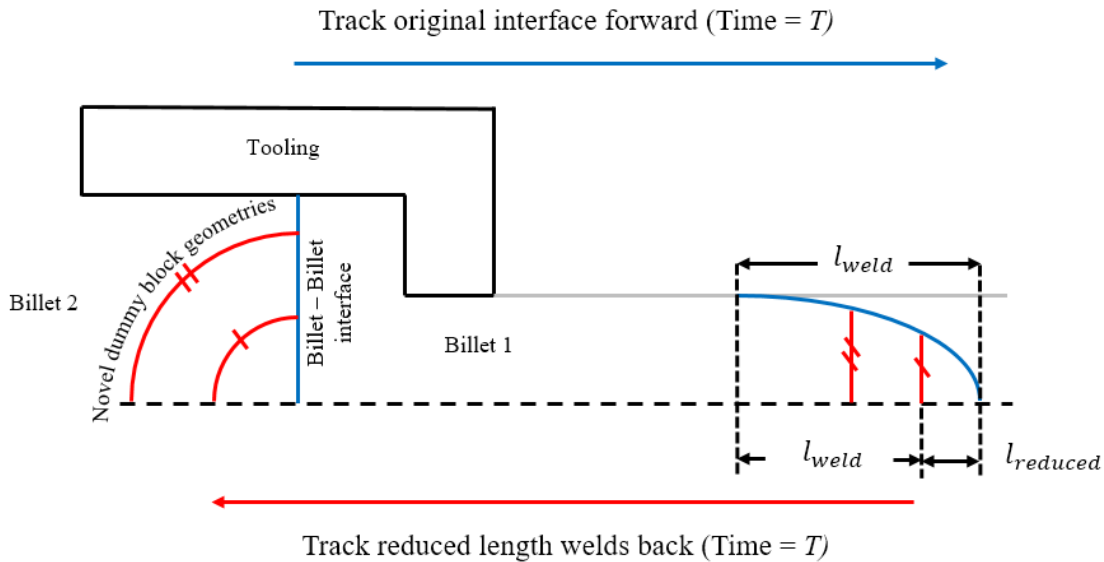


Figure C16: The conventional billet-billet interface can be tracked forwards through the velocity field method to determine the weld geometry. Planes of points can then be back-tracked from a reduced weld length through the velocity field method to determine novel dummy block geometries.

The step size used in the forward tracking is 0.01 seconds which was determined by repeatedly reducing the step size until it no longer made a difference to the final result (weld geometry), and is continued until a sufficient length of the weld has emerged from the die. This corresponds to a total time of 30 seconds; i.e., 3,000 increments. A sufficient length of weld is considered to be the length at which 95% of the profile's cross sectional area is inhabited by new billet. This is the location at which the weld is assumed to have satisfactory strength in industry and previous literature (Oberhausen et al., 2021). The result of this incremental tracking is a 3-dimensional representation of the weld geometry (Figure C10).

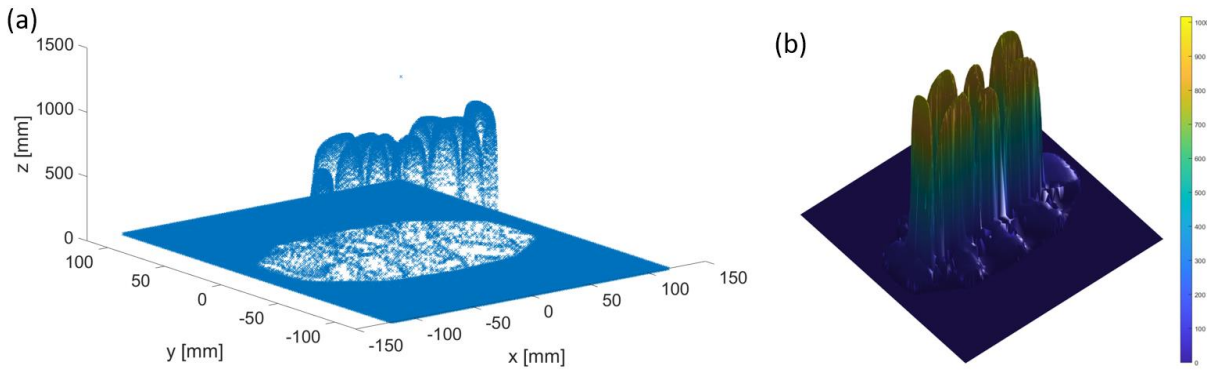


Figure C17: 3D representation of Ford / Can Art transverse weld.

Now a plane of points can be generated at the location on the conventional weld that has been determined to have satisfactory strength to represent a flat, ideal weld. This plane can be tracked back through the velocity field, from the die exit to the die entrance, over the same time length and using the same time increments as the forward tracking (see Equation C1 and Figure C9) to determine the shape of a dummy block profile that would create this ideal weld (see Figure C11).

The generated dummy block profile is ideal in its ability to reduce the weld length, however, may not be mechanically, or even geometrically feasible. Mechanical feasibility is defined as the dummy block experiencing minimal plastic and elastic deformation, just as in the case of the conventional dummy block. Geometric feasibility addresses the need for the generated profile to be compatible with the extrusion process. The profile must be able to exist in the interface between a dummy block and back-face of a billet. The ideal geometry for a 100% weld length reduction generated for the Ford / Can Art profile is a good example of a geometrically infeasible block. As seen in Figure C11, the concavities on the ideal dummy block profile are both expanding and overlapping; the entrances of the concavities on the face of the dummy block have a smaller opening than the internal geometry of the concavities. This geometry would prevent the mating with and release of a billet from the dummy block face.

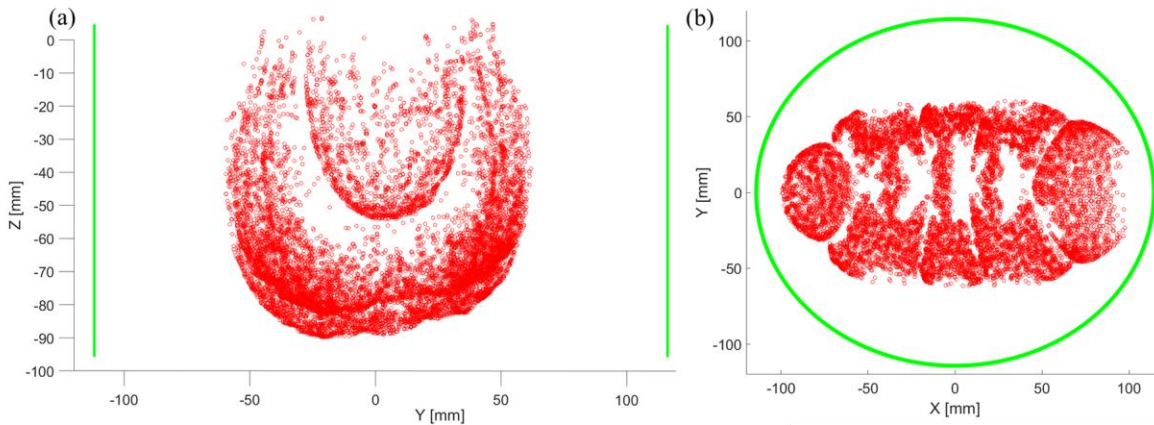


Figure C18: The (a) x-axis and (b) a-axis view of the Ford / Can Art ideal dummy block geometry, determined through backtracking of the plane of points at the location of satisfactory weld strength on the conventional weld geometry for a 100% weld length reduction. Note that the concavities are expanding from the dummy block face (0 mm plane). The points in green represent the outer diameter of the billet/dummy block.

If the design were to be altered such that this ideal profile was widened at the dummy block face, the weld length would be increased at the edges. Instead, the design is compromised in its goal of weld length reduction. The ideal profile above was designed for a weld length reduction of 1000 mm (500 mm gap between stop mark and nose remains). A geometrically feasible design was approached by incrementally shifting the pre-backtracked plane (red flat line on the right in Figure C11) closer to the weld tip. This process reduces the weld length reduction from its ideal 100%, though is necessary to produce a design which is compatible with the extrusion process.

To facilitate this process graphs depicting the contours of weld length reductions can be created. A contour graph is necessary for each axis (x and y) of every concavity (A-G). Figure C12 shows the contours for the x and y axis of concavity A, alongside two example created tooling geometries (ideal, which follows the 15.5% reduction line, and Reduced X and Y, which has a reduced width in the x and y axes). The example line with reduced x and y widths shows that by crossing the contour lines the reduction of the weld varies across the radius (the outside of the weld created from the geometry shown will correspond with only an 8% reduction, whereas the center corresponds with a 15.5% reduction. For this reason, all tooling geometries in this work are created to exactly follow the weld length reduction contours.

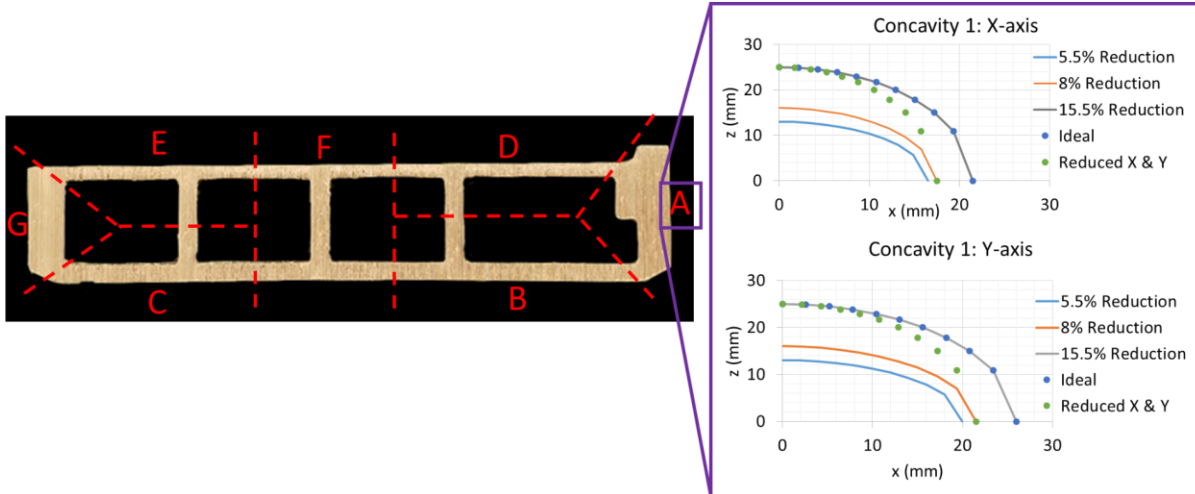


Figure C19: Two example tooling geometries for concavity A (Ideal and Reduced X & Y) plotted against the weld length reduction contours for the x and y axes of concavity A.

When a design that is geometrically feasible is found the next step is to create a CAD model of the design. The process by which the design is translated from point clouds output by MATLAB to a CAD model is currently to overlay semi-ellipsoids on each individual concavity. Semi-ellipsoids of best fit are currently found via manual comparison, and then created using the ellipse sketch feature in SolidWorks. This process does not perfectly recreate the backtracked design but provides a close approximation. Figure 13 shows the design for a dummy block which shortens the transverse weld by 155 mm, approximately 15.5%, and shows the ellipsoids of best fit (blue).

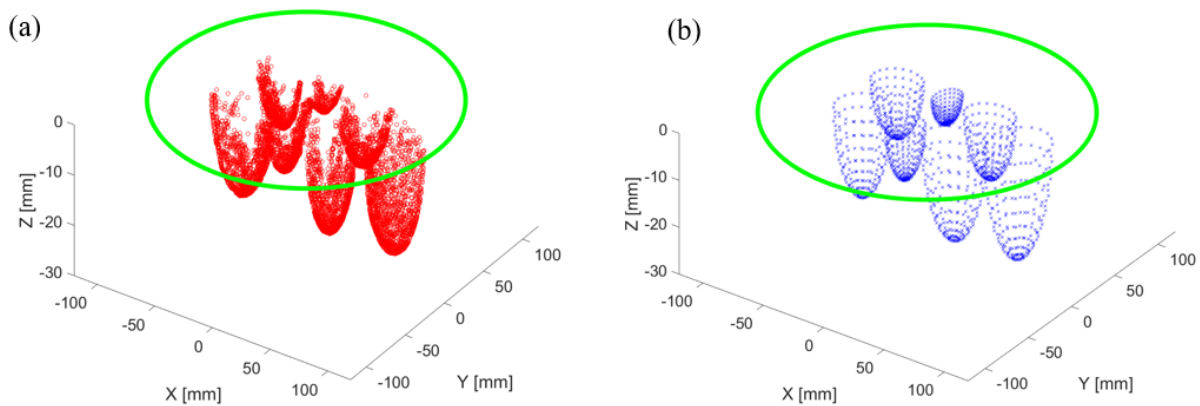


Figure C20: (a) Ideal dummy block geometry and (b) semi-ellipsoids of best fit for weld length reduction of 155 mm. The green circles represent the outer diameter of the dummy block. Note the seven semi-ellipsoids present, one for each of the seven die portholes and weld noses.

Figure C14 below provides a side-by-side comparison of the idealized resultant reduced length transverse weld with the original weld geometry. The dummy block has the effect of flattening the portion



of the weld which it is reducing. In this example the top 155 mm, or 15.5 % of the 1 m weld length, is flattened.

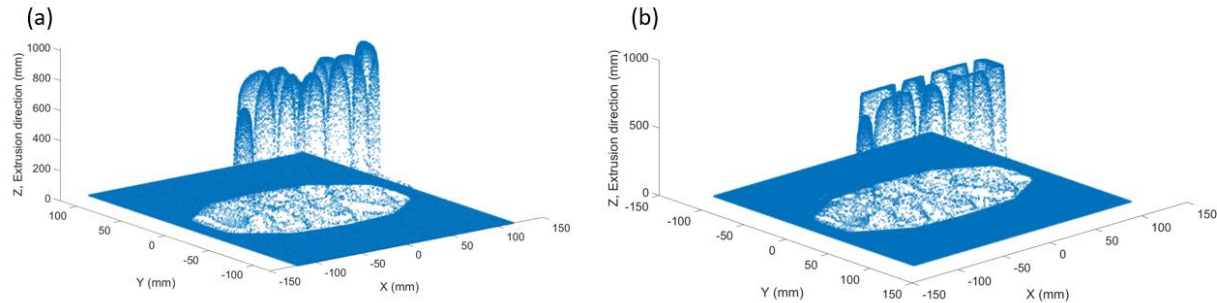


Figure C21: Weld geometry of (a) conventional transverse weld and (b) 15.5% reduced length transverse weld.

### C.3.4.2 Dummy block analysis

To determine the mechanical feasibility of the dummy block design under extrusion conditions, the stresses and strain experienced by the dummy block are evaluated. There are two methodologies for analysis of tool performance in DEFORM simulations: coupled and decoupled. In the coupled analysis the simulation is run from start to finish with the tool as a deformable object. This allows the tool's response to be monitored for the entire duration of the procedure, however, is much more computationally expensive as it introduces an additional deformable object. In decoupled analysis the simulation is run with a rigid tool. Then, at the step in the simulation at which tool analysis is desired (in the case of this work, the step with peak ram forces) the tool is converted to an elastic, or elasto-plastic object and the reaction forces from the workpiece are interpolated onto the tool. A single step simulation is then run to analyze the response of the tool to these forces. In this method the speed of simulation is much increased, however the scope of the analysis is limited to a single step. In this work the coupled method is utilized as only the highest tool response is of interest.

Additionally, there is the option of modeling the tool as either a purely elastic, or an elasto-plastic material. Modeling the tool as an elasto-plastic enables modeling of the tool to failure, however, will increase the computational expense of the simulation. It is recommended by DEFORM that elasto-plastic simulations are used only when failure of the tool is expected. Due to the dummy block being modeled as a solid block, for which failure cannot be accurately predicted, the analysis is performed using an elastic material model. However, a single elasto-plastic model is analyzed to consider the possible result.

To create the elastic, decoupled model used first the conventional dummy block with flat face is evaluated. Evaluation of the conventional case allows the profiled block results to be placed in context. In this analysis the earlier created DEFORM3D model with prefilled die is utilized. A single step simulation

is created at the step in the original model at which the ram forces are at their peak (corresponding to the maximum billet length). The billet is then removed from the simulation, then the dummy block is converted to an elastic object and meshed with 500,000 elements. The mesh is generated with a region of fine (2 mm) elements on the billet facing third of the block, and a region of coarser elements (5 mm) on the remaining two-thirds. The boundary conditions include the restriction of the x, y and z velocities on the back face of the dummy block to prevent movement of the block. The dummy block is given elastic material property data for H-13 steel at 426°C (Uddeholm, 2020) (an elastic modulus of 175 GPa and a yield strength of 950 MPa). The forces present on the back of the billet in the initial simulation are interpolated onto the face of the dummy block and a single step, stress analysis is run.

To analyze the profiled dummy blocks, a new original model must be created and run with both a modified billet and dummy block geometry. The dummy block can simply be imported in STL or SLDPRT form from the SolidWorks model that was previously created. The altered billet is generated in Blender using a Boolean subtraction of the dummy block profile on the back face of the billet, to create a surface that mates with the dummy block profile. The results of the simulation can then be observed in the DEFORM post-processor.

Also considered is plasticity of the dummy block, to account for strain hardening and to measure the presence of plastic strain. An identical model is created with the dummy block represented by an elasto-plastic object. The elastic material data remains unchanged, and additional plastic material data is derived (Figure C15) from the elastic data (modulus [ $E$ ], yield stress [ $\sigma_{yield}$ ] and ultimate tensile strength) using the Ramberg-Osberg equation (Ueng and Chen, 1992) (Equation C2). A yield off-set ( $\alpha$ ) of 0.2% is assumed.

$$\varepsilon = \frac{\sigma}{E} + \alpha \left( \frac{\sigma}{\sigma_{yield}} \right)^{\frac{1}{n}} \quad (C2)$$

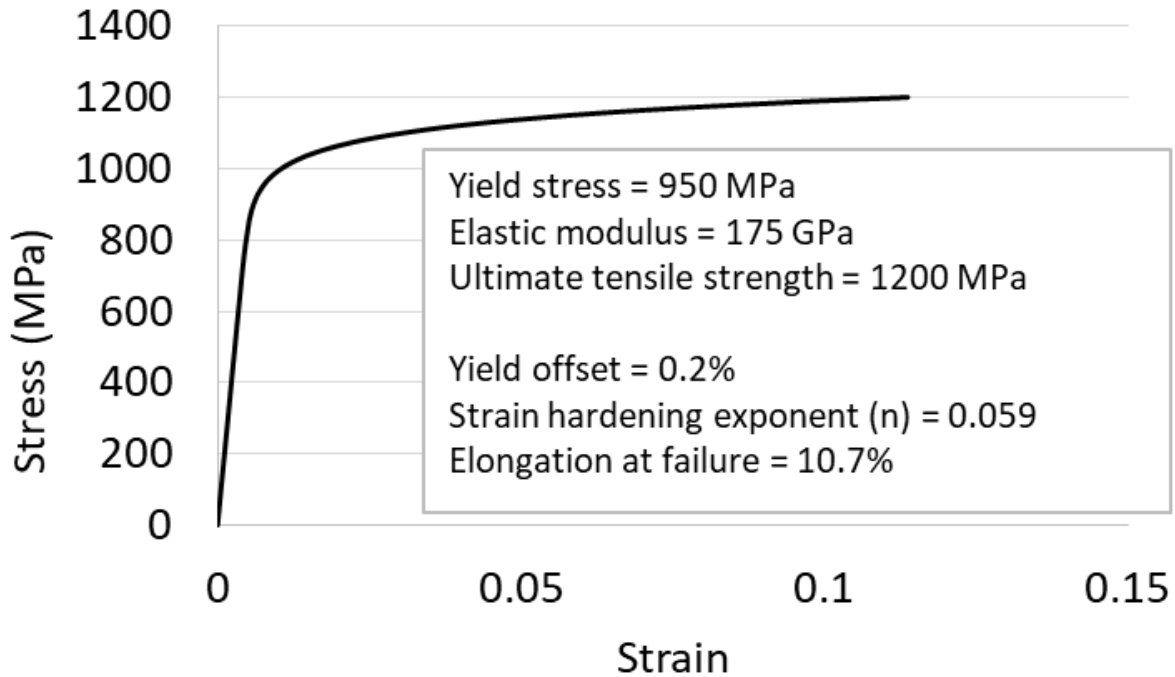


Figure C22: Derived plastic stress strain curve for H13 steel based on elastic properties and assumed offset and hardening terms.

### C.5 Section discussion

This work presents a preliminary techno-economic analysis of profiled dummy block tooling for the Ford / Can Art aluminum extrusion profile. The technical analysis on the presented dummy block geometries show that there is feasible and significant scope for decreasing the weld length under extrusion conditions. In the Ford / Can Art profile studied, the weld length reduction is found to be limited by the geometric feasibility of the dummy block design. The analysis of the financial trade-offs demonstrate the potential savings offered by the novel extrusion tooling but that these savings might be compromised if a 15 minute dummy block change were required every 2 hours.

#### C.5.1 Opportunities

Manufacturing scrap represents a significant portion of aluminum extrusion impacts and costs, of which the transverse weld is a significant component (Oberhausen et al., 2022). The models presented in this article have found feasible scope to reduce the transverse weld and therefore the costs and impacts in the aluminum extrusion process. The Ford / Can Art profile studied in this work has an original transverse weld length of 1.5 m, though the first 50 cm of this distance represents just the span from the stop mark to the tip of the weld. The stop mark is an aesthetic mark on the extrudate perimeter made at the location in contact with the die bearing during the brief pause in extrusion for a new billet to be placed in the container

(Mahmoodkhani et al., 2014). Removal of this gap between the stop mark and tip increases the transverse weld scrap rate in this case by 33%, the mass scrapped by 2.1 kg and cost of each billet push by \$7.50. The reason for its removal in non-aesthetic applications such as this profile is the ease and consistency of the stop mark as a locator for the transverse weld. To analyze, measure and cut the weld out of the extrudate more accurately will require greater effort and time than using the stop mark as a guide, however there may be greater overall savings with a more accurate, and reduced length cut.

In the profile studied, the limitation restricting greater weld length reduction was the geometric feasibility of the ideal dummy block profile as well as the increase in maximum effective stress on the dummy block face. In simpler extrusion profiles, both in terms of geometric complexity and those with smaller extrusion ratios, these limitations would be relaxed.

An example of extruded profiles with simpler geometries would be the tube, rod and bar market, together representing almost 20% of the total North American extrusion market (Oberhausen et al., 2022) (Figure C23). The increased production volume per profile (when compared to custom, complex profiles) of these products would also result in a greater amortization of any additional tool design costs. Profiled dummy blocks may present a much greater potential for weld length, cost and impact reduction in these high-volume, commodity markets. Due to the closeness in die-design, the designed dummy block profiles for rod and bar of similar geometries are equally close in geometry. Therefore, there is an opportunity in the case of simpler profiles to design a single dummy block profile which provides moderate weld reduction on two or more extruded profiles of similar geometry. This multi-profile dummy block approach can reduce the overall design costs and tooling inventory requirements.

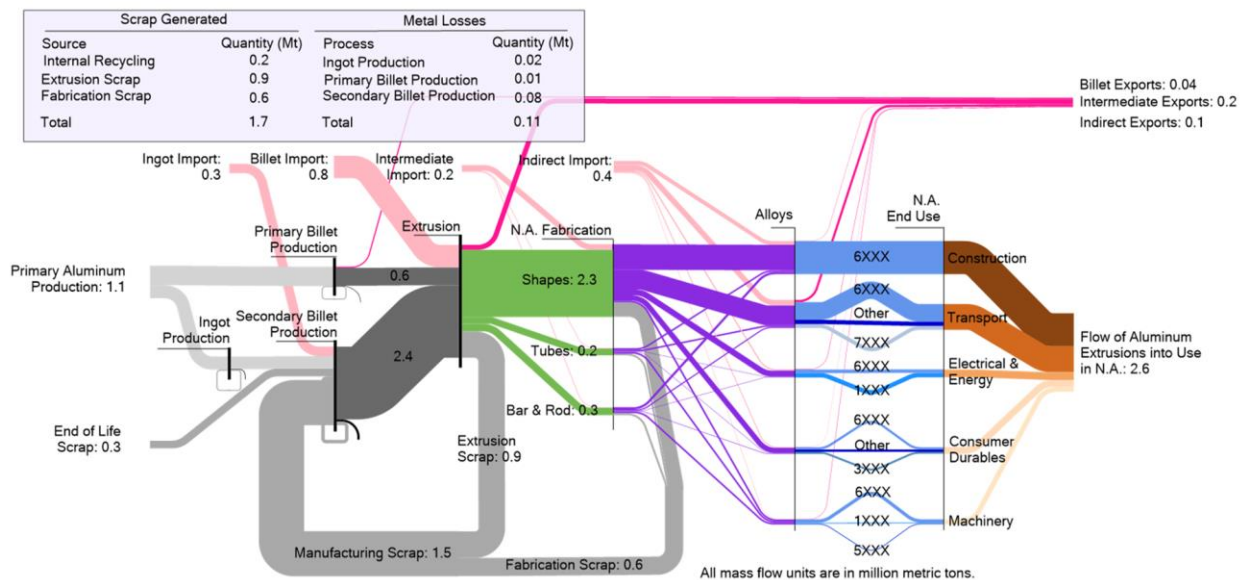


Figure C23: The 2018 North American Extrusion Industry material flow analysis (Oberhausen et al., 2022).

### **C.5.2 Barriers to Implementation**

The technical analysis of the presented dummy block geometries highlights transverse weld savings up to 15.5%. The global cost model and North American extrusion industry mass flow values presented in Oberhausen et al. (2022) suggest that these weld length reductions applied at the scale of the whole industry could save almost 175 million USD per year and prevent the release of 0.65 Mt.CO<sub>2</sub>eq annually. However, there are several barriers uncovered through this case study which must be overcome before widespread adoption of this technology can be expected in the extrusion industry.

One fundamental barrier is the necessity for the billets to mate with the dummy block profile. In this work it was assumed that the back face of billets were created with a convex profile to match the dummy block. During interviewing for NSF I-CORPs, the project team discovered that extrusion billets are not cast individually but conventionally direct chill (DC) cast in approximately 7 m logs. These logs are then shipped to the extrusion facilities and cut to their extruded lengths (0.66 - 1.83 m) (AEC, 2021) with flat faces. Direct chill casting of extrusion length billets, rather than logs, with profiled ends is unlikely to be feasible. First there are the economic concerns; reducing the length of each casting will cut throughput significantly (74-90% reduced throughput) if it is assumed that the same number of DC casting molds are used, and they are merely adapted to a shorter length. Second, in DC casting of billet logs, the top portion of the cast log, known as the liquid sump, is removed as scrap due to a change in composition caused by altered cooling profile (Pelayo, 2012). The removal of this section of the cast billets would eliminate the profiled ends necessary for the profiled dummy blocks.

It is more feasible to consider the methods which would shape the billet after it has been cut to billet length at the individual extrusion facilities. The billets could be hot-forged into shape prior to being placed into the extrusion container, or it can be formed in-situ at the start of the extrusion process within the extrusion container. External pre-forging will require an additional step, increasing per part production time and cost. Though it may not decrease overall process throughput, as the extrusion step would likely remain the process bottleneck (Kaiser Aluminum, 2020). In-situ forming has the added benefit of minimally impacting the process flow chain; a flat-faced billet of conventional size would be inserted into the container where it would then be shaped to the required profile. In both circumstances there are concerns regarding the quality of the material on the billet at the locations of deformation. Microstructural analysis would be necessary to determine if deformation required to form the billets would result in ductile damage, or crack formation, on the faces of the billet. Additionally, experiments to identify and reconcile the potential for air trapped within the concavity as the billet fills the dummy block to cause blister formation, or other surface defects.

An additional barrier to widespread adoption is the need for the profiled back-end of the billet to persist between extrusion strokes. In conventional extrusion the dummy block would stop with around 10% of the billet length remaining in the container to allow for removal of the backend defect. The extrusion back end defect refers to the remaining 5-15% of the length of a billet which remains unextruded in the container following a billet push and is instead removed as scrap by a hydraulic shear. This section of the billet contains impurities (e.g., oxides, spinels, and intermetallics) which are initially dispersed on the surface, or skin, of the billet, but are then concentrated due to the metal flow within the container during extrusion (Oberhausen et al., 2021). If this section of the billet were to be extruded into the final profile, it would result in a reduction of aesthetic, mechanical and electrical properties (Saha, 2000). Removal of this section of the billet would include removal of the necessary profiled back face of the billet. An older method known as Dick's extrusion method (Sheppard, 1999) includes extruding the back end and its contained contaminants through the die and into the extrudate, where it is sectioned out just as in the case of the transverse weld. The billet shear was innovated as it saved time and costs, however with the added benefit of transverse weld length reduction it may be more efficient to use Dick's extrusion method.

Elsewhere, Liu et al. (2016) investigated the effect of dummy block geometry on the formation of the back-end defect. Liu et al. tested dummy block designs with concavities over a range of diameters, as well as blocks with beveled edges over a range of angles. Their study parametrically evaluated these two design aspects, measuring their effect on back end defect reduction for a simple axisymmetric extrusion profile. They found that a concave-center dummy block can reduce the formation of the back-end funnel defect (reduce the length of the back-end defect extruded into the extrudate). These results would suggest that the concave dummy blocks designed in this work could reduce the back-end defect. The authors of this work preliminary FEA analysis which produced similar results; the extruded back-end defect length was found to be reduced with a concave, profile dummy block (Figure C24). Importantly, the preliminary results also showed the extruded back-end defect clustering around the nose of the transverse weld. This would allow extruders to remove both defects in one cutting operation.

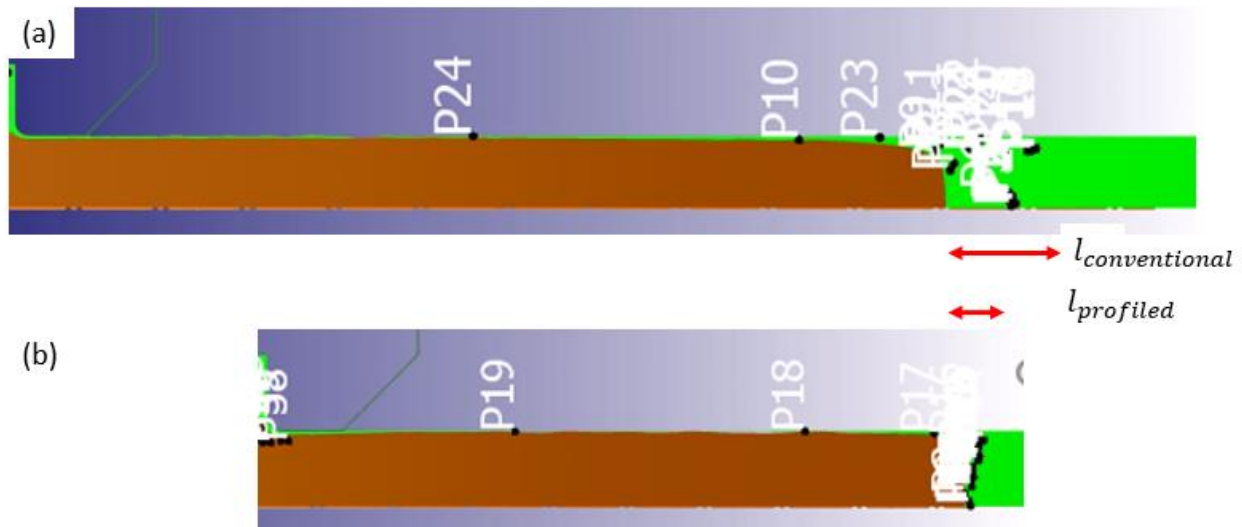


Figure C24: Results of preliminary FEA comparing the extruded back-end defect length in an axisymmetric extrusion using (a) conventional, flat dummy block and (b) a novel, concave profiled dummy block.

FEA or experimental trials should be performed to validate this effect in profiles that are more complex than the axisymmetric case studied in Liu et al. An economic analysis of extended scope will be required to evaluate if the profiled dummy block implemented with Dick's extrusion method results in a net reduction of costs and material usage over the conventional dummy block and shear methods used today.

### C.6 Conclusion and Next steps

In this work, a methodology to design dummy blocks to reduce the transverse weld length in aluminum extrusion is presented. A number of velocity field driven designs are produced and then evaluated under extrusion conditions using FEA. The material and mechanical constraints are identified, and an ideal design is chosen. A thorough financial analysis is performed to determine the potential savings as well as the effect on productivity expected from a change of dummy block.

There are several areas within the methods presented which would need to be improved for full-scale production implementation. Firstly, the translation of the dummy block designs from a Matlab point cloud to a CAD design was done with manually fit ellipsoids. This both creates only a rough representation of the shape, but also leaves too much room for differences due to interpretation. A more precise method of translation should be developed. Secondly, the mechanical response of the dummy block was evaluated with a solid block in FEA, which is an imperfect representation of expanding dummy block designs. A more accurate representation of the dummy block should be evaluated in FEA, however this was outside of the scope of the work presented.

An NSF Partnerships for Innovation (PFI) project kicked off at the beginning of 2022 and will run through December 2023 to tackle some of the barriers to implementation outlined in the discussion. Table C4 summarizes the work to be completed in the NSF PFI project.

Table C4: The knowledge gaps, technical barriers and corresponding tasks in the ongoing PFI project to overcome novel dummy block implementation into the extrusion industry.

<b>Knowledge gap</b>	<b>Technical barriers</b>	<b>Corresponding Task</b>
The minimum length of extruded profile that must be removed to ensure sufficient profile strength.	A predictive model of the local transverse weld strength.	Task 1: Validating a mechanistic transverse weld strength model.
Hot billet properties (microstructure, cracks, back-end defects) after in-situ profiling between a profiled dummy block and warm billet butt or hard tooling. Location and removal of any trapped air surrounding the formed billet.	A ductile damage criterion to determine the onset of billet cracking. Predictive FEA modeling of back-end (funneling and coring) defects in new technology. Using deformation, air vents, and burp cycles to prevent and release trapped air. A process window for in-situ pre-forming of billets.	Task 2: Pre-forming crack-free aluminum billets in-situ
The technology customization trade-off between higher process yields & higher upfront tool costs.	Optimizing the same hardware across multiple extrusion profiles/alloys. Cost modeling to inform the trade-off.	Task 3: A TEA & experimental analysis of technology customization.
Confirm that extruders will pay for the technology.	Integration of all process steps to physically demonstrate a Minimum Viable Product.	Task 4: Pilot-scale proof-of-concept.

In this NSF PFI project a mechanistic transverse weld strength model will be developed to better locate the length of the transverse weld at which satisfactory strength is reached. This will help to reduce the unnecessary removal of extrudate with mechanical properties equal to that of bulk material. Next, a series of physical experiments will be conducted to investigate the issues surrounding in-situ forming of profiled billets in the extrusion container and determine a process window. The issues addressed include avoiding the onset of billet cracking and the prevention of entrapped air. FEA analysis to develop a complete understanding of the potential consequences or benefits of extruding the back-end defect into the extrudate will also be completed.

The project will also include an investigation into the potential benefits of the multi-profile tooling outlined in Section C.5.1, as well as a more complete techno-economic analysis for the implementation of profiled dummy blocks into all parts of the extrusion industry. The project culminates in an integration of all process steps in the production of a minimum viable product in a pilot-scale proof-of-concept trial. We hope to continue dialogue with Ford as we continue down the road of exploring the novel profiled dummy block concept in the PFI project.

### C.7 References



- AEC, 2021. Aluminum Extrusions are part of the Truck/Trailer Solution [WWW Document]. URL <https://www.aec.org/page/extrusion-applications-truck-trailer> (accessed 6.9.21).
- Allwood, J.M., Cullen, J.M., Carruth, M.A., Cooper, D.R., McBrien, M., Milford, R.L., Moynihan, M.C., Patel, A.C., 2012. Sustainable Materials - with Both Eyes Open: Future Buildings, Vehicles, Products and Equipment, 1st ed. UIT Cambridge Ltd., Cambridge, UK.
- Allwood, J.M., Cullen, J.M., Milford, R.L., 2010. Options for achieving a 50% cut in industrial carbon emissions by 2050. *Environ. Sci. Technol.* 44, 1888–1894. <https://doi.org/10.1021/es902909k>
- Avitzur, B., 1963. Analysis of Wire Drawing and Extrusion Through Conical Dies of Small Cone Angle. *J. Eng. Ind.*
- Can Art, 2021. Can Art Roundtable Discussions.
- Chen, L., Zhao, G., Yu, J., 2015. Effects of ram velocity on pyramid die extrusion of hollow aluminum profile 2117–2125. <https://doi.org/10.1007/s00170-015-7059-5>
- Chen, X., Önal, H., 2016. Renewable energy policies and competition for biomass: Implications for land use, food prices, and processing industry. *Energy Policy* 92, 270–278. <https://doi.org/10.1016/j.enpol.2016.02.022>
- Cooper, D.R., Rossie, K.E., Gutowski, T.G., 2017. The energy requirements and environmental impacts of sheet metal forming : An analysis of five forming processes. *J. Mater. Process. Tech.* 244, 116–135. <https://doi.org/10.1016/j.jmatprotec.2017.01.010>
- Cullen, J.M., Allwood, J.M., 2013. Mapping the global flow of aluminum: From liquid aluminum to end-use goods. *Environ. Sci. Technol.* 47, 3057–3064. <https://doi.org/10.1021/es304256s>
- Den Bakker, A.J., Katgerman, L., Van Der Zwaag, S., 2016. Analysis of the structure and resulting mechanical properties of aluminium extrusions containing a charge weld interface. *J. Mater. Process. Technol.* 229, 9–21. <https://doi.org/10.1016/j.jmatprotec.2015.09.013>
- Dyla, J.E., 2019. Aluminum Extrusion Tooling II, 134–138.
- Gutowski, T.G., Sahni, S., Allwood, J.M., Ashby, M.F., Timothy, G.M., Ashby, F., Worrell, E., 2013. The energy required to produce materials: constraints on energy-intensity improvements, parameters of demand. *Philos. Trans. Math. Phys. Eng. Sci.* 371, 1–14.
- Hatzenbichler, T., Buchmayr, B., 2010. Finite element method simulation of internal defects in billet-to-billet extrusion. *Proc. Inst. Mech. Eng. Part B J. Eng. Manuf.* 224, 1029–1042. <https://doi.org/10.1243/09544054JEM1830>
- Heinemann, H.H., 1961. Flow Stress of Different Aluminum and Copper Alloys for High Strain Rates and Temperature.
- International Aluminum Institute, 2021. IAI current statistics [WWW Document]. URL <https://www.world-aluminium.org/statistics/> (accessed 9.6.21).
- International Energy Agency, 2017. Energy Technology Perspectives 2017 - Executive Summary [WWW Document]. [https://doi.org/10.1787/energy\\_tech-2014-en](https://doi.org/10.1787/energy_tech-2014-en)
- Kaiser Aluminum, 2020. Kaiser Aluminum roundtable discussion.
- Liu, C.H., Yang, J. Bin, Lin, H.C., 2016. Design of a novel dummy block by finite element simulation to eliminate back end defects in direct extrusion. *Trans. Indian Inst. Met.* 69, 1699–1710. <https://doi.org/10.1007/s12666-016-0830-y>
- Liu, G., Bangs, C.E., Müller, D.B., 2011. Unearthing potentials for decarbonizing the U.S. aluminum cycle. *Environ. Sci. Technol.* 45, 9515–9522. <https://doi.org/10.1021/es202211w>
- Mahmoodkhani, Y., Wells, M.A., Parson, N., Poole, W.J., 2013. Numerical modelling of the material flow during extrusion of aluminium alloys and transverse weld formation. *J. Mater. Process. Technol.* 214, 688–700. <https://doi.org/10.1016/j.jmatprotec.2013.09.028>
- Milford, R.L., Allwood, J.M., Cullen, J.M., 2011. Assessing the potential of yield improvements, through process scrap reduction, for energy and CO<sub>2</sub>abatement in the steel and aluminium sectors. *Resour. Conserv. Recycl.* 55, 1185–1195. <https://doi.org/10.1016/j.resconrec.2011.05.021>
- Moreau, V., Dos Reis, P.C., Vuille, F., 2019. Enough metals? Resource constraints to supply a fully renewable energy system. *Resources* 8. <https://doi.org/10.3390/resources8010029>

- Oberhausen, G., Zhu, Y., Cooper, D.R., 2022. Reducing the environmental impacts of aluminum extrusion. *Resour. Conserv. Recycl.* 179, 106120. <https://doi.org/10.1016/j.resconrec.2021.106120>
- Oberhausen, G.J., Christopher, A.A.A., Cooper, D.R., 2021. Reducing aluminum extrusion transverse weld process scrap, in: *International Conference on the Technologies of Plasticity*. The Minerals, Metals & Materials Society, Virtual.
- Pedneault, J., Majeau-Bettez, G., Krey, V., Margni, M., 2021. What future for primary aluminium production in a decarbonizing economy? *Glob. Environ. Chang.* 69, 102316. <https://doi.org/10.1016/j.gloenvcha.2021.102316>
- Pelayo, R., 2012. *Direct Chill and Fusion Casting of Aluminum Alloys* 150.
- Robbins, P., Dixon, B., Chien, K., Jowett, C., 2016. Today 's Understanding of the Function and Benefits of Dummy Block Design 387–404.
- Ryberg, D.S., Robinius, M., Stolten, D., 2018. Evaluating land eligibility constraints of renewable energy sources in Europe. *Energies* 11, 1–19. <https://doi.org/10.3390/en11051246>
- Saha, P.K., 2000. *Aluminum Extrusion Technology*. ASM International, Materials Park, Ohio.
- Sano, H., Ishikawa, T., Yukawa, N., Yoshida, Y., Kaneko, T., 2008a. Effect of extrusion mode and die shape on billet skin behavior in aluminum extrusion. *Keikinzoku/Journal Japan Inst. Light Met.* 58, 183–188. <https://doi.org/10.2464/jilm.58.183>
- Sano, H., Ishikawa, T., Yukawa, N., Yoshida, Y., Kaneko, T., Sakamoto, J., 2008b. Effect of back end lubricant conditions on billet skin behavior in direct extrusion. *Keikinzoku/Journal Japan Inst. Light Met.* 58, 189–193. <https://doi.org/10.2464/jilm.58.189>
- Sheppard, T., 1999. *Extrusion of Aluminium Alloys*, 1st ed, *Extrusion of Aluminium Alloys*. Springer Science + Business Media, Dordrecht. <https://doi.org/10.1007/978-1-4757-3001-2>
- Suhara, M., 2019. IPCC AR5 183–220. [https://doi.org/10.1007/978-981-13-8429-5\\_6](https://doi.org/10.1007/978-981-13-8429-5_6)
- Superior Aluminum, 2019. Superior Aluminum roundtable discussion.
- The Imaging Source, 2019. IC Measure [WWW Document]. URL <https://www.theimagingsource.com/support/downloads-for-windows/end-user-software/icmeasure/> (accessed 4.13.20).
- Thumb Tool & Engineering, 2021. Thumb Tool & Engineering Roundtable Discussion.
- Thumb Tool & Engineering, 2018. Thumb Tool & Engineering roundtable discussion.
- Uddeholm, 2020. Orvar® Supreme H-13 Steel Data Sheet [WWW Document]. URL [https://www.uddeholm.com/app/uploads/sites/54/2018/05/uddeholm-orvar-supreme-eng\\_p\\_2003-e11.pdf](https://www.uddeholm.com/app/uploads/sites/54/2018/05/uddeholm-orvar-supreme-eng_p_2003-e11.pdf) (accessed 3.15.22).
- Ueng, T.-S., Chen, J.-C., 1992. Computational Procedures for Determining Parameters in Ramberg-Osgood Elastoplastic Model Based on Modulus and Damping Versus Strain. *Lawrence Livermore Natl. Lab* 22.
- Walters, J., Foster, M., Bandar, A., 2012. The 'State of the Art' in Aluminum Extrusion Simulation Using the Finite Element Method 541–552.
- Worighi, I., Maach, A., Hafid, A., Hegazy, O., Van Mierlo, J., 2019. Integrating renewable energy in smart grid system: Architecture, virtualization and analysis. *Sustain. Energy, Grids Networks* 18, 100226. <https://doi.org/10.1016/j.segan.2019.100226>
- Zhang, C., Dong, Y., Wang, C., Zhao, G., Chen, L., Sun, W., 2017. Evolution of transverse weld during porthole extrusion of AA7N01 hollow profile. *J. Mater. Process. Technol.* 248, 103–114. <https://doi.org/10.1016/j.jmatprotec.2017.05.017>

## Appendix D. Previous LIFT Rectangular Bar Trial Using DEFORM Point Tracking Algorithm

In this section, the methodology and results of the 2021 concave dummy block trials performed at LIFT will be described. This trial took place before the trial described in Section 4.2 and used the DEFORM built-in point tracking algorithm for billet design, rather than the velocity field method.

### D.1 DEFORM Model

The DEFORM model was run as a quarter-sized model using the multifrontal massively parallel sparse direct solver and the Newton-Raphson iteration method. The billet was modeled as von Mises materials with isotropic hardening and the flow curve of AA6061 at 530°C (Figure D1). The die, container, and dummy block were modeled as rigid bodies. Contact between the billet-die and billet-container were modeled using sticking friction and between the billet-dummy block as frictionless, reflecting the use of boron nitride lubricant on the dummy block in industry. The typical element size used in the models was  $\approx 0.75$  mm in the die region and  $\approx 1.5$  mm elsewhere. Remeshing occurred when the billet-tooling interference exceeded 0.25 mm. An axisymmetric model was used to simulate extrusion of the round bar.

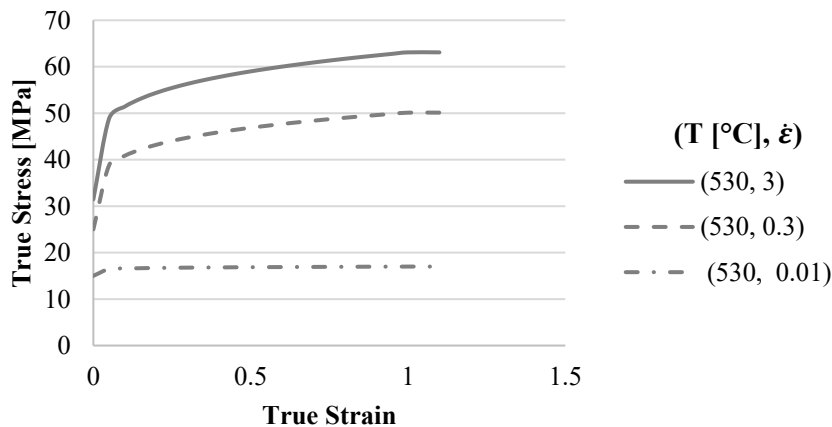


Figure D1: The material properties of AA6061 at 530°C at several strain rates.

The accuracy of the simulations was ensured by performing several checks. A mesh refinement study ensured sufficient mesh density for accurate prediction of both the extrusion ram force and the transverse weld geometry. The ram force and new billet area predictions were within  $\pm 10\%$  of the experimentally

measured forces and new billet areas (determined by sectioning and etching the profiles). Figure D2 shows a comparison between the simulated and measured weld geometry on the major and minor axes.

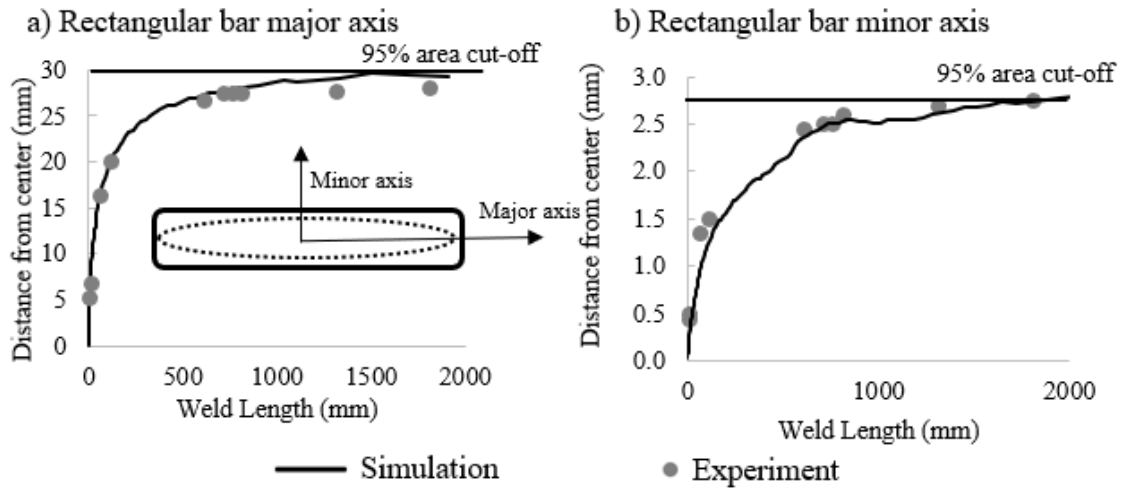


Figure D2: The modeled and experimental transverse weld curves on the rectangular billet major and minor axes.

## D.2 The Billet Assembly

The trial was run using profiled billets as a proxy for a modified dummy block, to decrease the risk of damaging the extrusion press. The profiled billets were designed as a two-piece assembly, with the front billet having a convex profile machined onto a cap, and the back billet having the identical, but convex, profile machined out to allow the two parts to mate together (Figure D3).



Figure D3: The profiled-billet pairs extruded during the 2021 rectangular bar study.

The LIFT press is side-loading, the billets are hoisted by an automated billet loader which holds the billet in-line with the container until the ram is brought forward to hold it against the back face of the die. The billet loader is then retracted, and the container is brought forward around the billet. The billet loader has a length of 13", and some overhang is required to allow the billet to contact and be held against the die-face. Therefore, a minimum billet length of 18" must be used. Additionally, a maximum billet length of 31" prevents the billet from contacting the container during loading. The billet pair must be positioned relative to the billet holder to allow for the billets to balance on the holder during loading. The billet holder can be moved +/- 2" relative to the lengthwise center of the billet (i.e. if a billet length of 18" is input, the billet holder can be centered at 7-11" from the back die face). The two-piece billet assembly was therefore created at the minimum (18") length to minimize the length of the front cap.

A center of gravity equation was performed on the created profile to understand the minimum length of the front billet cap which would allow the billet assembly to balance. This process output a minimum length of 140 mm or about 5.5". The front billet cap therefore had a 5.5" outer length, with the convex profile beginning at that length. The back billet had an outer length of 12.5", with the concave profile being machine out of the front face. The billets were machined by Casemer Machining and then delivered to LIFT. Due to the asymmetry of the rectangular bar profile, it was critical that the profiled billet interface was aligned correctly to the die. At LIFT the billets were scored on the back face to mark the vertical plane. This way the billets could be rotated on the billet loader without having to manually open the billet pair once at extrusion temperatures.

A flat-billet pair was extruded with lengths equal to the lengths of the profiled billet pair in order to create a baseline weld with the same starting billet-billet interface. The extruded profiles were cut cross-sectionally and etched to reveal the weld lines.

### **D.3 Point Tracking and Billet Design**

To start the point tracking process, the initial billet-billet interface is input on both the major and minor axes at the height of the desired interface ( $Z = 140$  mm in this design), and at the first step of the extrusion (full billet unextruded). A spacing of 0.25 mm is used for a high degree of resolution. Tracking the entire billet-billet interface plane is possible, however, the conversion process of the output points to a 3D shape in a modeling software is currently unknown.

The output from the point tracking process at the final step of the simulation is the conventional transverse weld geometry. To determine the profiled dummy block geometry a plane of points is input the desired distance back from the weld nose, identically to the velocity field methodology. This plane of points should span from the radial center of the extrudate to the radius of the conventional weld at the desired weld length. The plane is then input to the point tracking plug-in at the final step of the simulation and tracked

back through the simulation. The output at the first step of the simulation is the profiled dummy block geometry that will result in the desired weld shape. Two billet designs were produced for this initial trial. The first design (Figure D3, left) was for a 100% weld length reduction of the conventional weld. In this way, it was designed for a billet-billet interface at the die face, however was extruded from the back-set location. The second design (Figure D3, right) was created for a 66% reduction in the weld length of the back-set weld with billet-billet interface starting at 140 mm. The results in Section D.4 will focus on only the second design, as the first design was only created and extruded to show that the original billet-billet interface profile could be produced.

#### D.4 LIFT Trial 1 Results

The geometry of the baseline and profiled billet welds are shown in Figure D4. It can be seen that the length of the baseline weld is approximately 5250 mm, and the new, profiled weld was produced to a length of 3500 mm. Hand-drawn Figure D5 shows a more detailed depiction of the weld geometry, with the start, radial nose and cut-off points all marked with both their distance from the nose and distance from the stop mark.

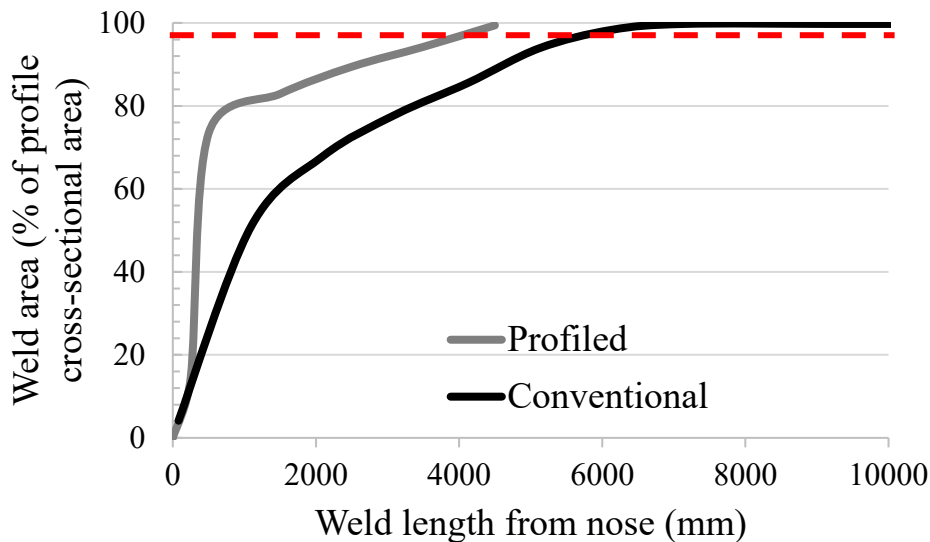


Figure D4: Conventional and profiled weld geometry from the billet-billet interface starting plane of  $Z = 140$  mm.

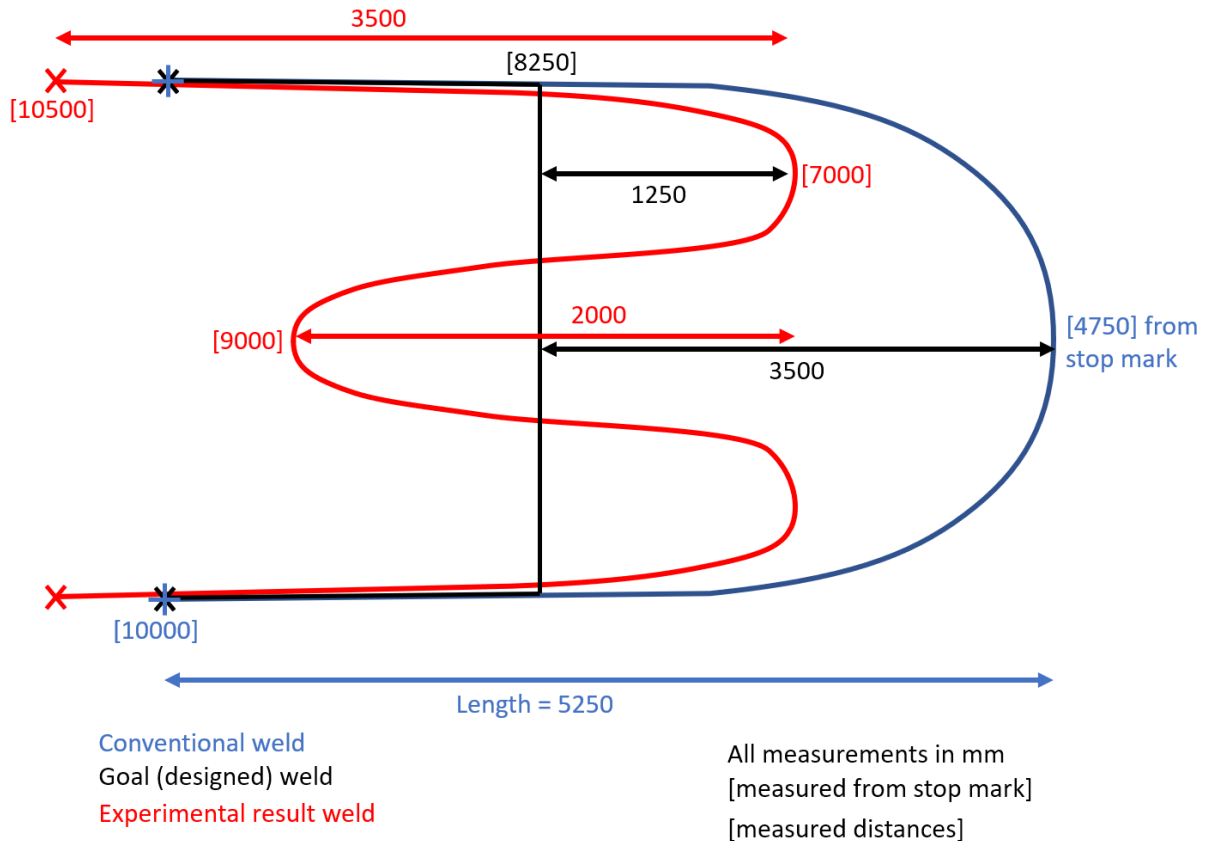


Figure D5: Detailed comparison of weld geometry from conventional (blue), profiled (red) and ideal (black) weld geometry. Locations from stop mark are denoted in brackets [], and the distances between key locations are marked with double sided arrows.

In this figure it can be seen that the nose of the profiled-billet weld (red) lies 1250 mm in front of the goal weld line (black). Additionally, the radial center of the profiled-billet weld is inverted, lying 750 mm back from the goal line, and 2000 mm back from the forward most point of the weld. The radial cut-off point at the back of the weld also was found to be further back than intended, creating an additional 500 mm elongation.

These observations show that the dummy block / billet profile that was created for this trial is not consistent with a single contour line on the weld reduction map (see Section 4.2). Figure D6 below shows the trends of inaccuracy at 4 critical points on the dummy block profile, in comparison to the ideal design. At point 1, the radial center, the inversion would be a result of a profile that is too concave. This would cause the point on the dummy block to not enter the die in alignment with the rest of the weld profile. Next, points 2 and 3 represent the crossovers of the tested- and ideal-designs. The weld created had a nose that moved significantly in front of the ideal weld shape. This protrusion of weld material would be the result of a profile shape that is too shallow, causing the material to travel through the die significantly forward of

the rest of the billet-billet interface. The final point, 4, represents the radial cut-off point of the weld geometry (the point on the weld that reaches 95% cross-sectional area). This point is intended to fall on the intersection of the dummy block profile and the original billet-billet interface. On this comparison image it is shown to fall to the right of that intersection, which caused an elongated cut-off point.

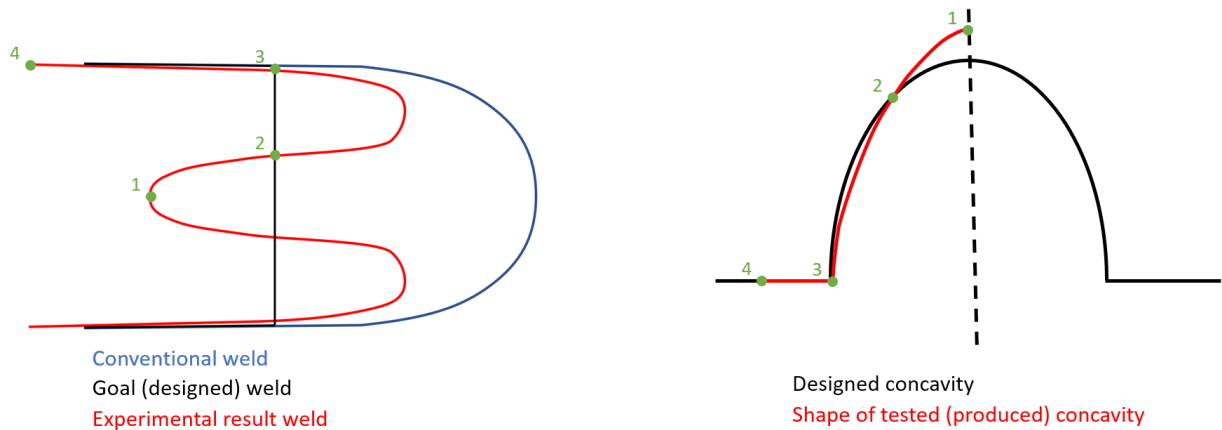


Figure D6: The comparison between profiled design 2, and the ideal dummy block interface geometry based on observations in experimental results.

### D.5 Learnings and the Design of the Second Trial

The analysis performed on the weld created in this preliminary trial was able to be applied to the contour maps produced from the velocity field method in Section 4.2 to get an initial estimate of their accuracy. Figure D7 below shows the comparison of the dummy block profiles created in DEFORM and the velocity field method for an equal weld length reduction. In this comparison we can see that the velocity field profile is shallower at the radial center, crosses over the DEFORM design and then hits the billet-billet interface at a wider location. These are all changes that we would expect given the analysis around Figure D6. It is this comparison that gave confidence to the velocity field method and pushed the second trial forward.



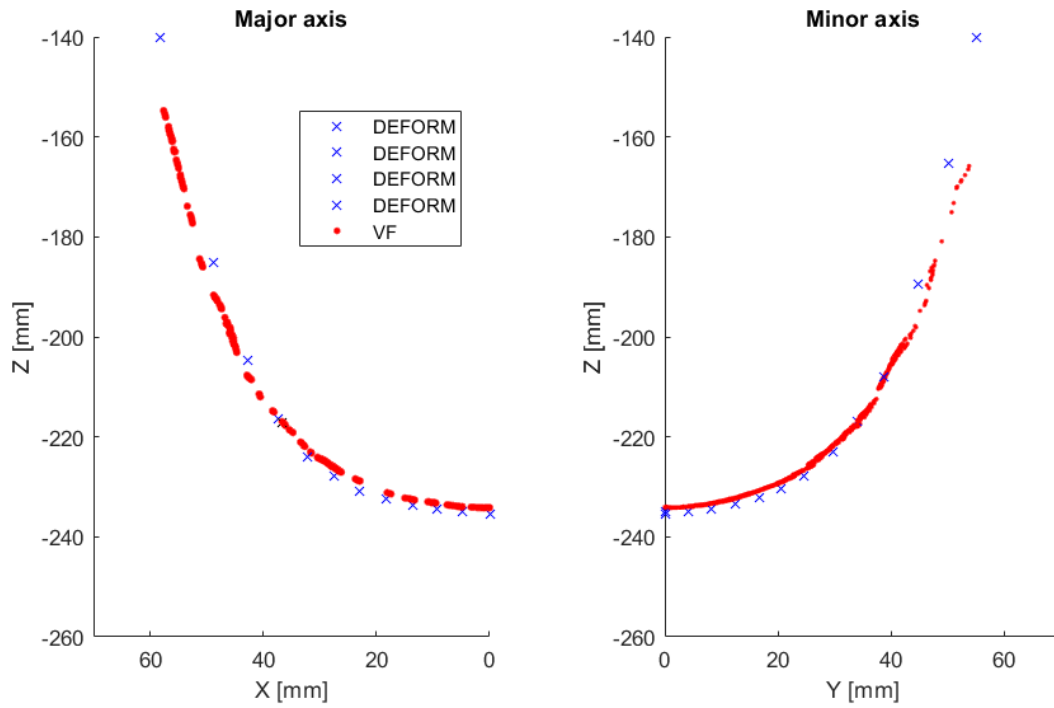


Figure D7: New, velocity field design plotted against DEFORM-based design tested in this section.

## Bibliography

- Afseth, A. (2021). *Aluminum Battery Enclosure Design*.
- Agrawal, D. C., & Raj, R. (1989). Measurement of the ultimate shear strength of a metal-ceramic interface. *Acta Metallurgica*, 37(4), 1265–1270. [https://doi.org/10.1016/0001-6160\(89\)90120-X](https://doi.org/10.1016/0001-6160(89)90120-X)
- Akeret, R. (1972). Properties of pressure welds in extruded aluminum alloy sections. *Journal of the Institute of Metals*, 100, 202–207.
- Allwood, J. M., Cullen, J. M., Carruth, M. A., Cooper, D. R., McBrien, M., Milford, R. L., Moynihan, M. C., & Patel, A. CH. (2012). *Sustainable Materials - with Both Eyes Open: Future Buildings, Vehicles, Products and Equipment* (1st ed.). UIT Cambridge Ltd.
- Allwood, J. M., Cullen, J. M., & Milford, R. L. (2010). Options for achieving a 50% cut in industrial carbon emissions by 2050. *Environmental Science and Technology*, 44(6), 1888–1894. <https://doi.org/10.1021/es902909k>
- Altair Engineering, Inc. (2023). *Altair Inspire Extrude, Simulation software for extrusion process*. <https://www.altair.com/inspire-extrude-metal>
- Aluminum Extruders Council. (2015). *Cadillac Ups Its Game Using Aluminum Extrusions in the CT6*. <https://www.aec.org/page/aluminum-extrusions-cadillac-ct6#>
- Aluminum Extruders Council. (2018). *Aluminum Extrusion Manual* (4.2). <https://www.aec.org/page/aluminum-extrusion-manual>
- Aluminum Extruders Council. (2021). *Aluminum Extrusion Backgrounder*. <https://cdn.ymaws.com/www.aec.org/resource/resmgr/PDFs/BackgrounderAlExt.pdf>
- Aluminum Extruders Council. (2022). *Body & Chassis Structures - Rockers*. <https://www.aec.org/page/automotive-rockers>
- Anacker, S. (2020). *Higher productivity and energy efficiency with hybrid drive concept for aluminum extrusion presses*. Steel Grips. <https://www.steel-grips.com/10-news/336-higher-productivity-and-energy-efficiency-with-hybrid-drive-concept-for-aluminum-extrusion-presses>
- Argonne National Laboratory. (2020). *GREET Model*. <http://greet.es.anl.gov>
- Ashby, M. F. (2020). *Materials and the Environment* (S. Merken, Ed.; 3rd ed.). Elsevier. <https://doi.org/10.1016/B978-0-12-821521-0.15001-7>
- Assaad, A. (2016). *Quench Sensitivity of 6xxx Aluminum Alloys*.

- ASTM. (2010). *ASTM B831-05 Standard Test Method for Shear Testing of Thin Aluminum Alloy Products*.
- Avitzur, B. (1963). Analysis of Wire Drawing and Extrusion Through Conical Dies of Small Cone Angle. *Journal of Engineering for Industry*.
- Bakker, A. J. Den. (2016). *Weld Seams in Aluminium Extrusions: Microstructure and Properties*.
- Bai, S.W., Fang, G., & Zhou, J. (2017). *Analysis of the bonding strength and microstructure of AA6082 extrusion weld seams formed during physical simulation*. *Journal of Materials Processing Technology*, 250, 109–120. <https://doi.org/10.1016/j.jmatprotec.2017.07.012>
- Bai, S. wen, Fang, G., & Zhou, J. (2019). *Integrated physical and numerical simulations of weld seam formation during extrusion of magnesium alloy*. *Journal of Materials Processing Technology*, 266(August 2018), 82–95. <https://doi.org/10.1016/j.jmatprotec.2018.10.025>
- Barlow, C. Y., Nielsen, P., & Hansen, N. (2004). Multilayer roll bonded aluminium foil: Processing, microstructure and flow stress. *Acta Materialia*, 52(13), 3967–3972. <https://doi.org/10.1016/j.actamat.2004.05.012>
- Bauser, M., Sauer, G., & Siegert, K. (2006). The Production of Extruded Semifinished Products from Metallic Materials. In *Extrusion* (pp. 195–321). ASM International. <https://doi.org/10.31399/asm.tb.ex2.t69980195>
- Bay, N. (1983). Mechanisms Producing Metallic Bonds in Cold Welding. *Welding Journal*, 137s–142s. <https://doi.org/10.1093/jpids/pix105/4823046>
- BBC. (2010). *Villagers despair in Hungary's red wasteland*. BBC News. <https://www.bbc.com/news/world-europe-11523573>
- Bertram, M., Ramkumar, S., Rechberger, H., Rombach, G., Bayliss, C., Martchek, K. J., Müller, D. B., & Liu, G. (2017). A regionally-linked, dynamic material flow modelling tool for rolled, extruded and cast aluminium products. *Resources, Conservation and Recycling*, 125(May), 48–69. <https://doi.org/10.1016/j.resconrec.2017.05.014>
- Billy, R. (2012). *Material Flow Analysis of Extruded Aluminium in French Buildings* [Norwegian University of Science and Technology]. <http://www.diva-portal.org/smash/get/diva2:566400/FULLTEXT01.pdf>
- Blomberg, J., & Söderholm, P. (2009). The economics of secondary aluminium supply: An econometric analysis based on European data. *Resources, Conservation and Recycling*, 53(8), 455–463. <https://doi.org/10.1016/j.resconrec.2009.03.001>
- Boeing. (2020). *Boeing roundtable discussion*.
- Boin, U. M. J., & Bertram, M. (2005). Melting standardized aluminum scrap: A mass balance model for Europe. *Jom*, 57(8), 26–33. <https://doi.org/10.1007/s11837-005-0164-4>

- Cai, C., Liang, X., An, Q., Tao, Z., Ming, W., & Chen, M. (2021). Cooling/Lubrication Performance of Dry and Supercritical CO<sub>2</sub>-Based Minimum Quantity Lubrication in Peripheral Milling Ti-6Al-4V. *International Journal of Precision Engineering and Manufacturing - Green Technology*, 8(2), 405–421. <https://doi.org/10.1007/s40684-020-00194-7>
- Cai, W., Daehn, G., Li, J., Mishra, R., Vivek, A., Khan, H., & Komarasamy, M. (2018). a State-of-the-Art Review on Solid-State Metal Joining. *Journal of Manufacturing Science and Engineering*, c. <https://doi.org/10.1115/1.4041182>
- Can Art. (2021). *Can Art Roundtable Discussions*.
- Cann, J. L., De Luca, A., Dunand, D. C., Dye, D., Miracle, D. B., Oh, H. S., Olivetti, E. A., Pollock, T. M., Poole, W. J., Yang, R., & Tasan, C. C. (2020). Sustainability through alloy design: Challenges and opportunities. *Progress in Materials Science*, 117(August 2020). <https://doi.org/10.1016/j.pmatsci.2020.100722>
- Chen, F. L., He, X., Prieto-Muñoz, P. A., & Yin, H. M. (2015). Opening-mode fractures of a brittle coating bonded to an elasto-plastic substrate. *International Journal of Plasticity*, 67, 171–191. <https://doi.org/10.1016/j.ijplas.2014.10.007>
- Chen, L., Zhao, G., Yu, J., & Zhang, W. (2015). Evaluation of a pyramid die extrusion for a hollow aluminum profile using FE simulation. *Journal of Mechanical Science and Technology*, 29(5), 2195–2203. <https://doi.org/10.1007/s12206-015-0440-3>
- Chen, X., & Önal, H. (2016). Renewable energy policies and competition for biomass: Implications for land use, food prices, and processing industry. *Energy Policy*, 92(2016), 270–278. <https://doi.org/10.1016/j.enpol.2016.02.022>
- Chien, K., Robbins, P., Jowett, C., & Wang, Y. (2018, May). Extrusion Productivity, Part I – Billet Geometry. *Light Metal Age*. <https://www.lightmetalage.com/news/industry-news/extrusion/article-extrusion-productivity-part-billet-geometry/>
- Christiansen, P., Nielsen, C. V., Bay, N., & Martins, P. A. F. (2019). Internal shear cracking in bulk metal forming. *Proceedings of the Institution of Mechanical Engineers, Part L: Journal of Materials: Design and Applications*, 233(4), 603–614. <https://doi.org/10.1177/1464420716681592>
- Christiansen, P., Nielsen, C. V., Martins, P. A. F., & Bay, N. (2017). Predicting the onset of cracks in bulk metal forming by ductile damage criteria. *Procedia Engineering*, 207, 2048–2053. <https://doi.org/10.1016/j.proeng.2017.10.1106>
- Coker, E. N. (2013). *The oxidation of aluminum at high temperature studied by Thermogravimetric Analysis and Differential Scanning Calorimetry*. <http://www.ntis.gov/help/ordermethods.asp?loc=7-4-0#online>

- Consulting Collaborative. (2017). *An Overview of the N.A. Aluminum Extrusion Market 2016*. Consulting Collaborative.  
[https://cdn.ymaws.com/www.aec.org/resource/resmgr/2017\\_SMW/1\\_Extrusion\\_Overview\\_-\\_Brown.pdf](https://cdn.ymaws.com/www.aec.org/resource/resmgr/2017_SMW/1_Extrusion_Overview_-_Brown.pdf)
- Cooper, D. R. (2013). *Reuse of steel and aluminium without melting* [PhD]. University of Cambridge.
- Cooper, D. R., & Allwood, J. M. (2014a). Influence of diffusion mechanisms in aluminium solid-state welding processes. *Procedia Engineering*, 81(October), 2147–2152.  
<https://doi.org/10.1016/j.proeng.2014.10.300>
- Cooper, D. R., & Allwood, J. M. (2014b). The influence of deformation conditions in solid-state aluminium welding processes on the resulting weld strength. *Journal of Materials Processing Technology*, 214(11), 2576–2592. <https://doi.org/10.1016/j.jmatprotec.2014.04.018>
- Cooper, D. R., & Gutowski, T. G. (2017). The Environmental Impacts of Reuse: A Review. *Journal of Industrial Ecology*, 21(1), 38–56. <https://doi.org/10.1111/jiec.12388>
- Cooper, D. R., Rossie, K. E., & Gutowski, T. G. (2017). The energy requirements and environmental impacts of sheet metal forming : An analysis of five forming processes. *Journal of Materials Processing Tech.*, 244, 116–135. <https://doi.org/10.1016/j.jmatprotec.2017.01.010>
- Crosio, M., Hora, D., Becker, C., & Hora, P. (2018). Realistic representation and investigation of charge weld evolution during direct porthole die extrusion processes through FE-analysis. *Procedia Manufacturing*, 15, 232–239. <https://doi.org/10.1016/j.promfg.2018.07.214>
- Cullen, J. M., & Allwood, J. M. (2013). Mapping the global flow of aluminum: From liquid aluminum to end-use goods. *Environmental Science and Technology*, 47(7), 3057–3064.  
<https://doi.org/10.1021/es304256s>
- Cullen, J. M., & Cooper, D. R. (2022). *Annual Review of Materials Research Material Flows and Efficiency*. <https://doi.org/10.1146/annurev-matsci-070218>
- da Silva, T. (2016). The Extrusion of Two-Piece Billets. *International Aluminum Extrusion Technology Seminar*, 239–254.
- Dassault Systemes. (2023). *SolidWorks*.
- DEFORM. (2021). *Discussion with DEFORM®* .
- den Bakker, A. J., Katgerman, L., & van der Zwaag, S. (2016). Analysis of the structure and resulting mechanical properties of aluminium extrusions containing a charge weld interface. *Journal of Materials Processing Technology*, 229, 9–21. <https://doi.org/10.1016/j.jmatprotec.2015.09.013>
- Design News Staff. (2014). *From the Ford GT to the F-150: Aluminum Extrusion Aids Auto Lightweighting*. Design News. <https://www.designnews.com/materials-assembly/ford-gt-f-150-aluminum-extrusion-aids-auto-lightweighting>

- Ding, S., Shi, Q., & Chen, G. (2021). Flow stress of 6061 aluminum alloy at typical temperatures during friction stir welding based on hot compression tests. *Metals*, 11(5). <https://doi.org/10.3390/met11050804>
- Dinsmore, E. (2018). *Electric vehicles to transform aluminium demand*. CRU Group. <https://www.crugroup.com/knowledge-and-insights/insights/2018/electric-vehicles-to-transform-aluminium-demand/>
- Donati, L., & Tomesani, L. (2004). Evaluation Of A New FEM Criterion For Seam Welds Quality Prediction In Aluminum Extruded Profiles. *Proceedings of Eighth International Aluminum Extrusion Technology Seminar*, 221–235.
- Donati, L., & Tomesani, L. (2008). Seam welds modeling and mechanical properties prediction in the extrusion of AA6082 alloy. *Key Engineering Materials*, 367, 125–136. <https://doi.org/10.4028/0-87849-467-7.125>
- Ducker Worldwide. (2017). *ALUMINUM CONTENT IN NORTH AMERICAN LIGHT VEHICLES*.
- Dyla, J. (2013). *Lubrication of Extrusion Press Tooling*. <https://www.yumpu.com/en/document/read/11672160/lubrication-of-extrusion-press-tooling>
- Dyla, J. E. (2019). *Aluminum Extrusion Tooling. II*(1988), 134–138.
- Edwards, S. P., den Bakker, A. J., Neijenhuis, J. L., Kool, W. H., & Katgerman, L. (2006). The influence of the solid-state bonding process on the mechanical integrity of longitudinal weld seams. *JSME International Journal, Series A: Solid Mechanics and Material Engineering*, 49(1), 63–68. <https://doi.org/10.1299/jsmea.49.63>
- Edwards, S. P., den Bakker, A. J., Zhou, J., & Katgerman, L. (2009). Physical simulation of longitudinal weld seam formation during extrusion to produce hollow aluminum profiles. *Materials and Manufacturing Processes*, 24(4), 409–421. <https://doi.org/10.1080/10426910802714290>
- Enkvist, P.-A., & Klevnäs, P. (2018). The Circular Economy - A powerful force for climate mitigation - Full Report. *Material Economics*, 176. <https://materialeconomics.com/publications/the-circular-economy-a-powerful-force-for-climate-mitigation-1>
- European Aluminum Association. (2018). *ENVIRONMENTAL PROFILE REPORT Life-Cycle inventory data for aluminium production and transformation processes in Europe. March*.
- Evertsson, J., Bertram, F., Zhang, F., Rullik, L., Merte, L. R., Shipilin, M., Soldemo, M., Ahmadi, S., Vinogradov, N., Carlà, F., Weissenrieder, J., Göthelid, M., Pan, J., Mikkelsen, A., Nilsson, J. O., & Lundgren, E. (2015). The thickness of native oxides on aluminum alloys and single crystals. *Applied Surface Science*, 349, 826–832. <https://doi.org/10.1016/j.apsusc.2015.05.043>
- Ford Motor Company. (2013). *Mechanical Properties Measurements after Thermal Processing of Aluminum Alloy*.

- Frischknecht, R. (2010). LCI modelling approaches applied on recycling of materials in view of environmental sustainability, risk perception and eco-efficiency. *International Journal of Life Cycle Assessment*, 15(7), 666–671. <https://doi.org/10.1007/s11367-010-0201-6>
- Furu, T., Østhus, R., Søreide, J., & Myhr, O. R. (2017). A novel methodology for optimization of properties, costs and sustainability of aluminium extrusions. *Materials Science Forum*, 877, 625–632. <https://doi.org/10.4028/www.scientific.net/MSF.877.625>
- Ghalehbandi, S. M., & Malaki, M. (2019). *applied sciences Accumulative Roll Bonding — A Review*.
- GRANCO CLARK. (2022). *FusionBond®*. [https://www.granoclarck.com/media/uploads/pdf/granco\\_clark\\_fusionbond.pdf](https://www.granoclarck.com/media/uploads/pdf/granco_clark_fusionbond.pdf)
- Grand View Research. (2020). *Aluminum Extrusion Market Size, Share & Trends Analysis Report By Product (Shapes, Rods & Bars, Pipes & Tubes), By Application (Building & Construction, Consumer Goods), By Region, And Segment Forecasts, 2019 - 2025*. <https://www.grandviewresearch.com/industry-analysis/aluminum-extrusion-market>
- Granta Design Limited. (2020). *CES EduPack software*.
- Grigoriev, A. Y. (2015). Slope angles of rough surface asperities after machining. *Journal of Friction and Wear*, 36(3), 197–199. <https://doi.org/10.3103/S106836661503006X>
- Gutowski, T. G., Sahni, S., Allwood, J. M., Ashby, M. F., Timothy, G. M., Ashby, F., & Worrell, E. (2013). The energy required to produce materials: constraints on energy-intensity improvements, parameters of demand. *Philosophical Transactions: Mathematical, Physical and Engineering Sciences*, 371(1986), 1–14.
- Haraldsson, J., & Johansson, M. T. (2018). Review of measures for improved energy efficiency in production-related processes in the aluminium industry – From electrolysis to recycling. *Renewable and Sustainable Energy Reviews*, 93(June), 525–548. <https://doi.org/10.1016/j.rser.2018.05.043>
- Hatzenbichler, T., & Buchmayr, B. (2010). Finite element method simulation of internal defects in billet-to-billet extrusion. *Proceedings of the Institution of Mechanical Engineers, Part B: Journal of Engineering Manufacture*, 224(7), 1029–1042. <https://doi.org/10.1243/09544054JEM1830>
- Hauser, D., Kammer, P. A., & Martin, D. C. (1965). *Fundamentals of Solid State Welding and their Application to Beryllium, Aluminum, and Stainless Steel*. June. <https://doi.org/10.1021/jz3014425>
- Heinemann, H. H. (1961). *Flow Stress of Different Aluminum and Copper Alloys for High Strain Rates and Temperature*. RWTH Aachen University.
- Hosford, W. F., & Caddell, R. M. (2007). *Metal Forming: Mechanics and Metallurgy*. Cambridge University Press.
- ifu hamburg. (2020). *Umberto LCA+*. <https://www.ifu.com/umberto>

- Ingarao, G., Priarone, P. C., Gagliardi, F., Di Lorenzo, R., & Settineri, L. (2014). Environmental comparison between a hot extrusion process and conventional machining processes through a Life Cycle Assessment approach. *Key Engineering Materials*, 622–623, 103–110. <https://doi.org/10.4028/www.scientific.net/KEM.622-623.103>
- International Aluminum Institute. (2021). *IAI current statistics*. <https://www.world-aluminium.org/statistics/>
- International Energy Agency. (2017). *Energy Technology Perspectives 2017 - Executive Summary*. [https://doi.org/10.1787/energy\\_tech-2014-en](https://doi.org/10.1787/energy_tech-2014-en)
- IEA. (2019). Material efficiency in clean energy transitions. Report: *International Energy Agency*, Paris. <https://www.iea.org/reports/material-efficiency-in-clean-energy-transitions>
- ISO. (2016a). *ISO Standard 14040 — Environmental management — Life cycle assessment — Principles and framework*. <https://www.iso.org/standard/37456.html>
- ISO. (2016b). *ISO Standard 14044 — Life cycle assessment — Requirements and guidelines*. <https://www.iso.org/standard/38498.html>
- Johannes, V. I., Jowett, C. W., & Dickson, R. F. (1996). Transverse Weld Defects. *Rubber Chemistry and Technology*, 67(3), 481–503. <https://doi.org/10.1093/jpids/pix105/4823046>
- Jowett, C., Adams, J., Daughetee, C., Lea, G., Huff, O. A., & Fossil, N. (2008). Scrap Allocation. *International Aluminum Extrusion Technology Seminar*, 223–244.
- Kniazkin, I., & Vlasov, A. (2020). Quality prediction of longitudinal seam welds in aluminium profile extrusion based on simulation. *Procedia Manufacturing*, 50(2019), 433–438. <https://doi.org/10.1016/j.promfg.2020.08.079>
- Kolpak, F., Schulze, A., Dahnke, C., & Tekkaya, A. E. (2019). Predicting weld-quality in direct hot extrusion of aluminium chips. *Journal of Materials Processing Tech.*, 274(April), 116294. <https://doi.org/10.1016/j.jmatprotec.2019.116294>
- Kopec, G. M., Allwood, J. M., Cullen, J. M., & Ralph, D. (2016). A General Nonlinear Least Squares Data Reconciliation and Estimation Method for Material Flow Analysis. *Journal of Industrial Ecology*, 20(5), 1038–1049. <https://doi.org/10.1111/jiec.12344>
- Lennon, A., Lunardi, M., Hallam, B., & Dias, P. R. (2022). The aluminium demand risk of terawatt photovoltaics for net zero emissions by 2050. *Nature Sustainability*, 5(4), 357–363. <https://doi.org/10.1038/s41893-021-00838-9>
- Liu, Z., Li, L., Yi, J., Li, S., & Wang, G. (2017). Influence of extrusion speed on the seam weld quality in the porthole die extrusion of AZ31 magnesium alloy tube. *International Journal of Advanced Manufacturing Technology*, 92(1–4), 1039–1052. <https://doi.org/10.1007/s00170-017-0200-x>



- Lou, S., Wang, A., Lu, S., Guo, G., Qu, C., & Su, C. (2019). Tensile property and micro-texture evolution of the charge weld in a billet-to-billet extrusion of AA6061 aluminum profile. *International Journal of Advanced Manufacturing Technology*, 103(1–4), 1309–1323. <https://doi.org/10.1007/s00170-019-03573-w>
- Lou, S., Wang, Y., Liu, C., Lu, S., Liu, S., & Su, C. (2017). Analysis and Prediction of the Billet Butt and Transverse Weld in the Continuous Extrusion Process of a Hollow Aluminum Profile. *Journal of Materials Engineering and Performance*, 26(8), 4121–4130. <https://doi.org/10.1007/s11665-017-2771-y>
- Low, J. S. C. (2009). Cost modelling of the aluminum extrusion process. *SIMtech Technical Reports*, 10(1), 60–63. <https://www.yumpu.com/en/document/read/11672095/cost-modelling-of-the-aluminium-extrusion-process>
- Lv, J., Yu, J., Shi, Z., Li, W., & Lin, J. (2023). Feasibility study of a novel multi-container extrusion method for manufacturing wide aluminium profiles with low force. *Journal of Manufacturing Processes*. vol. 85, p. 584-593
- Macedonio, G. (2021). *NEW, DANIELI 40-MN FRONT-LOADING EXTRUSION PRESS FOR PMS ALUMINIUM*. Danieli. [https://www.danieli.com/en/news-media/news/new-danieli-40-mn-front-loading-extrusion-press-pms-aluminium\\_37\\_604.htm](https://www.danieli.com/en/news-media/news/new-danieli-40-mn-front-loading-extrusion-press-pms-aluminium_37_604.htm)
- Mag Specialties. (2019). *Mag Specialties roundtable discussion*.
- Magnode Aluminum. (2019). *Magnode Aluminum roundtable discussion*.
- Mahmoodkhani, Y., Wells, M. A., Parson, N., & Poole, W. J. (2014). Numerical modelling of the material flow during extrusion of aluminium alloys and transverse weld formation. *Journal of Materials Processing Technology*, 214(3), 688–700. <https://doi.org/10.1016/j.jmatprotec.2013.09.028>
- Mahmoodkhani, Y., Wells, M., Parson, N., Jowett, C., & Poole, W. (2014). *Modeling the Formation of Transverse Weld during Billet-on-Billet Extrusion*. 3470–3480. <https://doi.org/10.3390/ma7053470>
- Masri, K., & Warburton, A. (1998). Using optimization to improve the yield of an aluminium extrusion plant. *Journal of the Operational Research Society*, 49(11), 1111–1116. <https://doi.org/10.1057/palgrave.jors.2600616>
- Merklein, M., & Biasutti, M. (2011). Forward and reverse simple shear test experiments for material modeling in forming simulations. In G. Hirt & A. E. Tekkaya (Eds.), *International Conference on Technology of Plasticity* (pp. 702–707).
- Metson, J. (2011). Production of alumina. In R. Lumley (Ed.), *Fundamentals of aluminium metallurgy: Production, processing and applications*. Woodhead Publishing Limited. <https://doi.org/10.1016/B978-1-84569-654-2.50002-X>
- MI Metals. (2019). *MI Metals roundtable discussion*.

- Milford, R. L., Allwood, J. M., & Cullen, J. M. (2011). Assessing the potential of yield improvements, through process scrap reduction, for energy and CO<sub>2</sub> abatement in the steel and aluminium sectors. *Resources, Conservation and Recycling*, 55(12), 1185–1195. <https://doi.org/10.1016/j.resconrec.2011.05.021>
- Misiolek, W. Z., & Kelly, R. M. (2005). Extrusion of Aluminum Alloys. In S. L. Semiatin (Ed.), *ASM Handbook Metalworking: Bulk Forming* (Vol. 14A, pp. 522–527). ASM International. <https://doi.org/10.1361/asmhba0004015>
- Mulholland, E. (2016). *Aluminum Extrusion EPD Background Report*. <https://www.alumicor.com/wp-content/uploads/Industry-Aluminum-Background-EPD-LCA-LEED-V4-2.pdf>
- Nadel, S., Shepard, M., Greenberg, S., Katz, G., & Almeida, A. T. De. (2002). *Energy-Efficient Motor Systems: A Handbook on Technology, Program, and Policy Opportunities* (2nd ed.). American Council for an Energy-Efficient Economy.
- Nanninga, N., White, C., & Dickson, R. (2011). Charge weld effects on high cycle fatigue behavior of a hollow extruded AA6082 profile. *Journal of Materials Engineering and Performance*, 20(7), 1235–1241. <https://doi.org/10.1007/s11665-010-9755-5>
- Nieto, J. T. (2010). *Feature based costing of extruded parts*. University of Illinois at Urbana-Champaign.
- Norsk Hydro. (2020). *Norsk Hydro roundtable discussion*.
- Oberhausen, G., & Cooper, D. R. (2023). The Formation and Strength of Aluminum Extrusion Transverse Welds. *SSRN Electronic Journal*. <https://doi.org/10.2139/ssrn.4369479>
- Oberhausen, G. J., Christopher, A. A. A., & Cooper, D. R. (2021). Reducing aluminum extrusion transverse weld process scrap. *International Conference on the Technologies of Plasticity*.
- Oberhausen, G. J., & Cooper, D. R. (2022). *Semi-structured interviews with North American Extrusion Industry Experts*.
- Oberhausen, G., Zhu, Y., & Cooper, D. R. (2022). Reducing the environmental impacts of aluminum extrusion. *Resources, Conservation and Recycling*, 179, 106120. <https://doi.org/10.1016/j.resconrec.2021.106120>
- Oberhausen, G.J., & Cooper, D.R. (2023). Exploring a novel process for reducing aluminum extrusion process scrap. Proceedings of the *International Conference on the Technologies of Plasticity*.
- Page, I. (2020). *Nemak Supplies New Battery Housings for the Mustang Mach-E*. Spotlight Metal. <https://www.spotlightmetal.com/nemak-supplies-new-battery-housings-for-the-mustang-mach-e-a-898095/>
- Pedneault, J., Majeau-Bettez, G., Krey, V., & Margni, M. (2021). What future for primary aluminium production in a decarbonizing economy? *Global Environmental Change*, 69(March), 102316. <https://doi.org/10.1016/j.gloenvcha.2021.102316>

- Plata, M., & Piwnik, J. (2000). Theoretical and experimental analysis of seam weld formation in hot extrusion of aluminium alloys. *7th International Conference on Aluminum Extrusion Technology*. Precedence Research. (2022). *Aluminum Market*. <https://www.precedenceresearch.com/aluminum-market>
- Reggiani, B., & Donati, L. (2018). Experimental, numerical, and analytical investigations on the charge weld evolution in extruded profiles. *International Journal of Advanced Manufacturing Technology*, *99*(5–8), 1379–1387. <https://doi.org/10.1007/s00170-018-2595-4>
- Reggiani, B., Pinter, T., & Donati, L. (2020). Scrap assessment in direct extrusion. *International Journal of Advanced Manufacturing Technology*, *107*(5–6), 2635–2647. <https://doi.org/10.1007/s00170-020-05127-x>
- Reggiani, B., Segatori, A., Donati, L., & Tomesani, L. (2013). Prediction of charge welds in hollow profiles extrusion by FEM simulations and experimental validation. 1855–1872. <https://doi.org/10.1007/s00170-013-5143-2>
- Ritchie, H., Roser, M., & Rosado, P. (2020). *CO<sub>2</sub> and Greenhouse Gas Emissions*. Our World in Data. <https://ourworldindata.org/co2-and-other-greenhouse-gas-emissions>
- Robbins, P., Dixon, B., Chien, K., & Jowett, C. (2016). *Today ' s Understanding of the Function and Benefits of Dummy Block Design*. 387–404.
- Rodriguez León, J. M., & Stark, A. (2018). *Current Trends in Aluminum Extrusion*. Spotlight Metal. <https://www.spotlightmetal.com/current-trends-in-aluminum-extrusion-a-753015/>
- Ryberg, D. S., Robinius, M., & Stolten, D. (2018). Evaluating land eligibility constraints of renewable energy sources in Europe. *Energies*, *11*(5), 1–19. <https://doi.org/10.3390/en11051246>
- Saha, P. K. (2000). *Aluminum Extrusion Technology*. ASM International.
- Sano, H., Ishikawa, T., Yukawa, N., Yoshida, Y., & Kaneko, T. (2008). Effect of extrusion mode and die shape on billet skin behavior in aluminum extrusion. *Keikinzoku/Journal of Japan Institute of Light Metals*, *58*(5), 183–188. <https://doi.org/10.2464/jilm.58.183>
- Sano, H., Ishikawa, T., Yukawa, N., Yoshida, Y., Kaneko, T., & Sakamoto, J. (2008). Effect of back end lubricant conditions on billet skin behavior in direct extrusion. *Keikinzoku/Journal of Japan Institute of Light Metals*, *58*(5), 189–193. <https://doi.org/10.2464/jilm.58.189>
- Schlesinger, M. E. (2014). *Aluminum Recycling* (2nd ed.). CRC Press.
- Schoenberger, R. (2016). *Automotive aluminum extrusion market grows*. Today's Motor Vehicles. <https://www.todaymotorvehicles.com/article/automotive-aluminum--extrusion-market-grows/>
- Schreiber, M., Sacristani, G., Gullotta, G., Fraternali, P., Breda, D., & Balasmo-mi, C. (2016). Energy Saving in Extrusion Presses - Latest Developments. *Eleventh International Aluminum Extrusion Technology Seminar & Exposition*, 471–488.
- Scientific Forming Technologies Corporation. (2023). *DEFORM, Simulation software*.

- Seow, Y., Rahimifard, S., & Woolley, E. (2013). Simulation of energy consumption in the manufacture of a product. *International Journal of Computer Integrated Manufacturing*, 26(7), 663–680. <https://doi.org/10.1080/0951192X.2012.749533>
- Sheppard, T. (1999). Extrusion of Aluminium Alloys. In *Extrusion of Aluminium Alloys* (1st ed.). Springer Science + Business Media. <https://doi.org/10.1007/978-1-4757-3001-2>
- Sherman, E. (2009). *New Apple Technology to Produce Seamless Metal iPhone Case*. CBS News. <https://www.cbsnews.com/news/new-apple-technology-to-produce-seamless-metal-iphone-case/>
- Singh, V. P., Patel, S. K., Ranjan, A., & Kuriachen, B. (2020). Recent research progress in solid state friction-stir welding of aluminium–magnesium alloys: A critical review. *Journal of Materials Research and Technology*, 9(3), 6217–6256. <https://doi.org/10.1016/j.jmrt.2020.01.008>
- Sluzalec, A. (1991). Analysis of dead zones in the process of direct extrusion through single-hole flat die. *Communications in Applied Numerical Methods*, 7(4), 281–287. <https://doi.org/10.1002/cnm.1630070405>
- SMS Group. (2020). *ecoDraulic: Energy efficient operation of an extrusion press for aluminum*. <https://www.sms-group.com/sms-group-magazine/overview/ecodraulic-energy-efficient-operation-of-an-extrusion-press-for-aluminum/>
- Sofuoglu, H., & Rasty, J. (1999). On the measurement of friction coefficient utilizing the ring compression test. *Tribology International*, 32(6), 327–335. [https://doi.org/10.1016/S0301-679X\(99\)00055-9](https://doi.org/10.1016/S0301-679X(99)00055-9)
- Sofuoglu, H., & Rasty, J. (2000). Flow behavior of Plasticine used in physical modeling of metal forming processes. *Tribology International*, 33(8), 523–529. [https://doi.org/10.1016/S0301-679X\(00\)00092-X](https://doi.org/10.1016/S0301-679X(00)00092-X)
- S&P Global Platts. (2019). *Platts Aluminum Midwest Premium Explained*. <https://www.spglobal.com/en/perspectives/platts-aluminum-midwest-premium-explained>
- Superior Extrusion Inc. (2022). *Superior Extrusion Inc. roundtable discussion*.
- Sutherland, J., Skerlos, S., Haapala, K., Cooper, D., Zhao, F., & Huang, A. (2020). Industrial sustainability: Reviewing the Past and Envisioning the Future. *Journal of Manufacturing Science and Engineering*, 142(November), 1–33. <https://doi.org/10.1115/1.4047620>
- Tabereaux, A. T., & Peterson, R. D. (2014). Aluminum Production. In *Treatise on Process Metallurgy, Volume 3: Industrial Processes* (Vol. 3, Issue V). Elsevier Ltd. <https://doi.org/10.1016/B978-0-08-096988-6.00023-7>
- Tada, T., Fukuyama, E., & Madariaga, R. (2000). Non-hypersingular boundary integral equations for 3-D non-planar crack dynamics. In *Computational Mechanics* (Vol. 25). Springer-Verlag.
- Tang, J., Chen, L., Li, Z., Zhao, G., Zhang, C., & Zuo, Y. (2022). Evolution mechanisms of charge weld during porthole die extrusion of ZK60 Mg profile. *Journal of Materials Processing Technology*, 300. <https://doi.org/10.1016/j.jmatprotec.2021.117401>

- Tekkaya, A. E., Schikorra, M., Becker, D., Biermann, D., Hammer, N., & Pantke, K. (2009). Hot profile extrusion of AA-6060 aluminum chips. *Journal of Materials Processing Technology*, 209(7), 3343–3350. <https://doi.org/10.1016/j.jmatprotec.2008.07.047>
- The Economist. (2021). Missing ingredients – The bottlenecks which could constrain emission cuts. *The Economist*, 16–18. <https://www.economist.com/briefing/2021/06/12/the-bottlenecks-which-could-constrain-emission-cuts>
- The Imaging Source. (2022). *IC Measure*. <https://www.theimagingsource.com/support/downloads-for-windows/end-user-software/icmeasure/>
- Thouless, M. D., Olsson, E., & Gupta, A. (1992). Cracking of brittle films on elastic substrates. In *Acta metall, mater* (Vol. 40, Issue 6).
- Thumb Tool & Engineering. (2018). *Thumb Tool & Engineering roundtable discussion*.
- Thumb Tool & Engineering. (2021). *Thumb Tool & Engineering Roundtable Discussion*.
- TopSteel. (2023). *TQ1 Steel Mechanical Properties*. <https://www.topsteel.be/en/hot-work-tool-steels/tq1/>
- Tylecote, R. F. (1968). *The Solid Phase Welding of Metals*. Edward Arnold.
- UN. (2018). *UN Comtrade Database 2018*. <https://comtrade.un.org/data/>
- U.S. Bureau of Labor Statistics. (2020a). *51-4021 Extruding and Drawing Machine Setters, Operators, and Tenders, Metal and Plastic*. <https://www.bls.gov/oes/current/oes514021.htm>
- U.S. Bureau of Labor Statistics. (2020b). *EMPLOYER COSTS FOR EMPLOYEE COMPENSATION – DECEMBER 2020*. <https://www.bls.gov/news.release/pdf/ecec.pdf>
- U.S. Bureau of Labor Statistics. (2021a). *Midwest Average Electricity Costs*. [https://data.bls.gov/timeseries/APU020072610?amp%253bdata\\_tool=XGtable&output\\_view=data&include\\_graphs=true](https://data.bls.gov/timeseries/APU020072610?amp%253bdata_tool=XGtable&output_view=data&include_graphs=true)
- U.S. Bureau of Labor Statistics. (2021b). *Utility (piped) gas per therm in Midwest urban, average price, not seasonally adjusted*. [https://data.bls.gov/timeseries/APU020072620?amp%253bdata\\_tool=XGtable&output\\_view=data&include\\_graphs=true](https://data.bls.gov/timeseries/APU020072620?amp%253bdata_tool=XGtable&output_view=data&include_graphs=true)
- U.S. Department of Energy. (2003). *Alcoa : Plant-Wide Energy Assessment Finds Potential Savings at Aluminum Extrusion Facility*. <https://www.nrel.gov/docs/fy03osti/32917.pdf>
- van Rijkom, J., & Bolt, P. H. (2000). A review of new approaches and technologies in extrusion welds related to the background of existing knowledge. *Seventh International Aluminum Extrusion Technology Seminar*, 249–260.
- Wagiman, A., Sukri Mustapa, M., Asmawi, R., Shamsudin, S., Mohd, & Lajis, A., & Mutoh, Y. (2020). A review on direct hot extrusion technique in recycling of aluminium chips. *The International Journal of*

- Advanced Manufacturing Technology*, 106, 641–653. <https://doi.org/10.1007/s00170-019-04629-7>/Published
- Walters, J., Foster, M., & Bandar, A. (2012). *The ‘ State of the Art ’ in Aluminum Extrusion Simulation Using the Finite Element Method*. 541–552.
- Wang, Y., Zhao, G., Zhang, W., Sun, L., Wang, X., & Lv, Z. (2022). Interfacial bonding mechanism and length evaluation method of the longitudinal welds in the unsteady deformation process of porthole die extrusion of aluminum alloy profiles. *Journal of Materials Research and Technology*, 20, 1624–1644. <https://doi.org/10.1016/j.jmrt.2022.07.163>
- Wernet, G., Bauer, C., Steubing, B., Reinhard, J., Moreno-Ruiz, E., and Weidema, B. (2016). *EcoInvent Version 3*.
- World Economic Forum. (2020). *Aluminium for Climate: Exploring pathways to decarbonize the aluminium industry 2020*.
- Wu, H.-Y., Lee, S., & Wang, J.-Y. (1998). Solid-state bonding of iron-based alloys, steel-brass, and aluminum alloys. In *Journal of Materials Processing Technology* (Vol. 75).
- Wünning, J. G. (2007). Energy-saving possibilities for gas-fired industrial furnaces. *Heat Treating Progress*, 7(6), 37–42.
- Xie A', J. X., Murakami, T., Ikeda, K., & Takahashi, H. (1995). Experimental simulation of metal flow in porthole-die extrusion. In *Journal of Materials Processing Technology* (Vol. 49).
- Xie, C., & Tong, W. (2005). Cracking and decohesion of a thin Al<sub>2</sub>O<sub>3</sub> film on a ductile Al-5%Mg substrate. *Acta Materialia*, 53(2), 477–485. <https://doi.org/10.1016/j.actamat.2004.10.005>
- Yin, Q., Zillmann, B., Suttner, S., Gerstein, G., Biasutti, M., Tekkaya, A. E., Wagner, M. F. X., Merklein, M., Schaper, M., Halle, T., & Brosius, A. (2014). An experimental and numerical investigation of different shear test configurations for sheet metal characterization. *International Journal of Solids and Structures*, 51(5), 1066–1074. <https://doi.org/10.1016/j.ijsolstr.2013.12.006>
- Yu, J., Zhao, G., & Chen, L. (2016a). Investigation of interface evolution, microstructure and mechanical properties of solid-state bonding seams in hot extrusion process of aluminum alloy profiles. *Journal of Materials Processing Technology*. 230, 153–166.
- Yu, J., Zhao, G., Chen L. 2016b. Analysis of longitudinal weld seam defects and investigation of solid-state bonding criteria in porthole die extrusion process of aluminum alloy profiles. *Journal of Materials Processing Technology*. 237, 31-47
- Yu, J., Zhao, G., Cui, W., Chen, L., & Chen, X. (2019). Evaluating the welding quality of longitudinal welds in a hollow profile manufactured by porthole die extrusion: Experiments and simulation. *Journal of Manufacturing Processes*, 38(February), 502–515. <https://doi.org/10.1016/j.jmapro.2019.01.044>
- Yu, J., Zhao, G., Zhao, X., Chen, L., & Chen, M. (2019). Microstructures of longitudinal/transverse welds and back-end defects and their influences on the corrosion resistance and mechanical properties of

aluminum alloy extrusion profiles. *Journal of Materials Processing Technology*, 267, 1–16. <https://doi.org/10.1016/j.jmatprotec.2018.12.006>

Zhang, C., Dong, Y., Wang, C., Zhao, G., Chen, L., & Sun, W. (2017). Evolution of transverse weld during porthole extrusion of AA7N01 hollow profile. *Journal of Materials Processing Technology*, 248(January), 103–114. <https://doi.org/10.1016/j.jmatprotec.2017.05.017>

Zhang, X. M., Feng, D., Shi, X. K., & Liu, S. D. (2013). Oxide distribution and microstructure in welding zones from porthole die extrusion. *Transactions of Nonferrous Metals Society of China (English Edition)*, 23(3), 765–772. [https://doi.org/10.1016/S1003-6326\(13\)62527-3](https://doi.org/10.1016/S1003-6326(13)62527-3)

Zhu, Y. (2021). *Carbon Abatement Options for U.S. Transport and Industry*.

Zyp Coatings. (2021). *Boron Nitride Spray*. <https://www.zypcoatings.com/product/bn-glass-release-spray/>